ORNL/tr--91/23

DE92 000159

FOEHN:
The Critical Experiment for the Franco-German High Flux Reactor

K. Scharmer and H. G. Eckert

Institut fuer Neutronenphysik und Reaktortechnik
Institut fuer Angewandte Kernphysik
Kernforschungszentrum Karlsruhe

Translated from the German.* Report KFK 1064 issued by Kernforschungszentrum Karlsruhe, December 1971, 185 pages.

---

* By LANGUAGE SERVICES, Knoxville, Tennessee

Abstract

A critical experiment for the Franco-German High Flux Reactor was carried out in the French reactor EOLE (CEN Cadarache). The purpose of the experiment was to check the calculation methods in a realistic geometry and to measure effects that can only be calculated imprecisely (e.g. beam hole effects). The structure of the experiment and the measurement and calculation methods are described. A detailed comparison between theoretical and experimental results was performed.

Table of Contents

---

* First page of table of contents (page i) missing from copy supplied to translator and reconstructed from text -- Translator's Note.

** Section missing from copy supplied to translator--Translator's Note.

Page

Page

Page

ABSTRACT

A critical experiment was carried out for the heavy-water-cooled Franco-German High Flux Reactor that made it possible to test the calculation methods used to design the reactor and to determine the parameters that cannot be calculated.

The factors investigated were the control rod characteristics, the reactivity value of B^{10} dissolved in the core, the flux and power distributions, and gamma heating for reactors with and without solid boron and for experimental equipment in the reflector. In addition, the safety rod shutdown effect, the temperature coefficient and the reactivity of experimental equipment was measured. The experimental and theoretical results are in satisfactory agreement, except for the reactivity of the beam holes, which is underestimated by the calculation.

PREFACE

The structure of the FOEHN experiment and the performance of the measurements were handled by the SPM/EOLE Group at the Centre d'Etudes Nucleaires Cadarache in France. The following persons were responsible for the various areas:

J. BAILLY	Management and Organization
J. BERGERON	Measurements at the Exiting Beam Hole
Ph. de BEAUCOURT	(SEPP, Fontenay-aux-Roses) Fast Flux Measurement Using Sulfur Probes, Gamma Flux Measurement Using Ionization Chambers
P. COULON	Flux and Power Measurements
P. COURBIERE	Evaluation of Reactivity Measurements
J. CRAY	B^{10} Analyses
R. DEL NEGRO	Technical Management
R. JAQUEMART	Kinetic Measurements
J. TASTE	Spectrum Measurements and Data Processing

The successful performance of the critical experiment FOEHN is largely due to the participation of the above individuals and the technical staff of EOLE.

We would also like to take this opportunity to thank Mireille Nobile and Jeanine Thibor for their help in carrying out the extensive calculations and E. Piesch in evaluating the glass dosimeters.

The authors are especially grateful to M. Kuechle for his help is setting up the measurement program, for his experienced advice in selecting measurement methods and for countless discussions regarding evaluation of the results.

LIST OF FIGURES

5.6.2	a = reactivity of the reactor during heatup, normalized to = 0 at 20°C; b = reactivity by heating the reflector; c = reactivity by heating the core; d = reactivity by heating the stack; e = reciprocal value of D_2O density as a function of temperature
5.6.3	Curve of temperature coefficient
5.8.1	Aluminum reactivity in the reflector midplane as a function of the radius
5.9.1	Gamma heating in the reflector
5.9.2	Gamma heating in the reflector
5.9.3	Gamma heating on the axis of the exiting beam hole
5.9.4	Gamma heating on the longitudinal axis of the cold source
5.9.5	Gamma heating on the longitudinal axis and the transverse axis of the hot source
5.10.1	Curve of the inverse counting rate during reactor startup
5.11.1	$_c$ as a function of control rod position
6.1	Longitudinal section through the reactor block of the Franco-German High Flux Reactor
6.2	Cross section through the reflector tank of the High Flux Reactor

1. INTRODUCTION

As regards neutron physics, the Franco-German High Flux Reactor [1, 2] was designed almost exclusively on the basis of an extended theoretical study. The critical experiment ALIZE III [3, 4] made it possible to check at a relatively early state the validity of the calculation methods used. This experiment reproduced only a few of the characteristic properties of the High Flux Reactor correctly, namely the narrow fuel zone and the heavy water reflector, but it had a core moderated with light water and did not correspond very closely to the High Flux Reactor as regards core and reflector geometry. The High Flux Reactor has a very specific structure: the core consists of only a single fuel element; consequently there is no possibility of varying the critical mass, the total control reactivity is housed in one rod, and the reactivity of the solid boron zones and the experimental equipment in the reflector cannot be calculated very well. Because of this it was necessary to carry out a critical experiment, the structure of which would correspond to the High Flux Reactor as accurately as possible in all parts. This was implemented in the experiment FOEHN.

The main goal was to obtain answers to the following questions:

- To what extent are the methods for calculating reactivity and also flux and power distribution valid?

- How great is the reactivity of internal components for which calculation does not provide satisfactory results, such as experimental equipment, solid boron, etc., and what are the corresponding flux distributions?

- How must the calculation methods used to date be changed in order to be extrapolated from the experiment to the High Flux Reactor?

The experimental program is constructed accordingly. The first part of the test program deals with a reactor without reflector internals and solid boron. The excess reactivity is compensated for by boron dissolved in the core and by the central control rod. This relatively simple geometry lends itself most readily to checking the calculation methods experimentally.

In the second part of the program the solid boron zones are attached to the core ends and their effect investigated. In the third part dummies for the high flux reactor experimental equipment are installed in the reflector, and their effect on reactivity and flux and power distribution in the system is measured.

The fourth and last part of the test program deals with the safety rods, the void and temperature coefficients, and the effect of the spatial position of the source and detector on the 1/M curve during reactor startup.

The most important test results are summarized in this report and are compared with the theoretical results.

2. STRUCTURE OF THE EXPERIMENT

The experiment entitled FOEHN was carried out in the French reactor EOLE [5] at Centre d'Etudes Nucleaires Cadarache. EOLE was appropriately modified for this purpose. The reactor and its internals will be described below to the extent necessary for understanding the tests (see also [6]). Figure 2.1 shows a vertical section through the reactor.

2.1 Description of the Reactor

2.1.1 The Core

The fuel zone has the shape of a hollow cylinder and a height of 80 cm, an outside radius of 19.5 cm and an inside radius of 14 cm. It is constructed of plates bent in the shape of involutes; they contain the fuel, which is in the form of a uranium-aluminum alloy. In order to obtain the most unambiguous fuel zone geometry possible, the fuel is not clad along the edges of the plates.

Characteristics of the fuel plates:

Fuel	U-Al alloy with 90% U-235
Load	0.0568 g U-235/cm^2
Total U-235 mass	8556 g
Number of plates in core	276
Plate length	80 +0/-0.05 cm
Plate width	6.83 +0/-0.02 cm
Plate thickness	0.127 +0/-0.005 cm
Thickness of lateral Al cladding	0,01 cm

The plates are involute-shaped between the radii 14 cm and 19.5 cm. The evolute radius is 13.4855 cm. A gap of 0.18 cm remains between the assembled plates (see Figure 2.2).

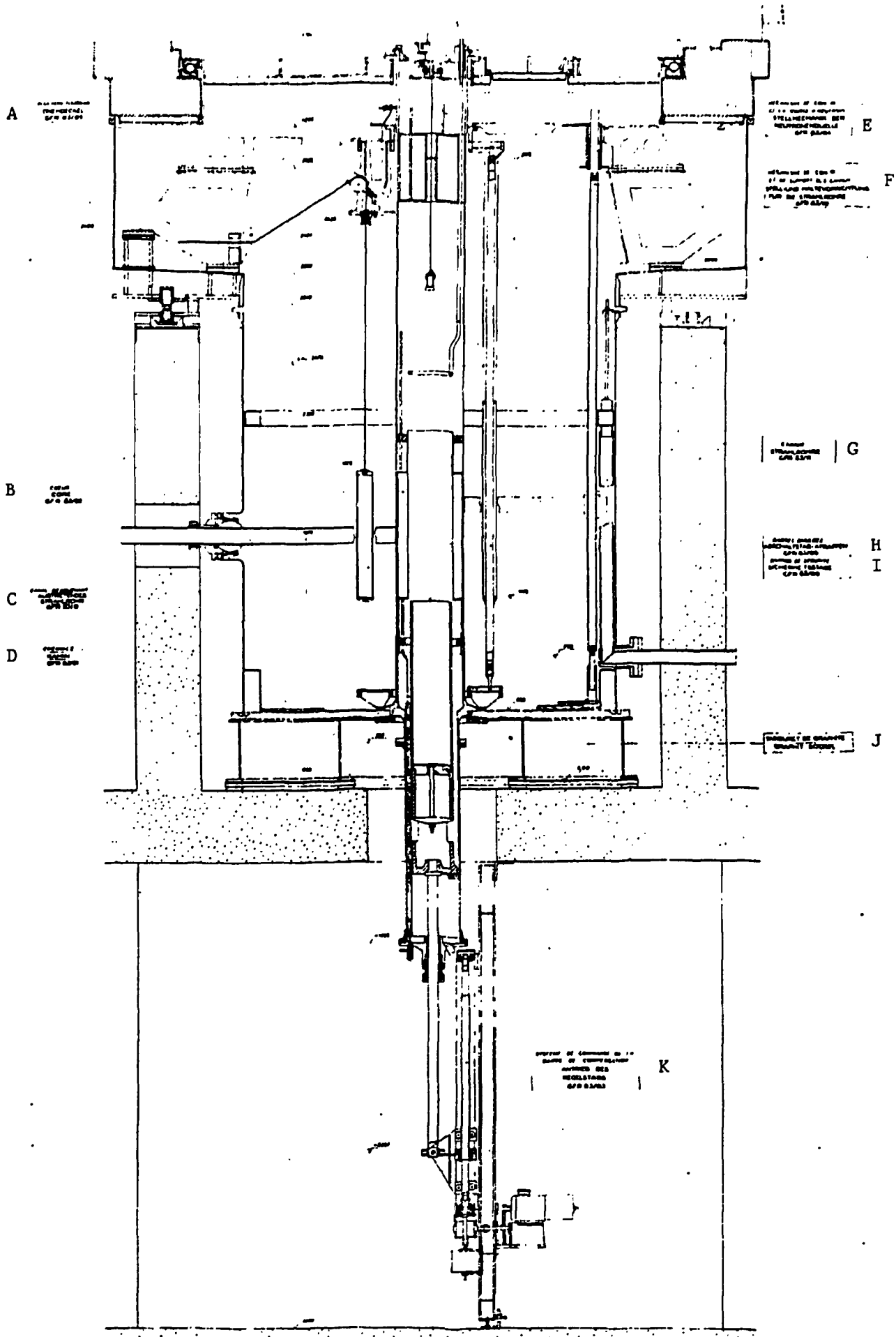

Fig. 2.1. Vertical section through FOEHN [see next page for key]

[Key to Figure 2.1:]

A rotating plug
B core
C protruding beam hole
D stack
E adjustment mechanism of neutron source
F adjustment and holding device for the beam holes
G beam holes
H shutdown rod dummies
I safety rods
J graphite base
K control rod drive

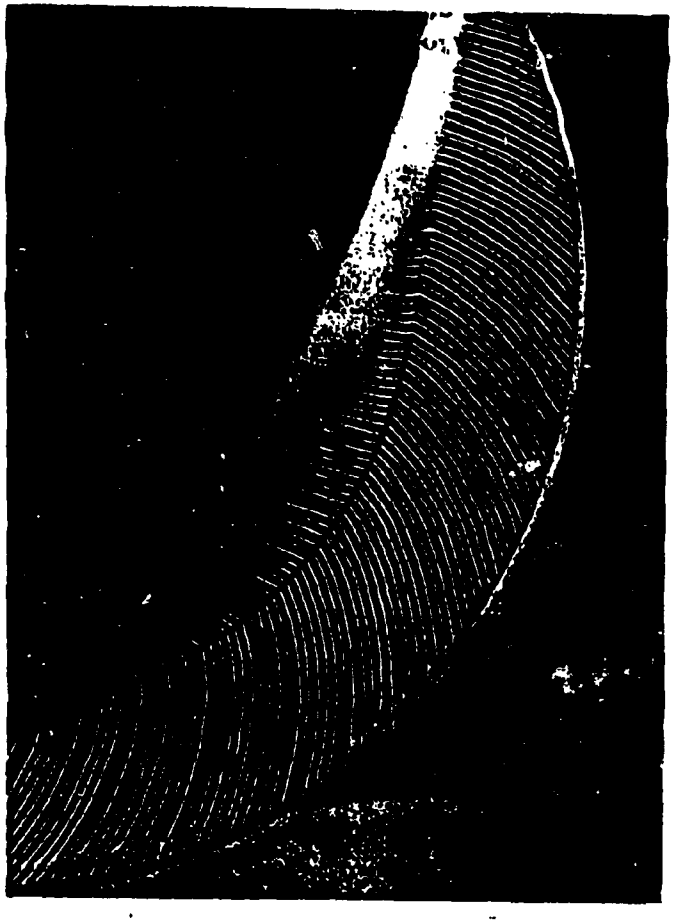

Fig. 2.2 Assembled fuel plates -- top view

Fig. 2.3 Structure of the fuel zone

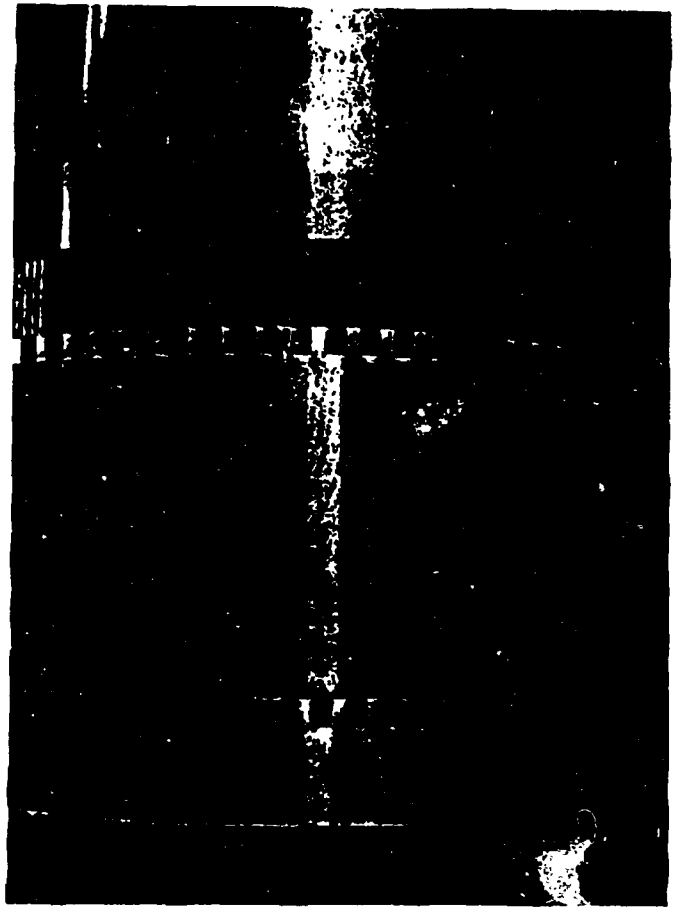

Fig. 2.4 Holding fuel plates on outside radius by means of riders

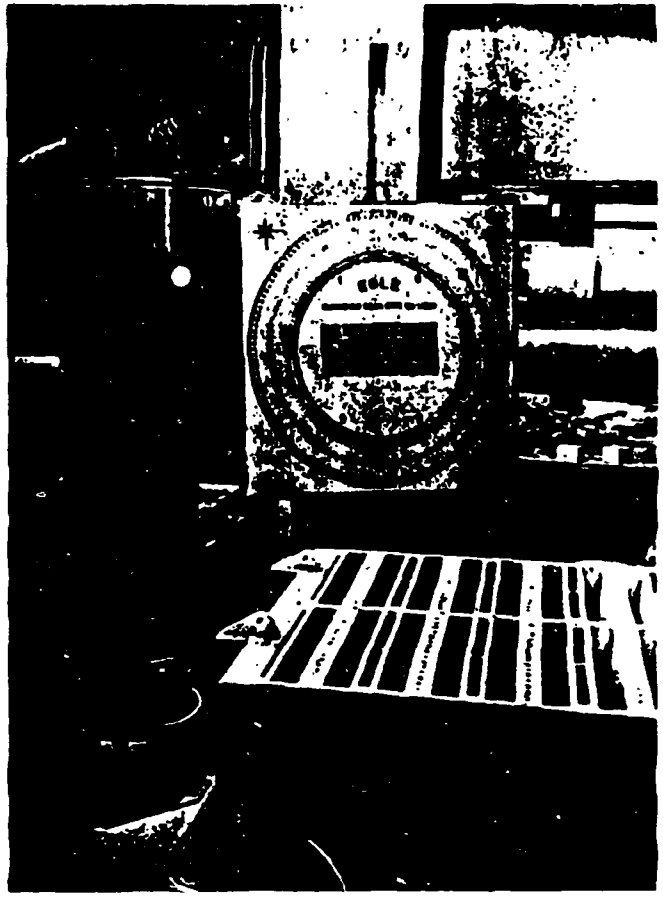

Fig. 2.5 View of core, almost completely assembled

The plates are assembled in a core barrel. On the inner radius they are held by 6 combs distributed over the core height and milled out of the inside wall of the core barrel. The comb teeth are 1 cm long and 0.2 cm high (see Figure 2.3). On the inside radius the plates are held by small riders, which are mounted on the plates. The portion of the riders that protrudes to the outside fits in recesses of the outer 7 holding rings, which separate the fuel zone from the outside over its entire height (see Figures 2.4 and 2.5). The outside wall of the core barrel is fitted over the core, assembled as described above, so that a watertight vessel is formed, which is connected to the core loop by a 1 cm thick Al pipe (see Figure 2.6). The core barrel must be leaktight because a portion of the excess reactivity is compensated by boron dissolved in the core, and the entry of boron into the reflector must be avoided. All core structures are fabricated from the aluminum alloy AG 3-NE.

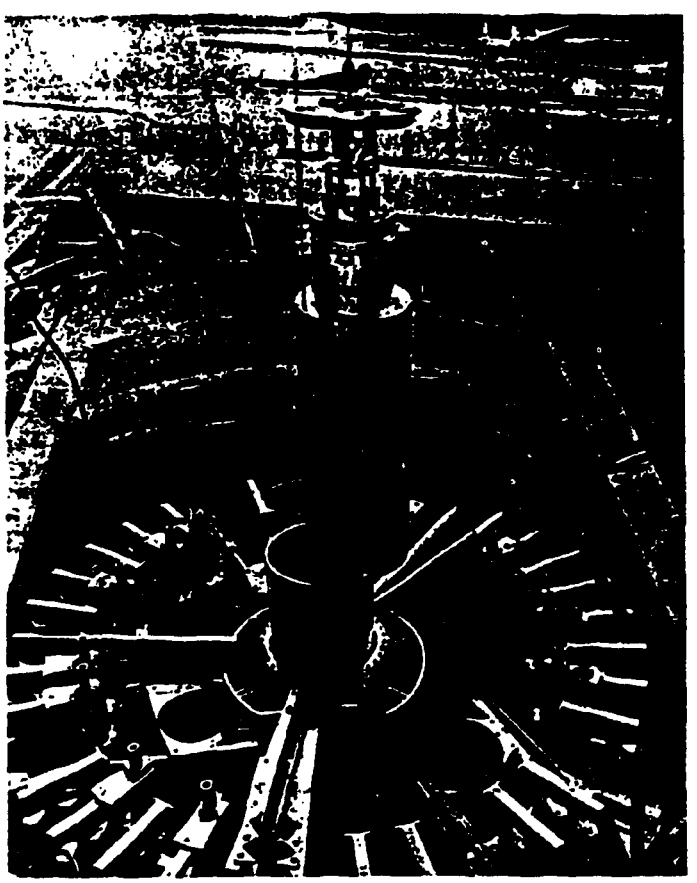

Fig. 2.6 The core is installed in the central stack

All parts of the core are coated with an epoxy phenol resin so that good runoff of the heavy water from the gaps is guaranteed and contamination of the surfaces by the boron dissolved in the loop will be avoided. The resin was deuterized before startup.

The free volume in the fuel zone was determined on the basis of the dimensions of the fuel plates and core structures as measured after fabrication. We obtain

$$V_{D2O\ solution} = 27{,}000\ cm^3.$$

The total free volume in the core barrel, i.e., including the gaps around the fuel zone, was measured as

$$28{,}850\ cm^3.$$

The exact knowledge of these volumes is necessary in order to be able to compare the experiment with the calculations.

2.1.2 The Reflector

The core is located in the center of a cylindrical tank filled with D_2O having the following dimensions:

diameter:	230 cm,
height of D_2O:	220 cm.

A stack passes through the tank axially; it extends to the upper rotating plug and has the function of guiding the core and preventing the entire amount of heavy water in the reflector from being contaminated by boron in the event of a leak in the core barrel. In addition, the stack simulates more or less the structures of the High Flux Reactor above and below the core.

2.1.3 The Loops

2.1.3.1 The Core Loop

The core loop makes it possible to fill the core barrel with heavy water or a solution of heavy water and boron anhydride or to empty it into a supply vessel. Samples of the solution can be taken by way of a suitably designed valve in order to analyze the boron concentration. To avoid an overflow of the solution and contamination of the D_2O in the stack, a collector vessel is mounted above the core.

2.1.3.2 The Stack Loop

The stack is sealed off from the radial reflector. It has its own loop, which can be heated and cooled (see Figure 2.7).

2.1.3.3 The Reflector Loop

The reflector look can also be heated and cooled like the stack loop. In order to guarantee uniform temperature distribution in the reflector, the tank is thermally insulated from the outside.

All loops are equipped with electrical level indicators and temperature measuring points.

2.1.4 Control Elements and Safety System

The excess reactivity of the reactor is compensated partly by the boron dissolved in the D_2O of the core and partly by a control rod that is inserted from below into the central flux trap that is surrounded by the core. The absorber section of this control rod is a tube of metallic nickel having the following dimensions:

length	100 cm
outside radius	12.6 cm
wall thickness	0.5 cm

It sits on a sled, which is driven by an electric motor via a rod and a worm gear (see Figure 2.7). The rod can be operated at two speeds:

upwards at 0.2 cm/sec and 0.1 cm/sec,
downwards at 0.1 cm/sec.

The rod position is indicated by a phase valve (Selsyn) with an accuracy of $\pm$0.01 cm. The total distance that the rod can travel is 103 cm (see Figure 2.1).

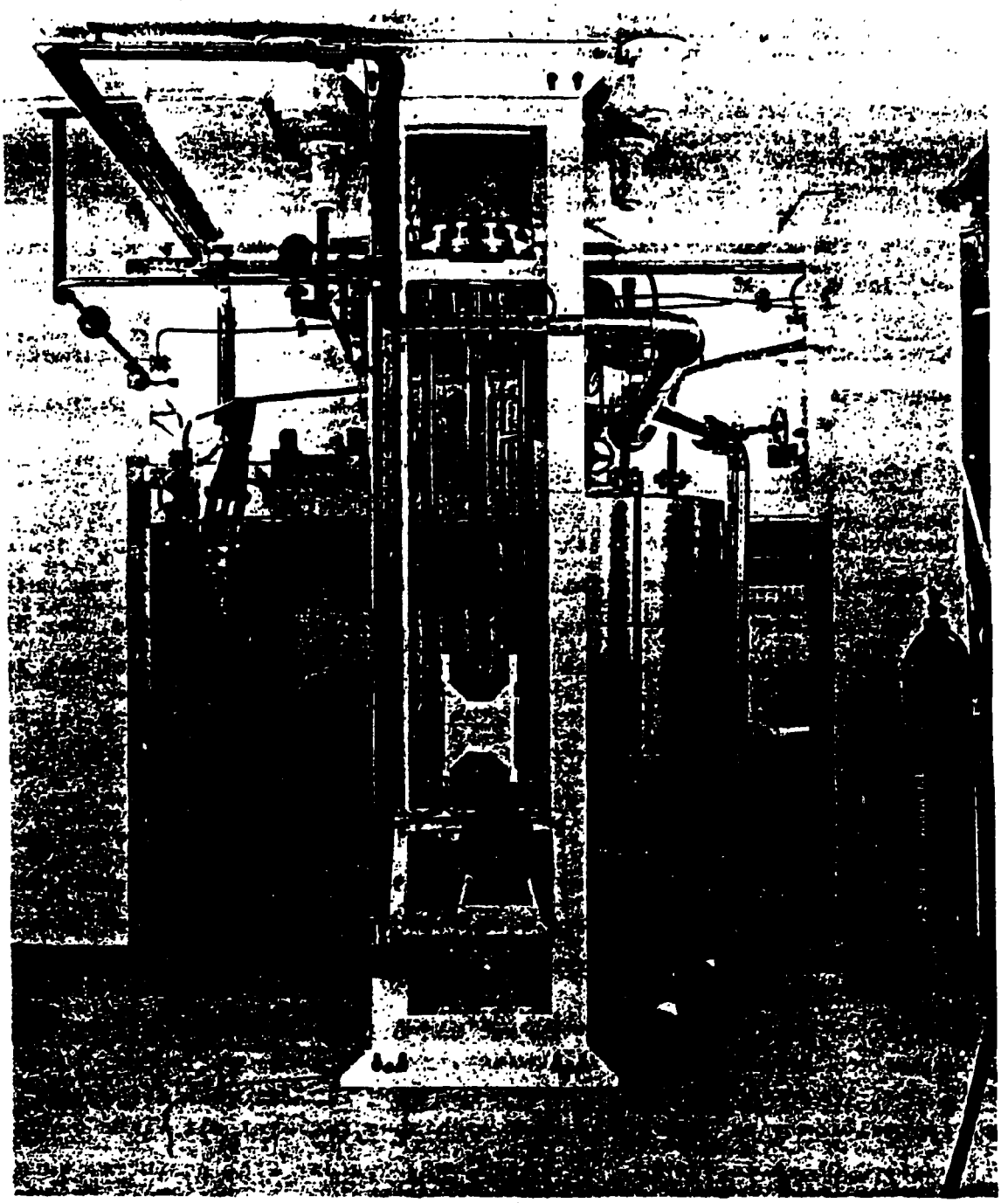

Fig. 2.7 Space below the reactor. In the foreground the control rod drive is visible, in the background on the left the supply tank for the core loop, and on the right the heat-insulated tank of the stack loop.

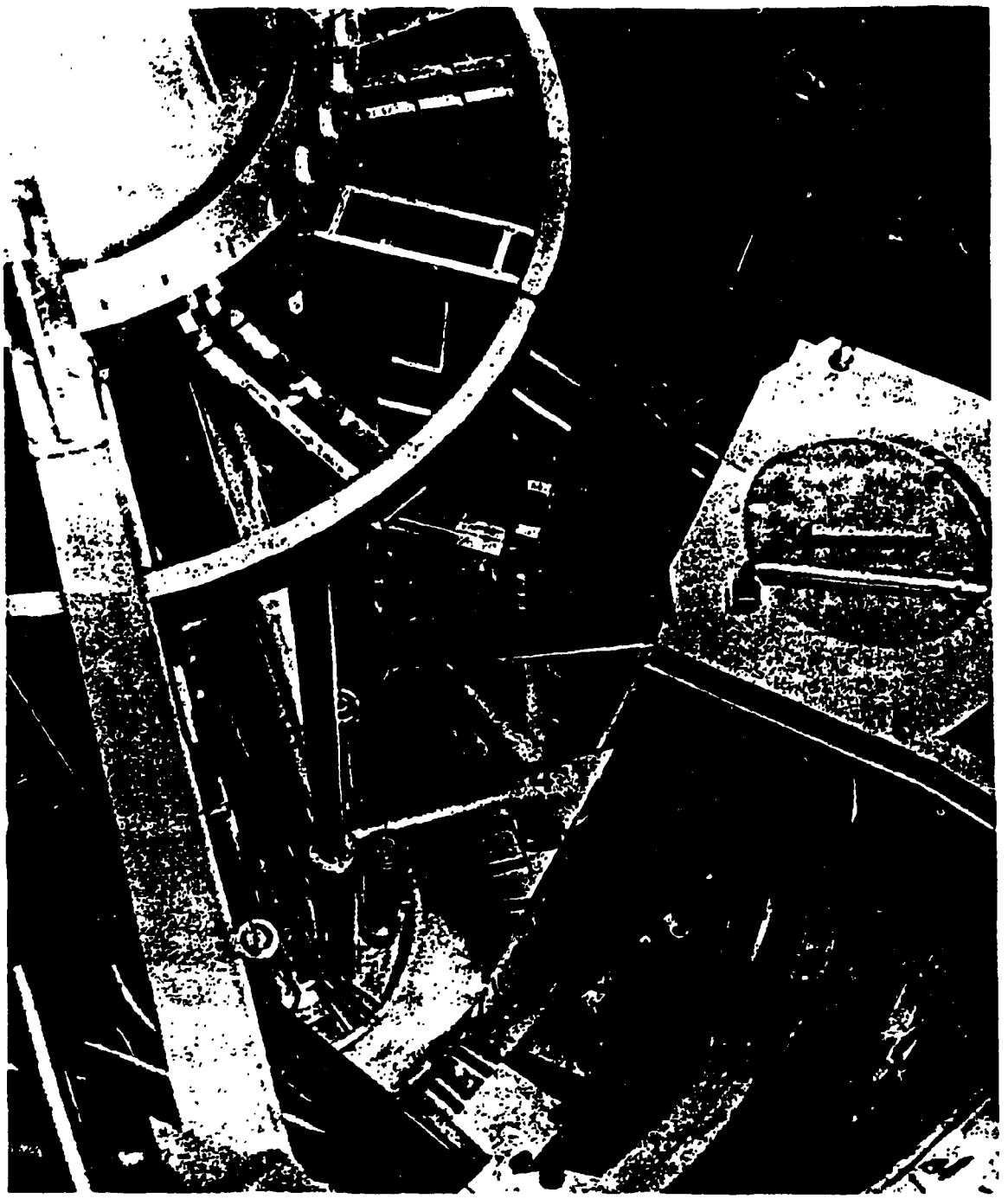

Fig. 2.8 View into the reflector tank. - (1) Reactor safety rod, (2) simulated safety rod, (3) support rod for the simulated rod, (4) beam hole dummies, (5) beam hole dummy for conversion electrons, (6) central stack.

[Pages 11 and 13 of the original German text were missing from the copy provided to the translator. Thus the final portions of Section 2.1, the entire Section 2.2 and the beginning portions of Section 2.3 (including the first part of 2.3.1) are missing. Since the first page of the table of contents, page i, was also missing, it is impossible to include even the titles for these missing sections.

The text continues with the end of Section 2.3.1

-- Translator's Note.]

... it is flanged to a vertical support rod. The beam hole can be adjusted as regards angle and height by means of a mechanism on the upper end of the support rod, which is accessible through an opening in the rotary plug (see Figure 2.9).

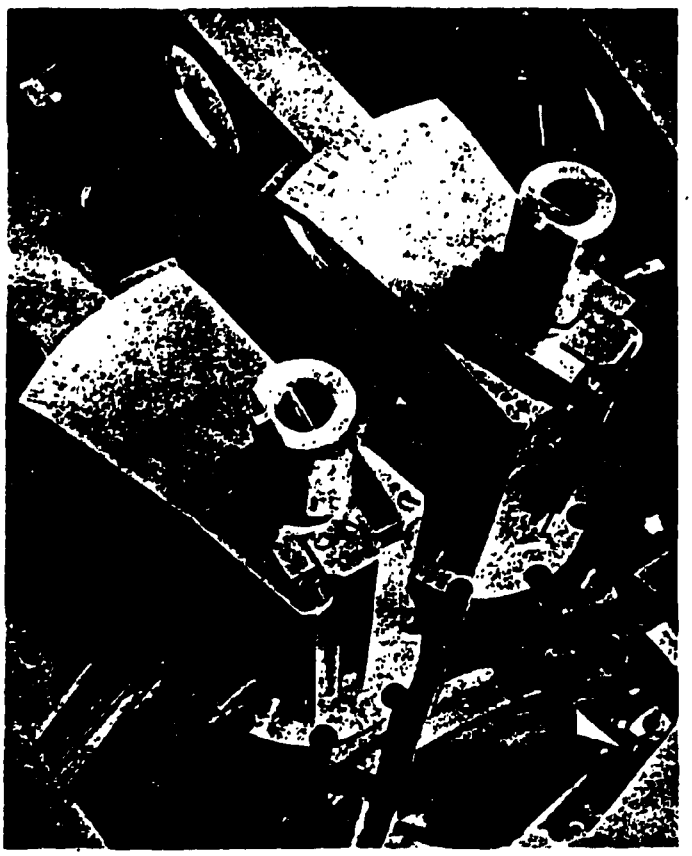

Fig. 2.9. Positioning mechanism of the dummy beam holes

Figure 2.12 shows a section through the dummy of the hot source. It is held by cross beams above the D_2O surface.

The cold source is simulated by an aluminum vessel having an inside diameter of 40 cm and a height of 50 cm. The wall thickness is 0.5 cm. The liquid deuterium is replaced by heavy water. The effect of the cold moderator on the absorption is the wall is simulated by an increase in the wall

thickness, by an aluminum bell having a wall thickness of 0.3 cm, which can be fitted over the source container (see Figure 2.13).

The vertical channel for beta spectrometry has in inside diameter of 20 cm and a wall thickness of 0.2 cm. It passes through the reflector to its total height.

The pneumatic transport systems are simulated by vertical Al tubes with an inside diameter of 4 cm and a wall thickness of 0.2 cm.

A horizontal beam hole is led through the reflector tank wall to the outside. It can be adjusted in the azimuthal and axial directions (see Figure 2.10). Figure 2.11 gives a view of the reactor with the rotary plug removed.

2.3.2 Safety Rods

For safety reasons it was not possible to install the shutdown rods of the High Flux Reactor in the same slanted position in FOEHN. In addition, the decision to use only 5 rods instead of 6 was made at a time when it was no longer possible to change the FOEHN design.

Six (6) dummy safety rods are used; they are supported by upright aluminum guide tubes having a diameter of 4 cm and a wall thickness of 0.4 cm. The safety rods consist of 0.2 cm thick cadmium tubes having an outside diameter of 9 cm and a length of 150 cm. The cadmium has a 0.05 cm thick stainless steel cladding. In the inside of the rods is located D_2O and the aluminum guide tube. The rod insertion depth and the radius on which they stand can be varied gradually.

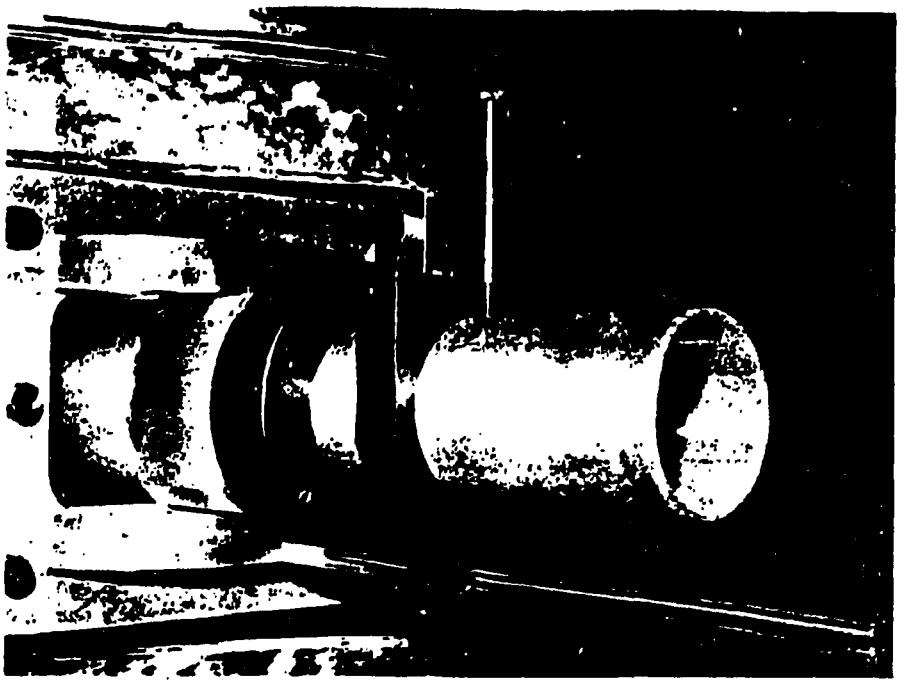

Fig. 2.10 Exiting beam hole. Turning knuckle and beam hole end outside the D_2O tank.

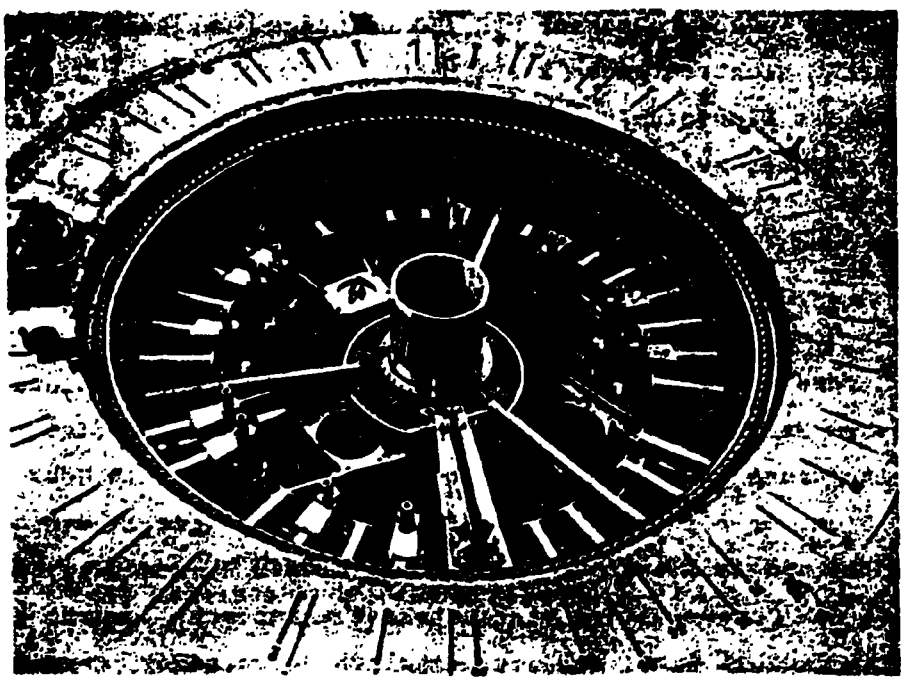

Fig. 2.11 View of reactor without rotary plug. - (1) beam hole positioning mechanism, (2) cold source guide tube, (3) hot source guide tube, (4) beam hole for conversion electrons.

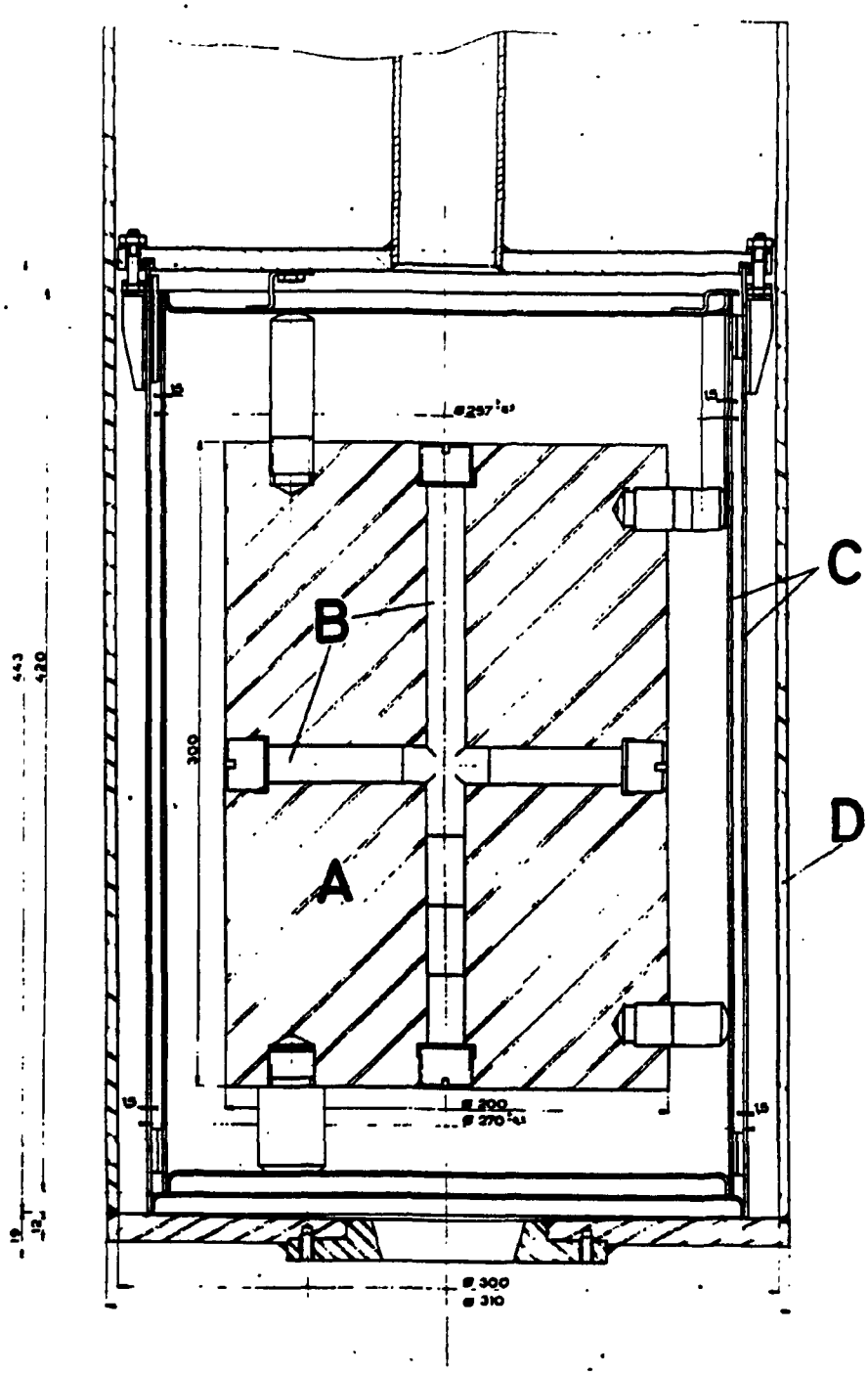

Fig. 2.12 Vertical section through the hot source dummy. (A) Graphite block, (B) measuring probe holes, (C) Zircaloy vessel, (D) Al guide tube.

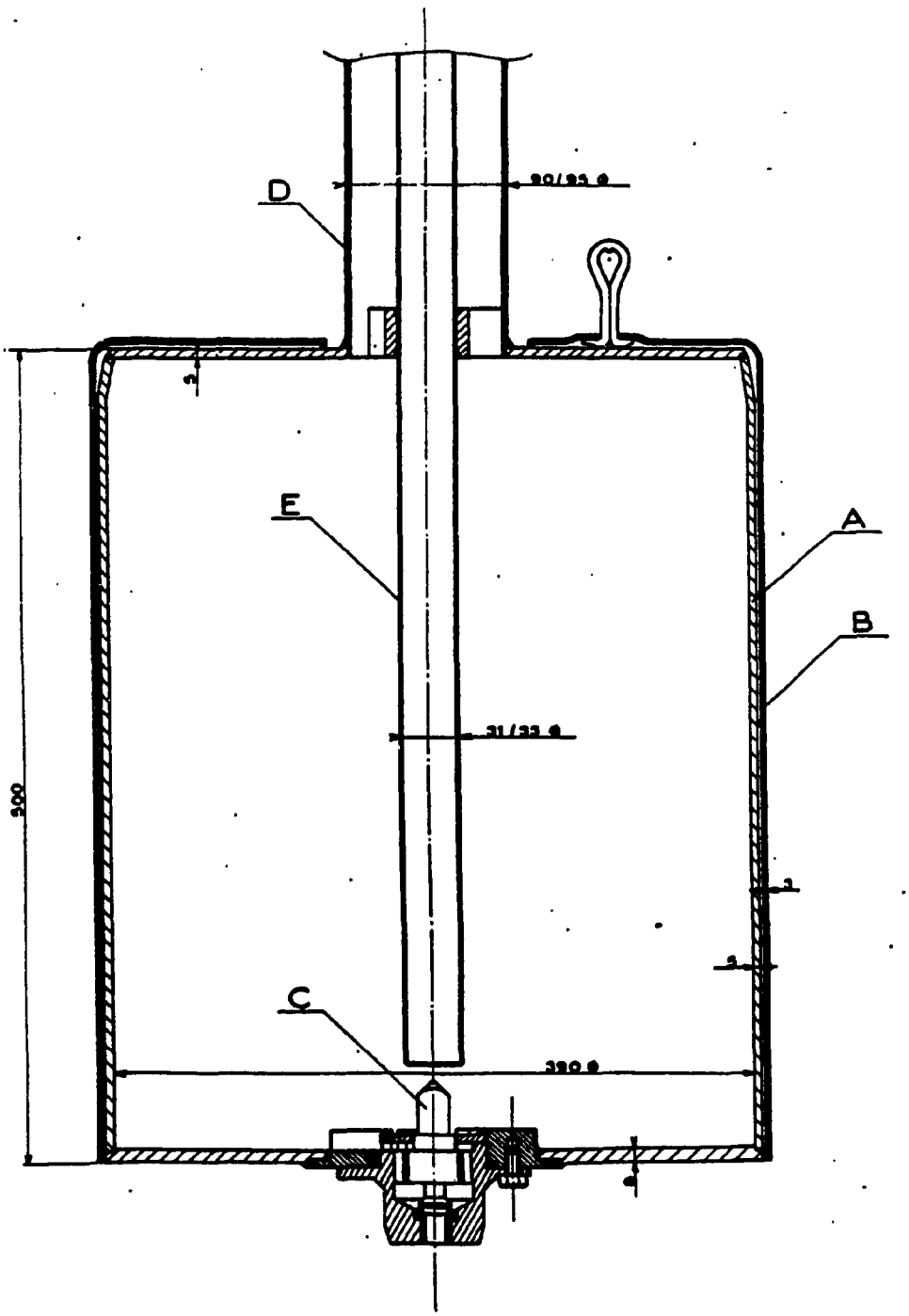

Fig. 2.13 Vertical section through the dummy of the cold source. (A) source vessel, (B) bell, (C) valve, (D) holding tube, (E) guide tube for test probes.

2.3.3 Solid Boron

A portion of the excess reactivity of the High Flux Reactor is compensated by boron zones at both core ends, which also flatten the power peaks there at the same time. The boron burns off in the course of the reactor cycle. It is housed in the extension of the fuel plate, it is 3 cm high, and it is limited by the same radii as the fuel, i.e., 14 and 19.5 cm. For simulating these boron zones in FOEHN it is possible to attach to the ends of the core barrel plate packages, the composition of which is selected such that they correspond with respect to boron load, geometry and metal to D_2O ratio to the boron zones of the High Flux Reactor. The packages consist of horizontal, borated aluminum plates and pure aluminum plates 0.1 cm thick, which are assembled by means of vertical pins and spacer rings.

2.4 Differences between FOEHN and the High Flux Reactor

The structure of FOEHN accurately reproduces the High Flux Reactor (HFR) in so far as possible. In some cases, however, this was not feasible. We present below a list of the differences that are significant from a neutron-physical standpoint (cf. Figures 2.1 and 6.1).

D_2O Reflector Dimensions:

FOEHN: R = 115 cm, H = 221 cm

HFR: R = 125 cm, H = 250 cm.

In addition, the D_2O tank of the HFR is surrounded by an effectively infinite, thick H_2O reflector.

The D_2O reflector of the HFR is precisely cylindrical, and the core sits 10 cm above the reflector midplane.

Aluminum Structural Material around the Core:

External wall thickness	1.1 cm Al	0.8 cm Al
Internal wall	0.61 cm Al	0.68 cm Al
Between fuel and solid boron	0.6 cm Al	0.41 cm Al

Control Rod:

The HFR control rod has in its lower section to a length of 40 cm twice the wall thickness as the FOEHN control rod.

Boron Zones:

The load of individual boron plates in FOEHN is higher than that in the HFR, i.e., there the self-shielding in the plate is smaller.

Dissolved Boron in the Core:

In FOEHN a part of the excess reactivity is compensated by dissolved boron, i.e., the absorption in the FOEHN core is greater than in the HFR core.

Safety Rods:

Only 6 upright rods of 0.1 cm cadmium [illegible]st having an outside diameter of 9 cm can be installed in FOEHN, whereas HFR is shut down

by 5 rods that are slanted slightly with respect to the vertical; they have an outside diameter of 10 cm and consist of an alloy of 0.80 Ag, 0.05 Cd and 0.15 In.

Reflector Internals (Beam Hole, Sources):

The wall thickness of the so-called standard beam holes in the High Flux Reactor having a diameter of 10 cm on the nose will amount to approximately 0.4 cm; they will be slightly tapered towards the outside and closed off at the nose by a 0.2 cm thick semi-spherical shell of aluminum, whereas the corresponding dummies in FOEHN are simple hollow cylinders 10 cm in diameter with a wall thickness of 0.2 cm, which are sealed on the ends by a flat 0.2 cm thick aluminum plate.

The dummy of the hot source corresponds essentially to the real hot source; no final solution has yet been reached for the cold source.

3. CALCULATION METHODS

3.1 Diffusion Calculations

All calculations of reactor reactivity and macroscopic thermal and epithermal flux distribution are carried out on the basis of diffusion theory using the program ALCI [7].

We use 6 energy groups having the following limits:

1	fast group	10 MeV - 0.821 MeV
2	intermediate group	821 keV - 5.5 keV
3	epithermal group	5.5 keV - 0.625 eV
4	thermal group, core	0.625 eV - 0 eV
5	thermal group, reflector	0.625 eV - 0 eV
6	thermal group, flux trap	0.625 eV - 0 eV.

The neutrons of the 3 thermal groups diffuse in the system independent of one another without any interaction.

3.1.1 Group Constants

The group constants for Groups 1 to 3 were calculated using the code MUFT IV in the version FORM [8], whereby braking in heavy water was based on the age theory. In these calculations the spectrum of an infinitely extended medium was assumed. However, this does not agree well with reality, especially for the core zone. By means of an iteration calculation it was found that the reactivity of a reactor is 750 pcm higher when the fast group constants are calculated in an infinitely extended medium (buckling $B^2 = 0$) that the reactivity of a reactor in which the outflow from the core in the fast groups is just as great as the outflow with which the fast core data were calculated. In order not to have to carry out this calculation again for each core mixture, all fast data are calculated without outflow and the calculated reactivity of the reactor reduced by 750 pcm.

The constants for thermal groups 4 to 6 were determined using the one-dimensional thermalization transport code THERMOS [9]. The geometry corresponded to a horizontal section through the reactor (see Fig. 3.1).

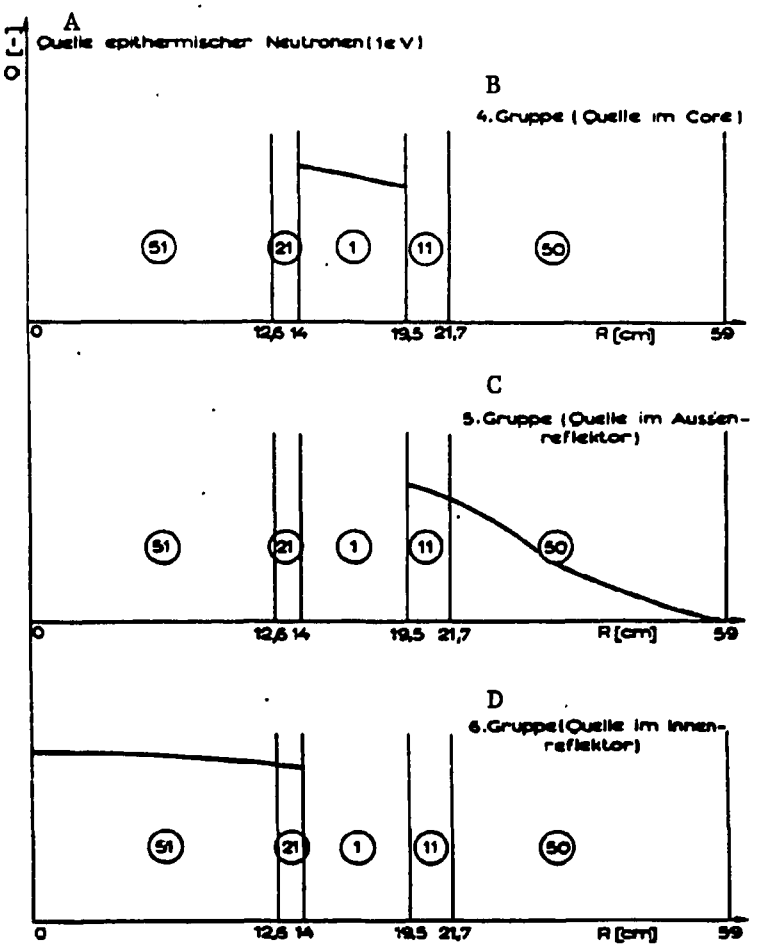

Fig. 3.1 Geometry and source distribution for the THERMOS calculations. 1 = core, 11 = external tank, 21 = internal tank, 50 = external reflector (D_2O), 51 = internal reflector (D_2O).
A source of epithermal neutrons (1 eV)
B 4th group (source in core)
C 5th group (source in external reflector)
D 6th group (source in internal reflector)

The source of epithermal neutrons (1 eV) corresponded to the epithermal flux distribution of a diffusion calculation. It was found for

Group 4 in the fuel zone

Group 5 in the external reflector,

Group 6 in the flux trap.

The absorption and fission cross sections are determined by the code as a mean value over the spectrum and the zone

$$\sigma = \frac{\int_E \int_R dE\ dr\ \phi(E,r)\ \sigma(E,r)}{\int_E \int_R dE\ dr\ \phi(E,r)} \qquad (3.1)$$

The group constants used for the most important materials are listed in Table 3.1.

The diffusion constants for the 5th and 6th groups were determined such that a diffusion calculation in the same geometry (infinite cylinder) for the corresponding energy group yields the same ratio of maximum to mean fission rate $S_{max}/\overline{S}$ in the fuel zone as the THERMOS calculation. (The fission rate in a 5 mm wide strip on the outer core rim is selected as the maximum fission rate. This corresponds more or less to the "hot thread of stream" for the core thermodynamics.)

In the 4th group the diffusion coefficient determine by THERMOS is used. Figure 3.2 shows the power distribution in an infinite cylinder, which is calculated using THERMOS and also using the diffusion theory. The fission rate ratio ($S_{max}/\overline{S}$) based on the diffusion calculation, which is obtained by superposition of the 3 thermal groups, is 4.3% lower than the ratio calculated with THERMOS. This effect must be taken into account in the thermodynamic design of the core.

3.1.2 Geometry for the Diffusion Calculations

The geometry of the reactor (see Figure 2.1) was simplified for the diffusion calculation so that the capacity of the code ALCI is not exceeded and the calculation times remain reasonable, but so that k_{eff} and the flux and power distributions are reproduced as accurately as possible. The

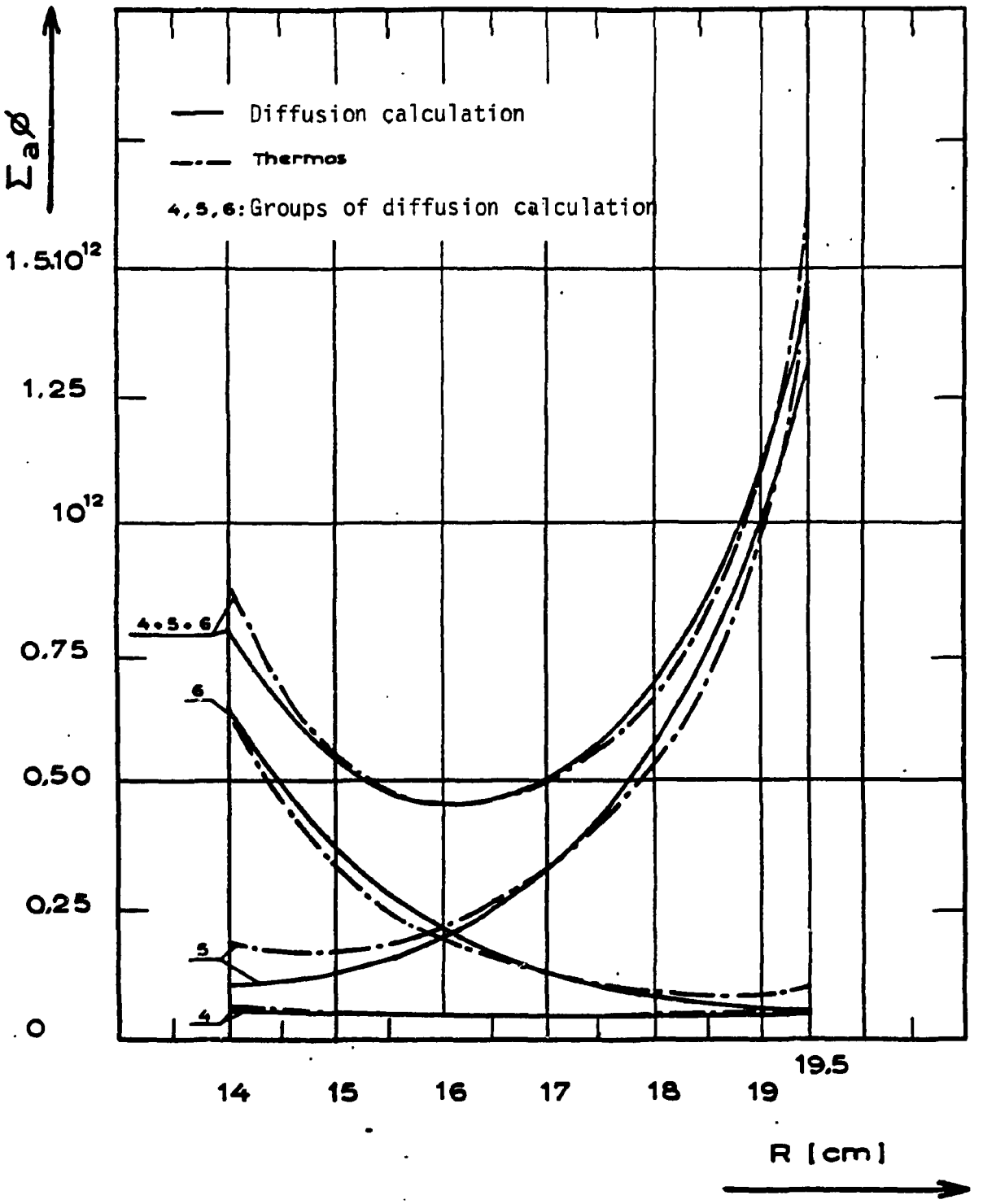

Fig. 3.2 Absorption distribution in an infinite hollow cylinder, calculated with THERMOS and on the basis of the diffusion calculation

structural material--aluminum--was mixed with D_2O so that zones that diffuse sufficiently well are formed. In the core zone the fuel plates were homogenized with the borated D_2O, whereby the fine structure of the flux was taken into account (see Section 3.2). In order not to eliminate the local perturbation of the central control rod with the flux and power distribution, the nickel was not mixed with D_2O but was treated in the calculation as a pure metal in its real geometry. The holding structure made of aluminum, which is inside the nickel pipe, was pounded on to the nickel, so that for calculation purposes an effective thickness of 0.51 cm was obtained.

Below the D_2O tank is a graphite base containing the counting tubes of the reactor instrumentation, and in a downward extension of the reactor axis is a D_2O-filled cylinder with the guide structure for the control rod. These parts act as a reflector, increase the k_{eff} value, and shift the flux distribution somewhat. They were simulated in the calculation by a D_2O layer which brings about the same flux shift but yields a 50 pcm higher reactivity amount.

Figure 3.3 shows the geometric diagram used in the diffusion calculations. The numbers in the individual zones correspond to the materials listed in Table 3.1 and the corresponding group constants.

3.2 The Disadvantage Factor in the Core

The fuel zone is constructed of aluminum plates that contain the uranium. Between these plates are gaps which contain boron-poisoned D_2O. Since the plates absorb to a much greater degree than the borated D_2O, the neutron flux in the plates will also be lower than in the water gap. This effect can be taken into account in the diffusion calculation--where fuel plates, D_2O and boron are considered to be a homogeneous mixture--by multiplying the boron absorption by a factor g, which is explained as follows:

$$k_{eff} \simeq \frac{\Sigma_f \phi_p}{\Sigma_{a,p} \phi_p + \Sigma_{a,B} \phi_B} \qquad (3.2)$$

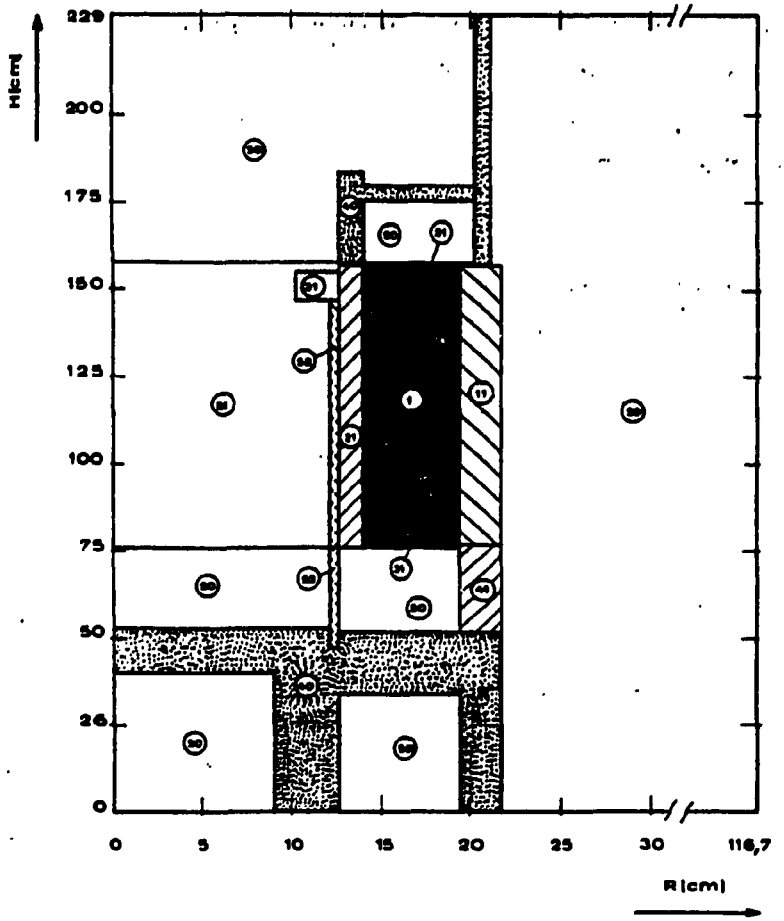

Fig. 3.3 Geometric diagram of the reactor for two-dimensional diffusion calculations

$$k_{eff} \simeq \frac{\Sigma_f}{\Sigma_{a,p} + \Sigma_{a,B} \frac{\phi_B}{\phi_p}} = \frac{\Sigma_f}{\Sigma_{a,p} + \frac{1}{g} \Sigma_{a,B}} , \qquad (3.3)$$

where $\Sigma_{a,p}$ = absorption cross section of fuel plate,

$\Sigma_{a,B}$ = absorption cross section of boron,

ϕ_p = flux in the plate,

ϕ_B = flux in boron (in D_2O gap),

g = ϕ_p/ϕ_B.

In the homogeneous mixture the boron reactivity is underestimated, therefore, by a factor g.

The calculation of g is not simple in the present case, since the flux in the core is not isotropic everywhere and the strength of the anisotropy varies with the radius. This is due to the fact that practically all thermal neutrons from the reflector into the core and that, in addition, the orientation of the plates with respect to the flux gradient varies with the radius.

The fine structure of the flux on three cylindrical plates was calculated using the program THERMOS. It is shown in Figures 3.4 and 3.5, together with the geometric diagram of the calculation. We obtain

$$g_{THERMOS} = 0.969.$$

For the isotropic flux in an infinitely extended plate lattice it is possible to calculate g easily on the basis of the integral transport theory [10]. The result is

$$g_{isotropic} = 0.947.$$

The real value will lie between the two. However, $g_{THERMOS}$ was used so that the calculation has the tendency of overestimating the boron reactivity.

3.3 Group Constants for the Solid Boron Zones

The solid boron zones on the core ends represent a much greater problem for treatment based on the diffusion theory than the fuel zone. Its absorption is even greater ($\Sigma_{a,\ therm.} \simeq 0.3$). And the flux drop in the plates is much more pronounced since the boron-aluminum plates have an absorption cross section that is about 2.3 times greater than the fuel plates. Because of the complicated, truly three-dimensional geometry it is difficult to cover the spectrum correctly and determine the diffusion coefficient so that it reproduces the flux distribution in the boron zone correction, if one only has available a one-dimensional thermalization program.

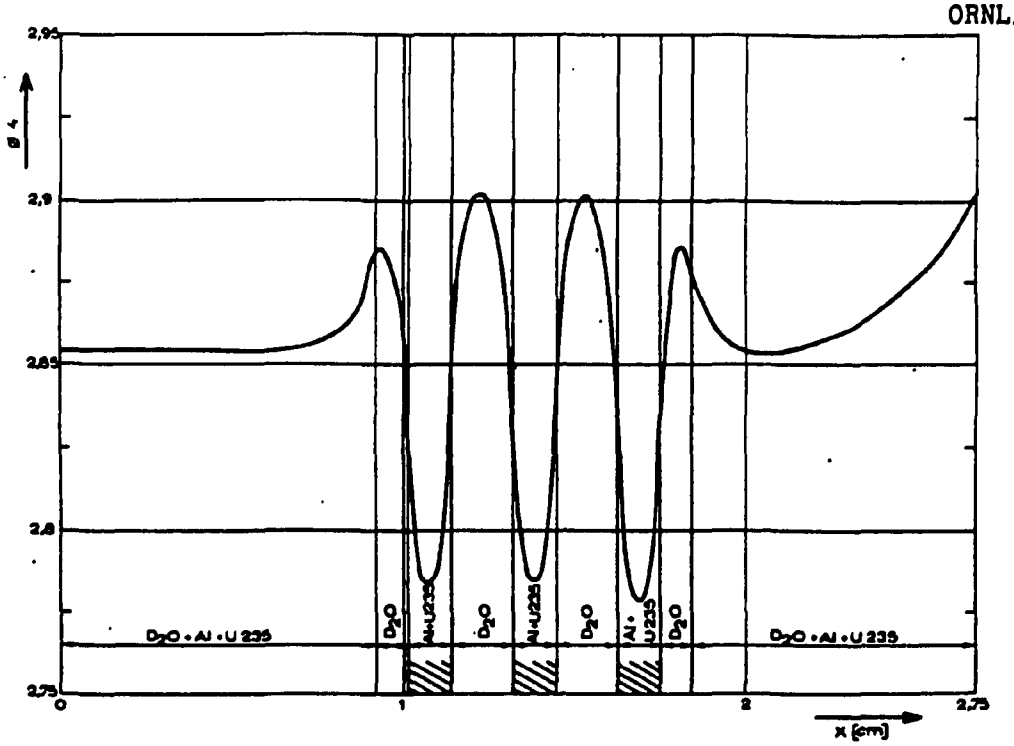

Fig. 3.4 Fine structure of the neutron flux of Group 4 on three individual fuel plates

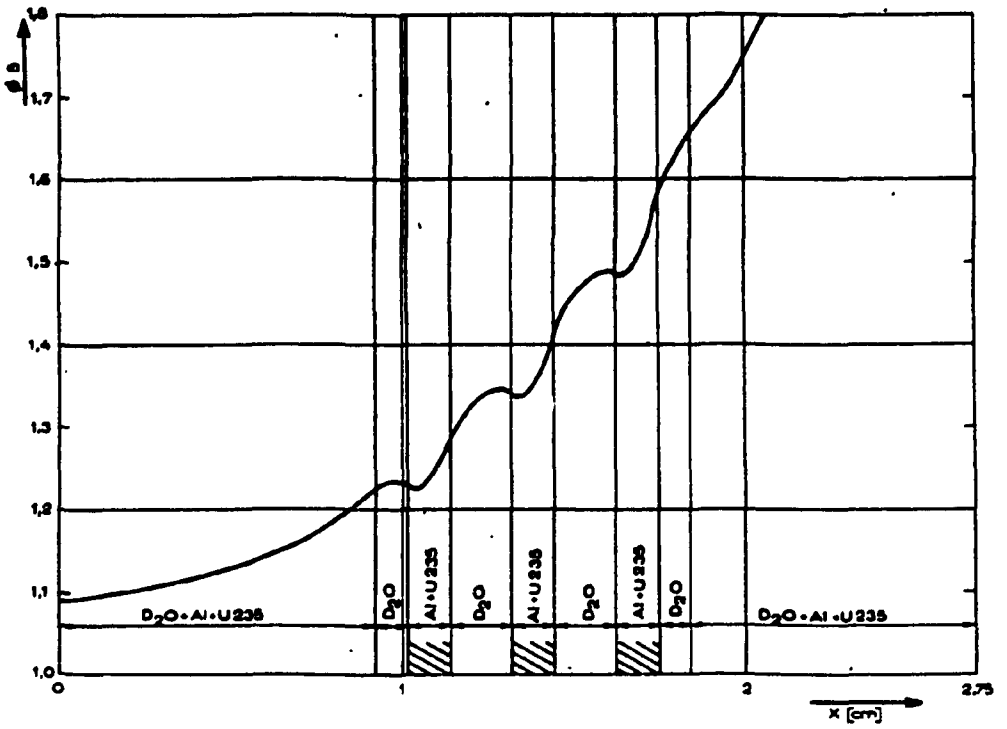

Fig. 3.5 Fine structure of the neutron flux of Group 5 on three individual fuel plates

The fast and epithermal group constants are determined using MUFT IV in accordance with Section 3.1. The thermal constants were calculated with THERMOS in plate geometry. The boron zone was 3 cm thick and contained Boron-10, aluminum and heavy water in a homogeneous mixture; on the right side it was reflected by 50 cm D_2O, and on the left was a zone that simulates the structural materials between solid boron and fuel and then a fuel layer that was reflected on the left by 10 cm D_2O (see Figure 3.6). The thickness of the fuel plate was selected such that the neutrons that are formed in the left D_2O reflector have, after they have passed through the fuel layer, the same spectrum as the mean spectrum of neutrons of the 5th and 6th groups in the core, i.e., their energy corresponds to the energy of the neutrons that stem from the fuel side, coming from the reflector and from the flux trap, and penetrate into the boron zones. The source distribution corresponded to the axial distribution of the epithermal flux (Group 3) on the radius R = 16.75 of a two-dimensional diffusion calculation. For Group 4 the source was in the fuel and in the boron zones; for Group 5 (= Group 6) it was in the D_2O of the reflector. This calculation yields the value $\Sigma_{a,o}$ for the boron zone that is averaged over the flux and the zone.

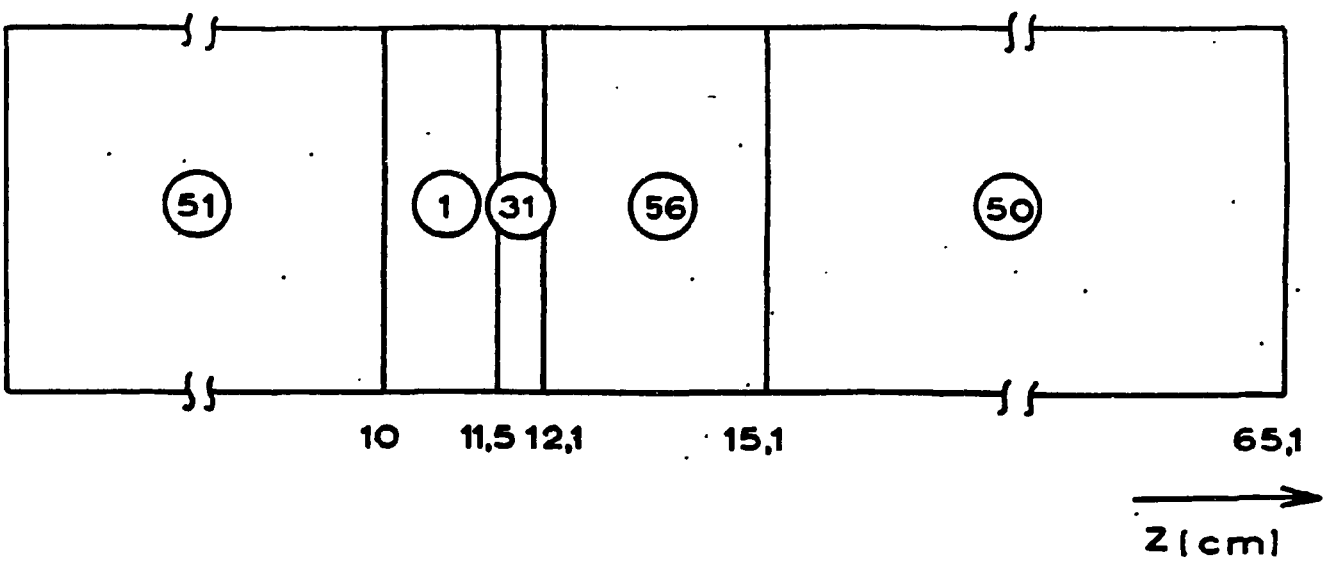

Fig. 3.6 Geometric diagram for calculation of the thermal group constants in the solid boron zones. 1 = core, 31 = structural material, 46 = solid boron, 50 = external reflector (D_2O), 51 = internal reflector (D_2O)

Using this result, the disadvantage factor in the boron plates was calculated according to the equation familiar from probe theory [11]:

$$g_o = \frac{\phi_o}{\phi_{Plate}} = \frac{1 - 2 \cdot E_3(d \cdot \Sigma_a)}{2 \cdot d \cdot \Sigma_a} , \qquad (3.4)$$

E_3 = 3rd order exponential integral ,
d = plate thickness,
Σ_a = absorption cross section in the plate.

Now the THERMOS calculation is repeated, whereby the homogeneous boron concentration is changed:

$$N_1(B^{10}) = N_o(B^{10}) \cdot g_o .$$

Thus we obtain an effective absorption cross section $\Sigma_{a,1}$, with which g_1 can be calculated and so on until the process converges. The result is

$$g = 0.81.$$

The diffusion coefficient of the 4th group is the following value, which was determined directly by THERMOS:

$$D = \frac{1}{3 \cdot \Sigma_{tr}} .$$

For the 5th group (= 6th group) D is determined such that a diffusion calculation in the same geometry as the THERMOS calculation yields the same ratio:

$$\frac{\text{absorption in the outermost-plate}}{\text{mean absorption in the boron zone}} .$$

3.4 Corrections

As already mentioned, several corrections must be made to the results of the diffusion calculations.

Due to the superposition of the three thermal groups, the ratio of power in the hot thread of stream to the mean power is overestimated by 4.3%.

The k_{eff} value of the diffusion calculation must be reduced by the following amounts:

Effect of the spectrum in calculating the group constants for Groups 1-3:	- 750 pcm
Effect of the D_2O layer, which simplifies the contour of the lower reflector edge:	- 50 pcm
Structural materials in the reflector. In the reflector tank there are a number of structures whose reactivity was calculated (e.g. holder for the safety rods at the bottom, etc.). This effect resulted in a correction of	- 50 pcm
Alloying constituents in AG 3-NE. The alloying constituents of AG 3-NE increase somewhat the absorption of the structural materials. The reactivity that is consumed as a result amounts to	- 475 pcm
H_2O concentration in the D_2O. The H_2O concentration in the D_2O increased in the course of the reactor operation period. The calculations were all done with 99.800% D_2O and 0.2% H_2O. For measurements where the H_2O concentration is higher, the corresponding diffusion calculation must be reduced by the following amount for every 0.01% H_2O:	- 38 pcm

3.5 Calculation of the Safety Rods

In theoretical treatment of the safety rods we encounter two difficulties:

a) The rods represent highly absorbent ("black"), non-diffusing zones that can strictly only be treated using the transport theory.

b) The geometry is truly three-dimensional (R,Θ,Z)* and cannot be treated a priori using a diffusion program that is only two-dimensional.

---

* R = radial, Θ = azimuthal, and Z = axial coordinates.

Point a) is solved very successfully by introducing suitable boundary conditions on the boundary surface of the absorbing zone [12], while Point b) the known methods, such as those used by RUDERMANN [12] and SPINKS [13], were unsuccessful. This led to the development of a new method that makes it possible to split the R-Θ-Z problem into a R-Θ problem and a R-Z problem, which can be treated separately.

3.5.1 Boundary Conditions and Constants for the Shutdown Rods

The majority of the measurements was carried out with cadmium rods, which can be considered "black" for thermal neutrons and completely transparent for neutrons of higher energies. The boundary condition for a black plate is as follows according to transport theory:

$$\frac{1}{\Phi} \cdot \frac{\delta \Phi}{\delta r} = \frac{1}{d} = \frac{1}{0.71 \cdot \lambda_{tr}} , \qquad (3.5)$$

d = extrapolation length,

λ_{tr} = transport path length in the surrounding medium.

For calculation of the "gray" rod made of stainless steel (18/8), the boundary conditions are determined using SPINKS' method [14]. The material composition of the "gray" rod was:

18 - 20% Cr
8 - 10% Ni
74 - 70 % Fe.

Thus we obtain the following cross sections for the gray rod:

$$\Sigma_a = 0.2421 \pm 0.0024$$
$$\Sigma_{transport} = 0.843 \pm 0.011.$$

The extrapolation length d for a gray rod becomes

$$d_{gray} = d_{black} + \frac{4(1-\beta)}{3\beta} \cdot \lambda_{tr} , \qquad (3.6)$$

where β = blackness of the rod.

β is tabulated in [14] as a function of the absorption and transport properties of the rod. One obtains

$$\beta = 0.596$$

and

$$d_{gray} = 1.612 \cdot \lambda_{tr}.$$

The epithermal absorption of the gray rod cannot be disregarded. The effective microscopic cross sections of the rod material in the fast and epithermal groups are calculated with MUFT IV in a mixture of 80% D_2O and 20% rod material, in order to better take into account the moderation effect of the D_2O that surrounds the rod.

3.5.2 The Method of the Equivalent Absorber

The absorber rods are positioned more or less symmetrically with the core axis and form a type of semi-transparent curtain for neutrons between fuel and external reflector. Their effect consists in the fact that they absorb the neutrons that were moderated in the reflector on their way back to the core. This is expressed in an azimuthal and radial (R-Θ) buckling of the neutron flux, the form and degree of which is a function of the radial and azimuthal position of the rods and of the different composition of the reactor. In addition, the axial flux distribution is disturbed depending on how far the rods are inserted into the reactor. One assumes that the R-Θ perturbation can be calculated independently of the axial perturbation, and that the curtain formed by the rods can be replaced by a "gray" curtain, which is homogeneous in the Θ direction and has the same absorption effect as the rod lattice. Therefore the R-Θ perturbation is replaced by a basic R perturbation. If then the ...

[Text missing at this point in copy supplied to translator: page 33 of the original German. Translation continues on page 34. -- Translator's Note]

3.5.2.2 The R-Z Problem

After the equivalent "gray" curtain has been determined for all heights Z where the radial composition of the reactor changes, the rod lattice is represented in R-Z geometry by the corresponding cylindrical "gray" zones, the axial configuration of which corresponds to that of the rods. Thus the axial flux perturbations are correctly taken into account, such as the conditions at the core ends, the insertion depth of the rods, the position of the central control rod, etc. The value k_{eff} yielded by this calculation corresponds to the k_{eff} value for the correct reactor.

The individual steps in the calculation are shown schematically in Figure 3.7.

It should also be noted that the method is not only valid for rods that are distributed uniformly over the circumference but even yields good results in extreme cases, such as with a single eccentric rod.

3.6 Calculation of the Kinetic Parameters

3.6.1 The Generation Time in the Critical Reactor

The generation time was calculated according to the customary formulation of perturbation theory:

$$\Lambda_0 = \frac{\int_V \int_E \frac{\phi(E,r)\ \phi^+(E,r)}{v(E,r)}\ dE\ dr}{\int_V \int_D \Sigma_f(E,r)\ \phi(E,r)\ \phi^+(E,r)\ dE\ dr}, \qquad (3.8)$$

where the direct (ϕ) and adjoint (ϕ^+) fluxes from a diffusion calculation where $k_{eff} = 1$ are used. The neutron velocity was averaged over the group in the epithermal zone by using as a basis a 1/E behavior of the flux. In the thermal zone the velocities in the individual regions were determined using THERMOS.

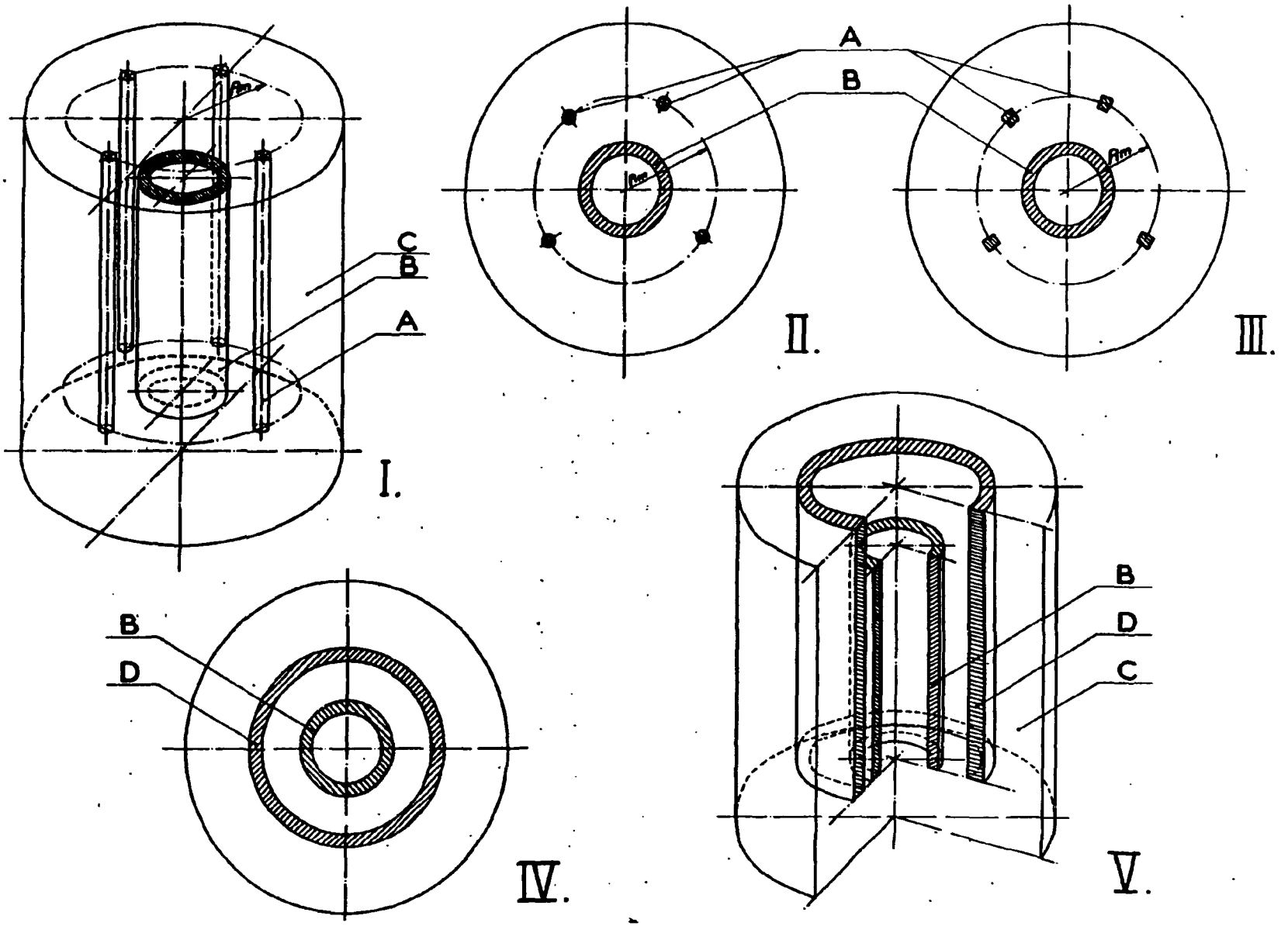

Fig. 3.7 Schematic diagram of the steps for calculation of the safety rods.
I Reactor with 4 safety rods (A), ring core (B) and reflector (C)
II Horizontal section throuth the reactor (I)
III Geometric diagram for the R-θ calculation with rods
IV Geometric diagram for the R-θ calculation for determining the "gray" zone (D)
V Geometric diagram for the R-Z calculation for determining the reactivity of the rods.

ORNL/TR-91/23

3.6.2 Delayed Neutrons

Determination of the effective fraction of delayed neutrons was based on the values measured by KEEPIN [15]. Weighting was carried out in accordance with perturbation theory [16]:

$$\beta_{eff} = \frac{\int_V \int_E \beta\, \chi_d\, \phi^+\, \nu\, \Sigma_f\, \phi\, dV\, dE}{\int_V \int_E (\chi_p(1-\beta) + \beta\, \chi_d)\, \phi^+\, \nu \Sigma_f\, \phi\, dV\, dE} \qquad (3.9)$$

where $\beta = \sum_{i=1}^{6} \beta_i$,

χ_d = spectrum of delayed neutrons,

χ_p = spectrum of prompt neutrons.

In this case it was assumed that the delayed neutrons of Groups 2 to 6 are formed with an energy of 620 keV and those of Group 1 with 250 keV [15].

In the diffusion calculation these groups were treated as neutrons diffusing separately from the prompt neutrons. The group constants were calculated with the program MUFT IV, whereby the source neutrons had an energy of 620 or 250 keV, respectively. In the third group the group constants for prompt and delayed neutrons do not differ for all practical purposes; they can therefore be combined. Thus we obtain the following group scheme for the diffusion calculation:

Groups	Type of Origin	Energy Limits	Fission Spectrum (χ)	Scattering
1	prompt	10 MeV-821 keV	$\chi_1(1-\beta)$	
2	prompt	821 keV-5.53 keV	$\chi_2(1-\beta)$	
2a	delayed	620 keV-5.53 keV	$\sum_{i=2}^{6} \beta_i$	
2b	delayed	250 keV-5.53 keV	β_1	
3	delayed and prompt	5,53 keV-0.625 eV	o	
4+5+6	delayed and prompt	0.625 eV- 0 eV	o	

Using the group fluxes we can write Equation (3.5) for N groups:

$$\beta_{eff} = \beta \frac{\int_V \sum_i^N \sum_j^N (\chi_d \phi^+)_i (\nu \Sigma_f \phi)_j \, dV}{\int_V \sum_i \sum_j [\chi_{p,i}(1-\beta)+\beta \chi_{d,i}] \phi_i^+ (\nu \Sigma_f \phi)_j dV} . \qquad (3.10)$$

With a value $\beta = 0.00650$ we obtain

$$\beta_{eff} = 0.00679.$$

In addition to delayed neutrons, the fission fragments emit delayed gamma quanta, which allow photoneutrons to form due to (γ,n) reactions in the D_2O moderator. The probability that gamma quanta formed in the core generate a photoneutron was estimated for an infinite cylinder geometry that corresponded to a horizontal section through the reactor. Thus we obtained the effective delayed photoneutron fraction as

$$\beta_{eff,ph} = 0.00033.$$

This value involves a relatively great uncertainty. Therefore great effort was made to determine it more precisely experimentally and to study its effect on the results of reactivity measurements (see [17] and Section 4.4).

The following was obtained as the value for the entire effective fraction:

$$\beta_{eff} = 0.00712.$$

The constants for the delayed neutrons are listed in Table 3.2; they are used for evaluation of kinetic measurements.

The decay constants for the photoneutrons correspond to the first 4 groups that BERNSTEIN measured [18].

Tab. 3.2 Data for delayed neutrons

	Group	a_i	$\beta_{i,eff}$	λ_i (s^{-1})
U^{235}	1	0.0315	0.000224	0.0124
	2	0.2093	0.001488	0.0305
	3	0.1875	0.001333	0.111
	4	0.3772	0.002682	0.301
	5	0.110	0.000782	1.13
	6	0.0399	0.000284	3.00
Photo-neutrons	7	0.0301	0.000214	0.2772
	8	0.0094	0.000067	0.0169
	9	0.0031	0.000022	0.00481
	10	0.001	0.000013	0.0015

3.7 Calculation of Fast Flux and Gamma Heating Rates

Calculation of the fast flux was carried out using the programs NIOBE [24] and MERCURE 3 [25]. NIOBE yields the flux distribution and the angle distribution of the flux in a spherical geometry. For this purpose the cylinder geometry of the reactor was converted to volume-equivalent spherical shells. Starting with the result of a NIOBE calculation, the cylinder geometry of the reactor can be taken into account correctly using MERCURE 3. A more detailed description of the method is given in [26].

MERCURE 3 calculates the gamma attenuation according to a linear attenuation model, taking into account the build-up factors. The library described in [27] was used for the starting values.

Table 3.1 Group constants for diffusion calculations

(continued on next page)

Mixture	Concentration		Fast Groups			Thermal Groups		
			1	2	3	4	5	6
1 Fuel w/o boron	N_{U5}=0,0004736	D	2,158923	1,399054	1,644823	1,0312	0,60235	0,67385
	N_{U8}=0,0000468	$\Sigma_a+\Sigma_r$	0,061924	0,023376	0,019341	0,11931	0,20333	0,17702
	N_H =0,000078	$\nu\Sigma_f$	0,001511	0,002337	0,021805	0,241702	0,413688	0,359745
	N_O =0,019432	Σ_r	-	0,060563	0,022034	0,005274	-	-
	N_D =0,038786	Σ_a	0,001421	0,001342	0,014067	0,11931	0,20333	0,17702
	N_{AL}=0,02456	Σ_f	0,000549	0,000947	0,008872	0,099058	0,169544	0,147436
	N_{B10}=0,0							
5 Fuel	N_{B10} = $0{,}10407\cdot10^{-4}$	D	2,158658	1,398616	1,636978	1,0031	0,58279	0,63897
		$\Sigma_a+\Sigma_r$	0,061989	0,023390	0,019742	0,130707	0,226182	0,196803
		$\nu\Sigma_f$	0,001511	0,002336	0,021640	0,232642	0,407390	0,353483
		Σ_r	-	0,060566	0,022017	0,004748	-	-
		Σ_a	0,001423	0,001374	0,014994	0,130707	0,226182	0,196803
		Σ_f	0,000549	0,000947	0,008804	0,095345	0,166963	0,144870

[Translator's Note: Commas in the above table and in the continuation on the following pages should be read as decimal points.]

Mixture	Concentration		Fast Groups			Thermal Groups		
			1	2	3	4	5	6
7 Fuel	$N_{B^{10}}$ = $0,19513 \cdot 10^{-4}$	D	2,158428	1,398233	1,630791	0,9794	0,5672	0,6282
		$\Sigma_a+\Sigma_r$	0,061994	0,023403	0,020079	0,14053	0,24594	0,21355
		$\nu\Sigma_f$	0,001511	0,002336	0,021504	0,22592	0,40245	0,34807
		Σ_r	-	0,060569	0,022002	0,004342	-	-
		Σ_a	0,001425	0,001401	0,015737	0,14053	0,24594	0,21355
		Σ_f	0,000549	0,000946	0,008749	0,092597	0,16494	0,14265
11 Outer tank w/o B^{10}	$N_{Al}=0,02654$ $N_H=0,735 \cdot 10^{-4}$ $N_D=0,036682$ $N_O=0,01838$ $N_{B10}=0,0$	D	2,223280	1,469213	1,792440	1,4379	1,3222	1,3639
		$\Sigma_a+\Sigma_r$	0,058491	0,021674	0,011488	0,003814	0,004922	0,004462
		Σ_r	-	0,057711	0,021581	-	0,011091	-
		Σ_a	0,000780	0,000092	0,000397	0,003814	0,004922	0,004462
15 Outer tank	N_{B10} = $0,116 \cdot 10^{5}$	D	2,223248	1,469156	1,790685	1,4323	1,3094	1,3599
		$\Sigma_a+\Sigma_r$	0,058492	0,021676	0,01154	0,006331	0,008290	0,007377
		Σ_r	-	0,057711	0,021580	-	0,010953	-
		Σ_a	0,000780	0,000096	0,000586	0,006331	0,008290	0,007377
17 Outer tank	N_{B10} = $0,217 \cdot 10^{-5}$	D	2,223221	1,469105	1,789181	1,4271	1,2985	1,3500
		$\Sigma_a+\Sigma_r$	0,058492	0,021677	0,011585	0,008458	0,011194	0,009953
		Σ_r	-	0,057712	0,021578	-	0,010835	-
		Σ_a	0,000780	0,000099	0,000749	0,008458	0,011194	0,009953
21 Inner tank	$N_{Al}=0,02654$ $N_H=0,735 \cdot 10^{-4}$ $N_D=0,036682$ $N_O=0,01838$ $N_{B10}=0,0$	D	2,223280	1,469213	1,792440	1,4736	1,3598	1,3894
		$\Sigma_a+\Sigma_r$	0,058491	0,021674	0,011488	0,003473	0,004462	0,004263
		Σ_r	-	0,057711	0,021581	-	-	0,011091
		Σ_a	0,000780	0,000092	0,000397	0,003473	0,004462	0,004263
25 Inner tank	N_{B10} = $0,281 \cdot 10^{-6}$	D	2,223271	1,469199	1,792012	1,4768	1,3637	1,3868
		$\Sigma_a+\Sigma_r$	0,058491	0,021674	0,011500	0,003991	0,005128	0,004971
		Σ_r	-	0,057711	0,021581	-	-	0,011057
		Σ_a	0,000780	0,000093	0,000443	0,003991	0,005128	0,004971
27 Inner tank	N_{B10} = $0,526 \cdot 10^{-6}$	D	2,223267	1,469188	1,791640	1,4787	1,3667	1,3862
		$\Sigma_a+\Sigma_r$	0,058492	0,021675	0,011511	0,004438	0,005693	0,005564
		Σ_r	-	0,057711	0,021581	-	-	0,011028
		Σ_a	0,000780	0,000094	0,000483	0,004438	0,005693	0,005564

Mixture	Concentration		Fast Groups			Thermal Groups		
			1	2	3	4	5	6
31 End plate w/o B^{10}	N_{Al}=0,031673 N_{D_2O}=0,015502 $N_{B^{10}}$=0	D	2,2953	1,54427	1,96489	1,6110	1,4972	1,4972
		$\Sigma_a+\Sigma_r$	0,053034	0,018766	0,009852	0,004271	0,005465	0,005465
		Σ_r	-	0,051719	0,018656	-	0,009393	-
		Σ_a	0,001318	0,0001102	0,0004597	0,004271	0,005465	0,005465
35 End plate	$N_{B^{10}} = 0,273 \cdot 10^{-5}$	D	2,295105	1,547448	1,963265	1,5765	1,4574	1,4574
		$\Sigma_a+\Sigma_r$	0,052396	0,018644	0,009851	0,10045	0,012891	0,012891
		Σ_r	-	0,051700	0,018525	-	0,008954	-
		Σ_a	0,000696	0,000119	0,000897	0,010045	0,012891	0,012891
37 End plate	$N_{B^{10}} = 0,5101 \cdot 10^{-5}$	D	2,295038	1,547304	1,959175	1,5482	1,4248	1,4248
		$\Sigma_a+\Sigma_r$	0,052397	0,018647	0,009955	0,01498	0,01927	0,01927
		Σ_r	-	0,051701	0,018521	-	0,008689	-
		Σ_a	0,000696	0,000126	0,001266	0,01498	0,01927	0,01927
40 Structural material	N_{Al}=0,031673 N_{DO}=0,015502	D	2,2953	1,54427	1,96489	1,5246	1,5246	1,5346
		$\Sigma_a+\Sigma_r$	0,053037	0,018766	0,009852	0,005235	0,005135	0,005135
		Σ_r	-	0,051719	0,018656	-	0,009393	-
		Σ_a	0,001318	0,0001102	0,0004597	0,005135	0,005135	0,005135
41 Bottom of outer tank w/o B^{10}	N_{Al}=0,034644 $N_{D^{20}}$=0,014125 $N_{B^{10}}$ = 0	D	2,0909	1,40677	1,7899	1,4601	1,4601	1,4601
		$\Sigma_a+\Sigma_r$	0,048429	0,017114	0,009052	0,007274	0,007274	0,007274
		Σ_r	-	0,047114	0,016995	-	0,008557	-
		Σ_a	0,001315	0,000119	0,000495	0,007274	0,007274	0,007274
45 Bottom of outer tank	$N_{B^{10}} = 2,294 \cdot 10^{-7}$	D	2,314821	1,579546	2,053584	1,4494	1,4494	1,4494
		$\Sigma_a+\Sigma_r$	0,049626	0,017283	0,008975	0,008143	0,008143	0,008143
		Σ_r	-	0,048970	0,017162	-	0,008443	-
		Σ_a	0,000655	0,000121	0,000531	0,008143	0,008143	0,008143
47 Bottom of outer tank	$N_{B^{10}} = 4,29 \cdot 10^{-7}$	D	2,314815	1,579533	2,053187	1,4455	1,4455	1,4455
		$\Sigma_a+\Sigma_r$	0,049626	0,017283	0,008984	0,008821	0,008821	0,008821
		Σ_r	-	0,048971	0,017161	-	0,008420	-
		Σ_a	0,000655	0,000122	0,000564	0,008821	0,008821	0,008821
50 Outer D_2O reflector	N_D=0,06637 N_O=0,03325 N_H=0,000133	D	1,912339	1,234363	1,233166	0,8198	0,8198	0,8198
		$\Sigma_a+\Sigma_r$	0,090267	0,036664	0,019877	$0,7485 \cdot 10^{-4}$	$0,7485 \cdot 10^{-4}$	$0,7485 \cdot 10^{-4}$
		Σ_r	-	0,089101	0,036664	-	0,019875	-
		Σ_a	0,001166	-	0,000002	$0,7485 \cdot 10^{-4}$	$0,7485 \cdot 10^{-4}$	$0,7485 \cdot 10^{-4}$

Mixture	Concentration		Fast Groups			Thermal Groups		
			1	2	3	4	5	6
51 D_2O flux trap	$N_D = 0,06637$	D	1,912339	1,234363	1,233166	0,8198	0,8198	0,8198
	$N_O = 0,03325$	$\Sigma_a+\Sigma_r$	0,090267	0,036664	0,019877	0,7485 $\cdot 10^{-4}$	0,7485 $\cdot 10^{-4}$	0,7485 $\cdot 10^{-4}$
	$N_H = 0,000133$	Σ_r	-	0,089101	0,036664	-	-	0,019875
		Σ_a	0,001166	-	0,000002	0,7485 $\cdot 10^{-4}$	0,7485 $\cdot 10^{-4}$	0,7485 $\cdot 10^{-4}$
52 Control rod core spectrum	Ni 100% $N_{Ni} = 9,13 \cdot 10^{-2}$	D	1,7454	0,78532	0,2062	0,18512	0,17940	0,17972
		$\Sigma_a+\Sigma_r$	0,0019	0,0076	0,023565	0,20732	0,26299	0,26196
		Σ_r	-	0,0019	0,0076	-	-	0,0059
		Σ_a	-	-	0,017665	0,20732	0,26299	0,26196
53 Contr. rod Maxwell spectrum	$N_{Ni} = 9,13 \cdot 10^{-2}$	D	1,7454	0,78532	0,2062	0,1401	0,1401	0,1401
		$\Sigma_a+\Sigma_r$	0,0019	0,0076	0,023565	0,3555	0,3555	0,3555
		Σ_r	-	0,0019	0,0076	-	0,0059	-
		Σ_a	-	-	0,017665	0,3555	0,3555	0,3555
56 Solid boron zone	$N_D=0,03867$ $N_O=0,01938$ $N_H=0,000078$ $N_{Al}=0,0248$ $N_{B^{10}}=1,517 \cdot 10^{-4}$	D	2,1971	1,4409	1,6390	0,8703	0,38	0,38
		$\Sigma_a+\Sigma_r$	0,0606	0,0229	0,0175	0,1917	0,2957	0,2957
		Σ_r	-	0,05976	0,0223	0,003167	-	-
		Σ_a	0,000841	0,000552	0,01434	0,1917	0,2957	0,2957

4. MEASUREMENT METHODS

4.1 Flux Measurements

4.1.1 Measurement of the Neutron Flux

All measurements of the static distribution of the neutron flux in the reflector were carried out using activation probes.

The probes were held in the reactor by Therphane ("Mylar") tape, to which they were affixed. Positioning in the axial direction was better than 0.2 cm, and in the radial direction better than 0.1 cm.

For detectors under cadmium covers, these errors are somewhat greater. The most important data for the detectors used are shown in Table 4.1.

4.1.2 Flux Measurement Corrections and Errors

If probes having a 1/v cross section are used, then the measured activities are proportional to the neutron density and not to the flux, as obtained from a diffusion calculation. In order to be able to compare calculation and measurement, corrections must be made in the measured values; these corrections take into account the epithermal activation (beyond 0.625 eV) and the mean energy of the thermal spectrum. For this purpose we make the following simplifying assumptions. The effective thermal cross section has a 1/v curve (for Mn this is exactly true; Dy deviates somewhat); the energy of the thermal neutrons exhibits everywhere a Maxwell distribution, which is characterized by the mean velocity v; and the effective cadmium separation energy is 0.625 eV. Then the flux Ø can be determine as follows from the activation A:

$$\phi_{th} = B \cdot \frac{v}{v_o} \cdot A \left(1 - \frac{1}{R_{Cd}}\right) , \qquad (4.1)$$

Table 4.1 Summary of the probes used for flux measurements

[Commas in numbers in following table should be read as decimal points -- Translator's Note]

	Energy Range	Probe Composition	Dimensions (cm)	Counting Method	Type of Reaction
1	thermal relative	0,9 Mn + 0,1 Ni (metal)	0,6 ø x 0,01	ß , 2π scintillation counter	$Mn^{55}(n,\gamma)\ Mn^{56}$ $T_{1,2}$ = 2,58 h σ_{act} = 13,2 ± 0,1 barn
2	thermal relative	Dy (metal)	0,2 ø x 0,005	ß , 2π scintillation counter	$Dy^{164}(n,\gamma)\ Dy^{165}$ $T_{1/2}$ = 140 min σ_{act} = 800 ± 100 barn
3	thermal absolute	Mn on Al substrate	1,0 ø; 100 - 300 µg/cm^2	ß , 4π proportional counter (methane flow rate meter)	$Mn^{55}(n,\gamma)\ Mn^{56}$ $T_{1/2}$ = 2,58 h σ_{act} = 13,2 ± 0,1 barn
4	epithermal relative	In metal under 0,08 cm Cd	0,6 ø x 0,01 with 0,005 Al cladding	ß , 2π scintillation counter	$In^{115}(n,\gamma)\ In^{116}$ $T_{1/2}$ = 54,22 min
5	epithermal relative	Au metal under 0,08 cm Cd	0,6 ø x 0,01 with 0,005 Al cladding	ß , 2π scintillation counter	$Au^{197}(n,\gamma)\ Au^{198}$ $T_{1/2}$ = 2,704 d
6	epithermal absolute	Au metal under 0,08 cm Cd	1,0 ø x 0,002	ß , 4π proportional counter (methane flow rate meter)	$Au^{197}(n,\gamma)\ Au^{198}$ $T_{1/2}$ = 2,704 d
7	fast relative	0,9 P (red) + 0,1 araldite under Cd	1,3 ø x 0,13 with 0,005 Al cladding	ß activity	$P^{31}(n,p)\ Si^{31}$ σ = 31 ± 2 mb $T_{1/2}$ = 157 min ($ß^-$)
8	fast absolute	0.9 P (red) + 0.1 araldite under Cd	1,3 ø x 0,13 with 0,005 Al cladding	2π scintillation counter, comparison w. probes calibrated in 4π geometry	$P^{31}(n,p)\ Si^{31}$ σ = 31 ± 2 mb $T_{1/2}$ = 157,5 min
9	fast absolute	sulfur under Cd	1,8 ø x 0,25 9,9 ø x 1,4	comparison with P probes calibrated in 4π geometry; β^- activity	$S^{32}(n,p)\ P^{32}$ $T_{1/2}$ = 14,2 d σ = 60 mb ($ß^-$)

ORNL/TR-91/23

where B = proportionality factor

$\frac{v}{v_o}$ = $\frac{\text{mean thermal neutron velocity}}{2/\sqrt{\pi} \cdot 2200 \text{ m/sec}}$,

R_{Cd} = cadmium ratio (see below).

v/v_o was calculated by the code THERMOS in cylinder geometry as a function of the radius (see Figure 4.1). In order to take into account the distribution near the core ends, it was assumed that the same spectrum prevails at all points that have the same distance from the core surface. Since the correction is only a few per cent, even close to the core, the errors of this simple scheme do not have much of an effect.

The error of the relative thermal flux measurements is about ± 2 %; for the absolute measurement it is about ± 3 %.

The epithermal flux measurements are carried out using resonance detectors (Au, In) below cadmium. The epithermal activation A_{epi} therefore corresponds to the following:

$$A_{epi} = N \cdot d \left[F_{Cd} \int_{E_{Cd}}^{\infty} \sigma^{1/v}(E) \, \phi_{epi} \frac{dE}{E} + \sum_i \phi_{epi}(E_i) \, \lambda_i \, I_{eff,i} \right] , \qquad (4.2)$$

where F_{Cd} = 1.046 cadmium correction factor [11],

E_{Cd} = cadmium separation energy,

$\sigma^{1/v}$ = 1/v portion of the activation cross section,

$\frac{\phi_{epi}}{E}$ = epithermal flux

λ_i = contribution of the i-th resonance

$I_{eff,i}$ = i-th effective resonance integral,

N·d = number of atoms in the probe.

The epithermal self-shielding $C_{epi} = I_{eff}/I_{act}$ was determined according to [19]. For gold probes 0.002 cm thick we obtained $C_{epi} = 0.384 \pm 0.004$. The resonance integral is 1535 ± 40 barn, according to [20]. Thus we can calculate the epithermal flux per lethargy unit.

Under the assumption that the epithermal flux per lethargy unit u is not a function of the energy (1/E curve), Eq. (4.2) can be written as follows:

$$A_{epi} = \phi_{epi}(u)\ N \cdot d \cdot F_{Cd} \cdot C_{epi} \cdot I_{act} \tag{4.3}$$

or

$$\phi_{epi}(u) = \frac{A_{epi}}{N \cdot d \cdot F_{Cd} \cdot C_{epi} \cdot I_{act}} \cdot \tag{4.4}$$

No absolute flux measurements were taken with indium probes. The absolute error is approximately ± 4 to ± 15 % in the present measurement, depending on the location of the measurement (except in the reflector, the flux is very low, which results in poor statistics).

The threshold reactions of phosphorus and sulfur were used to measure the fast flux:

$$A_{fast} = N \cdot d \int_{E_S}^{\infty} \sigma(E)\ \phi(E)\ dE = N \cdot d \cdot \bar{\sigma}_F \cdot \phi\ , \tag{4.5}$$

$\bar{\sigma}_F$ = the effective activation cross section averaged over the fission spectrum.

The flux is thus given as

$$\phi_{fast} = \frac{1}{\bar{\sigma}_F} \cdot \int_{E_S}^{\infty} \sigma(E)\ \phi(E)\ dE\ . \tag{4.6}$$

In order to determine the absolute value of ϕ_{fast}, the counting device was calibrated with thin phosphorus probes without beta self-shielding (20 mg/cm^2 P-31), which were irradiated in a known thermal flux. The reaction P-31(n,γ)P-32 with σ_{act} = 190 m barn was used (see [21]).

For phosphorus the calculation was based on the following values (E_S = threshold energy):

$\bar{\sigma}_F$ = 31 ± 2 mb [22]

E_S = 3 MeV

and for sulfur:

$\bar{\sigma}_F$ = 60 mb

E_S = 3.2 MeV.

The error is 13% for the fast flux measurements near the core.

4.1.3 Measurement of the Spectrum

The cadmium ratio R_{Cd} is the ratio of the activities of a Mn probe that was irradiated at the same spot, once under a cadmium cover and once without cadmium at the same reactor power. No additional corrections were made. The cadmium separation energy is 0.64 eV with the 0.08 cm thick covers used.

For measurement of the thermal spectrum, which varies sharply in the core and in the vicinity of the core, uranium-plutonium and lutetium-manganese probes were irradiated in pairs.

$$R_{Pu/U} = \left(\frac{A_{Pu}}{A_U}\right)_{\text{local spectrum}} \times \left(\frac{A_U}{A_{Pu}}\right)_{v = 2200\ m/sec}$$

$$R_{Lu/Mn} = \left(\frac{A_{Lu}}{A_{Mn}}\right)_{\text{local spectrum}} \times \left(\frac{A_{Mn}}{A_{Lu}}\right)_{v = 2200\ m/sec} \qquad (4.7)$$

Since the plutonium 239 resonance at 0.297 eV has more or less of an effect on the total activation of the probe depending on the hardness of the spectrum, a reference value for the thermal spectrum can be obtained from comparison with a probe having a 1/v cross section (U-235), as well as when lutetium-176 is used, where the resonance is 0.142 eV.

The probes that were used had the following characteristics:

Type of Measurement	Probe Composition	Dimensions (cm)	Comments
R_{Cd}	Mn under 0.08 cm thick Cd covers	Mn probe 0.6 Ø x 0.01 clad w. 0.005 Al	$Mn^{55}(n,\gamma)Mn^{56}$ $T_{1/2}$ = 2.58 h σ_{act} = 13.2 ± 0.1 barn
$R_{Pu/U}$	alloy of Al + Pu	0.7 Ø x 0.017 2.5 mg/cm^2 Pu^{239}	The gammas of the fission products above 511 keV are counted.
	alloy of Al + U	0.7 Ø x 0.03 5 mg/cm^2 U^{235}	4-6 hours after irradiation
$R_{Lu/Mn}$	Mn powder in plastic	1.1 Ø 5 mg/cm^2 with 0.005 Al cladding	The gamma activity above 275 keV is counted, 6-9 h after irradiation
	Lu powder in plastic	1.1 Ø 10 mg/cm^2 w. 0.005 Al cladding	The gamma activity above 35 keV is counted 4 days after irradiation

The prevailing error source for the spectrum measurements we utilized is the imprecise positioning of the probes, especially at locations having a sharp flux gradient.

On the tank surface in the core midplane the variation in thermal flux is about 30% per cm, i.e., R_{Cd} at this point with a positioning of ± 0.1 cm has an error of ± 3%. For $R_{Pu/U}$ and $R_{Lu/Mn}$ the probes were irradiated in pairs. In order to limit the error caused by the flux gradient, they were attached first so that the Pu or the Lu probe pointed towards the core and then so that they pointed towards the outside. The average of the two measurements was then taken as the measured value.

The measurement error without taking positioning into account is as follows: for R_{Cd} = 1%, for $R_{Pu/U}$ = 1% and for $R_{Lu/Mn}$ = 2%.

4.1.4 Measurement of Gamma Heating in the Reflector

The energy transferred by gamma radiation to the structural material was measured using two different methods, glass dosimeters and an ionization chamber.

Since the ionization chamber requires a much higher experimental expenditure, most measurements were carried out with the glass dosimeters.

4.1.4.1 Measurement of Gamma Heating by Glass Dosimeters

For several years we have had good results at Kernforschungszentrum Karlsruhe with glass dosimeters for radiation protection within the facility, and this experience indicated that they would also be suitable for measuring radiation doses at Eole. They have the advantage over other detection methods that they are very handy--their dimensions are 6.9 x 6.9 x 4.5 mm; in detection sensitivity they are energy-independent linearly up to doses of several 10,000 roentgen and with suitable encapsulation for attenuating the gamma radiation of smaller energies.

Since the Japanese Yokota dosimeters used in Karlsruhe had too high a neutron sensitivity because of their lithium content, other lithium-free and boron-free glass dosimeters were used for our purposes (supplied by Schott und Gen., Mainz). They consist of $AgPo_3$, $NaPO_3$, KPO_3 and $Al(PO_3)_3$. Their gamma sensitivity was determined using Cs-137 and Co-60 sources in a calibrated configuration, whereas the neutron sensitivity was determined in the thermal column of the critical configuration STARK in Karlsruhe. In this experiment the thermal flux was measured with Au probes and the γ+n dose with the dosimeters at the same time at different distances from the core. The separation of the total dose in gamma and neutron fractions yielded the following sensitivity p to thermal neutrons:

$$p = \left(8 \begin{smallmatrix} + 0.8 \\ - 0.4 \end{smallmatrix} \right) \cdot 10^{-16} \text{ Ws/g/Øt} .$$

Radiation causes in the dosimeters the formation of isolated Ag, Ag^{+} and Ag^{++} atoms, whose number is proportional to the radiation energy. (Thermal neutrons are detected via the decay products of activated atoms.) These isolated atoms are the cause of fluorescence centers that can be excited with UV light. The detection of the dose received by the glass lies in the measurement of the light emitted after excitation of the fluorescence centers, the intensity of which light is proportional to the number of these centers. The calibration and measurement of the irradiated glass dosimeters was done at the Institut fuer Strahlenschutz [Institute of Radiation Protection) at KFZ Karlsruhe.

Tin capsules having a wall thickness of 1 mm were used as filters for gamma radiation in the energy range up to 50 keV, in which the detection probability is higher than at greater energies.

For the purpose of irradiation in FOEHN the encapsulated glass dosimeters were affixed to Mylar tape, mounted in the desired position and subjected there to neutron and gamma flux for one hour at a constant reactor power (about 35 W).

4.1.4.2 Measurement of Gamma Heating Using an Ionization Chamber

Some measurements of the gamma dose were carried out using an ionization chamber through which CO_2 flowed. The chamber consists of a hollow graphite cylinder 250 mm long and 22 mm in diameter. It is enclosed by a Teflon cladding having a wall thickness of 2 mm. The active volume of the chamber is about 20 cm^3.

The gamma sensitivity determined with a Co-60 source is 1200 W/g/amp. The sensitivity to thermal neutrons was measured in the thermal column of the reactor NAIADE II in Fontenay-aux-Roses and is 1.2×10^{-16} Wsec/g/Øt.

4.2 Power Measurement

4.2.1 Probes for Measuring the Power Distribution

The power distribution in a fuel plate was measured with probes that have the same composition as the fuel plate itself. They have the dimensions 0.5 x 0.3 x 0.127 cm and are placed in correspondingly punched holes of special fuel plates. This method guarantees a very precise positioning of the probes, whereby at the same time the local flux perturbation remains small. Because of the great number of measuring points (123), the probes were distributed to three plates and activated in two separate irradiations. Common measuring points in the core and reflector make it possible to normalize the two measurements (see Figure 4.1).

The measuring plates can be installed at any point in the core so that even azimuthal power variations can be measured.

The probes were calibrated relative to one another by measurement of their natural gamma activity above 130 keV. Figure 4.2 shows the gamma spectrum of natural radiation. The threshold energy for the calibration lies between the two resonances of 95 and 146 keV.

After irradiation the gamma activity of the fission products above 511 keV is measured, which is proportional to the power that was released in the probe during irradiation. The counting rate was normalized on a monitor that had the same composition as the probes.

4.2.2 Error Involved in Power Measurement

The relative error of the individual measuring points is caused primarily by its positioning, i.e., since they are in the fuel plate itself, by the distance from the adjacent plates. For the majority of the measuring points the resulting error is < 1%, except for the points on the upper and lower plate edge, because the measuring plates had become somewhat deformed after long use. However, this error is not systematic and does not much

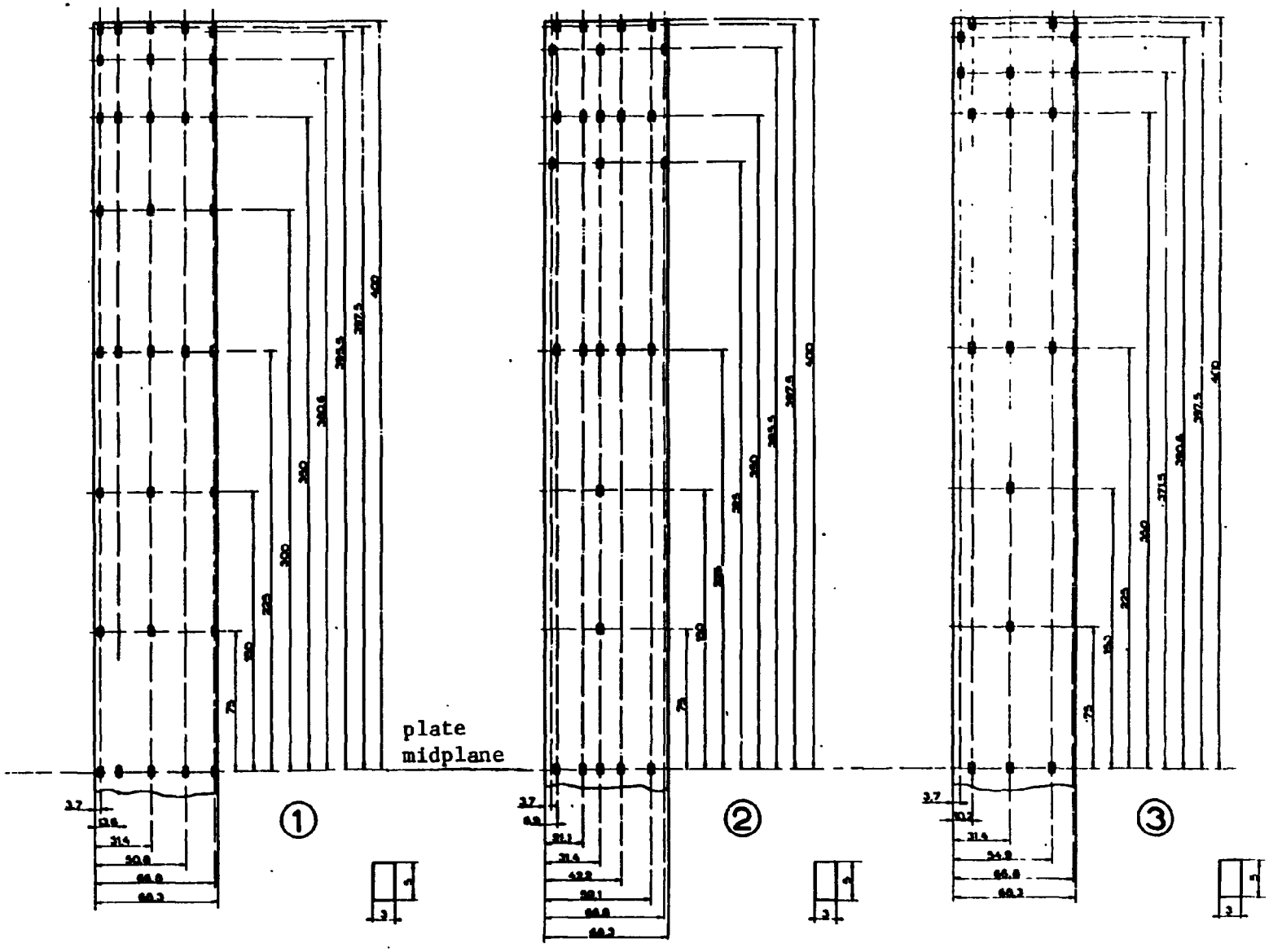

Fig. 4.1 Special fuel plate with holes for holding detectors for power measurement in the core

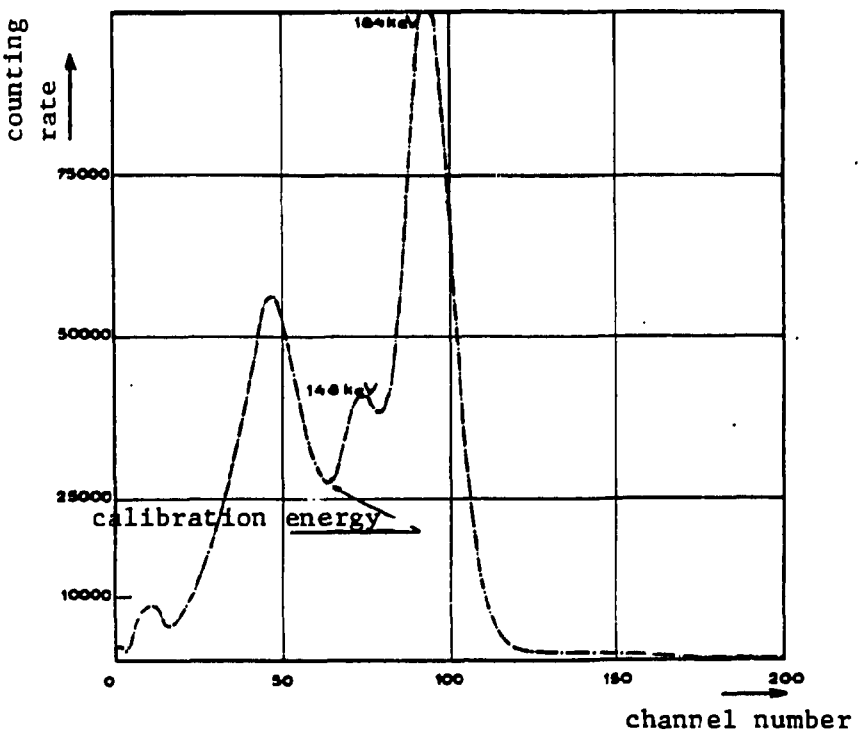

Fig. 4.2 Natural gamma spectrum of uranium detectors
A counting rate
B calibration energy
C channel number

affect the power integral or consequently the power in the hot thread of stream or the yield. The error for the power integral is ± 0.5%; the error for the power in the hot thread of stream is about ± 1%.

4.3 Determination of "Rendement"

"Rendement" [French term meaning "yield"], the measure of the "quality" of the High Flux Reactor, was defined as the ratio of the maximum thermal flux ($\phi_{max,th}$) in the reflector to the total core power (P_{tot}):

$$r = \frac{\phi_{max,th}}{P_{tot}} \quad . \tag{4.8}$$

For experimental determination of r we rewrite this equation somewhat:

$$r = \frac{\phi_{max,th}}{\Sigma_f \cdot \phi_c \cdot V_c \cdot p} \quad ,$$

$\Sigma_f \cdot \phi_c$ = mean fission rate in the core,

V_c = core volume,

p = $\frac{10^{-10}}{3.125}$ W per fission.

The measured mean fission rate is only known precisely with respect to a proportionality factor a, which is a function of the probe type and the counting device and differs from the factor b, which appears in measurement of the thermal flux.

We determine the factor b/a from the activity of an uranium probe of the same type, which was used for power measurement in the core, and a manganese probe, both of which had been irradiated together at a point in the reflector where the flux is well thermalized.

If we assume that

$A_{Mn,R} = b \cdot \Sigma^{Mn}_{a,th} \cdot \phi_{R,th}$ = activity of the Mn probe in the reflector,

$A_{Mn,max} = b \cdot \Sigma^{Mn}_{a,th} \cdot \phi_{max,th}$ = activity of the Mn probe in the flux maximum,

$A_{U,R} = a \cdot \Sigma^{U}_{f,th} \cdot \phi_{R,th}$ = activity of the uranium probe in the reflector,

$A_{U,C} = a \cdot \Sigma^{U}_{f} \cdot \phi_{C}$ = mean activity of the uranium probes in the core,

then we can write the "rendement" as follows, after several transformations:

$$r = \frac{A_{Mn,max}}{A_{Mn,R}} \cdot \frac{A_{U,R}}{A_{U,C}} \cdot \frac{1}{\Sigma^{U}_{f,th} \cdot V \cdot p} \cdot \qquad (4.10)$$

If we also consider that the neutrons are not completely thermalized at the point of the flux maximum but that they have a greater mean velocity v than

$$v_o = \frac{2}{\sqrt{\pi}} \cdot 2200 \frac{m}{sec} ,$$

then we can finally write:

$$r = \frac{A_{Mn,max}}{A_{Mn,R}} \cdot \frac{v}{v_o} \cdot \frac{A_{U,R}}{A_{U,C}} \cdot \frac{1}{\Sigma_{f,th}^{U} \cdot p} . \qquad (4.11)$$

The epithermal activation of the Mn probe has already been subtracted at $A_{Mn,max}$ and $A_{Mn,R}$ according to formula (4.1). The ratio v/v_o was calculated using THERMOS (Figure 4.3). The effective microscopic fission cross section $\sigma_{f,eff}$(U-235) = 503 barn at the measurement point (R = 50 cm) was also calculated with THERMOS.

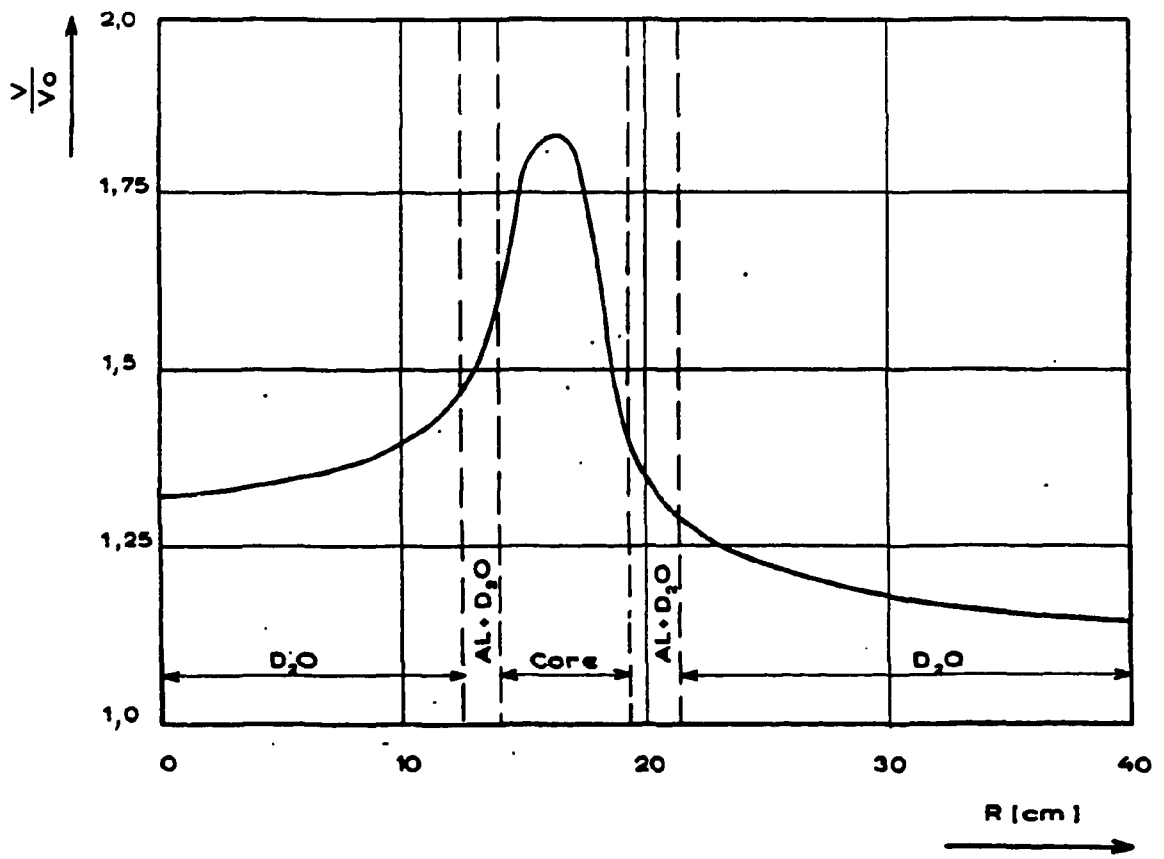

Fig. 4.3 Mean relative velocity of the thermal neutrons in the reactor midplane

4.4 Reactivity Measurements

4.4.1 Stable Period ("Approche cinetique")

The "approche cinetique" [French term meaning "kinetics approach"] involves measurement of the stable reactor period of variously supercritical states, which are generally selected between +1-- and +250 pcm. The reactivities corresponding to the periods are calculated using the Inhour equation and plotted against the rod position H. Since generally the differential quantity $\delta\rho/\delta H$ (ρ = reactivity, H = rod position) does not vary much within one interval δH of several mm, these points lie approximately on a straight line, the extrapolation of which according to $\rho = 0$ yields the rod position for the critical reactor. The slope of this curve is equal to the differential reactivity $\delta\rho/\delta H$, which characterizes the rod at the respective point (strictly speaking it applies to a mean rod position in the interval ΔH, within which the measuring points lie). See Figure 4.4.

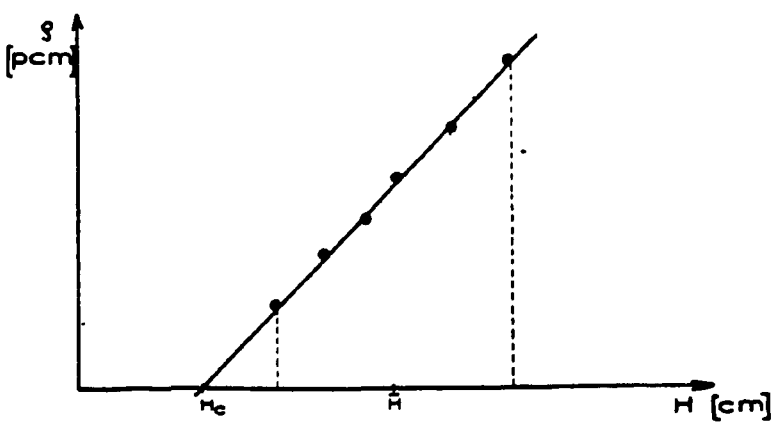

Fig. 4.4 Diagram of an "Approche cinetique"

In this way determinatien of the critical rod position Hc and of $\delta\rho/\delta H$ can be carried out even with great precision during measurement, which is a primary advantage of this method. Adaptation of the curves mentioned above to the measuring points using the method of least error squares increases the precision of the results even further.

The accuracy of the determination of critical rod position is not a function of kinetic parameters and is on the order of the accuracy of rod positioning--about $\pm$ 0.1 mm in accordance with a maximum $\pm$ 2 (reading accuracy). On the other hand the method proves to be laborious and generally not much more accurate than continuous reactivity measurement (see below) when it is used for calibration of the control rod, for example.

Since measurement is only possible within a small interval ΔH near the critical position Hc, a relatively large number of different boron poisonings are necessary for calibration, of the control rod for example.

If a sufficient number of values $\delta\rho/\delta H$ (about 10 in our case) have been measured as a function of rod position, then their graphic integration yields the reactivity of the rod with great accuracy, which is then a function only of the suitable selection of the kinetic parameters in the Inhour equation.

4.4.2 Continuous Reactivity Measurement (Continuous Run)

Changing the composition of the reactor, for example when the control rod is inserted, brings about a change in the time-dependent power curve. One measure of this is the reactivity, which is linked to the multiplication factor k_{eff} by

$$\rho = \frac{k_{eff}^{-1}}{k_{eff}} \quad .$$

The relationship between reactivity $\rho(t)$ and the neutron density $n(t)$ is given by the kinetic equations:

$$\rho(t) = \beta - \frac{S(t)}{n(t)} + \frac{\Lambda}{n(t)} \left(\frac{dn}{dt} - q \right) \quad ,$$

whereby S(t) represents the density of the delayed neutrons at time t; S(t) is a function of the "prehistory" of the reactor, i.e., of the curve of the function n(t) over time, and can be calculated from it and by using the

kinetic parameters β_i, λ_i and $\Lambda = 1/k$:

$$S(t) = \sum_i \beta_i \, e^{-\lambda_i t} \left(n(o) + \lambda_i \int_o^t n(\tau) \, e^{\lambda_i \tau} \, d\tau \right) .$$

If the reactor flux is measured at any point as a quantity proportional to the power as a function of time, then the reactivity can be calculated for any point in time or for the corresponding rod position.

A required initial condition is that the concentration of the precursor nuclei of delayed neutrons is in equilibrium, i.e., that the following is true at the start of the measurement at time t = 0:

$$S(0) = \beta \cdot n(0).$$

Since this condition in our measurements was only incompletely satisfied for the delayed groups with long decay time, the following procedure was used (see Figure 4.5).

Stabilization of the reactor for generation of the equilibrium of the precursor nuclei with short decay time was carried out for about 3-5 minutes at low power--about 10^{-3} W.

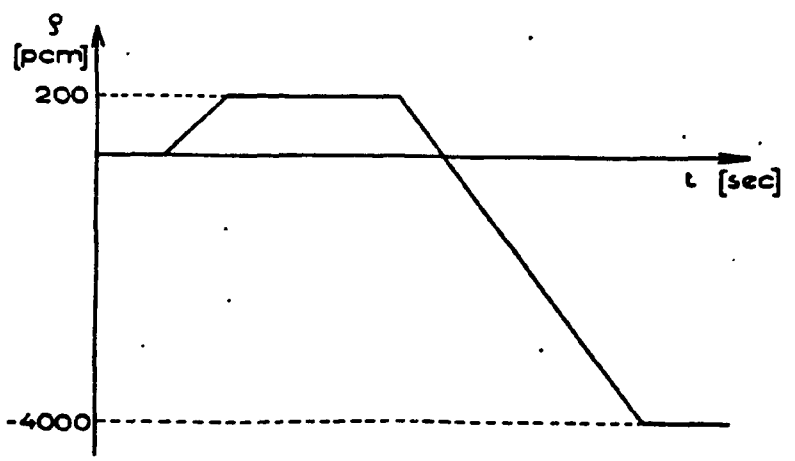

Fig. 4.5 Diagram of a continuous reactivity measurement

At the end of this phase we began to register the flux signal. Then the reactor was run with a period of about 15 sec = 200 pcm to a power of 30 W, which was reached accordingly after about 150 sec. During this phase precursor nuclei were accumulated, which provided the majority of the delayed neutrons in the subsequent third phase, in which the reactor was run subcritically--to -4000 pcm maximum. The precursor nuclei from the stabilization phase and thus the accuracy of the initial condition played a secondary role.

The velocity of the rod was 1.035 mm/sec during withdrawal and 2.07 mm/sec during insertion, and the corresponding reactivity velocities were 22 and/or 44 pcm/sec maximum.

The flux was measured by a BF-3 counter tube run in chamber operation (Type CCC2b, sensit. 2×10^{-14} A/n/cm^2/s). The d.c.-amplified signal (amplifier A.C.L.I.C.) was measured with a digital voltmeter (NLS 4200), and its output was punched on tape after appropriate modification with a recorder (Tally). The system permits coverage of 5 decades at a maximum of 10 information units [bits?] per second.

The switchover time between two decades is below 1/10 sec. The punched tape was transformed after measurement into punched cards, and the reactivity at every measuring points was figured using a computer program. The measuring points at which the rod was in motion were identified by means of an additional signal marking.

This continuous method of reactivity measurement has the advantage of great speed and also of the fact that the measured range is closely packed with measuring points. In a period of about 10 min, which was the time used per measurement, reactivities of up to 10 $ were measured by approximately 2000 measuring points (8/sec).

On the other hand, there is a sensitive dependence on kinetic parameters, especially in the subcritical range. The longer the measurement takes, i.e., the longer the reactor is run at a subcritical level, the greater the

degree to which the constants for the long delayed photoneutrons, which are unfortunately not well known, become part of the calculation.

For example, the differential reactivity $\delta\rho/\delta H$ at a certain rod position was a function of whether this rod position was reached at the beginning or at the end of a "continuous run"; in the end $\delta\rho/\delta H$ was several per cent smaller in each case. Furthermore it can be observed that the calculated reactivity does not remain constant if the reactor remains in a certain subcritical state. This phenomenon becomes especially clear about 2 min after the precursor nuclei are formed in the supercritical phase.

For this reason the measurements were always evaluated only during the first 80-100 sec, which corresponded to a mean "measuring section" of 2500 pcm per measurement. It can be shown that if the photoneutrons are not taken into account at all in a measurement lasting 100 sec, the error of reactivity is 6.5%; if we assume that the constants λ_i and β_i of the photoneutrons all involve an error of 20%, then we obtain by quadratic addition after 100 sec an error of 2% for the reactivity. For a measurement lasting up to 200 sec the corresponding errors for the reactivity are 18% and 6%, respectively, and for 50 sec then are 6% and 1.1%, respectively.

Not explained is the difference that exists between the results of period measurement and continuous measurement; the rod calibration with "approche cinetique" (kinetics approach) yielded a reactivity that was about 4% higher. This effect cannot be attributed to erroneous photoneutron constants.

On the other hand it was found that some other possible error sources are of secondary importance:

- The approximations used in the computer program had no effect on the result; in particular, an increase in the velocity of the variation of reactivity by a factor of 2 (rod velocity) had no effect on the result.
- The signal statistics are sufficient; a variation in power by a factor of 100 did not exhibit any effect.

- The quasi-static background of photoneutrons, which stems from the long-lived gamma activity of the core, does not have any significant effect on the measurement as long as this background remains small in comparison with the fission neutron flux. This was guaranteed with our measurement conditions. This background could also be approximately calculated from the critical rod position resulting from the "approche cinetique" and the rod position at which the reactor was stabilized before the "continuous run." The background source Q was taken into account in the calculation by the equation $\rho_o = -\Lambda/\emptyset_o \cdot Q$.

- Harmonic waves in the flux distribution at the location of the chamber do not play a role. This was deduced from the fact that the distance of the chamber from the core did not affect the measurement result; two measurements up to -4500 pcm at the radius 515 and 835 mm, respectively, yielded the same result.

- The perturbation of the chamber signal by gamma radiation is slight. A variation in gamma compensation voltage did not measurable affect the chamber current.

It is difficult to state exactly the errors that were made with this measurement method given the large number of parameters involved. We estimate that the measured reactivities are about 4% too small.

A more detailed analysis of the measurement method and sources of error as well as a description of the solution methods used for the kinetic equations are given in [23].

4.4.3 Pulsed Neutron Source

This classic method involves measurement of the decay constant α of a pulse of fast neutrons, which is shot into the subcritical system. From the equation

$$\frac{\rho}{\beta_{eff}} = \frac{\alpha - \beta_{eff}/\Lambda}{\beta_{eff}/\Lambda - \alpha \cdot \beta_{eff}}$$

we can then calculate immediately the reactivity of the system. Since the quantity $\alpha_c = \beta_{eff}/\Lambda$ was very much a function of the rod position, cf. Sec. 5.10, it had to be determined in a separate measurement as a function of the rod position.

This was done by extrapolating the values measured at different boron poisonings for subcritical states of different levels (between -300 and -1500 pcm) to the critical state. The respective reactivity of the subcritical state was taken from other measurements carried out with "continuous run" or "approche cinetique" methods.

By means of a suitable (computer) evaluation of the measurement signal it was possible to suppress the effect of the harmonic waves. An exponential function having the form $e^{-\alpha t}$ was fitted to the decay curve of the pulse after different times T after the start of the pulse. With increasing T, α converges towards a value that corresponds to the decay constant after damping-out of harmonic waves. The exponential function was fitted using the method of least error squares.

The main advantage of this method is also its greatest disadvantage. It is independent of all kinetic constants that affect the delayed neutrons; on the other hand the generation time Λ in the form $\alpha_0 = \beta/\Lambda$ is incorporated in the result to a great degree. Although it is possible to measure β/Λ rather accurately (see above), this quantity only applies to the critical reactor, and Λ corresponds to the life of the static case.

In the case of α measurement in the subcritical system, on the other hand, Λ corresponds to the dynamic life; the more subcritical the reactor is, the more this life differs from the static life. Thus it is not a surprise that the more subcritical the measured state is, the more the reactivities measured with pulsed neutrons differ from those measured with the "continuous run" method.

Since there was little information about the dynamic life, and since the pulsed measurements were also laborious in comparison with the "continuous run" measurements, this method was gradually dispensed with in the course of the measurements.

4.5 Determination of the Boron Concentration in the Core

It was found in the course of the measurements that the differential boron reactivity $\Delta\rho/\Delta C$ (pcm/g/l) is practically independent of other parameters (poisoning, configuration, etc.). Therefore the reactivity difference between two states could be expressed by the equivalent difference in boron concentration, independent of the respective state. Since it was also found that the reactivity value of the dissolved boron could be calculated rather accurately, it was desirable to have accurate knowledge of the boron concentrations, both relative to one another and also absolutely.

4.5.1 Preparation of the Boron Solutions

The starting product for preparation of the boron solutions was boron anhydride (B_2O_3) having the following characteristics:

moisture content	0.68% ($\pm$ 0.2%)
impurities	0.2% ($\pm$ 0.1%)
boron 10	90.1 at. % ($\pm$ 0.1%)
density of B_2O_3	1.812 g/cm^3
lithium is not detectable	
sodium	$\leq$ 80 ppm
ratio of starting product (B_2O_3 + impurities) to boron 10	3.814 $\pm$ 0.015.

The starting product was weighed in a nitrogen atmosphere and dissolved in an appropriate amount of D_2O, in order to obtain the desired boron 10 concentration for the respective experiment.

4.5.2 Chemical Analysis of the Boron Solutions

The precise boron concentration of the solutions used in the experiment was determined using an iodometric method. The boric acid that was formed when

B_2O_3 was dissolved in water

$$B_2O_3 + 3\ D_2O \longrightarrow 2\ B(OD)_3$$

dissociates, when laevulose is added, into H^+ ions and boron-laevulose compounds. When potassium iodide and potassium iodate are added, iodine (I^-) is released quantitatively, which was titrated using sodium thiosulfate.

5. PERFORMANCE OF MEASUREMENTS, COMPARISON OF RESULTS OBTAINED EXPERIMENTALLY AND THEORETICALLY

5.1 State I: Core without Solid Boron and without Experimental Equipment in the Reflector

5.1.1 Comparison of Measured and Calculated Critical Reactor States with Different Control Rod Positions

The critical control rod position H_c was determined for different concentrations C of the B-10 dissolved in the core using the "approche cinetique" method. During the measurements the degree of purity of the heavy water in the reflector was 99.747 % D_2O.

The measured critical states are listed in Table 5.1.1.

Table 5.1.1 Experimentally determined critical reactor states

Control Rod Position H_c (cm)	Boron Concentration C (g B-10/l)	Mean Control Rod Position for Measuring $\frac{d\rho}{dH}$ $\overline{H}$ (cm)	Differential Control Rod Reactivity $d\rho/dH$ (pcm/cm)
17.2	0.2477	19.5	146
35.7	0.3349	37.4	202
45.5	0.3863	48.6	195
46.73	0.3855	47.7	193
59.6	0.4501	61.8	154
60.1	0.4509	61.9	149
60.2	0.4536	62.4	149
66.1	0.4781	68.8	125
85.7	0.5268	89.6	74
89.0	0.5386	90.7	66
89.6	0.5386	91.2	65

(The error of H_c is smaller than 0.1 cm, and the error of $d\rho/dH$ is smaller than 0.1 pcm/cm.) Each point of $d\rho/dH$ was measured for different positions $\bar{H} \pm \Delta H$ and adjusted according to the method of least squares (see Sec. 4.4.1).

Table 5.1.2 gives the calculated reactivities for different boron concentrations and control rod positions. In order to find the critical boron concentration of a given control rod position, we interpolated graphically between the calculated reactivities (see Figure 5.1.1).

Table 5.1.2 Calculated reactivities for different control rod positions and boron concentrations

Control Rod Position (cm)	Boron Concentration (g B-10/l)	Reactivity +) = $\ln(k_{eff})$ (pcm)	Reactivity = $(k-1)/k$ (pcm)
no rod	0	24,449	21,709
no rod	0.1438	17,885	16,367
no rod	0.2877	11,785	11,110
no rod	0.3955	7,455	7,184
no rod	0.5394	1,963	1,944
0	0.1438	2,780	2,743
0	0.2877	- 3,036	- 3,076
0	0.3955	- 7,163	- 7,411
20	0.2877	- 815	- 821
34	0.2877	11,875	1,857
34	0.3955	- 2,338	- 2,364
50	0.3955	918	915
50	0.4585	- 1,568	- 1,581
51	0.4585	- 1,397	- 1,409
61	0.4585	408	408
61	0.5394	- 2,608	- 2,646
82	0.4585	2,870	2,829
82	0.5394	- 160	- 160
100	0.5394	1,028	1,020

+) The quantity $\rho = \ln(k_{eff}$ was used when designing the High Flux Reactor for setting up the reactivity balance. In the present report $\rho = (k-1)/k$ is used uniformly for the reactivity (unless otherwise specified.

The measured and calculated control rod positions for $k_{eff} = 1$ are plotted in Figure 5.1.2 as a function of boron concentration.

The curves show that the calculation overestimates the reactor reactivity; the higher the boron concentration and the further the control rod is withdrawn, the more the reactivity is overestimated.

This effect can have the following causes:

the reactivity of the control rod is overestimated, or
the boron reactivity is underestimated

or the two causes can be combined. An additional factor is the shift parallel to the experimental curve caused by

overestimation of the excess reactor reactivity without boron and control rod,
imprecise knowledge of the solution volume in the core.

In order to be able to determine the actual amount of these errors, we must compare the calculated and measured reactivities of the control rod.

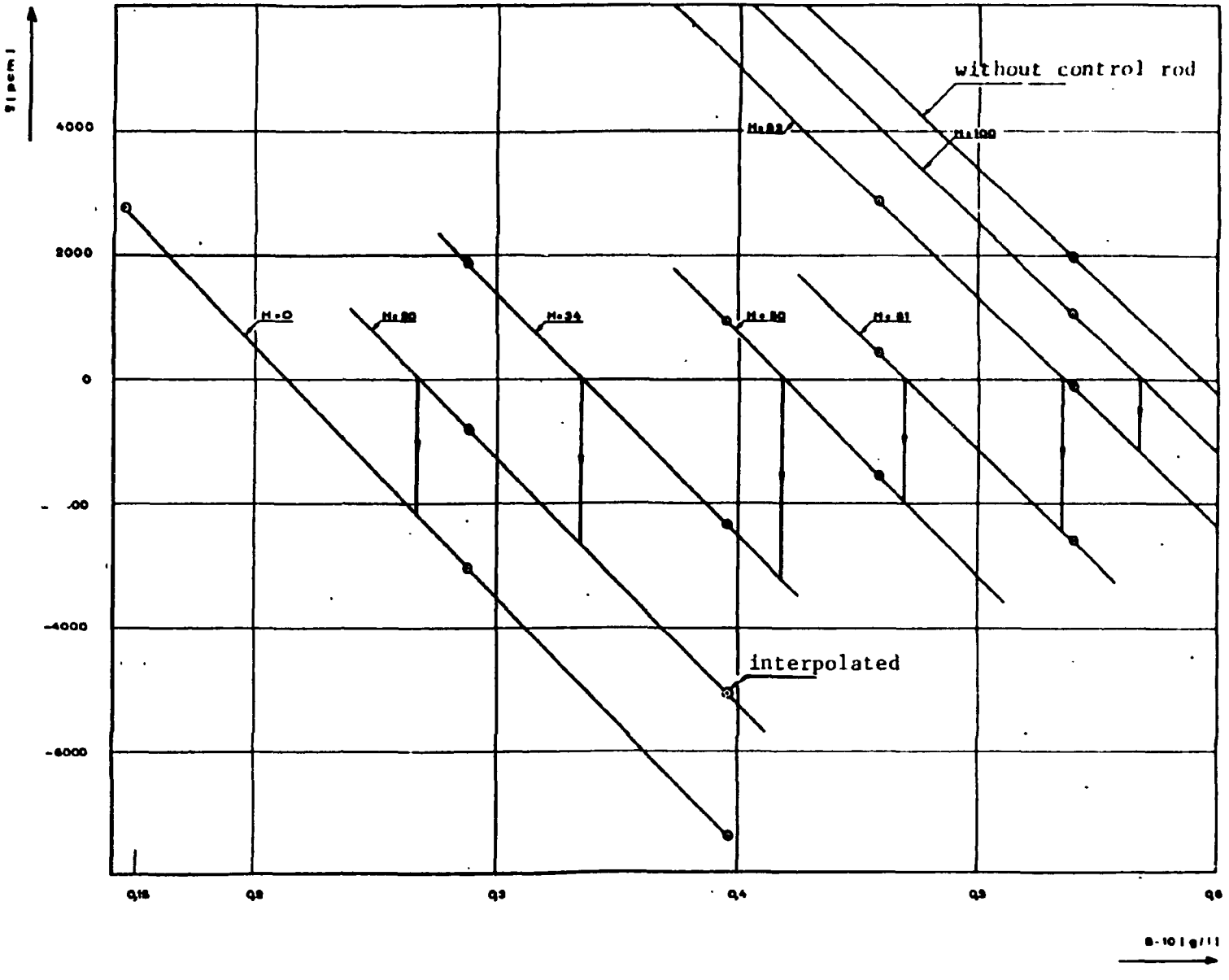

Fig. 5.1.1 Diagram for determinating the boron concentration of critical reactors without solid boron for certain control rod positions. The points correspond to the calculated reactors from Table 5.1.2.

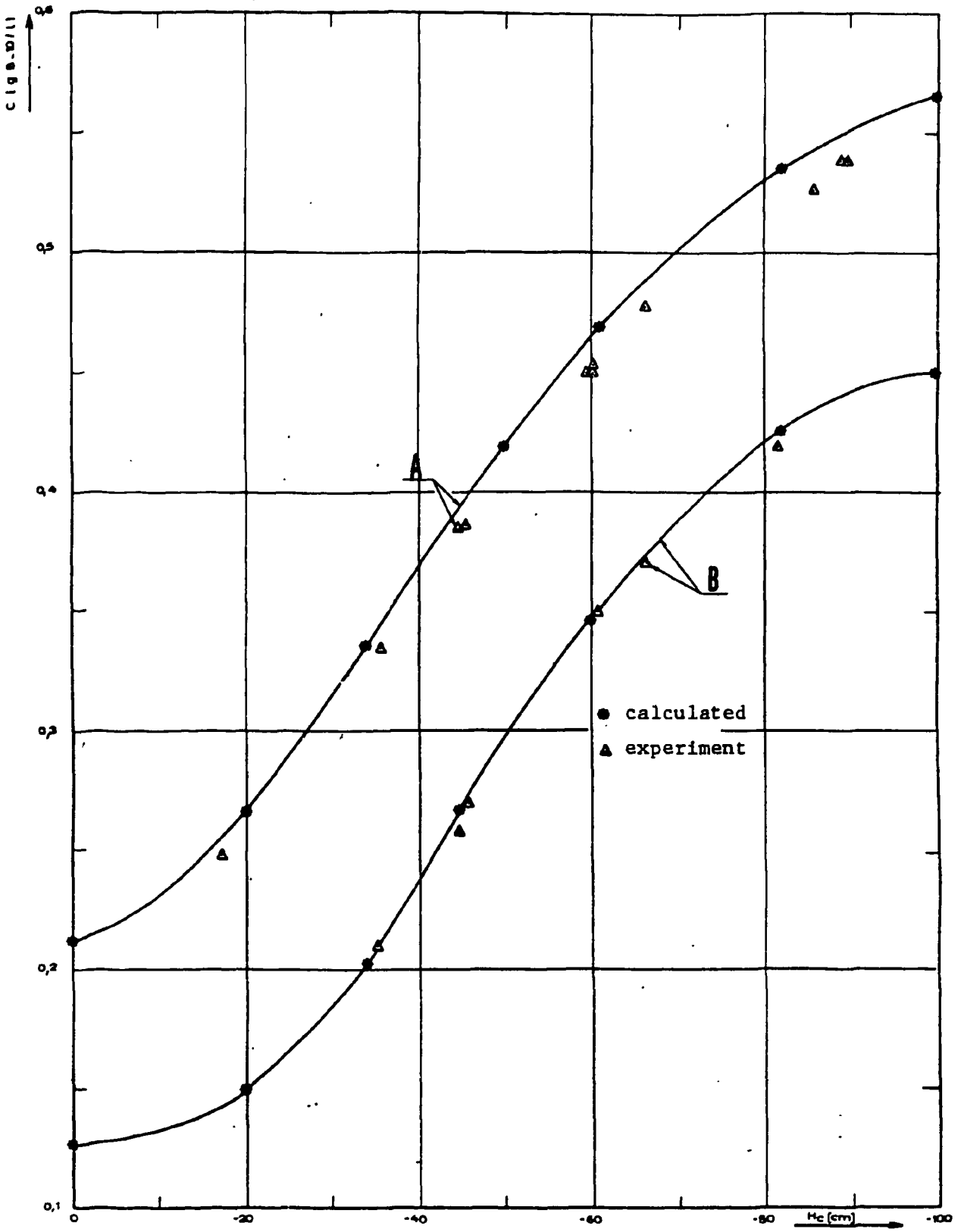

Fig. 5.1.2 Calculated and measured critical reactors with different control rod positions H_c and boron concentrations C.
A = reactors without solid boron and without dummy beam holes,
B = reactors with solid boron and without dummy beam holes.

5.1.2 The Reactivity of the Control Rod and the Boron Value

The reactivity of the control rod was determined experimentally using different methods (see Section 4.4).

With the "continuous run technique" (CRT) the procedure begins with the critical reactor and the control rod is inserted into the core. The reactivity variation $\rho(t)$ of the system can be calculated from the flux curve over time, which is observed during insertion. The control rod can be calibrated in pieces $\Delta\rho_n$ of about 2,000 to 3,000 pcm, whereby lowering of the boron concentration always brings about a return to the critical state. The total reactivity of the control rod is then

$$\Delta\rho_{\substack{\text{control}\\\text{rod}}} = \sum_{n=1}^{N} \Delta\rho_n .$$

In addition, the reactivity of a small variation ΔH was determined for different control rod positions H by observing the positive reactor period. The solution of the Inhour equation then yields the amount $\Delta\rho$, to which ΔH corresponds. A curve can be drawn through the measured points $\Delta\rho/\Delta H$ for different positions H (see Figure 5.1.3). The integral of this curve is then the control rod reactivity. In this case it is primarily the carefulness of graphic integration that affects the result, as well as the kinetic parameters β_i, λ_i. The effect of generation time is slight, assuming that small reactivities are involved (see Section 4.4).

The experimentally determined control rod characteristics are plotted in Figure 5.1.4. Several values are compiled in Table 5.1.3.

For reactivity jumps smaller than 4,200 pcm, the results of "continuous run" and pulsed source methods do not differ practically at all. For this reason only the continuous run result was given.

Using the stable period, only the rod characteristics between the rod positions -20 and -90 were determined. In order to be able to plot them with the other values in a common diagram, we assumed for the position -90 cm the same reactivity that had been determined using the continuous run technique.

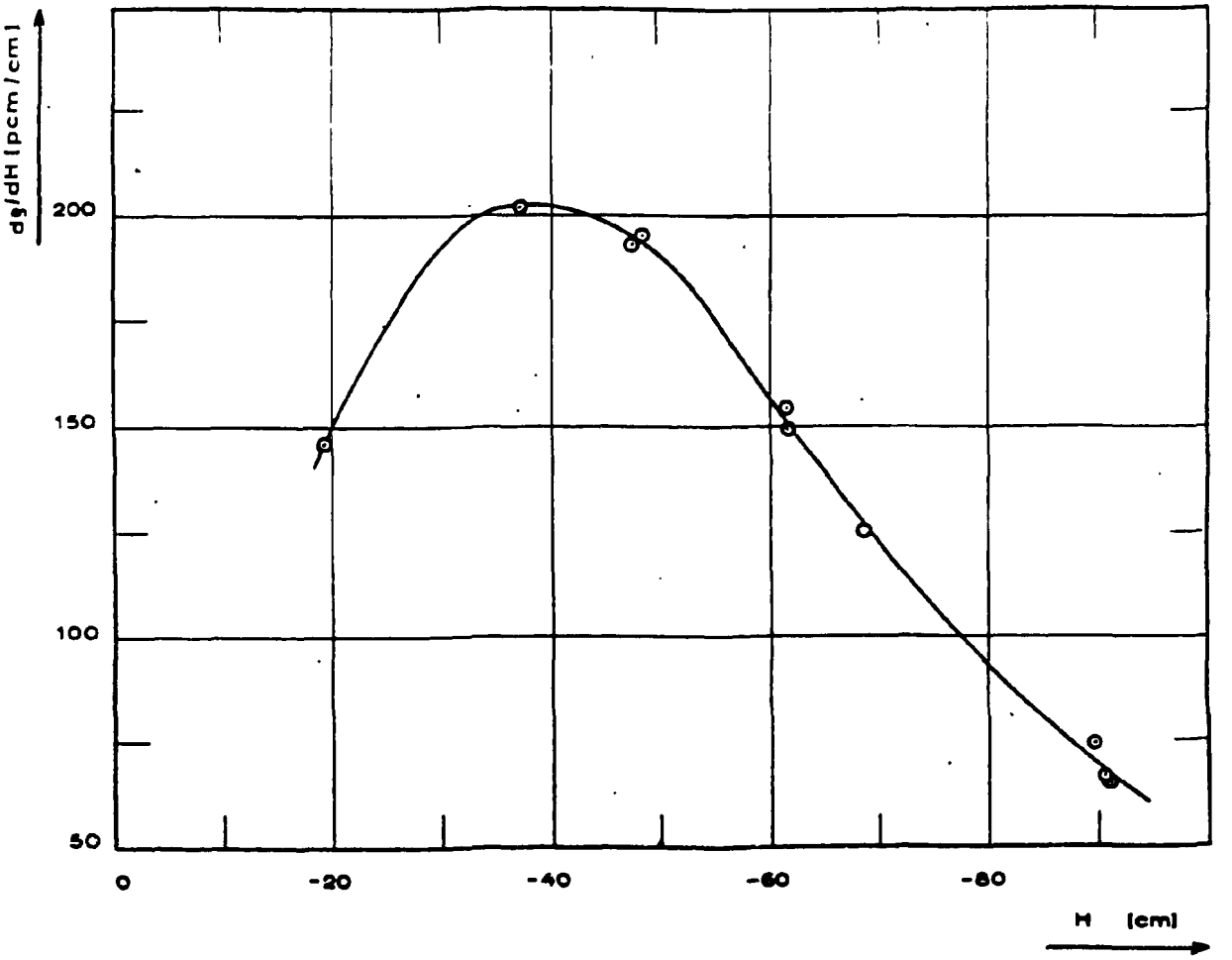

Fig. 5.1.3 Differential control rod reactivity dρ/dH as a function of the rod position for a reactor without solid boron

In order to calculate the control rod reactivity we proceed as with the continuous-run technique. Starting with a critical reactor having the boron concentration C_1 and the control rod position H_1, we move the control rod in accordance with an amount of about 2,000 to 3,000 pcm to H_2 and then reduce the boron concentration to C_2 until $k_{eff} = 1$ and so on.

The control rod characteristics can be constituted from the $\Delta\rho$ values between H_n and H_{n+1}. The procedure is indicated in Figure 5.1.1 by the thick arrows.

The result is entered in Fig. 5.1.4 and Table 5.1.5.

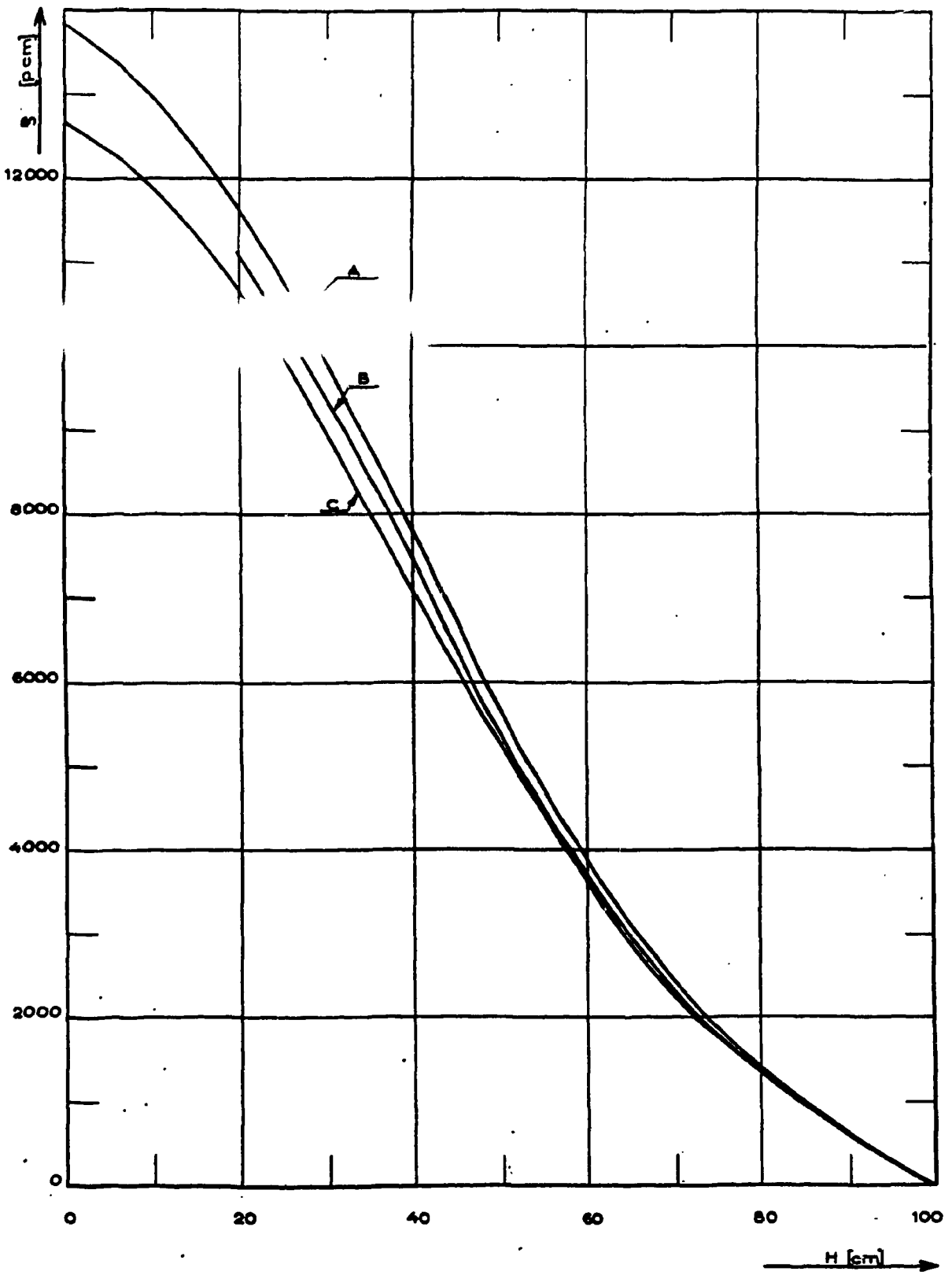

Fig. 5.1.4 Control rod characteristics of the reactor without solid boron. A = calculation, B = measurement using "approche cinetique," C = continuous-run measurement

Table 5.1.5 Reactivity of the control rod

	Reactivity of the rod between	
	H = 20 and 90 (pcm)	H = 0 and 100 (pcm)
Continuous-run technique	10,000	12,610
Stable period	10,500	--
Calculation	10,970	13,770

The calculation therefore overestimates the rod activity by 9% with respect to the CRT measurement and by 4.3% with respect to measurement using a stable period.

Since for the critical reactor any change in control rod position ΔH corresponds to a change in boron concentration ΔC, the boron value $d\rho/dC$ can be determined if the control rod reactivity curve is known. Calculation and measurement yield the following results:

Continuous-run technique $\frac{d\rho}{dC} = 35\,700 \pm 600$ pcm/g B^{10}/ltr,

Stable period $\frac{d\rho}{dC} = 37\,550 \pm 1000$ pcm/g B^{10}/ltr,

Calculation $\frac{d\rho}{dC} = 38\,700$ pcm/g B^{10}/ltr.

The measured values are obtained from the fitting of a curve to the measuring points $\Delta\rho/\Delta C$ as a function of the concentration C using the method of least error squares. The error limits correspond to the variation in the values $\Delta\rho/\Delta C$.

5.1.3 Flux Measurements

5.1.3.1 The Thermal Flux Distribution in the Reflector

The thermal flux distribution in the reflector was measured using manganese probes. The thermal flux was calculated from the activation values in accordance with 4.1.2 and normalized to 1 W reactor power using the measured "rendement. The control rod was at H = 60 cm, the boron concentration was 0.450 g/liter. The measurement values are listed in Table 5.1.4.

Several typical radial and axial flux distributions are plotted in Figures 5.1.5 through 5.1.9 in comparison with the calculated values.

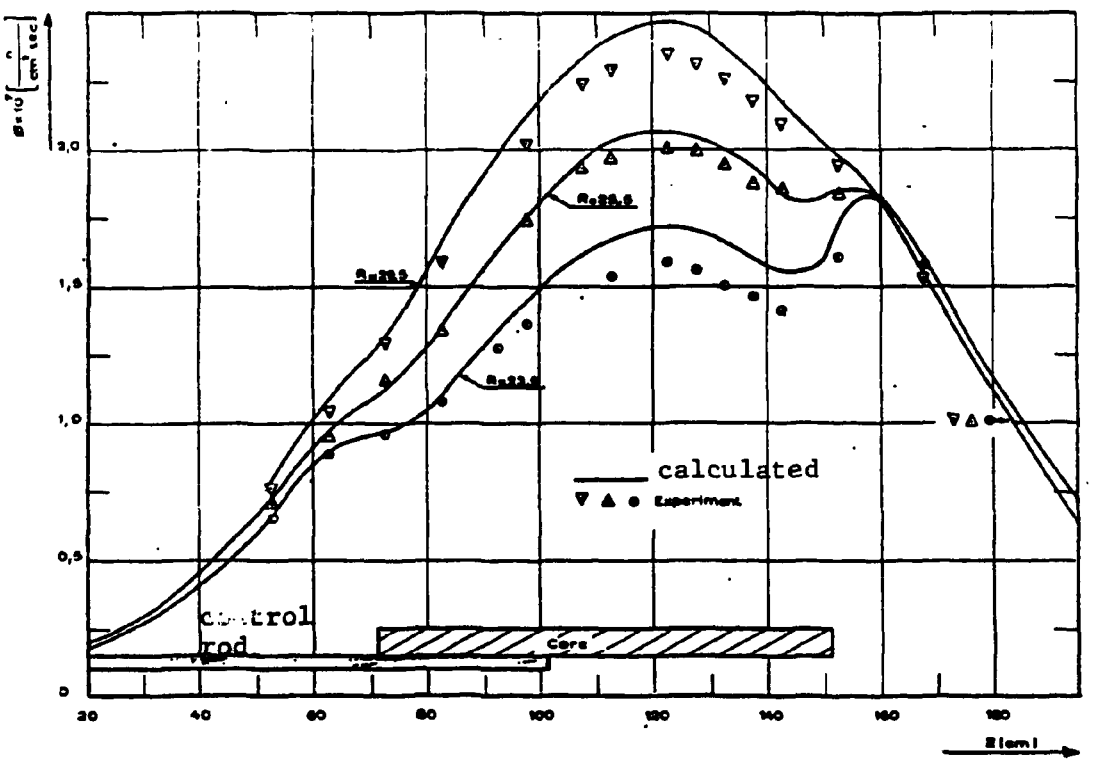

Fig. 5.1.5 Axial distribution of the thermal neutron flux at 1 W reactor power for the radii R = 23.5, R = 25.5, R = 29.5 (without solid boron)

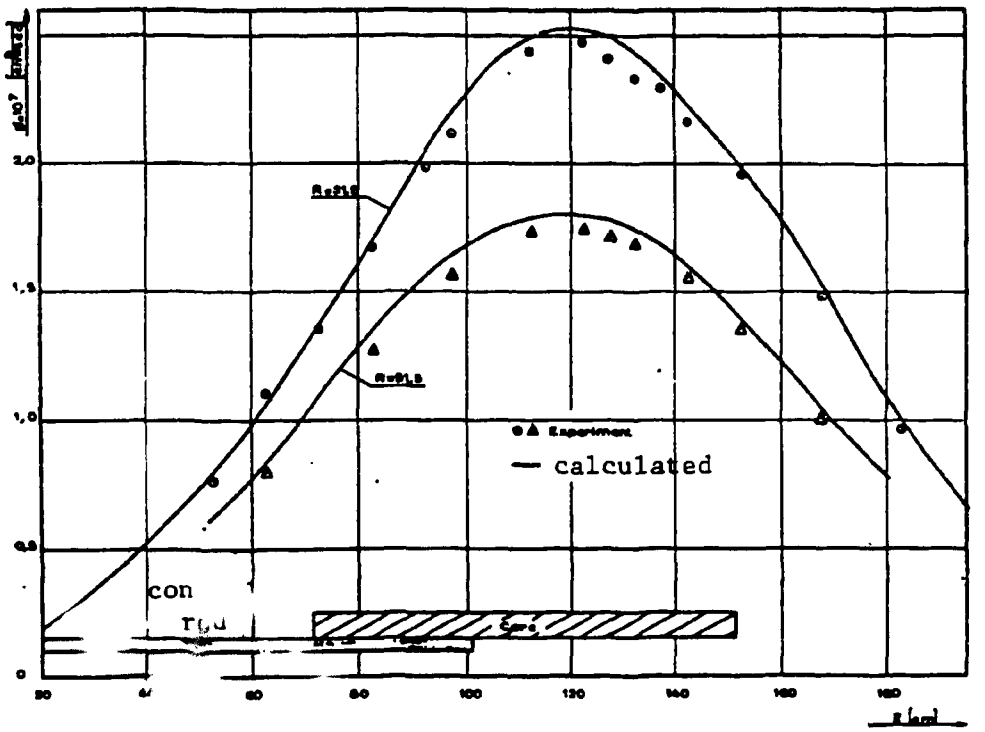

Fig. 5.1.6 Axial distribution of the thermal neutron flux at 1 watt reactor power for the radii R = 31.5 and R = 51.5 (without solid boron)

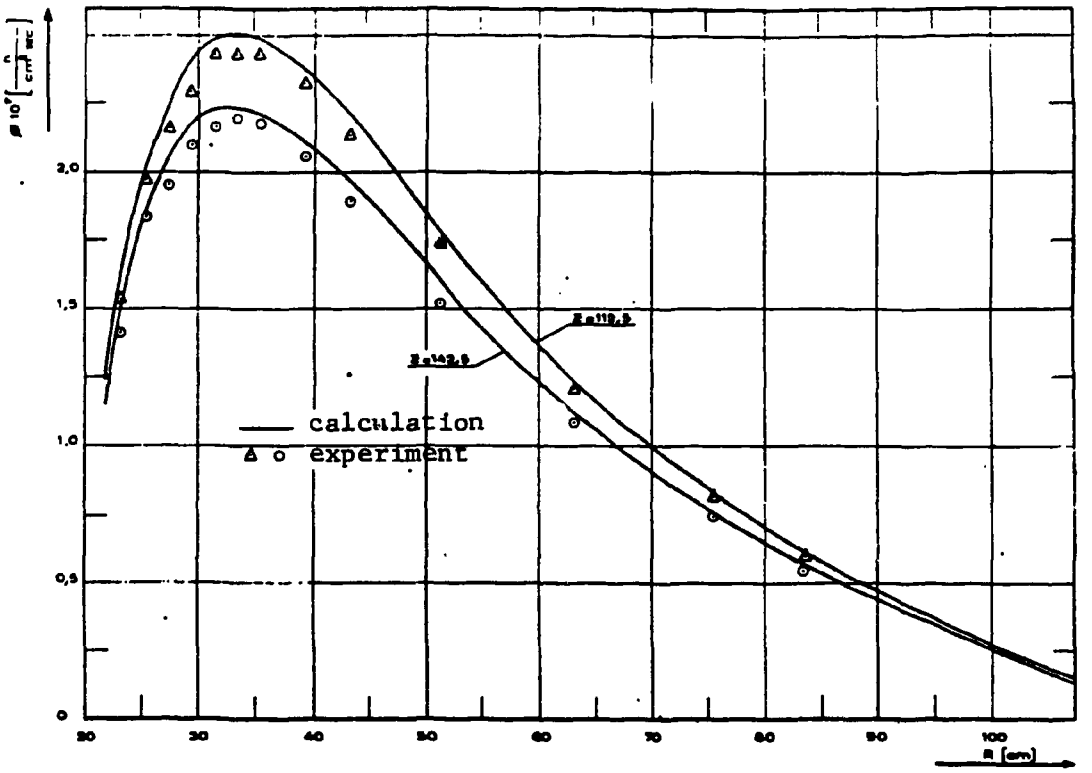

Fig. 5.1.7 Radial distribution of the thermal neutron flux at 1 watt reactor power for Z = 112.5 and Z = 142.5 (without solid boron)

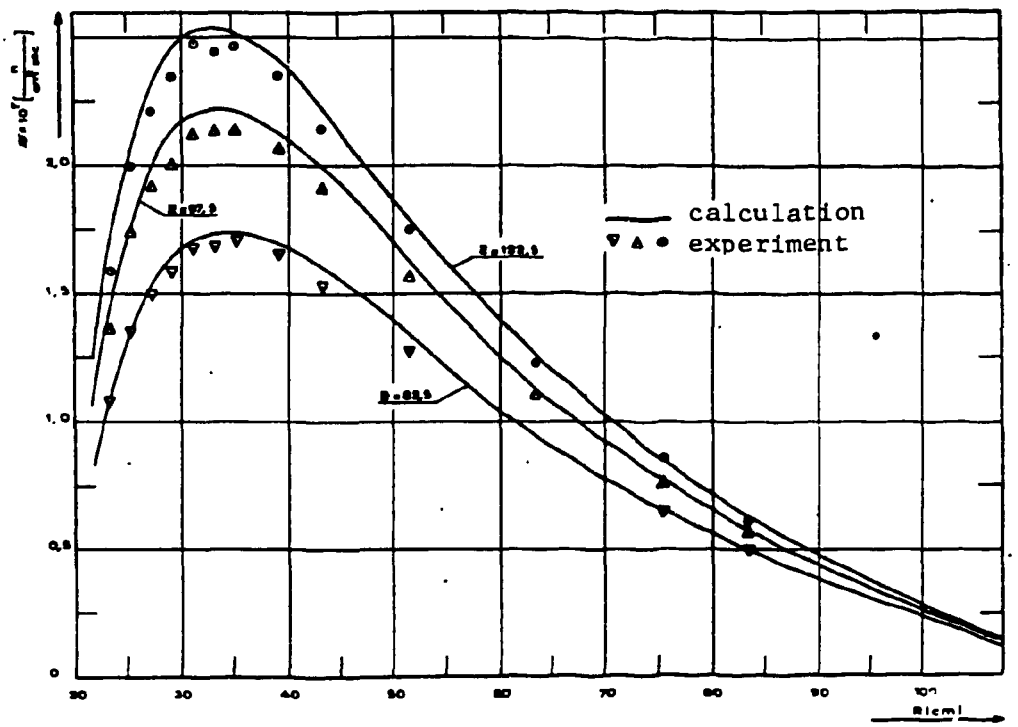

Fig. 5.1.8 Radial distribution of the thermal neutron flux at 1 watt reactor power for Z = 82.5, Z = 97.5 and Z = 122.5 (without solid boron

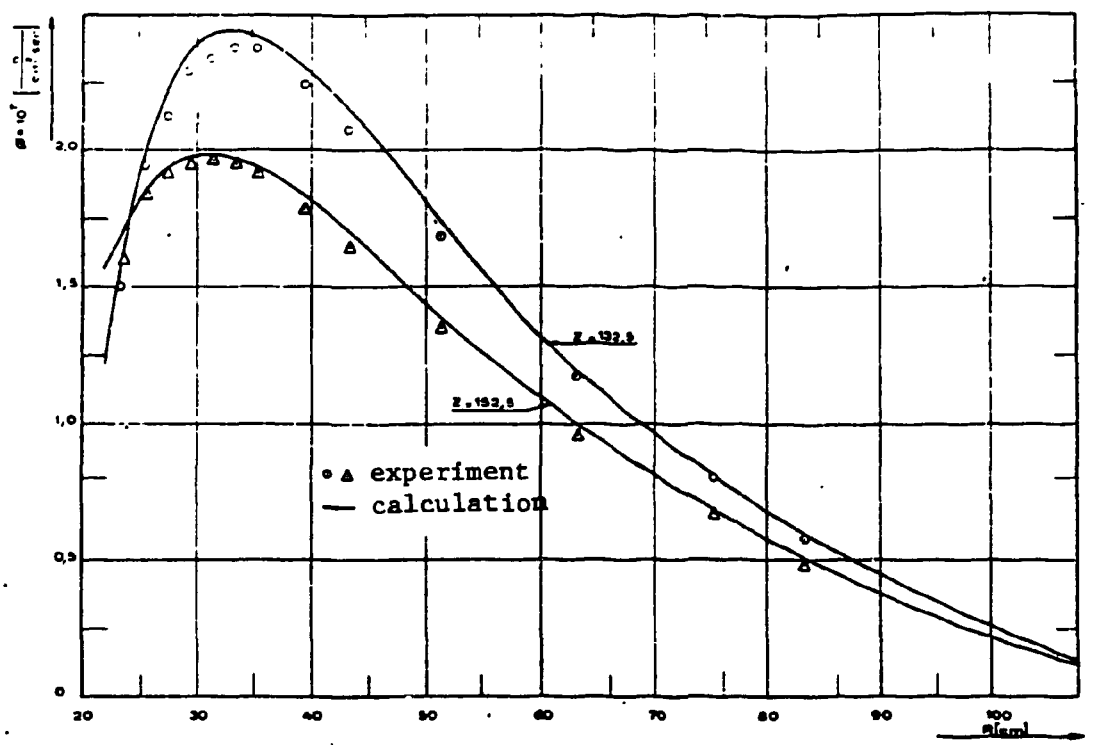

Fig. 5.1.9 Radial distribution of the thermal neutron flux at 1 watt reactor power for Z = 132.5 and Z = 152.5 (without solid boron)

Table 5.1.4 Measured thermal flux distribution in the reflector, corrected for epithermal absorption and spectrum hardening near the core, normalized to 1 x 10^{-7} W reactor power

[Commas should be read as decimal points -- Translator's Note]

R (cm) / Z (cm)	23,5	25,5	27,5	29,5	31,5	33,5	35,5	39,5	43,5	51,5	63,5	75,5	83,5
182,5	1,041	1,030	1,016	1,004	0,960		0,928	0,857	0,802				
167,5	1,566	1,568	1,561	1,523	1,477		1,414	1,303	1,211	1,003	0,740	0,523	0,384
152,5	1,604	1,840	1,912	1,943	1,957	1,950	1,919	1,782	1,644	1,351	0,963	0,674	0,488
142,5	1,411	1,834	1,950	2,096	2,167	2,194	2,173	2,055	1,892	1,521	1,082	0,746	0,541
137,5	1,462	1,873	2,063	2,174	2,294	2,304	2,277	2,147	1,992				
132,5	1,501	1,941	2,128	2,254	2,334	2,358	2,377	2,244	2,079	1,683	1,172	0,802	0,585
127,5	1,560	1,993	2,178	2,310	2,415	2,442	2,423	2,304	2,130	1,716	1,189		
122,5	1,590	2,017	2,209	2,348	2,476	2,441	2,466	2,349	2,142	1,748	1,222	0,852	0,602
112,5	1,538	1,970	2,160	2,292	2,438	2,434	2,432	2,326	2,139	1,736	1,209	0,822	0,594
107,5		1,931		2,239		2,365							
97,5	1,368	1,743	1,916	2,023	2,129	2,139	2,139	2,064	1,910	1,563	1,104	0,755	0,559
92,5	1,272		1,781		1,982		2,000						
82,5	1,076	1,366	1,492	1,585	1,673	1,682	1,706	1,654	1,526	1,271		0,644	0,484
72,5	0,956	1,154	1,230	1,298	1,356		1,365						
62,5	0,885	0,950	1,000	1,037	1,110		1,037	1,017	0,979	0,808			0,353
52,5	0,652	0,701	0,785	0,752	0,769								

The relative deviation between measurement and calculation is about 2-3%, except very close to the core for the measuring points at the radius 23.5 cm. There positioning errors due to the sharp flux gradient have a great effect. The difference between measurement and calculation at that point is 8%. Systematically the computed values are 2.2% higher than the measured values due to the difference between measured and calculated yield ("rendement") (see 5.1.5).

5.1.3.2 Thermal Spectrum Measurements

As described in 4.1.3, spectrum measurements were carried out with resonance detectors, with Pu/U probes and with Lu/Mn probes in the reflector midplane. The measurement results are plotted in Figures 5.1.10 and 5.1.11. The solid curves were calculated according to

$$R_{Pu/U} = \left[\frac{\sum_{j=4}^{6} \sigma_{a,j}^{Pu} \cdot \phi_j + \overline{\sigma_{a,epi}^{Pu}} \cdot \phi_3}{\sum_{j=4}^{6} \sigma_{a,j}^{U} \cdot \phi_j + \overline{\sigma_{a,epi}^{U}} \cdot \phi_3} \right] \cdot \left[\frac{\sigma_a^{Pu}(2200\ m/s)}{\sigma_a^{U}(2200\ m/s)} \right] \qquad (5.1)$$

and, correspondingly, for $R_{Lu/Mn}$. The activation cross section $\sigma_{a,j}$ was calculated for the thermal groups as a function of the radius by means of the code THERMOS; ϕ_j are the thermal group fluxes of a two-dimensional diffusion calculation, $\overline{\sigma_{a,epi}}$ is the effective absorption cross section in the lethargy interval of the 3rd group, and ϕ_3 is the flux in the 3rd group of the diffusion calculation.

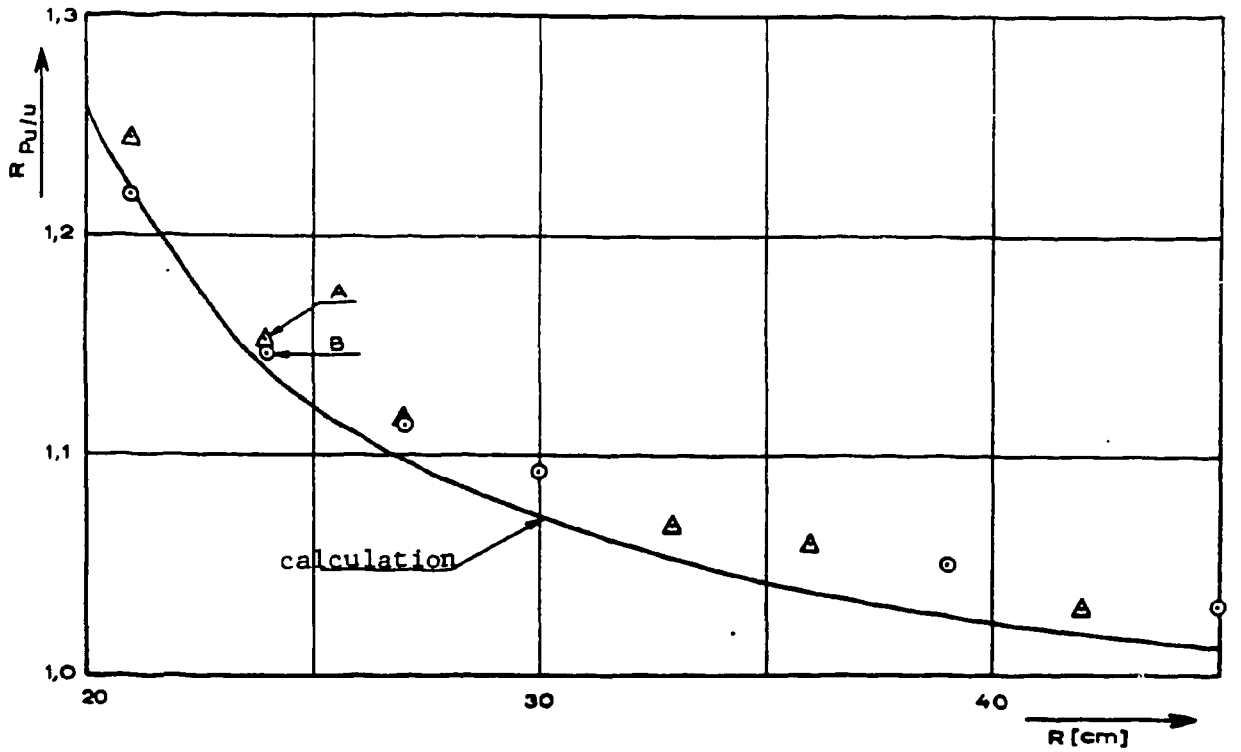

Fig. 5.1.10 Ratio of Pu-239 to U-235 in the reflector midplane. A = measuring point at which the Pu probe pointed at the core, B = measuring point at which the U prove pointed at the core.

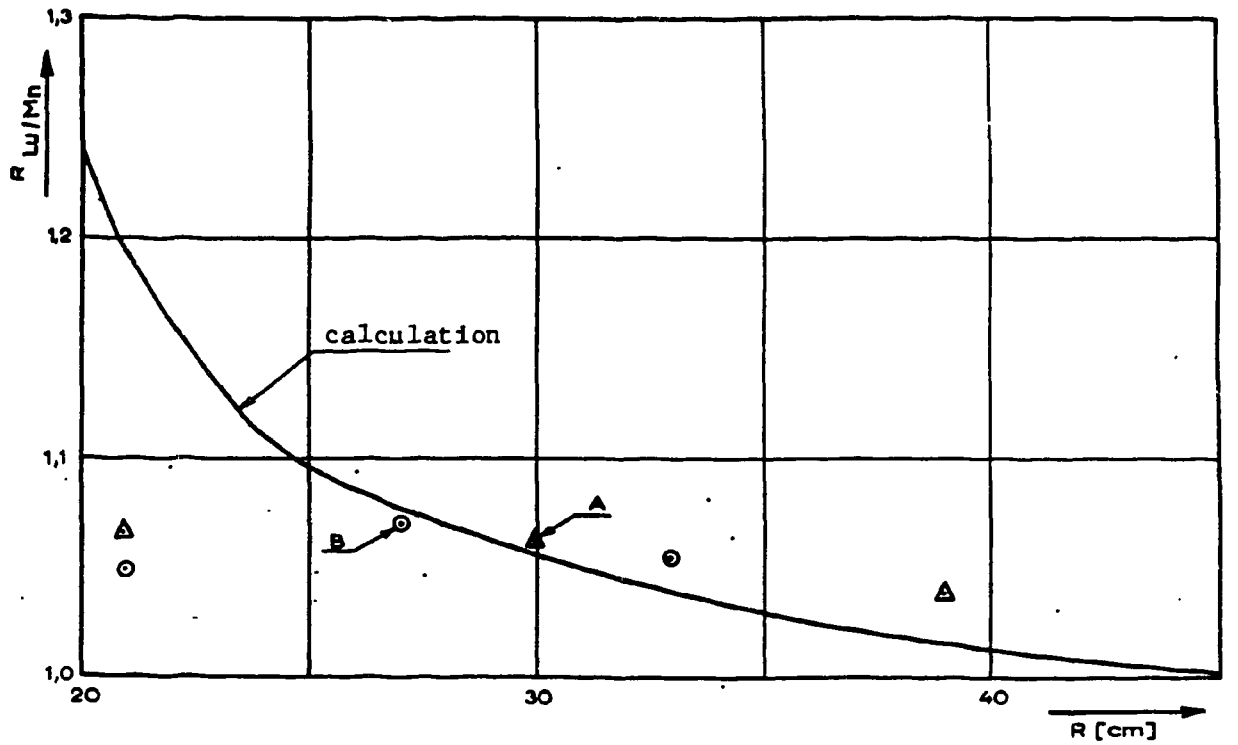

Fig. 5.1.11 Ratio of Lu-176 to Mn in the reflector midplane. A = measuring points at which the Lu probe pointed at the core, B = measuring point at which the Mn probe pointed at the core

5.1.3.3 The Cadmium Ratio

The cadmium ratio R_{Cd} was calculated using the same formulation as in [4]:

$$R_{Cd} = \frac{\sigma_a^{th} \frac{v_T}{v_o} \cdot \frac{\sqrt{\pi}}{2} \cdot \phi_{th} + \overline{\sigma_a^{epi}} \cdot \overline{\phi_{epi}}}{\overline{\sigma_a^{epi}} \cdot \overline{\phi_{epi}}} , \qquad (5.2)$$

where σ_a^{th} = 13.3 b for Mn probes,

$\overline{\sigma_a^{epi}}$ = 1.72 b for the lethargy interval of the 3rd group; the contribution of higher energy is negligible.

ϕ_{th} = $\phi_4+\phi_5+\phi_6$ of the diffusion calculation,

$\overline{\phi_{epi}}$ = ϕ_3 of the diffusion calculation,

v_T = most probable velocity in the real spectrum.

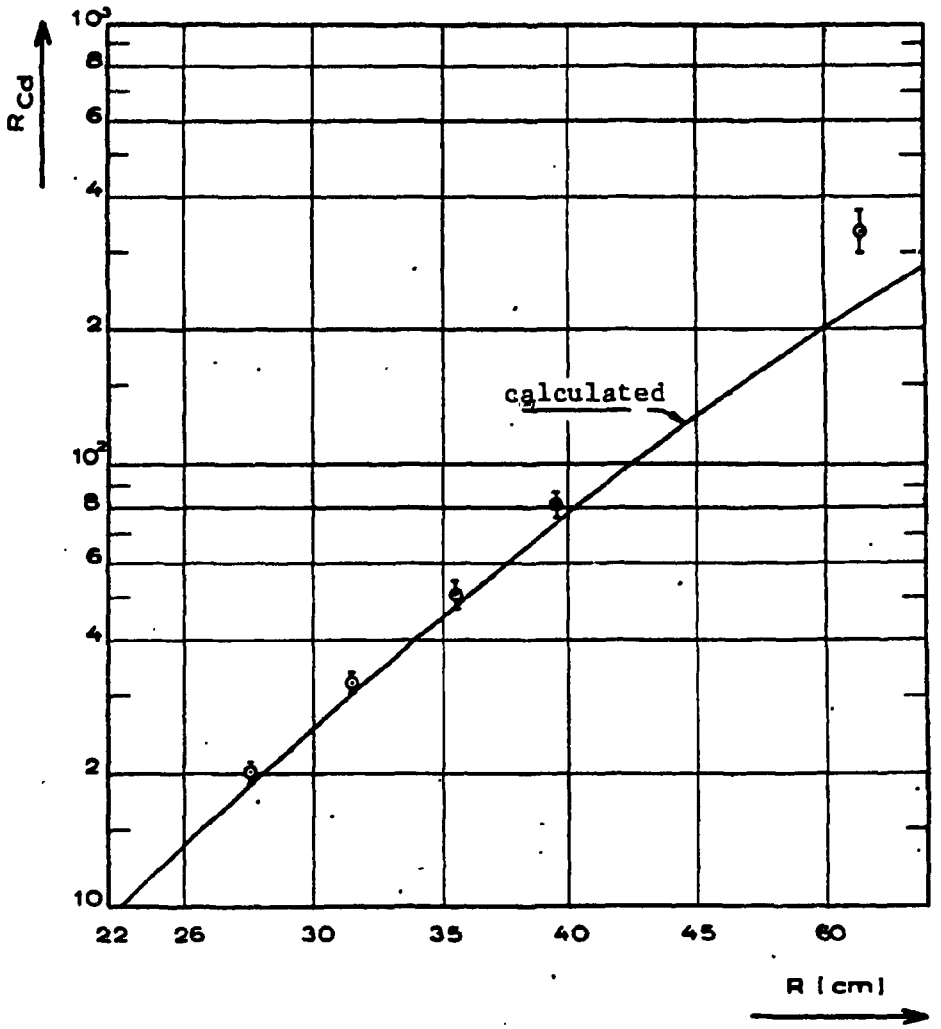

Fig. 5.1.12 The cadmium ratio in the midplane of the reactor without solid boron

R_{Cd} was measured in the reactor midplane and calculated (see 4.1). The theoretical and experimental values are plotted in Figure 5.1.12. Up to a value of about R_{Cd} = 100, measurement and calculation are in good agreement, i.e., even the epithermal flux of the diffusion calculation up to about 40 cm agrees well with the measurement, since it was shown in 5.1.3.1 that the thermal fluxes can be easily calculated.

5.1.3.4 Epithermal and Fast Flux Distribution in the Reflector

The epithermal flux distribution in the reflector midplane measured with gold and indium probes is plotted in Figure 5.1.13. For indium no absolute measurement was carried out, and for this reason the values were normalized to the measurement with gold probes on the radius R = 27.5 cm. The calculated curve was obtained from a diffusion calculation.

The distribution of the fast flux was measured with phosphorus and sulfur probes. The theoretical distribution was calculated for the threshold energy of phosphorus according to transport theory (Figure 5.1.14).

5.1.3.5 Absolute Measurement of the Thermal Flux

In order to be able to normalize thermal, epithermal and fast flux measurements among one another, we carried out absolute thermal flux measurements at two points in the reflector. Irradiation was done at 30.2 W for one hour.

$$R = 35.5 \text{ cm}, \quad Z = 111 \text{ cm}, \quad \Phi_{th} = 0.735 \pm 0.04 \times 10^9 \text{ n/cm}^2\text{s}$$

$$R = 87.5 \text{ cm}, \quad Z = 111 \text{ cm}, \quad \Phi_{th} = 0.164 \pm 0.02 \times 10^9 \text{ n/cm}^2\text{s}$$

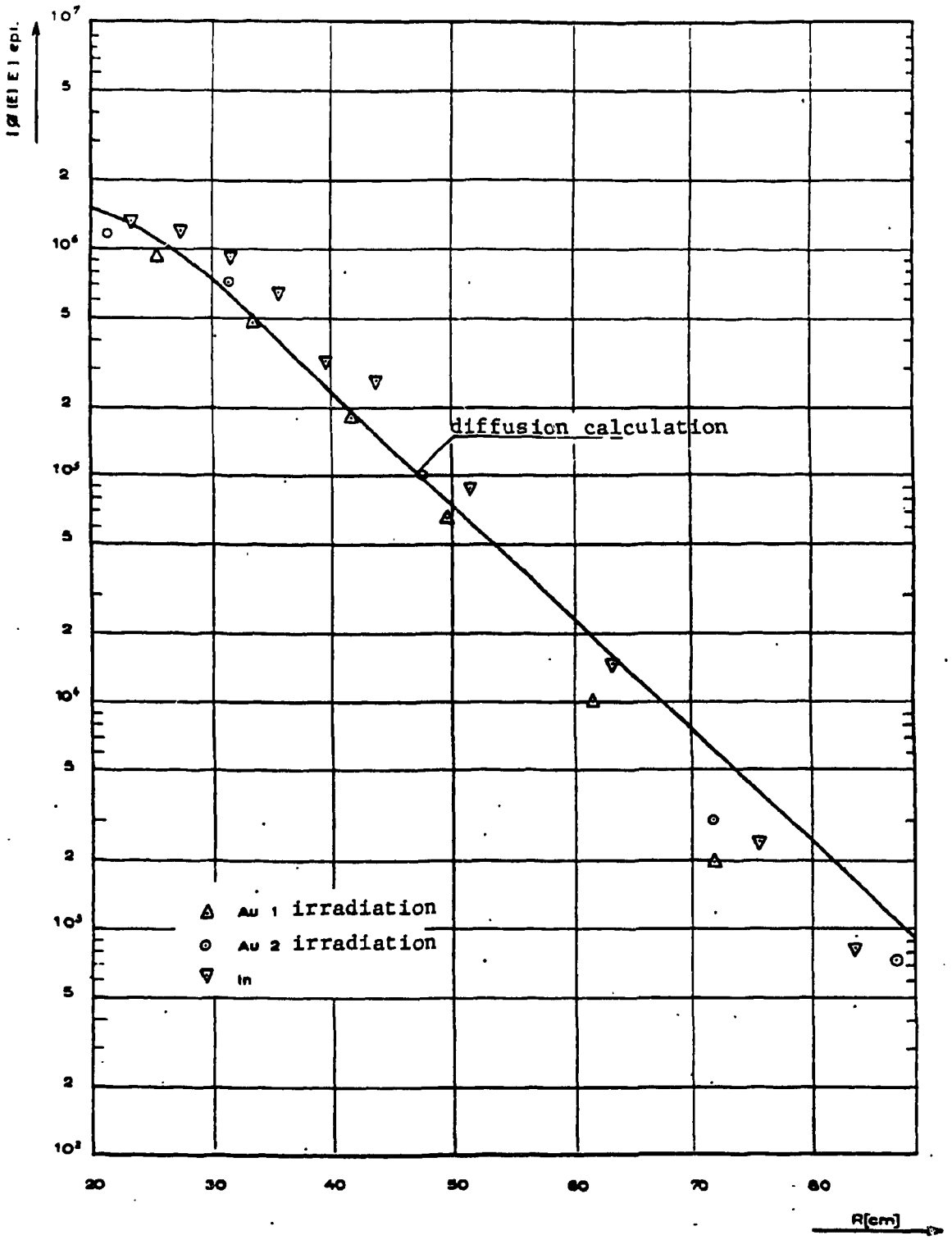

Fig. 5.1.13 Epithermal neutron flux distribution in the midplane of the reactor without solid boron

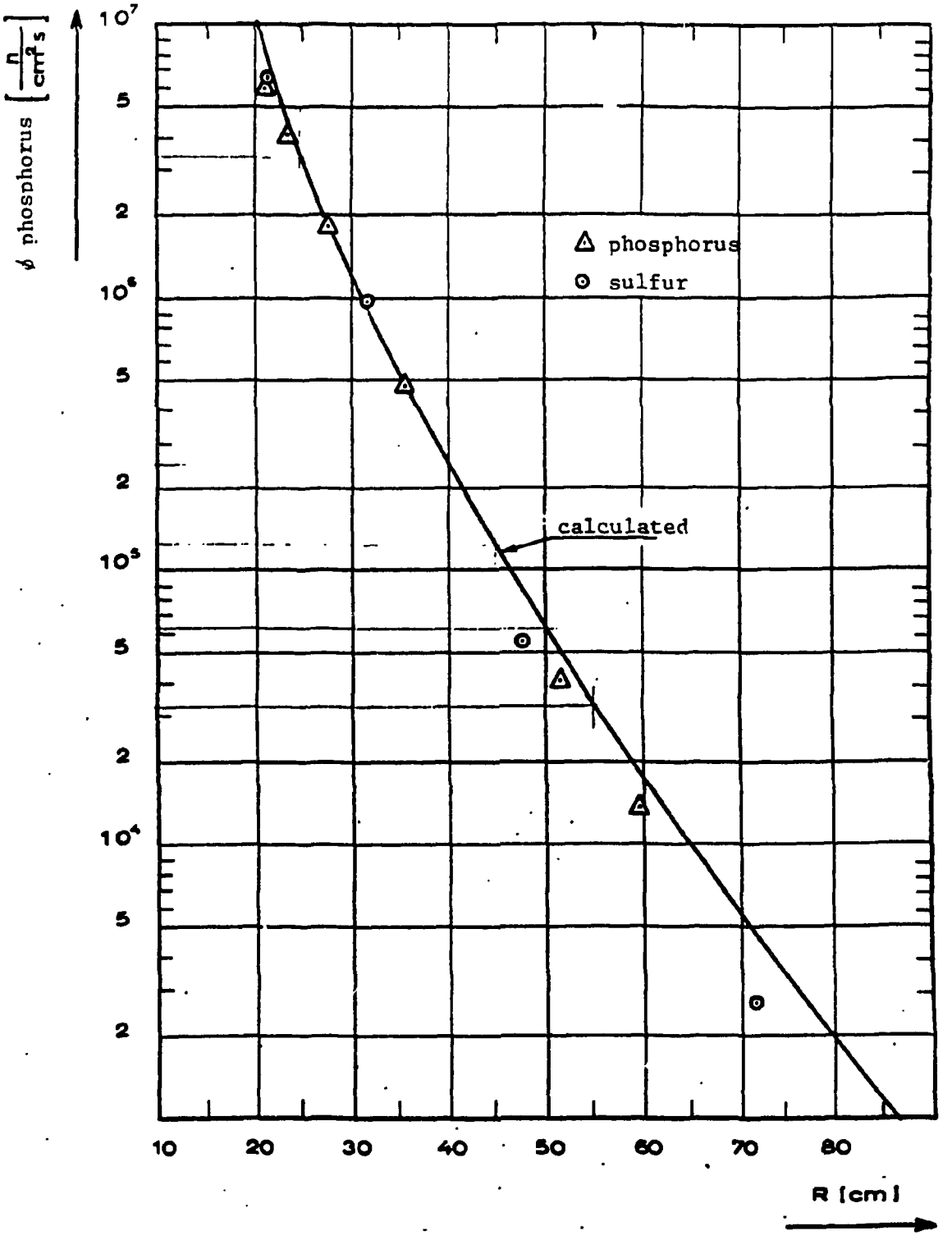

Fig. 5.1.14 Distribution of the "fast" neutron flux in the midplane of the reactor without solid boron

5.1.4 The Power Distribution in the Core

The power distribution in the core was measured using the method described in 4.2. The measuring points were integrated over the core volume and normalized to a mean power of one. The measurement results are compiled in Table 5.1.5. The coordinates relate in this case to the fuel zone: H = 0 is the lower plate edge, H = 80 is the upper plate edge; R = 14 is the inside radius and R = 19.5 the outside radius of the fuel zone. The error limit for about 90% of the measuring points is 1%. Some of the measuring points on the plate edge, especially for H = 79.75 cm, exhibit larger errors (of several percent), which can be explained by the positioning, which at that point is not very accurate, in connection with a sharp flux gradient. Figures 5.1.15 through 5.1.21 show the comparison between measurement and calculation for several typical radial and axial power distributions. In the case of the radial distribution far from the core ends we see clearly that the measuring points exhibit about the same difference from the calculated curve as we found between diffusion theory and THERMOS calculation (see Figure 3.2). Figure 5.1.22 shows a perspective view of the measured power distribution.

The gradient on the outer core edge is steeper in the measured distribution (as is the case with the THERMOS calculation) than is given by the diffusion calculation, whereby the differences between experiment and calculation are only about 2 to 3%, however, except for the points on the radius R = 19.395, where the measurement yields a 10% higher value than the calculation. In the case of the infinite cylinder (Figure 3.2), THERMOS also gives a 10% higher value for this radius. The power distribution at the core ends (H = 0.25 and H = 79.75) is given somewhat lower by the calculation than by the experiment. This effect is due to the assumption that was made in the calculation, namely that the spectrum does not change in the axial direction. This is certainly not correct on the upper and lower core edges. The spectrum there is softer, since the thermal reflector neutrons flow in from above and in a radial direction at the same time, and thus the local power there is higher than is given by the calculation.

Table 5.1.5 Relative power distribution in the core without solid boron, experimental values normalized to a mean power of 1.

[Commas should be read as decimal points -- Translator's Note]

Plate height H (cm)	Radius (cm) 14,35	14,65	14,95	15,25	15,90	16,75	17,60	18,25	18,55	18,85	19,395
79,75	2,5247	2,2931	2,3323	2,2518	2,1002	2,1656	2,1556	2,3767	2,5115	2,5618	2,9004 (H=79,55)
79,06	2,0302										2,6260
78,55	1,7642					1,2226					2,4228
78,06	1,6608					1,0912					2,3470
77,15	1,5239					0,9205					2,1803
75,00	1,3380	1,1518	1,0203	0,9272	0,8218	0,8020	0,9149	1,1075	1,2551	1,4642	2,0507
72,50	1,2673					0,7715					1,9772
70,00	1,2375					0,7730					1,9769
62,50	1,2820	1,1417	1,0136	0,9371	0,8407	0,8270	0,9440	1,1293	1,3157	1,4818	2,0233
55,00	1,3340					0,8600					2,1180
47,50	1,2910					0,8630					2,1315
40,00	1,1620	1,0985	0,9491	0,8971	0,8348	0,8280	0,9442	1,1541	1,3180	1,4889	2,0459
32,50	1,0266					0,7600					1,9600
25,00	0,7329					0,6440					1,7807
17,50	0,6279	0,6011	0,5472	0,5335	0,5237	0,5580	0,6627	0,8574	0,9755	1,1134	1,5648
10,00	0,5291					0,4706					1,3556
7,50	0,5354					0,4467					1,3130
5,00	0,5015	0,4839	0,4361	0,4241	0,4057	0,4440	0,5312	0,6897	0,7862	0,8977	1,2751
2,85	0,5315					0,4836					1,3029
1,94	0,5870					0,5430					1,3195
1,45	0,6646					0,5862					
0,94	0,6899										1,4421
0,25	0,8992	0,8945	0,8782	0,8707	0,8902	0,9384	1,0359	1,1621	1,2329	1,3258	1,5329 (H=0,45)

So that the calculated and measured values can be compared it is necessary to determine the mean relative core power from the measuring points. For this purpose two methods were used.

Mechanical Integration:

The radial power distributions were plotted and integrated. This yielded a mean axial distribution. The integral over this distribution gives the mean core power. For control purposes we started with the integration of the axial power distributions and then determined the mean radial power distribution. The results of both methods agreed.

Mathematical Integration:

By means of an electronic computer program, polynomials are fitted between the measuring points such that smooth curves are formed that make it possible to represent the power distribution as shown in Figure 5.1.20. This distribution can then be integrated with any accuracy. The result is about 1% lower than the result of mechanical integration.

An important parameter for the thermodynamic design of the High Flux Reactor is the radial flux form factor F_{rad}, which is defined as the ratio of the mean power in strips between R = 19 and R = 19.5 cm to the mean power of the entire core. From the measurement it follows that

$$F_{rad} \text{ (experiment)} = 1.727,$$

while the calculation yields

$$F_{rad} \text{ (calculation)} = 1.649.$$

The difference is therefore 4.7%. On the basis of the difference between the THERMOS and diffusion calculations (see 4.2) we would have expected that F_{rad} (experiment) would be 4.3% greater. The real error is only 0.4%, which is completely within the limits of error given by the integration and the measuring method.

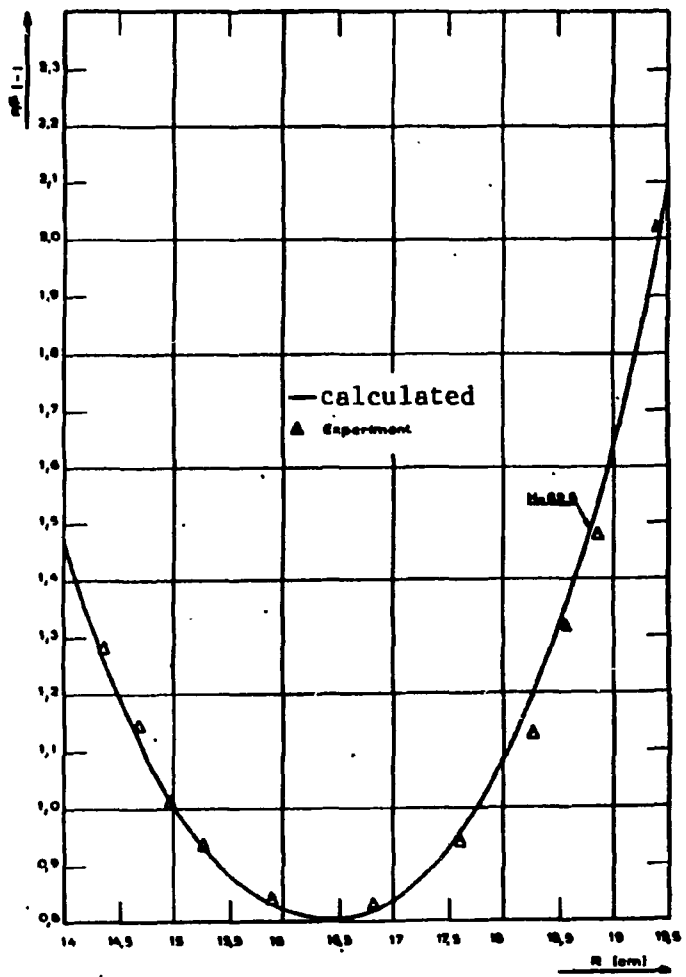

Fig. 5.1.15 Radial power distribution in the core without solid boron. H = 62.5 cm above lower core edge.

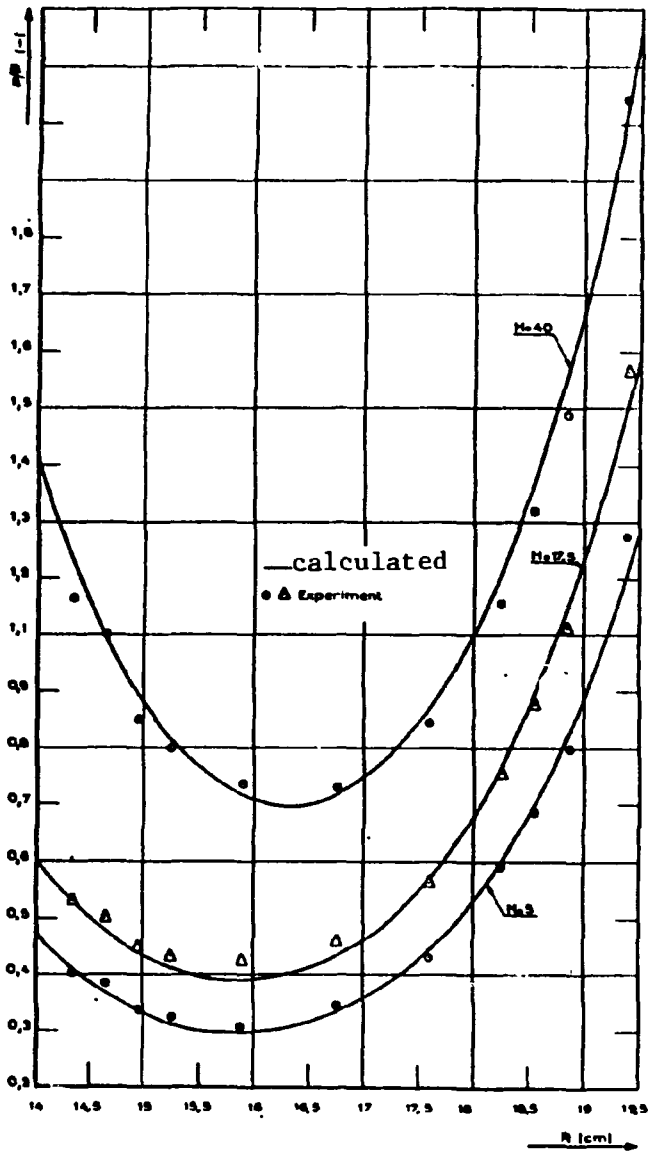

Fig. 5.1.16 Radial power distribution in the core without solid boron. H = 5, 17.5 and 40 cm above the lower core edge.

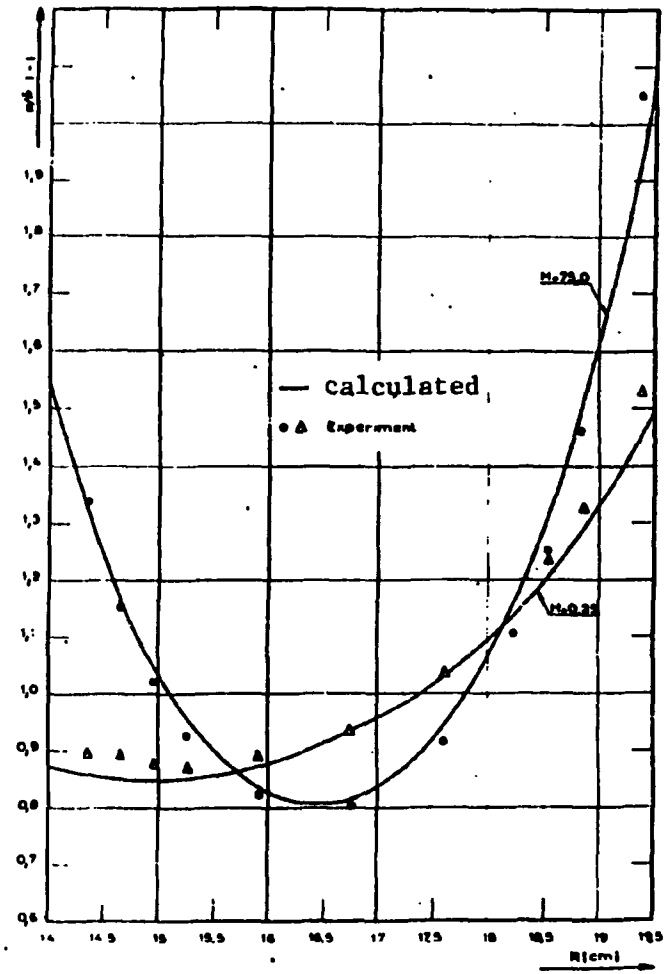

Fig. 5.1.17 Radial power distribution in the core without solid boron. H = 0.25 and 75 cm above the lower core edge.

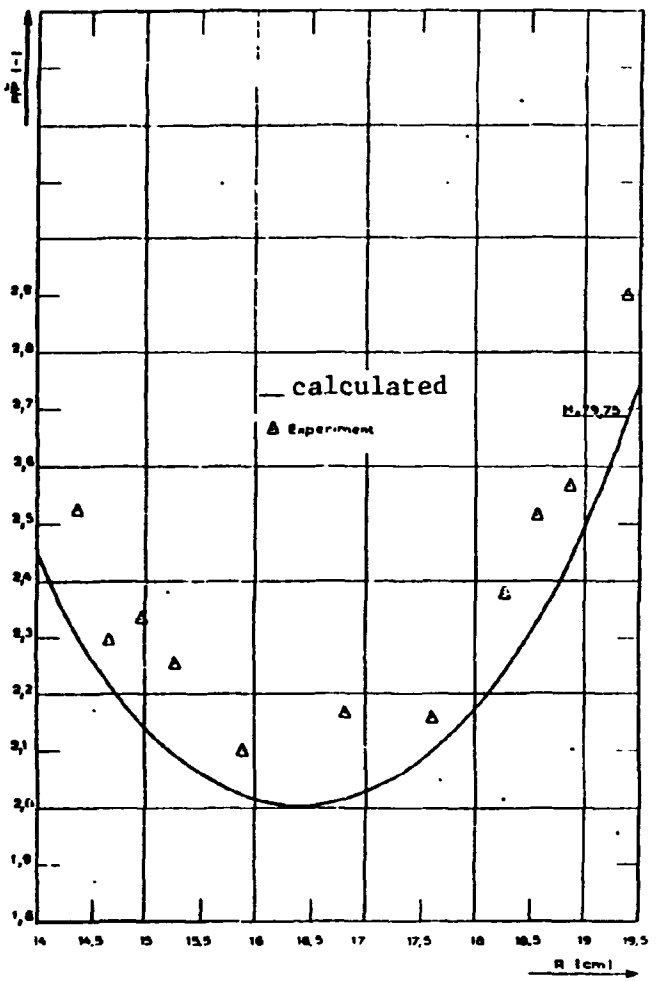

Fig. 5.1.18 Radial power distribution in the core without solid boron for H = 79.75 cm above the lower core edge.

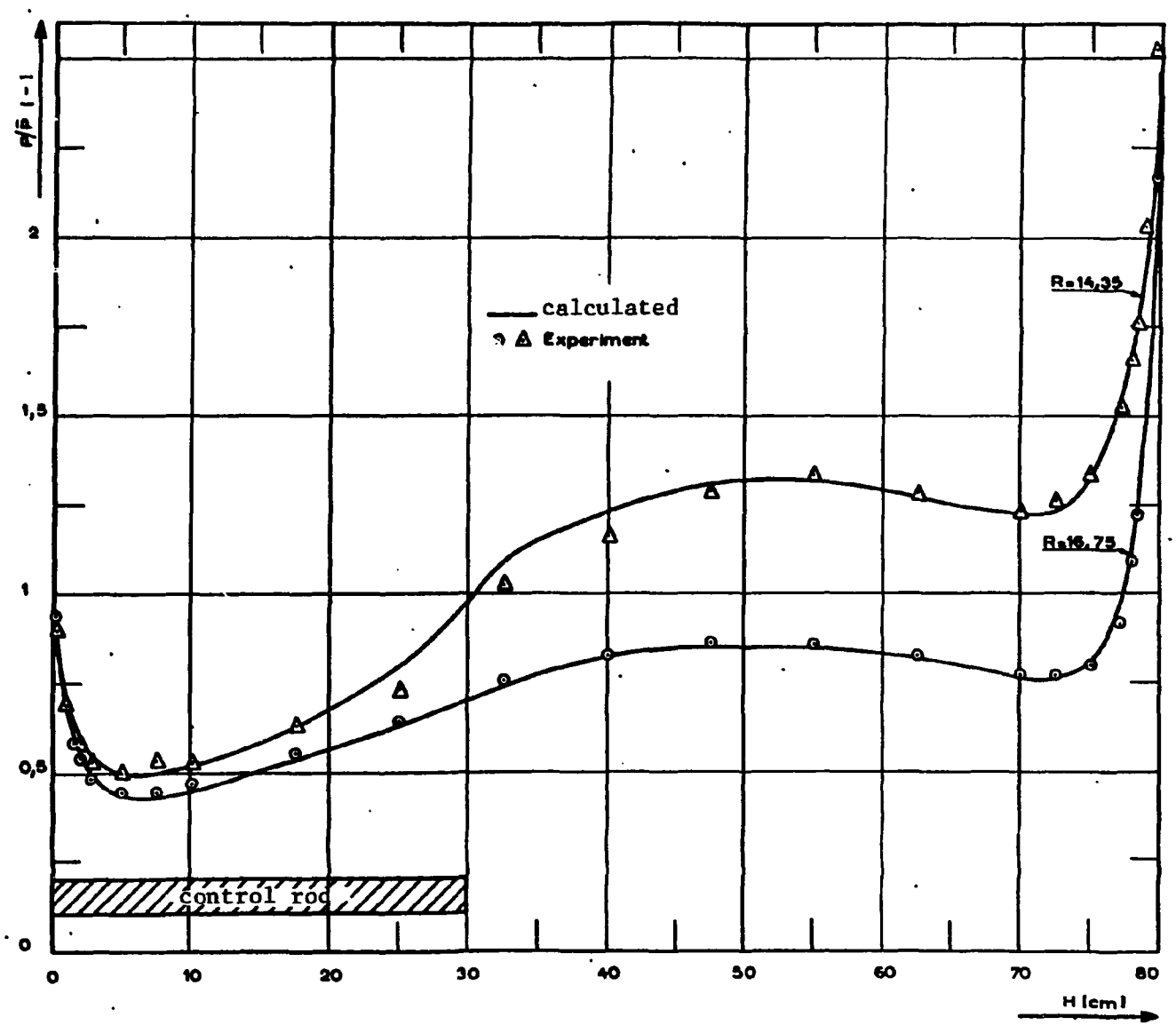

Fig. 5.1.19 Axial power distribution in the core without solid boron for the radii R = 14.35 amd 16.75.

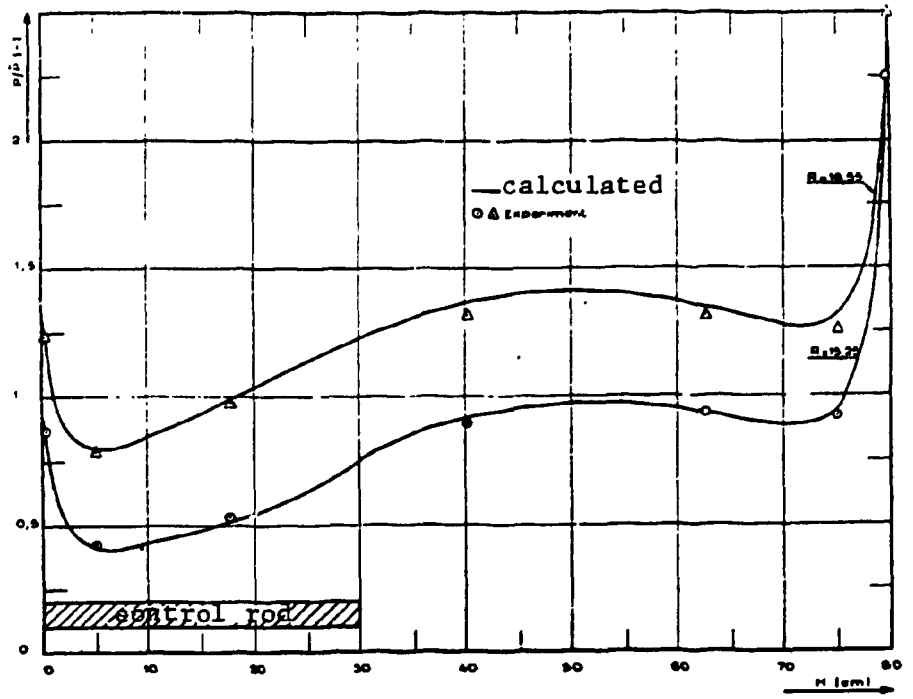

Fig. 5.1.20 Axial power distribution in the core without solid boron for the radii R = 15.25 and 18.55

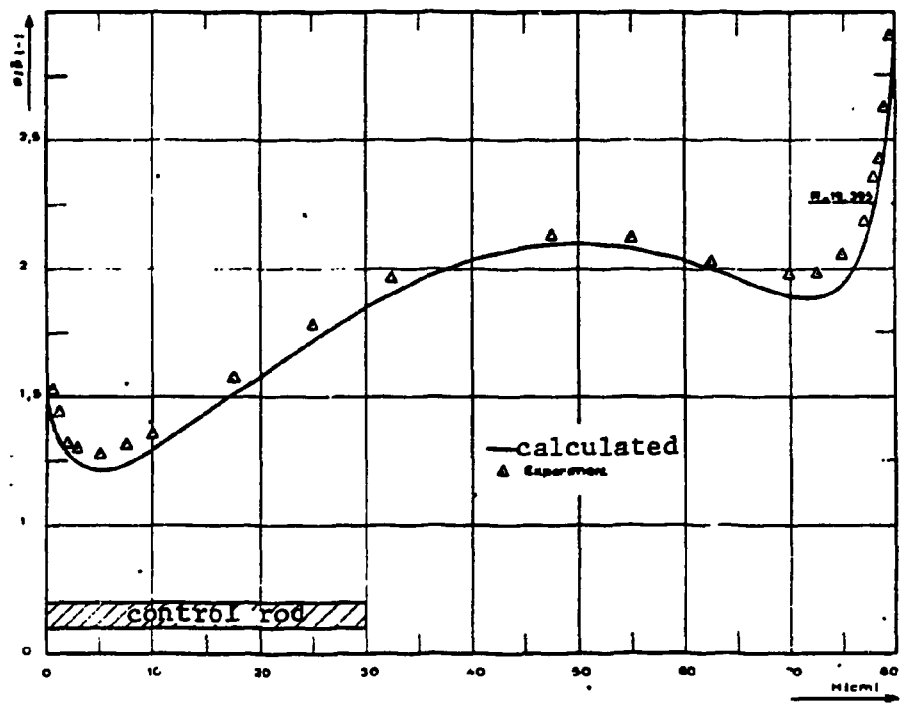

Fig. 5.1.21. Axial power distribution in the core without solid boron for the radius R = 19.395.

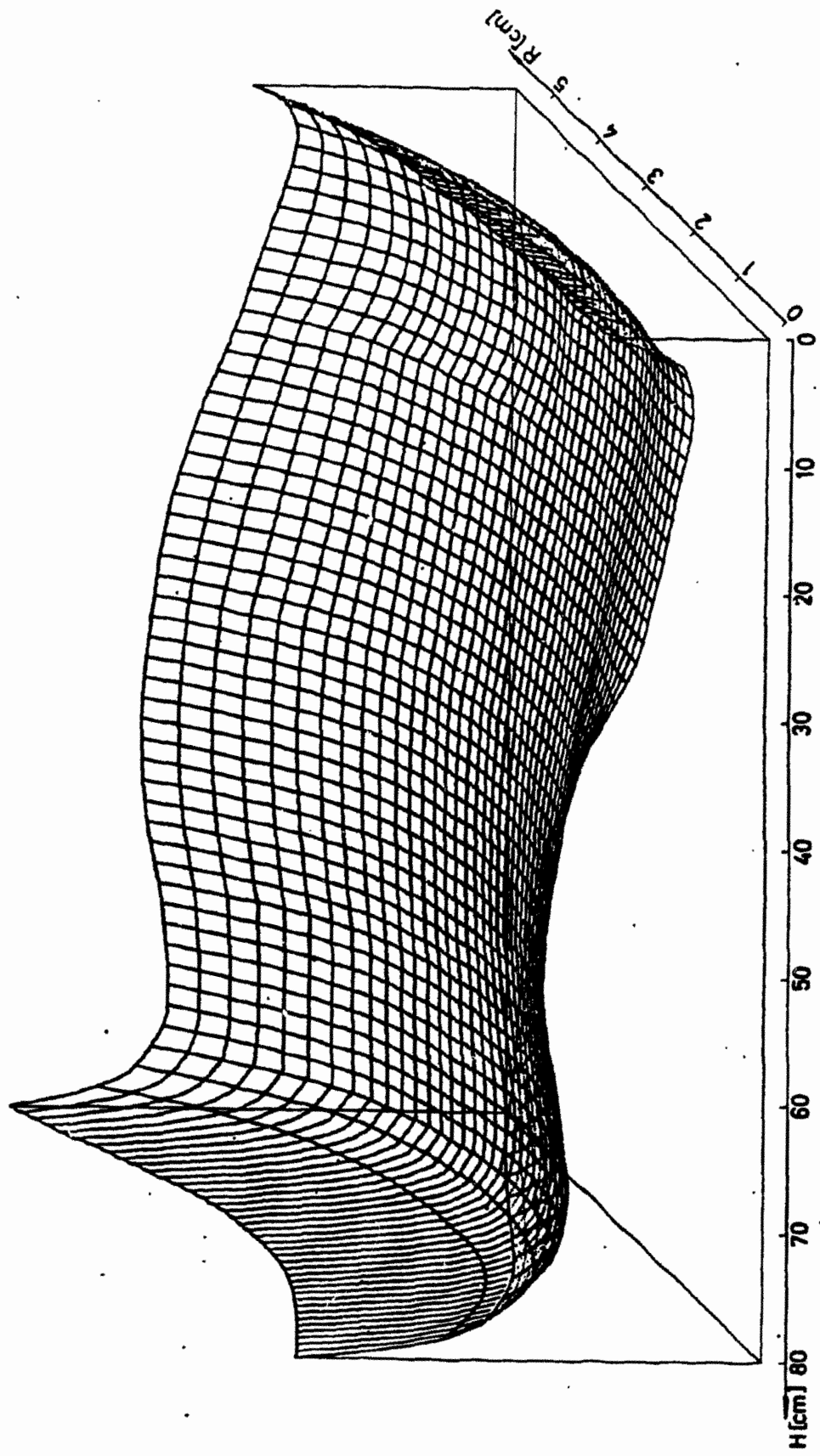

Fig. 5.1.22 Perspective view of the measured power distribution in the core without solid boron, position of the control rod H = 30 cm.

5.1.5 The "Rendement" (Yield)

The "rendement" ("yield" in French)

$$r = \frac{\phi_{th,max}}{p_{tot}}$$

was determined using the method described in 4.3. The uranium probes that are activated in the core do not bring about any perturbation of the flux distribution since then are a part of the fuel plate itself. If the same proves are irradiated in the D_2O reflector however, then a flux disturbed by the probe is measured there. This magnitude of the perturbation was calculated using the well-known formula [11], according to which the correction factor that must be applied to the measured value of $A_{U,R}$ is + 5.6%.

In addition, the H_2O concentration in D_2O during the measurement was 0.29%, whereby the "rendement" is reduced by 0.6% as compared with the 0.2% H_2O concentration. (The dependence of the "rendement" on the H_2O concentration in the reflector was determined using diffusion calculations.) Taking these effects into account, we obtain the measured "rendement" as

$$r_{measured} = 2.48 \times 10^7 \text{ n/cm}^2\text{sW}$$

with an error of ± 2%.

The diffusion calculation in the same geometry yields

$$r_{calculated} = 2.535 \times 10^7 \text{ n/cm}^2\text{sW},$$

i.e., a difference of + 2.2%, in other words exactly the error limit for the measurement.

5.2 State 2: Core with Solid Boron without Reflector Internals

State 2 differs from State 1 by the installation of solid boron zones on the core ends (see Sec. 2.3.3). These consisted of 12 horizontal plates

each, some made of pure aluminum (Al) and some of borated aluminum (AlB), with a loading of 5×10^{-3} g B_{nat}/cm^2. The boron zones were constructed according to the following scheme:

AlB, Al, AlB, AlB, Al, AlB, AlB, Al, AlB, AlB, Al, AlB.

5.2.1 Critical States

The experimentally determined critical states are shown in Table 5.2.1. The H_2O concentration in the heavy water was 0.265% during the measurements.

Table 5.2.1 Experimentally determined critical reactor states with solid boron

Control Rod Position H_c (cm)	Boron Concentration C (g B-10/l)	Mean Control Rod Position for Measuring $d\rho/dH$ $\bar{H}$ (cm)	Differential Control Rod Reactivity $d\rho/dH$ (pcm/cm)
35.22	0.210	37.5	215 ± 7
44.7	0.258	45.5	219 ± 1
45.7	0.270	48.0	219 ± 2
60.9	0.350	63.9	172 ± 5
66.4	0.371	69.9	142 ± 1
81.5	0.419	89.8	40 ± 2
81.5	0.419	98.0	2.6 ± 0.2

Table 5.2.2 contains the calculated reactivities for different boron concentrations and control rod positions.

We interpolated between the calculated reactivities in order to find the boron concentration that is obtained for a given control rod position = 0 (see Figure 5.2.1). The resulting critical reactor states are plotted in Figure 5.1.2 (Curve B).

Table 5.1.2 Calculated reactivities for different control rod positions and boron concentrations

Control Rod Position H (cm)	Boron Concentration C (g B-10/l)	Reactivity $\rho = \ln k_{eff}$ (pcm)	Reactivity $\rho = \frac{k-1}{k}$ (pcm)
no rod	0.4576	336	335
no rod	0.5384	-2678	-2710
0	0.1436	- 708	- 710
20	0.0	6442	6250
20	0.1436	303	303
20	0.2872	-5575	-5725
34	0.1436	2556	2525
34	0.2872	-3265	-3320
44.7	0.2872	- 708	- 710
44.7	0.3948	-4855	-4980
60	0.3948	-1682	-1700
60	0.4576	-4116	-4190
82	0.3948	1128	1120
82	0.4576	-1112	-1115
100	0.4576	- 238	- 238
100	0.5384	-3121	-3173

5.2.2 The Reactivity of the Control Rod and the Reactivity of the Boron Dissolved in the Core

The reactivity of the control rod and the boron value ($d\rho/dC$) was determined using the same methods described in Sec. 5.1.2.

The control rod reactivity is listed in Table 5.2.3, while Figure 5.2.2 shows the characteristics of the control rod for a core having solid boron zones at the ends.

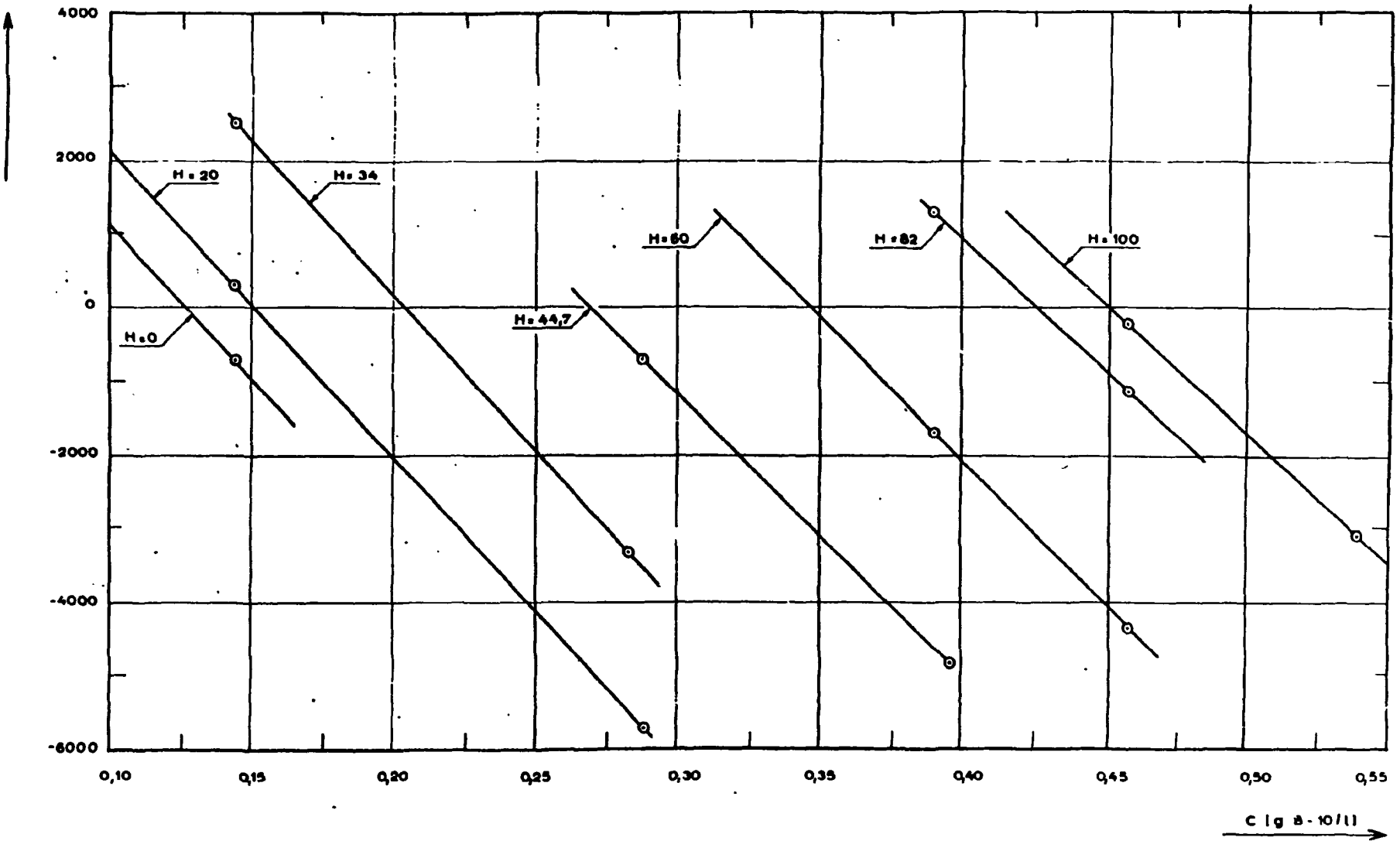

Fig. 5.2.1 Diagram for determination of the boron concentration of critical reactors with solid boron for certain control rod positions. The points correspond to the calculated reactors from Table 5.2.2.

Table 5.3 Reactivity of the control rod for a core containing solid boron

	Reactivity of the rod between H = 35 and 90 cm (pcm)	H = 0 and 100 cm (pcm)
Continuous-run technique	8350	11,920
Stable period	9200	--
Calculation	9150	12,990

The differential reactivity of the boron concentration was determined as described in 5.1.2. The following values were obtained:

Continuous-run technique $\frac{d\rho}{dC}$ = 38 230 pcm/g B^{10}/ltr,

Stable period $\frac{d\rho}{dC}$ = 40 230 pcm/g B^{10}/ltr,

Calculation $\frac{d\rho}{dC}$ = 40 150 pcm/g B^{10}/ltr.

5.2.3 The Reactivity of the Solid Boron Zones

The reactivity of the solid boron zones, expressed in a difference of boron concentration in the core (ΔC), can be read directly from Figure 5.1.2. It is equal to the vertical distance between the curves for reactors without solid boron and with solid boron for the calculated reactors. The measurements were unfortunately not carried out with precisely the same control rod position so that the measured control rod characteristics (Figures 5.1.4 and 5.2.2) must be relied on for assistance in determining the reactivity difference that results from the different rod positions.

To convert the difference in boron concentration to a reactivity difference, the average of the boron values from 5.1.2 and 5.2.2 was used:

Stable period $\frac{d\rho}{dC}$ = 38 890 pcm/g B^{10}/ltr,

Calculation $\frac{d\rho}{dC}$ = 39 430 pcm/g B^{10}/ltr.

Some measured and calculated values are given in Table 5.2.4.

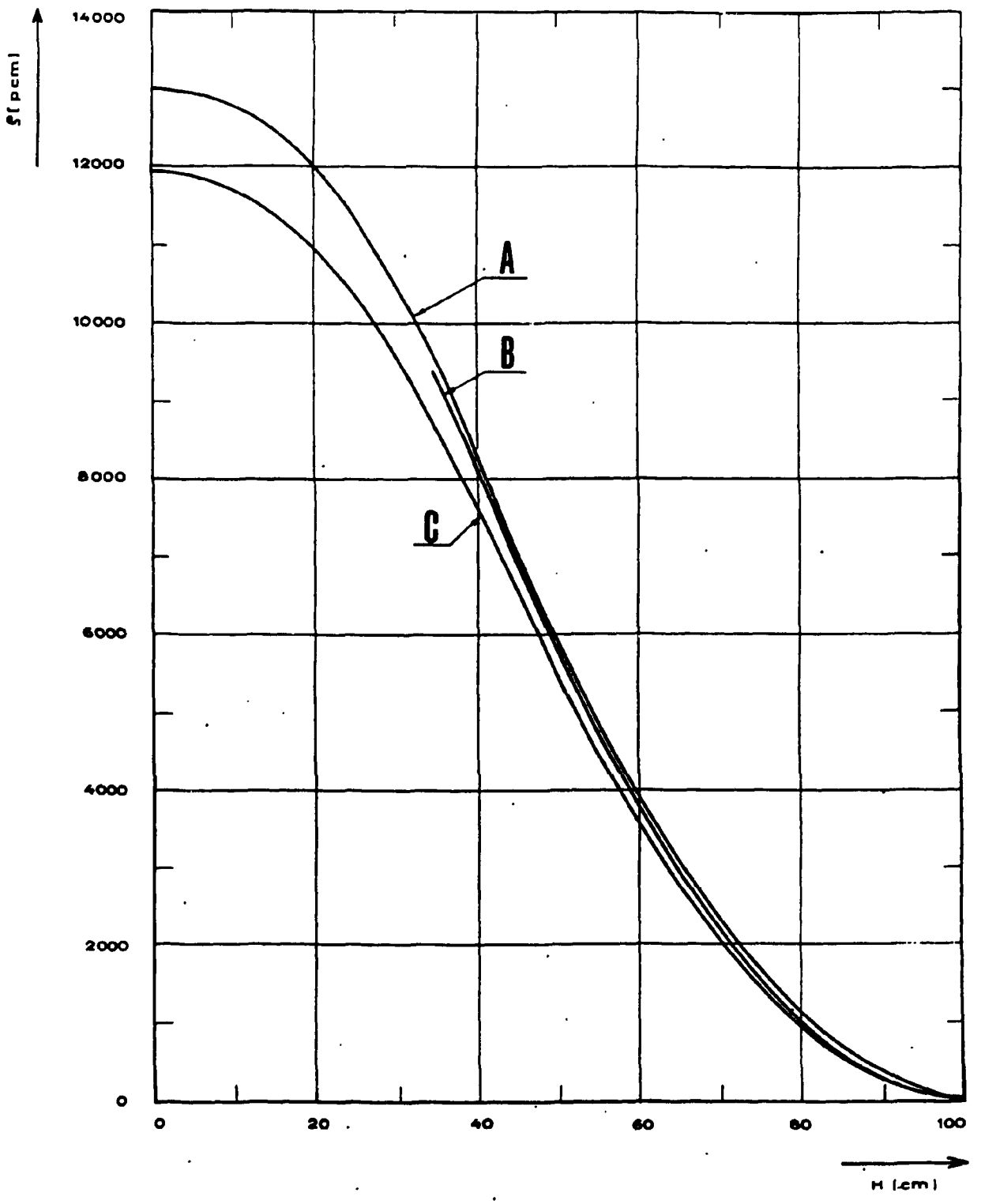

Fig. 5.2.2 Control rod characteristics of the reactor having solid boron. A = calculation, B = measurement using the "approche cinetique," C = continuous-run measurement

Table 5.2.4 Reactivity of the solid boron zones

Control rod position H (cm)	Reactivity of the solid boron (pcm)	
	Measurement (stab. period)	Calculation
17.2	4090	4830
35.5	4750	5200
45.5	4570	4940
46.7	4930	4930
60.9	4050	4610
66.1	4220	4540
81.5	4030	4340
90	--	4300
100	--	4550

The reactivity of the solid boron zones is plotted in Figure 5.2.3 against the control rod position. Two measuring points differ clearly from the curves that one can draw through the other points. This phenomenon is less highly pronounced but already visible in Figure 5.1.2, where the reactors that were used to calculate the boron reactivity also differ somewhat from a curve that one can draw through all critical states. The strong dependence of the solid boron reactivity on control rod position is evident. This can be explained by the strong flux bulging and importance shift, caused by the control rod.

The calculation overestimates the solid boron reactivity by about 8%. For the measuring points at H = 17.2 we obtain a larger error, but the determination of this point is very doubtful.

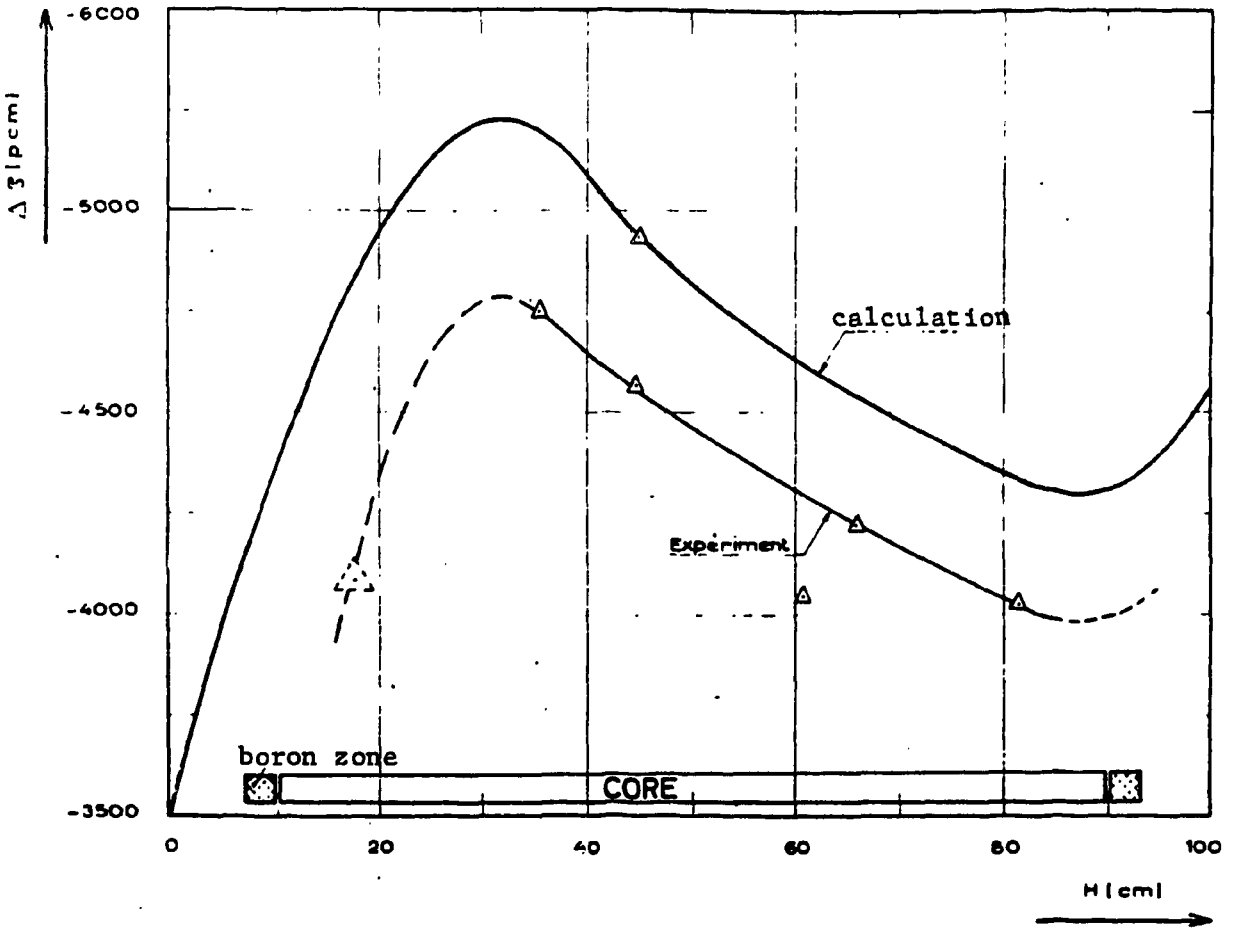

Fig. 5.2.3 Reactivity of the solid boron zones as a function of rod position

5.2.4 The Thermal Neutron Flux Distribution in the Reflector

The thermal flux distribution in the reflector was measured by using the same method as used in Sec. 5.1.3.1. The measured values are shown in Table 5.2.2. Several characteristic flux curves are shown in Figures 5.2.4 to 5.2.7. As regards the error limits, the same applies that was stated in Sec. 5.1.3.1. The boron concentration in the core was 0.258 g B-10/liter during the measurement, and the control rod was positioned at H = 44.7 cm.

5.2.5 The Power Distribution in the Core with Solid Boron

The power distribution was measured using the method described in sections 4.2 and 5.1.4. The measured values are shown in Table 5.2.6.

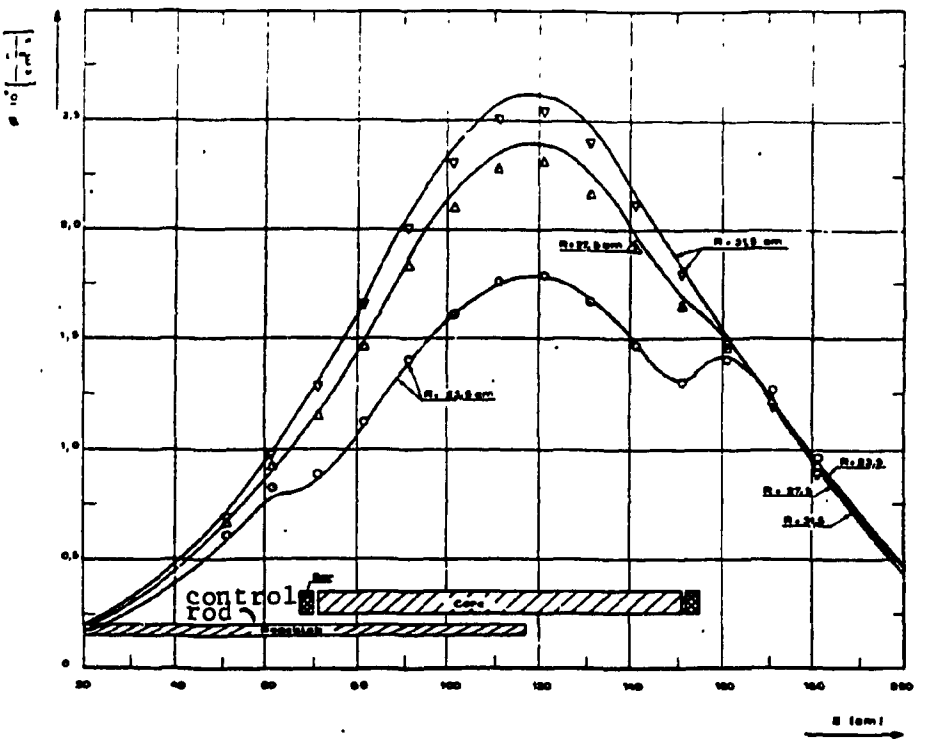

Fig. 5.2.4. Axial distribution of the thermal neutron flux at 1 watt reactor power for the radii R = 23.5, 27.5 and 31.5 (with solid boron)

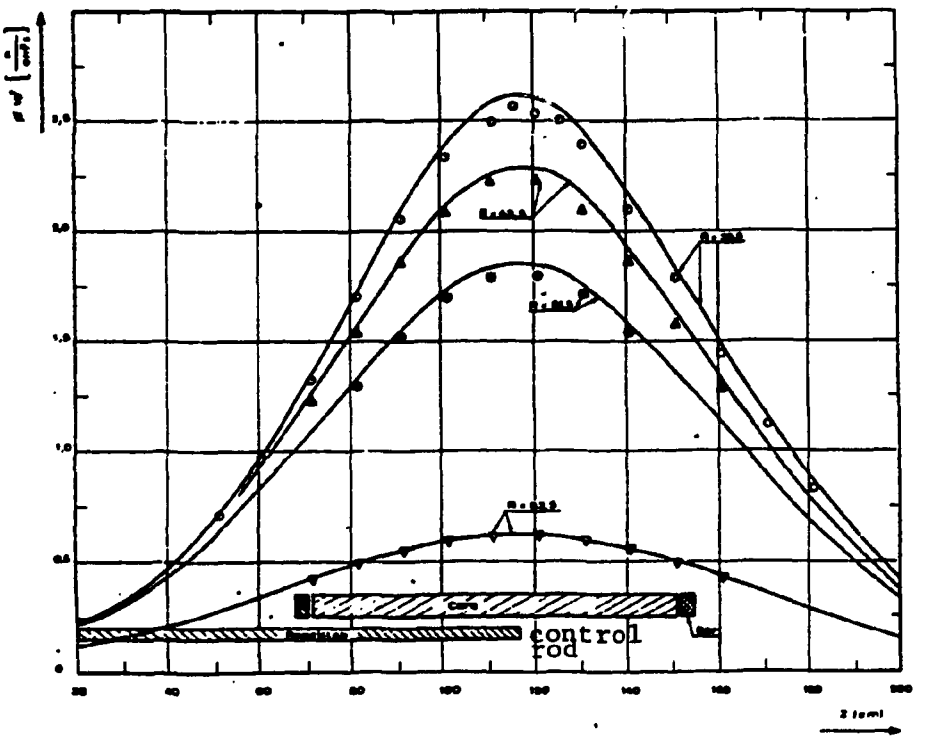

Fig. 5.2.5 Axial distribution of the thermal neutron flux at 1 watt reactor power for the radii R = 35.5, 43.5, 51.5 and 83.5 (with solid boron)

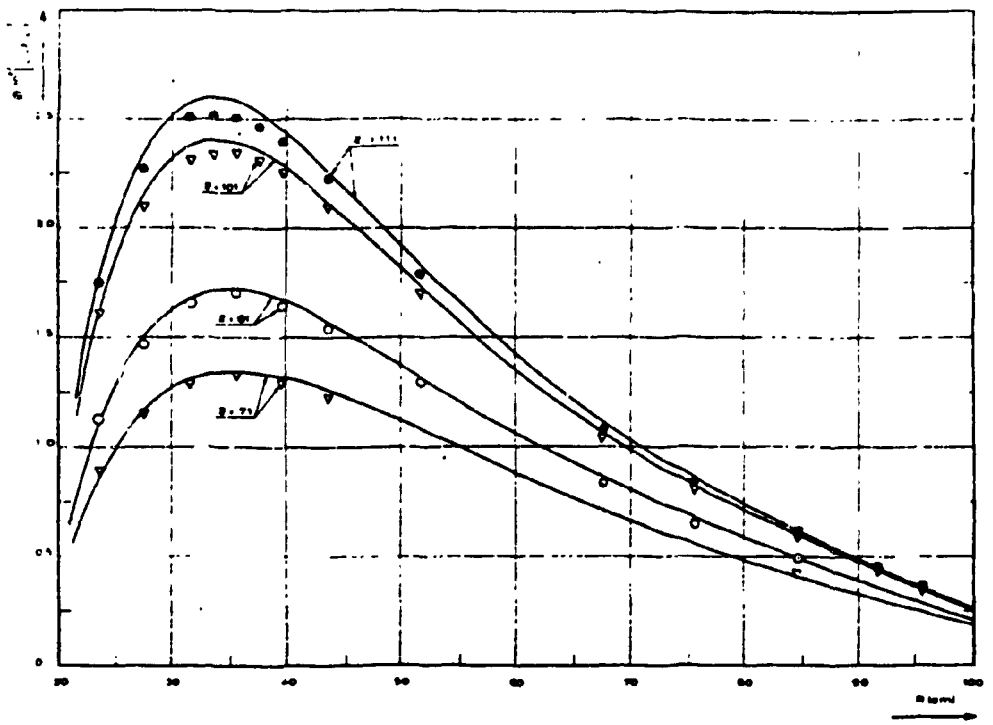

Fig. 5.2.6 Radial distribution of the thermal neutron flux at 1 watt reactor power for Z = 71, 81, 101 and 111 (with solid boron)

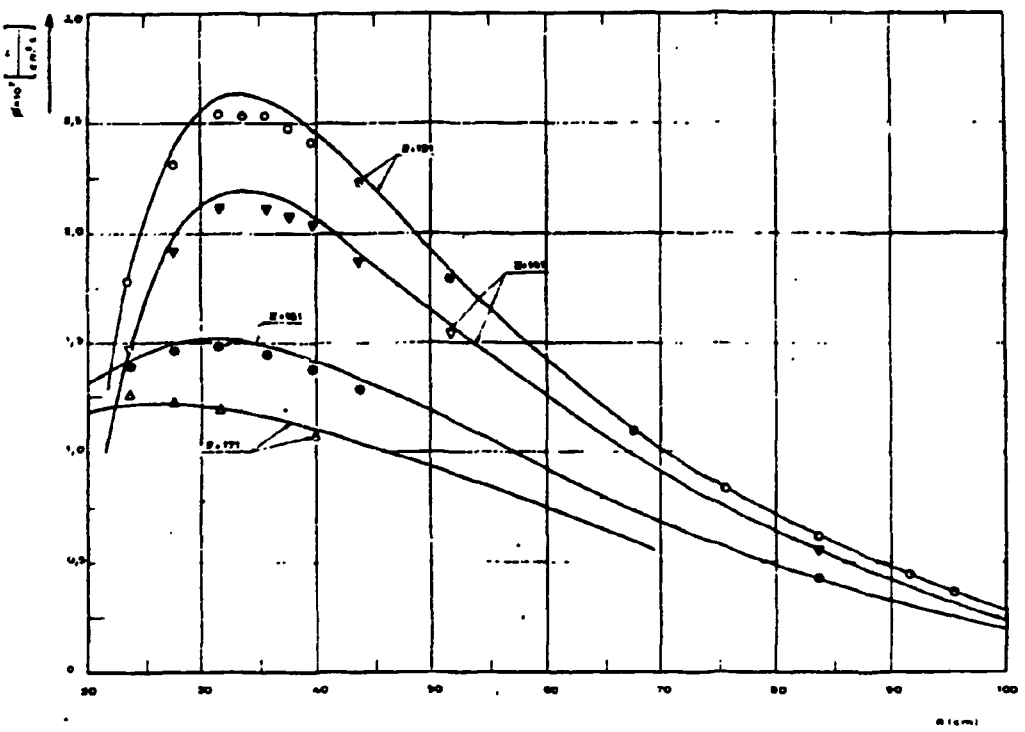

Fig. 5.2.7 Radial distribution of the thermal neutron flux at 1 watt reactor power for Z = 121, 141, 161 and 171 (with solid boron)

Table 5.2.5 Measured thermal neutron flux distribution $\emptyset \times 10^{-7}$ n/cm^{2}s in the reflector at 1 watt reactor power with solid boron

[Commas should be read as decimal points -- Translator's Note]

R(cm) / H(cm)	23,5	27,5	31,5	33,5	35,5	37,5	39,5
181	0,9574	0,9224	0,8768		0,8310		
171	1,2638	1,2162	1,1836		1,1168		1,0672
161	1.3973	1.4562	1.4784		1,4394		1,3761
151	1,2904	1,6412	1,7851		1,7830		1,7232
141	1,4636	1,9093	2,1072		2,0986	2,0637	2,0328
131	1,6640	2,1611	2,3967		2,3952	2,3266	2,3001
126				2,4761	2,5041	2,4317	2,3750
121	1,7829	2,3089	2,5402	2,5368	2,5333	2,4760	2,4152
116				2,5383	2,5641	2,4823	2,4292
111	1,7532	2,2716	2,5066	2,5170	2,4976	2,4631	2,3909
106				2,4383		2,3901	
101	1,6042	2,0957	2,3018	2,3356	2,3398	2,3056	2,2500
91	1,4069	1,8222	2,0323		2,0529	2,0178	1,9817
81	1,1239	1,4658	1,6560		1,6981		1,6400
71	0,8863	1,1489	1,2847		1,3208		1,2941
61	0,8242	0,9216	0,9719		0,9851		0,9560
51	0,6045	0,6648	0,6882		0,7016		

R(cm) / H(cm)	43,5	51,5	67,5	75,5	83,5	91,5	95,5
161	1,2787				0,4229		
151	1,5762				0,4879		
141	1,8666	1,5366			0,5460		
131	2,0950	1,7026	1,0479	0,7964	0,5892		
121	2,2340	1,7928	1,0887	0,8250	0,6118	0,4427	0,3581
111	2,2225	1,7824	1,0843	0,8266	0,6117	0,4427	0,3606
101	2,0846	1,6920	1,0342	0,7956	0,5858	0,4223	0,3479
91	1,8660	1,5200	0,9437	0,7312	0,5428		
81	1,5362	1,2937	0,8336	0,6438	0,4853		
71	1,2236				0,4176		

Table 5.2.6 Relative power distribution in the core with solid boron. Experimental values normalized to a mean power of 1. [Commas should be read as decimal points -- Translator's Note]

Height above lower core edge Z (cm)	Radius (cm) 14,35	14,65	14,95	15,25	15,90	16,75	17,60	18,25	18,55	18,85	19,39
79,75	1,2617	1,1367	1,0807	0,9924	0,9023	0,8946	0,9708	1,1586	1,2664	1,4038	1,8400
79,06	1,1577										1,7956
78,55	1,1152					0,7138					1,7609
78,06	1,030					0,7054					1,7518
77,15	1,0978					0,6885					1,7620
75,00	1,0947	0,9687	0,8770	0,7968	0,7082	0,6966	0,8015	0,9889	1,1146	1,2653	1,7799
72,50	1,1423					0,7301					1,8183
70,00	1,1813					0,7740					1,9097
62,50	1,3150	1,1794	1,0616	0,9743	0,8880	0,8800	0,9931	1,2161	1,3458	1,5414	2,1313
55,00	1,3564					0,9315					2,2620
47,50	1,3118					0,9275					2,3172
40,00	1,0142	0,9537	0,8855	0,8438	0,8084	0,8560	0,0112	1,2612	1,4062	1,6161	2,2504
32,50	0,9511					0,8000					2,1266
25,00	0,8502					0,7224					1,9383
17,50	0,7313	0,6753	0,6400	0,6051	0,5872	0,6257	0,7491	0,9407	1,0623	1,2310	1,7123
10,00	0,5930					0,5121					1,4317
7,50	0,5567					0,4770					1,3421
5,00	0,5110	0,4742	0,4459	0,4239	0,4093	0,4420	0,5392	0,6769	0,7785	0,8976	1,2601
2,85	0,4847					0,4245					1,2224
1,94	0,4794					0,4167					0,1911
1,45	0,4794					0,4238					1,2000
0,94	0,4839										1,1990
0,25	0,5018	0,4759	0,4512	0,4397	0,4338	0,4766	0,5805	0,7211	0,8090	0,9171	1,1850 (Z=0,45)

ORNL/TR-91/23

Several calculated power curves with the corresponding measuring points are plotted in Figures 5.2.8 through 5.2.13. The boron concentration was 0.258 g B-10/liter and the control rod was positioned at H = 44.7 cm.

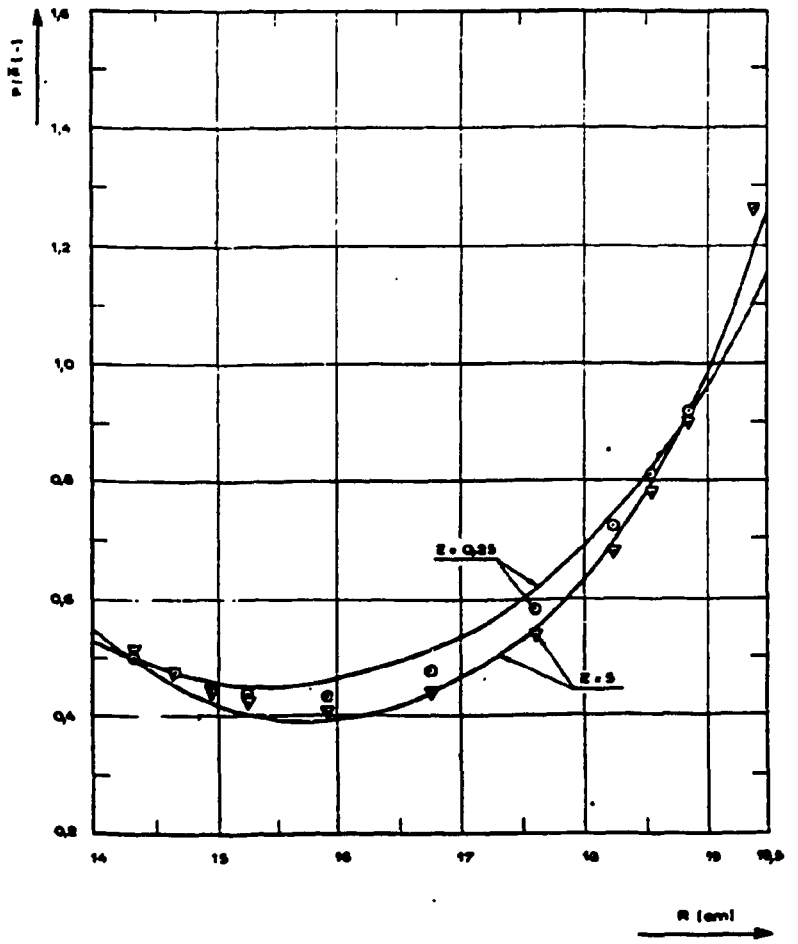

Fig. 5.2.8 Radial power distribution in the core with solid boron for Z = 0.25 and 5 cm above the lower core edge

A comparison with the power distribution without solid boron shows clearly the effect of the boron zones. The power peaks at the core ends are almost completely reduced. Likewise, the calculated power distribution at the ends (Z = 0.25 and 79.75 cm) with boron agrees much better with the measured values than when there is no boron, since in the first case the absorbing zone representing the core is almost extended by the boron zones and the complicated, three-dimensional spectrum conditions at the ends (which were not considered in the calculation) no longer have an effect on the power distribution in the fuel. The calculated power distribution in the core is shown in Figure 5.2.14 in a perspective representation.

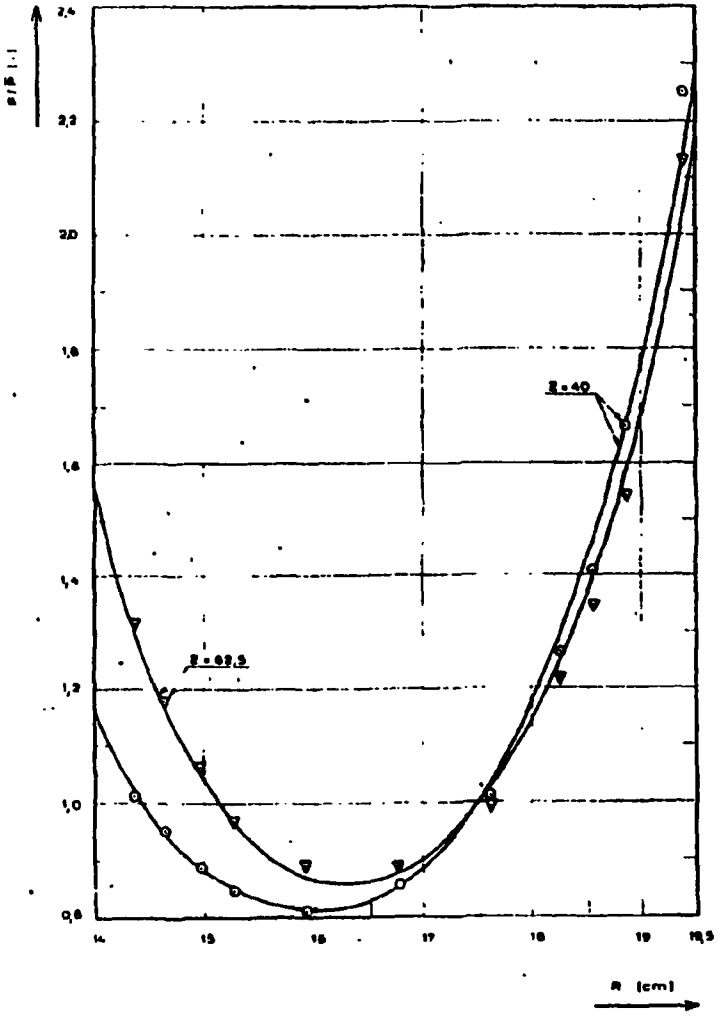

Fig. 5.2.9 Radial power distribution in the core with solid boron for Z = 40 and 62.5 cm above the lower core edge

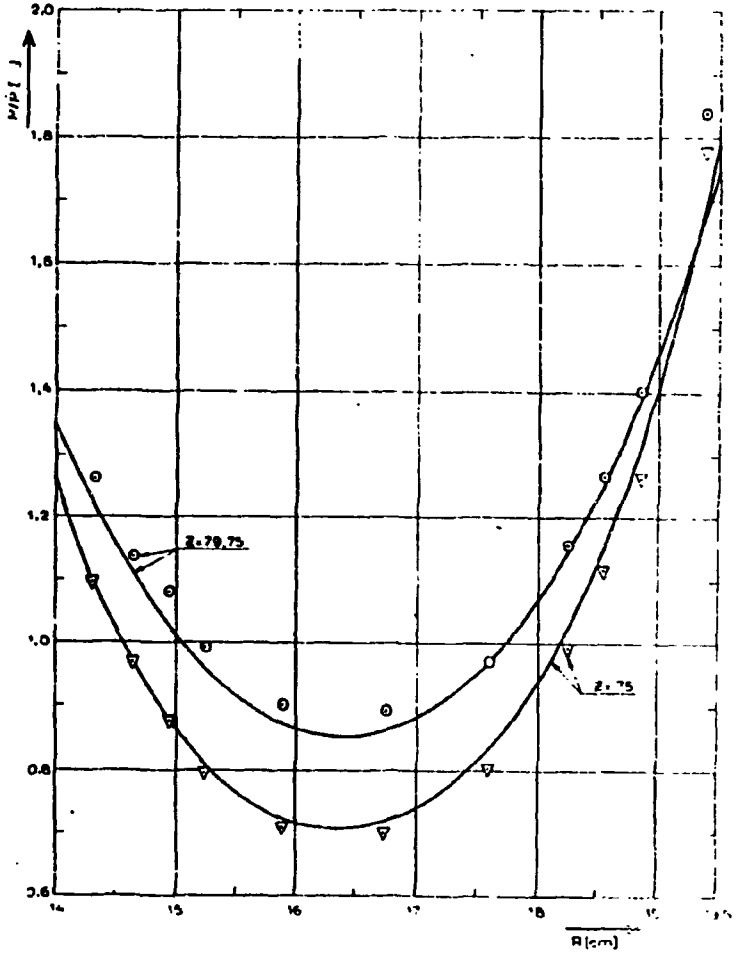

Fig. 5.2.10 Radial power distribution in the with solid boron for Z = 75 and 79.75 cm above the lower core edge

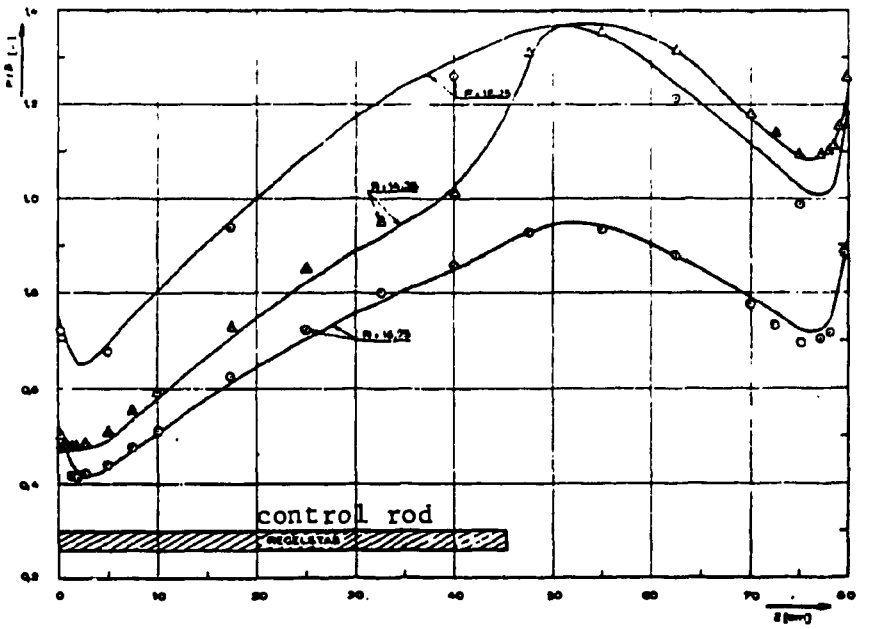

Fig. 5.2.11 Axial power distribution in the core with solid boron for the radii R = 14.35, 16.75 and 18.25

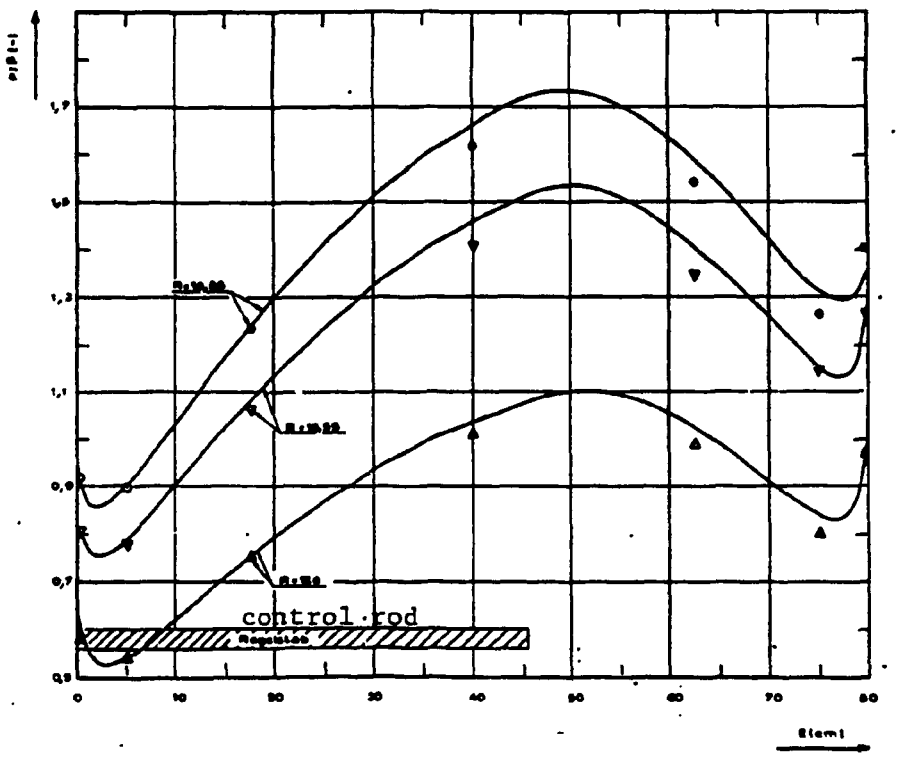

Fig. 5.2.12 Axial power distribution in the core with solid boron for the radii R = 17.6, 18.55 and 18.85 cm

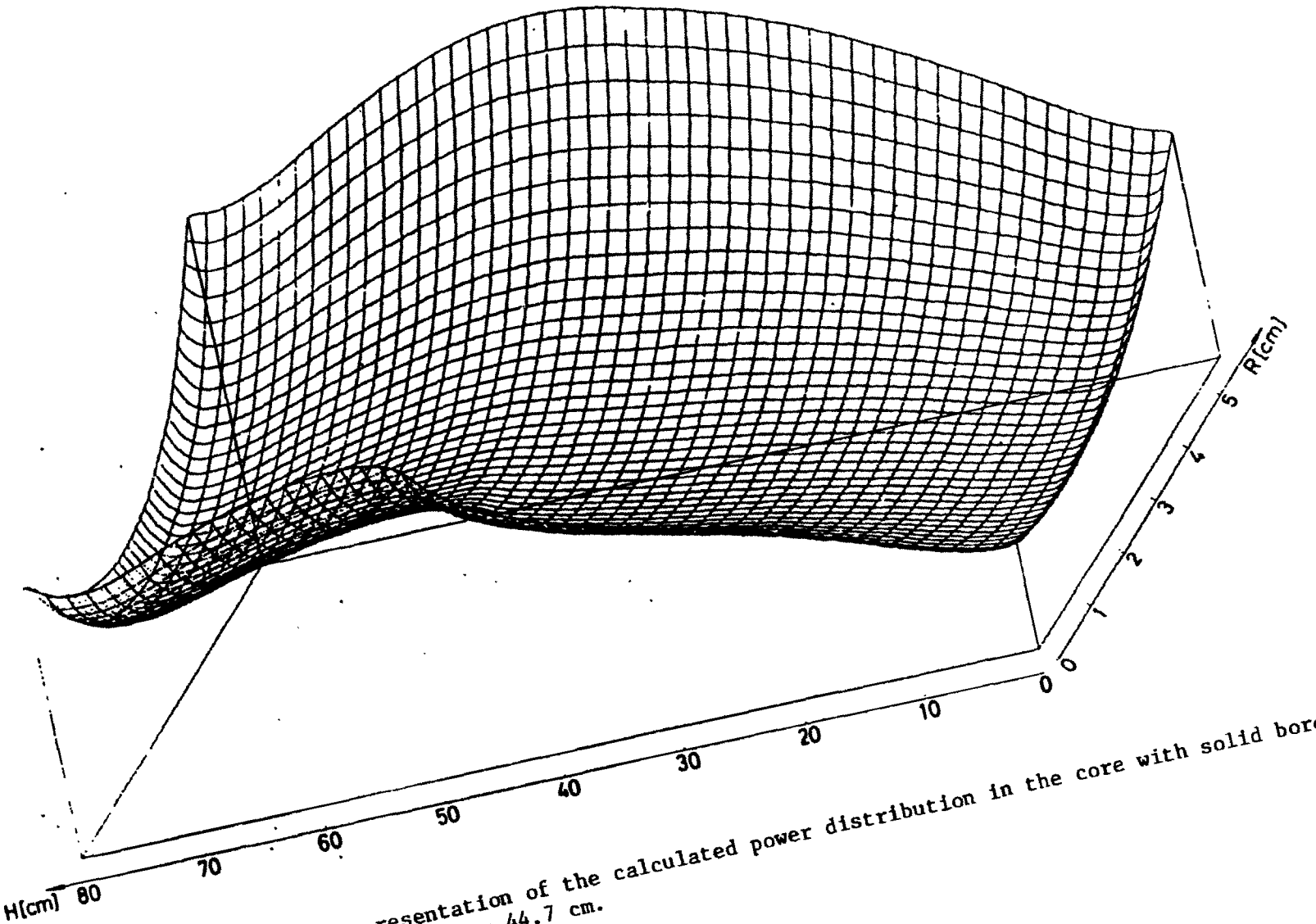

Fig. 5.2.14 Perspective representation of the calculated power distribution in the core with solid boron; control rod position H = 44.7 cm.

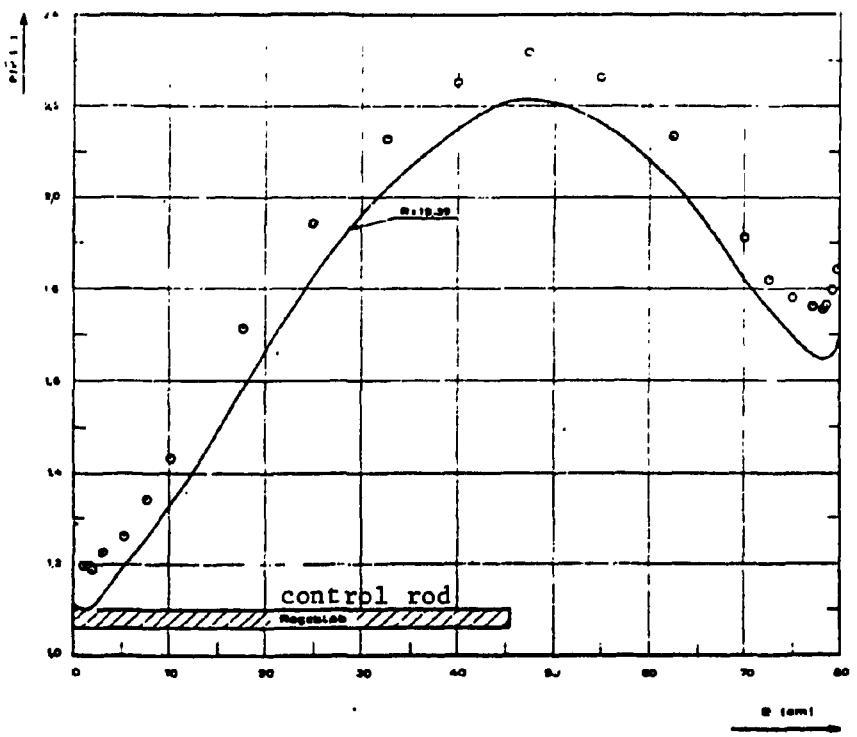

Fig. 5.2.13 Axial power distribution in the core with solid boron for the radius R = 19.39 cm

The radial power distribution averaged over the core height is plotted in Figure 5.2.15. Again we fine here the same differences between calculation and measurement as in Figure 3.2 between diffusion calculation and THERMOS calculation. The radial flux form factor, defined as in 5.1.4, was obtained as:

calculation (uncorrected)	$F_{rad} = 1.736$,
measurement	$F_{rad} = 1.786$.

If we consider that the diffusion calculation is expected to calculate F_{rad} too low by 4.3%, then we obtain

calculation (corrected)	$F_{rad} = 1.811$.

The calculation result is thus 1.4% higher than the result of the measurement.

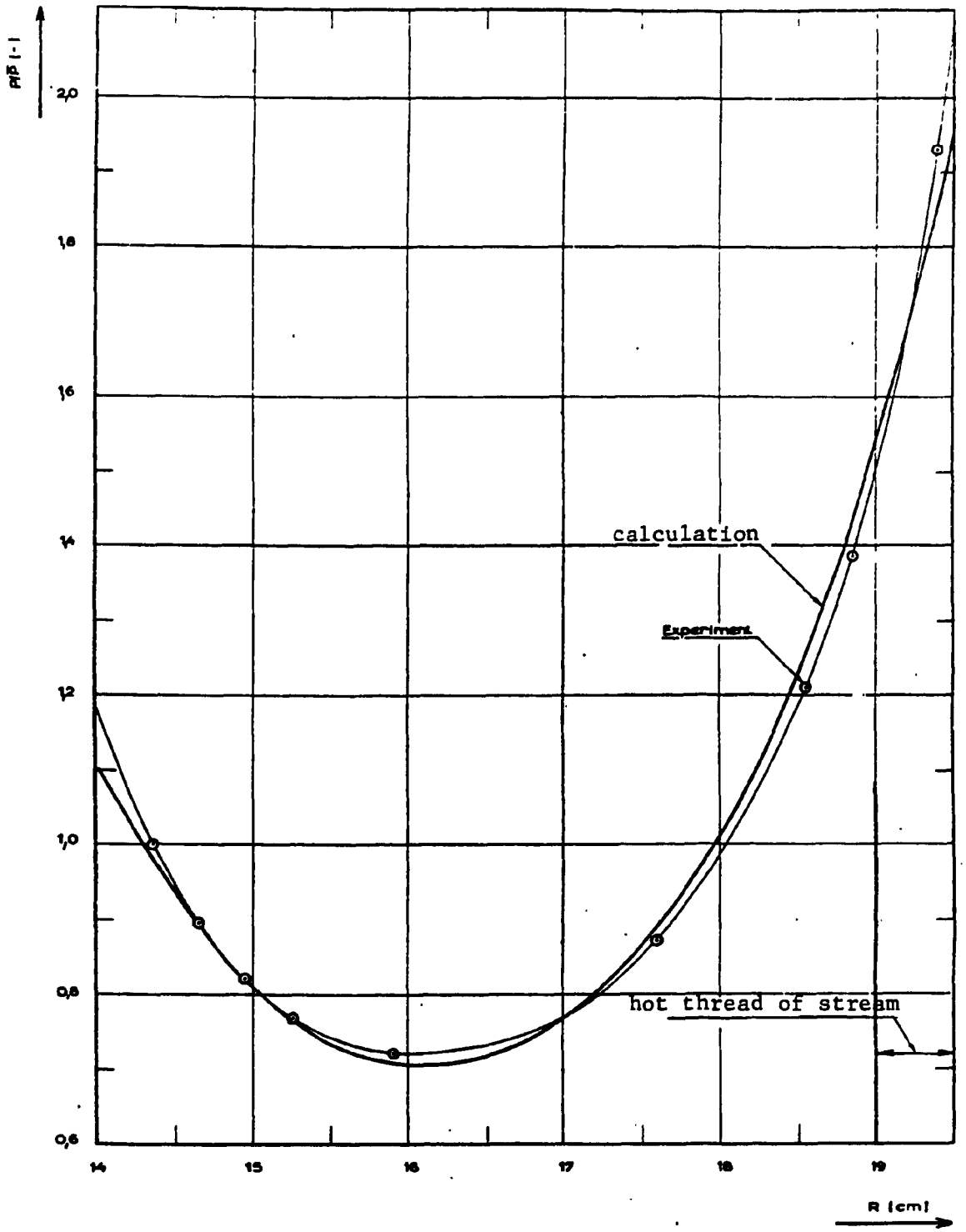

Fig. 5.2.15 Radial power distribution averaged over the core height Z for a core with solid boron

5.2.6 The "Rendement"

The "rendement" (yield)

$$r = \frac{\phi_{th,max}}{p}$$

was determined as in Sec. 5.1.5. Measurement yielded

$$r_{measured} = 2.56 \pm 0.05 \times 10^7 \text{ n/cm}^2\text{sW} .$$

The diffusion calculation yields

$$r_{calculated} = 2.64 \times 10^7 \text{ n/cm}^2\text{sW} .$$

The calculated value is thus 3% higher than the measured value.

5.2.7 Flux Distribution in the Boron Zones

In order for the burnup of the solid boron during the cycle period in the High Flux Reactor to be correctly calculated, it is important for the absorption in the boron zone ($\phi \times \Sigma_{a,eff}$) to be well known. For this purpose the neutron density in the Z direction was measured in and above the boron zones at the radius R = 17.1 cm with manganese probes and compared with the result of the diffusion calculation. According to (4.1) the activity A of a 1/v probe can be calculated as follows:

$$A = \frac{1}{B} \cdot \frac{v_o}{v_T} \cdot \frac{R_{Cd}}{R_{Cd}-1} \cdot \phi_{th} . \qquad (5.2)$$

The proportionality factor B is obtained from the measurement of the "rendement," v_T/v_o from a THERMOS calculation (the same with which the thermal group constants for the diffusion calculation had been determined), the cadmium ratio R_{Cd} according to Equation 5.1 (see 5.1.3.2) and $\phi_{th} = \phi_4+\phi_5+\phi_6$ from the diffusion calculation.

Measured and calculated values were normalized to a reactor power of 1 watt and plotted in Figure 5.2.16. The calculation reproduces the neutron density distribution in the boron zone rather well as far as form and absolute height, with differences of about 3 to 4% from the measured values. Further up in the axial reflector the calculated flux is approximately 10% below the measured values.

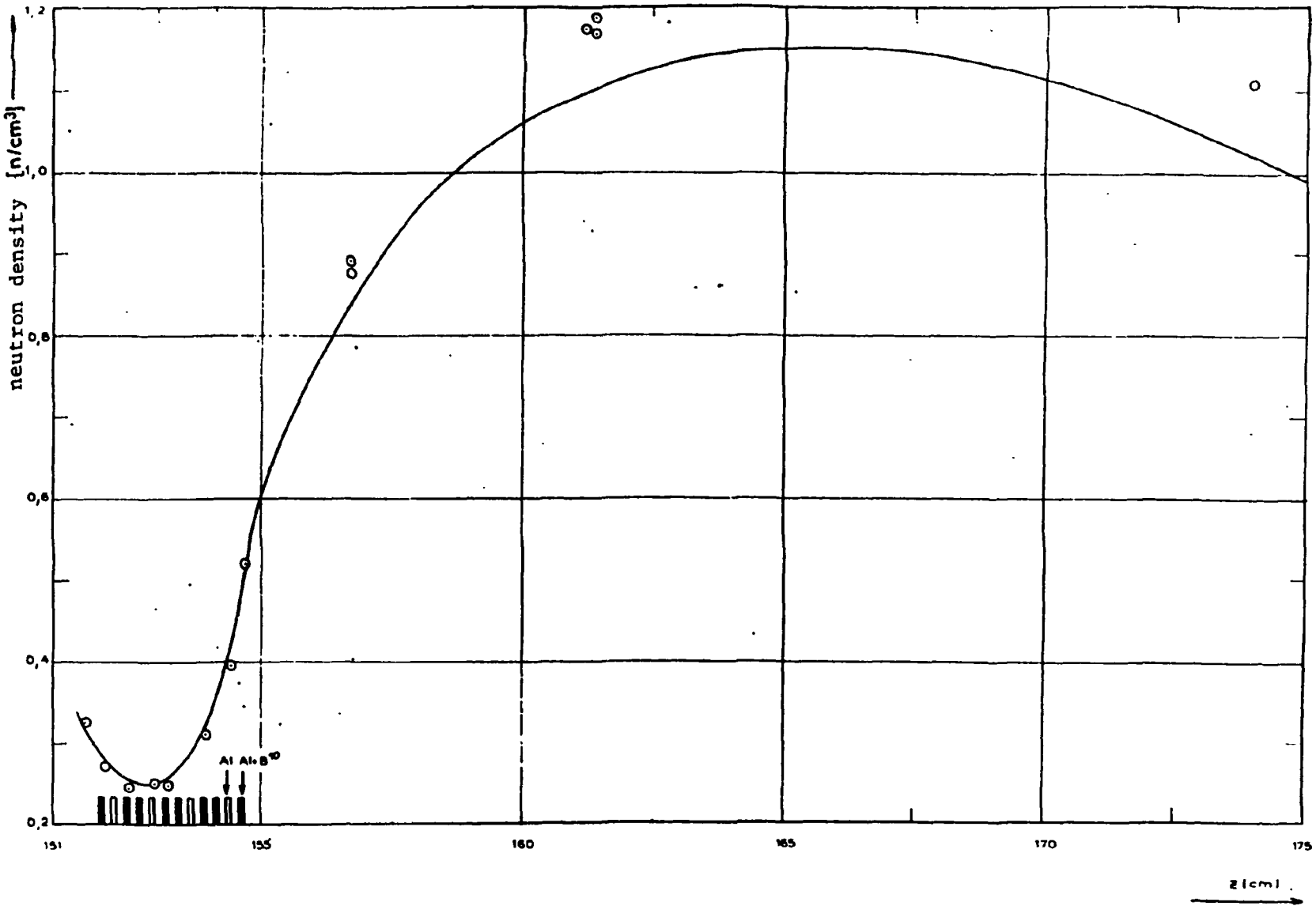

Fig. 5.2.16 Axial neutron density distribution in and above the solid boron zones on the radius R = 17.1 cm at 1 watt reactor power. The solid line was calculated.

5.3 State 3: Core with Solid Boron and the Totality of the Dummy Beam Holes

5.3.1 Geometry of the Structure

The basic scheme of the configuration of the beam hole dummies (Scheme 1) is shown in Figure 5.3.1 in a top view. The coordinates of the individual internals are given in Table 5.3.1.

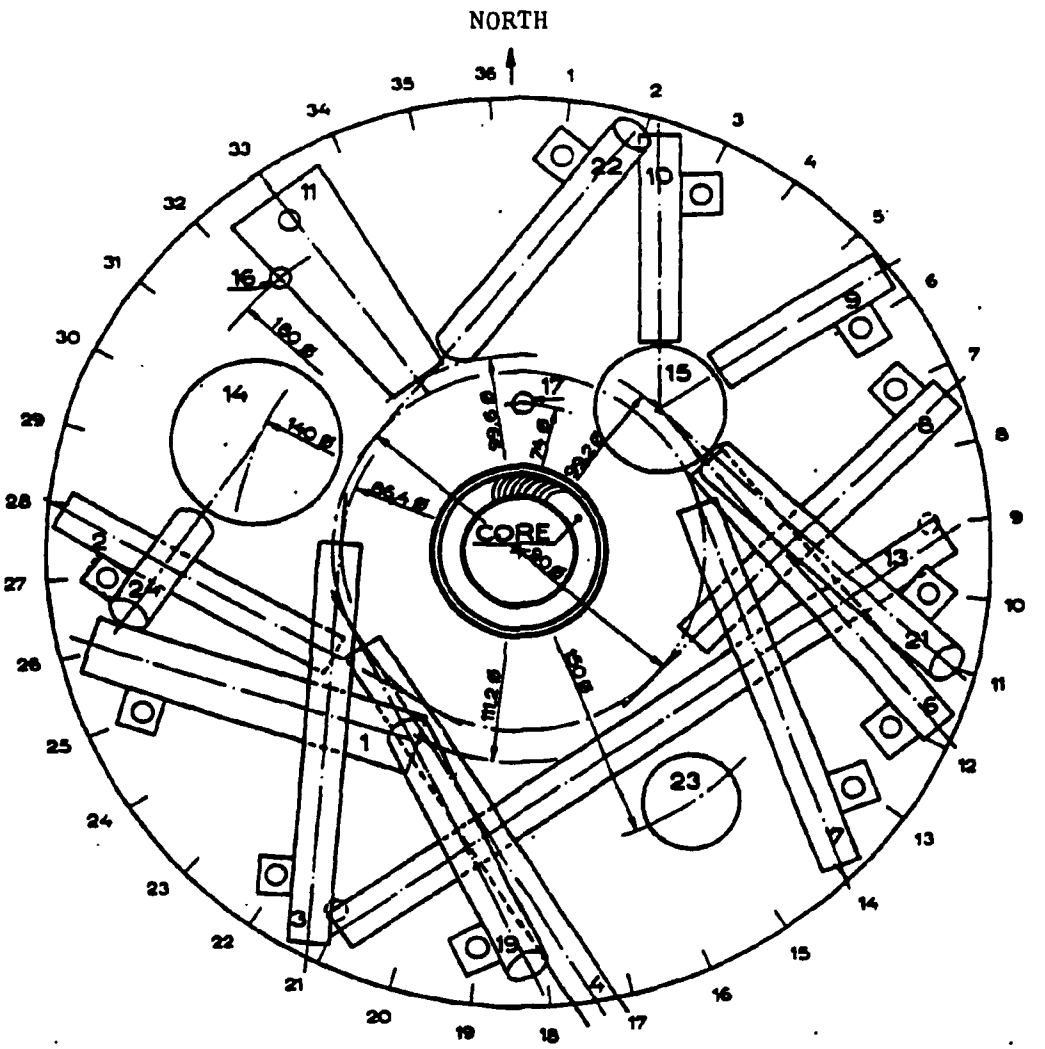

Fig. 5.3.1 Basic scheme of the configuration of the beam hole dummies in the reflector tank (Scheme 1). See Table 5.3.1 for explanation.

Table 5.3.1 Dimensional data for the installation scheme for beam hole dummies. L = overall length, e = wall thickness, D = inside diameter, r = radius of the circle to which the channel axis is a tangent (the values in parenthese relate to Scheme II), R = radius of the channel nose, x = distance between channel nose and center of holding flange, h = height of channel nose above or below core midplane. [Commas should be read as decimal points -- Translator's Note]

Nr.	Name and Function in the High Flux Reactor	L (cm)	e (cm)	D (cm)	r (cm)	R (cm)	x (cm)	h (cm)	Orientation
1	H13 Horizontal beam hole for fission products	83	0,2	15	55 (47)	55,6 (49,1)	67,5	- 25	horizontal
2	H12 Horizontal beam hole	76,5	0,2	10	45 (39,4)	52 (49,0)	59	- 25	horizontal
3	H11 Horizontal beam hole	101,2	0,2	10	43,3	43,2	85	+ 25	horizontal
4	H10 Horizontal beam hole	91	0,2	10	45 (37)	45 (37,2)	114,5	0	horizontal
6	H 8 Horizontal beam hole	88	0,2	10	49,6	50,7	81,3	+ 10	horizontal
7	H 9 Horizontal beam hole to the hot source	97,5	0,2	10	45	45,3	79,5	+ 15	
8	H 5 Horizontal beam hole	88,3	0,2	10	45 (37)	47,3 (40,8)	80	- 25	
9	H 4 Horizontal beam hole	48,8	0,2	10		65,3	36,65	+ 15	
10	H 3 Horizontal beam hole	53,2	0,2	10		62,2	39,2	+ 15	
11	H 2 Neutron conductor for thermal neutrons	58,8	0,2	15 kon. 5° · 30''		49,8		- 20	
13	H 7 Continuous horizontal beam hole for capture gammas	178,4	0,2	10	55	55		- 30	horizontal
14	V 1 Cold source	198,5	0,5	40		70,0		0	vertical
15	V 2 Hot source	256,3	0,5	30		49,6		- 10	
16	V 5 Pneumatic tube for irradiations	120	0,2	4	91	91		0	
17	V 4 Pneumatic tube for irradiations	100	0,2	4		37,5		+ 20	
19	IH4 Upward sloped beam hole	80	0,2	10	45 (37)	54 (48,8)	67,4	+ 25	sloped 35°
21	IH2 Upward sloped beam hole (to the hot source)	93,3	0,2	10	49,6	53,9	74,2	+ 22	sloped 35°
22	IH3 Upward sloped beam hole (to the hot source)	84	0,2	10	45 (37)	54,1 (48,9)	67,2	+ 25	sloped 35°
23	V 3 Vertical beam hole for conversion electrons	220	0,2	20		75		-110	vertical
24	IH1 Upward sloped beam hole (to the cold source)	35	0,2	10		78,75	25,25	+ 25	sloped 35°

5.3.2 Critical States, Reactivity of the Control Rod, of the Boron Dissolved in the Core, and the Total Reactivity of the Experimental Equipment

The critical states that were realized are shown in Table 5.3.2. Figure 5.3.2 shows the critical control rod position as a function of the boron concentration.

The H_2O concentration in the reflector was equal to 0.263% during the measurement.

Table 5.3.2. Critical reactor states with beam holes and solid boron

H_c (cm)	C (g B^{10}/ltr)	$\bar{H}$ (cm)	$d\rho/dH$ (pcm/cm)
80,4	0,347	90,3	40,5 ± 2
71,1	0,311	74,2	128 ± 1
59,6	0,260	61,8	184 ± 2
57,9	0,248	60,1	198 ± 2
50,3	0,210	52,2	222 ±10
38,5	0,143	40,3	229 ± 9
24,9	0,078	27,4	162 ± 2

[Commas should be read as decimal points -- Transl. Note]

The control rod reactivity was determined according to the methods described above. The reactivity as a function of rod position is plotted in Figure 5.3.3.

The total reactivity between H = 0 and H = 100 was measured using the continuous-run technique:

$$\Delta\rho_{\text{control rod}} = 12{,}250 \text{ pcm}.$$

Between the rod positions H = 30 and H = 90 we obtained the following values with the methods indicated:

continuous run: $\Delta\rho_{\text{control rod}} = 9{,}725$ pcm,

stable period: $\Delta\rho_{\text{control rod}} = 10{,}150$ pcm.

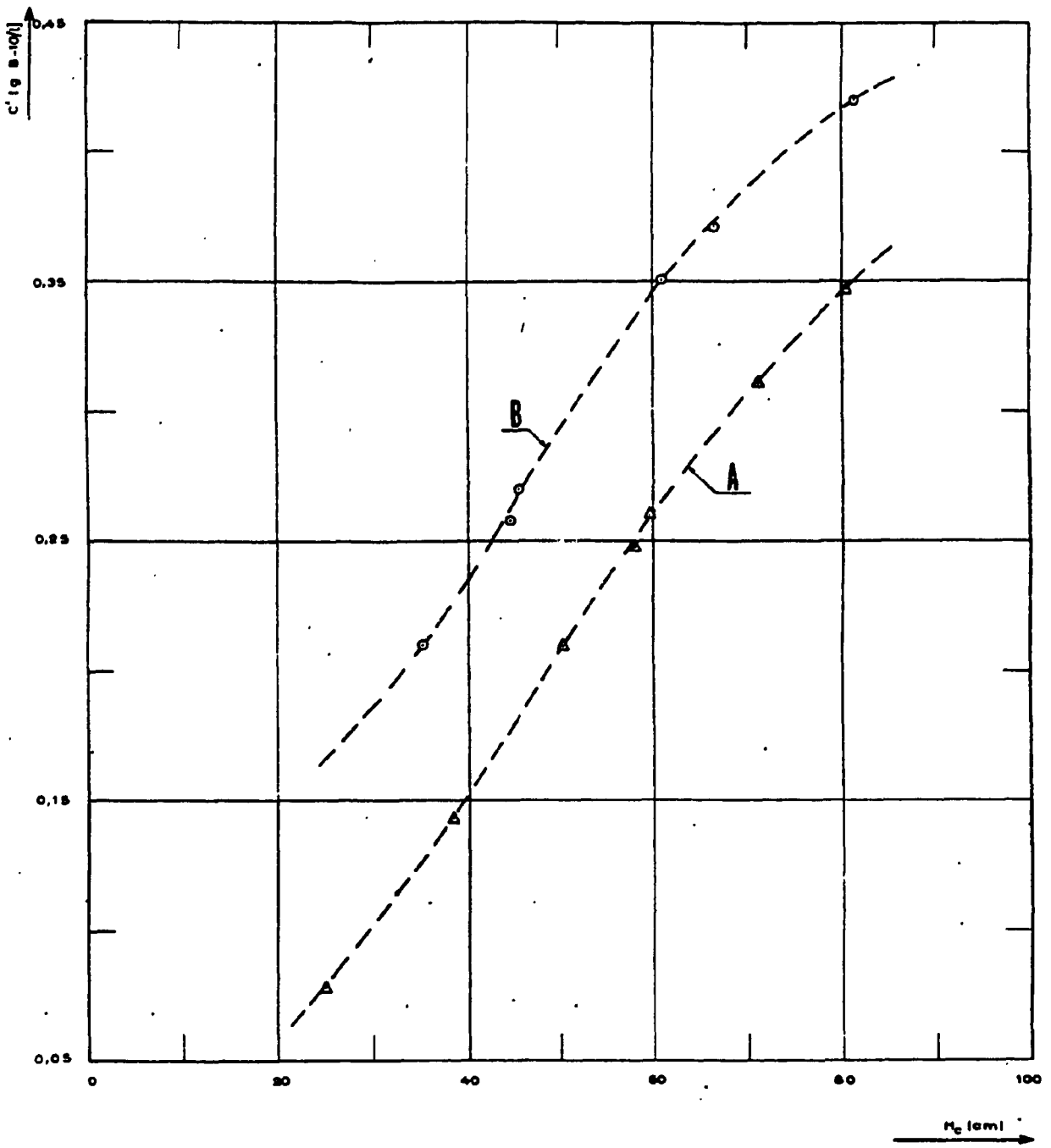

Fig. 5.3.2 Measured critical control rod position as a function of boron concentration for reactors with solid boron and dummy beam holes (Curve A) and for reactors with solid boron and without beam hole dummies (Curve B)

The differential reactivity of the boron dissolved in the core was determined as above:

continuous run technique $\frac{d\rho}{dC} = 37\,500$ pcm/g B^{10}/ltr,

stable period $\frac{d\rho}{dC} = 38\,900$ pcm/g B^{10}/ltr.

The total reactivity of the experimental equipment can be taken from Figure 5.3.2. The two curves for the reactors with and without beam holes for points with the same control rod position are characterized by a difference in the boron concentration. One $\Delta\rho$ unit corresponds to this difference. For the boron value we have selected the mean value from the measurements using the method of the stable period with and without beam holes; $d\rho/dC$ = 39,500 pcm/g B-10/liter.

The $\Delta\rho$ values determined in this way were plotted in Figure 5.3.4 as a function of the control rod position. Due to the variation in the critical states, the $\Delta\rho$ values for the beam holes do not lie on a smooth curve.

The point for H = 80 is especially doubtful. However, the fact that $\Delta\rho$ increases, the further the control rod is inserted, is characteristic.

For the control rod position H = 50 we obtain a beam hole reactivity of

$$\rho = -3300 \pm 160 \text{ pcm}.$$

When boron values measured with the continuous-run technique are used ($d\rho/dC$ = 37,850 pcm/g B-10/liter) we obtain

$$\rho = -3160 \pm 160 \text{ pcm}.$$

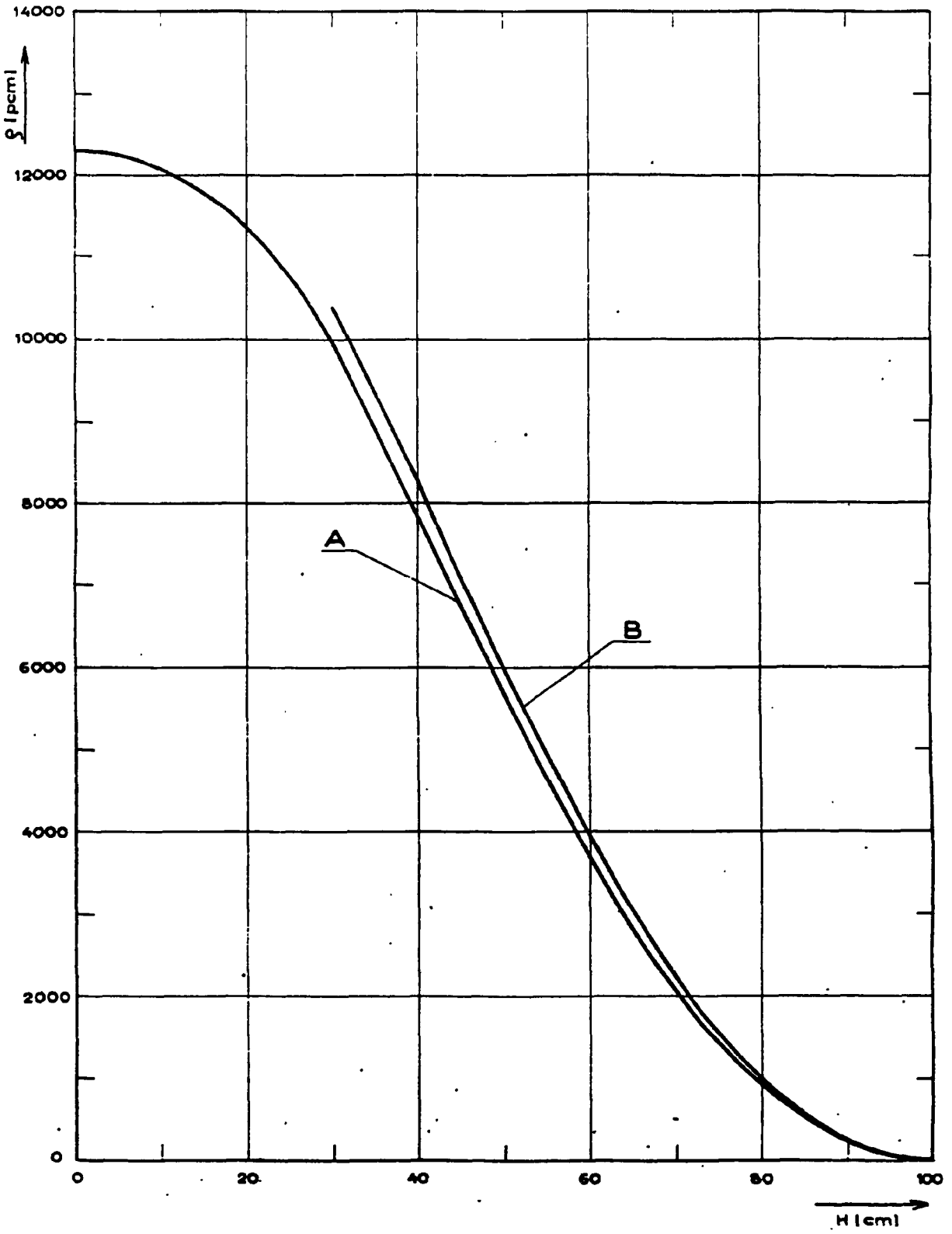

Fig. 5.3.3 Reactivity of the control rod in the reactor with solid boron and beam hole dummies. A obtained with the continuous-run method, B with the "approche cinetique"

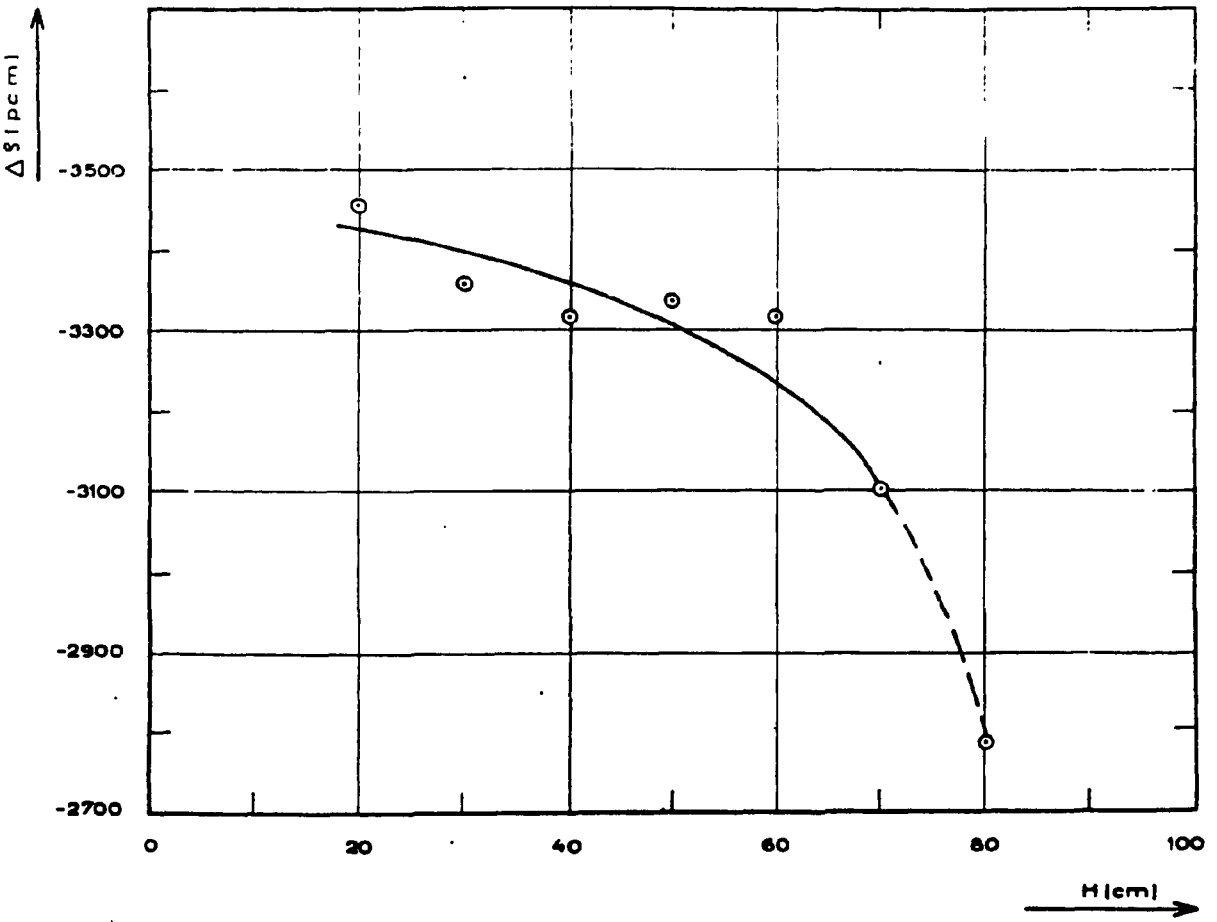

Fig. 5.3.4 Measurement of the reactivity of dummy beam holes (Scheme 1) as a function of control rod position

For calculation purposes the beam holes were homogenized in four radial zones over a height of 80 cm (symmetrical to the core midplane). Figure 5.3.5 shows the void and aluminum concentration as a function of the radius, as was used in the calculation. This method is actually only permissible with very small cavities in the moderator, since it can take the "streaming" effect in the beam hole into account only incompletely. It is difficult to determine this effect theoretically when there is such a complicated configuration of cavities as exists in the present case. An attempt has been made to use the theories of BEHRENS [28] and CARTER and JARVIS [29], but this led to completely unrealistic results. Therefore only the result of the calculation with homogenized beam holes is given here.

The following was obtained as the total reactivity of the beam holes for a control rod position of H = 50 cm:

Calculation: ρ (beam holes) = 2,380 pcm.

In addition the reactivity of the structural material of the beam holes was calculated, i.e., the cavities were filled with D_2O. This calculation yielded the following (also for the control rod position H = 50 cm):

ρ (aluminum of the beam holes) = 1615 pcm.

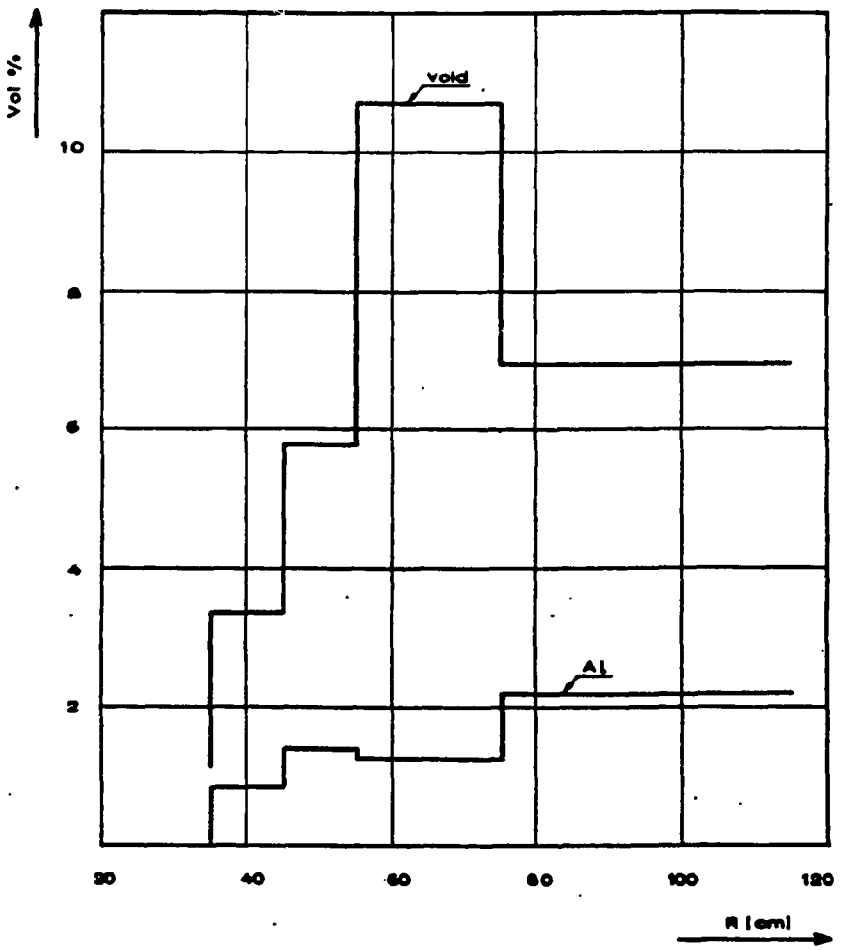

Fig. 5.3.5 Homogeneous void and aluminum concentration in the reflector as a function of the radius, as was used in the diffusion calculation

Under the assumption that the reactivity of thin aluminum structures can be calculated rather easily (see 5.8), we obtain the void effect of the measurement as

$$\rho\,(\text{void, measurement}) = 3300 - 1615 \text{ pcm}$$
$$= 1685 \text{ pcm}$$

and from the calculation as

$$\rho\,(\text{void, calculation}) = 2380 - 1616 \text{ pcm}$$
$$= 765 \text{ pcm},$$

i.e., the simple mathematical model used underestimates the void effect by a factor of 2.2, if we assume that the calculation reproduces the aluminum effect correctly.

5.3.3 The Reactivity of Several Experimental Devices

5.3.3.1 Cold Source

During the reactivity measurements on the cold and hot sources the boron concentration was 0.239 g B-10/liter. The control rod position ranged between H = 53 and H = 60 cm. The reactivities were determined by observing the stable period and using the control rod characteristics measured by means of the stable period method.

All other beam holes were installed during the measurements. The cold source of the High Flux Reactor was simulated in FOEHN by the dummy shown in Figure 2.13.

In the initial state the vessel was filled with D_2O and the bell fitted over it. The axis of the source was on the radius R = 70 cm. The bell simulates the higher absorption in the vessel wall caused by the softer spectrum of the "cold" neutrons in the actual cold source. A reactivity of

$$\Delta\rho = -194 \text{ pcm}$$

is inserted by the D_2O-filled cold source with bell.

The effect of the "bell" is

$$\Delta\rho = -41 \text{ pcm}.$$

If the 56.6 liter D_2O in the source vessel is replaced by nitrogen, we

obtain a reactivity contribution of

$$\Delta\rho = -390 \text{ pcm.}$$

If the cold source is moved from R = 70 cm to R = 65.6 cm, then follows that

$$\Delta\rho = -66 \text{ pcm.}$$

The aluminum volume of the cold source with "bell" is 5.9×10^3 cm^3, and that of the bell alone is 1.5×10^3 cm^3. From Figure 5.8.1 we obtain for the radius R = 70 cm an aluminum reactivity of -3.4×10^{-2} pcm/cm^3 Al and for R = 65.6 cm in accordance with -5.0×10^{-2} pcm/cm^3 Al. With this values the reactivity of the cold source at R = 70 is determined as

$$\Delta\rho \text{ (calculated)} = -201 \text{ pcm,}$$

the effect of the "bell" as

$$\Delta\rho \text{ (calculated)} = -51 \text{ pcm,}$$

and the effect of the shift in the source from R = 70 cm to R = 65.6 cm as

$$\Delta\rho \text{ (calculated)} = -94 \text{ pcm.}$$

5.3.3.2 Hot Source

The basic configuration of the dummy of the hot source of the High Flux Reactor is shown in Figure 2.12. The free space in the Zircaloy source vessel was filled with nitrogen, and the space between cladding and source vessel with D_2O. At the radius R = 49.6 this configuration brings about a reactivity of

$$\Delta\rho = -1100 \text{ pcm.}$$

If only the cladding is installed, then we obtain

$$\Delta\rho = -550 \text{ pcm,}$$

and if the source is installed without cladding, we obtain

$$\Delta\rho = -550 \text{ pcm,}$$

i.e., no measurable shielding of the source and cladding could be detected.

If in the source without cladding tube the graphite block and nitrogen volume is replaced by D_2O, then we obtain a reactivity gain of

$$\Delta\rho = +480 \text{ pcm.}$$

The reactivity of the hot and cold sources together was measured as

$$\Delta\rho = -1290 \text{ pcm.}$$

5.3.3.3 Channel No. 11

Channel no. 11 simulates the thermal neutron conductor of the High Flux Reactor. Its reactivity in the position given in Table 5.3.1 was measured as

$$\Delta\rho = -270 \text{ pcm.}$$

5.3.3.4 Channels 1 and 7

In order to be able to determine the effect of a modification of the configuration of channels H9 and H13 in the High Flux Reactor, we measured the change in reactivity that results when Channel 1 is put in the place of Channel 7 and Channel 7 in the place of Channel 1. This change yielded

$$\Delta\rho = -110 \text{ pcm.}$$

In addition, the total reactivity of Channel 1 was measured. For the installation position as given in Table 5.3.1 we obtained

$$\Delta\rho = 124 \text{ pcm,}$$

and for installation in place of Channel 7

$$\Delta\rho = 290 \text{ pcm.}$$

In this case its position is characterized by the radius of the circle tangential to the channel axis r = 45 cm and the distance of the channel nose from the middle of the flange x = 67.5 cm.

5.3.3.5 Reactivity Effect Resulting from Bringing Some Channels Closer to the Core (Scheme II)

Starting with the basic scheme, the beam holes No. 1, 2, 4, 8, 19, 22 and 24 were turned around their holding rods so that their axes become tangents to the radius r = 37 cm (see Table 5.3.1). This change brings about a

reactivity of

$$\Delta\rho = -215 \text{ pcm.}$$

5.3.4 Fluxes in the Reflector

5.3.4.1 Thermal Neutron Flux in the Reflector

Measurement of the thermal neutron flux in the reflector with beam holes had two goals. First of all, it is desirable to know the flux at each individual channel nose, and secondly the azimuthally averaged radial flux distribution is of interest, since it permits comparison with the fluxes of the diffusion calculation in which the channels had been homogenized. Figure 5.3.6 shows the radial and azimuthal distribution of the measuring points in the reflector.

The fluxes at the channel noses were measured as described above with manganese probes and normalized over the "rendement" (see Sec. 5.3.5) to 1 watt reactor power. The results are given in Table 5.3.3. The flux depression was calculated using the fluxes from Sec. 5.2.3. During the measurement the core was poisoned with 0.177 g B-10/liter, and the control rod was positioned at H = 47.1. The precision of the measurement is $\pm$ 4%.

In addition, the thermal flux in the cold and hot source dummies was measured, as well as on the surface of the irradiation channel No. 17. The cold source was filled with D_2O, the boron poisoning in the core was 0.255 g B-10/liter, the control rod was positioned at H = 59.4 cm. The flux curves are reproduced in Figures 5.3.7, 5.3.8, 5.3.9 and 5.3.10, and the measured values are given in Table 5.3.4.

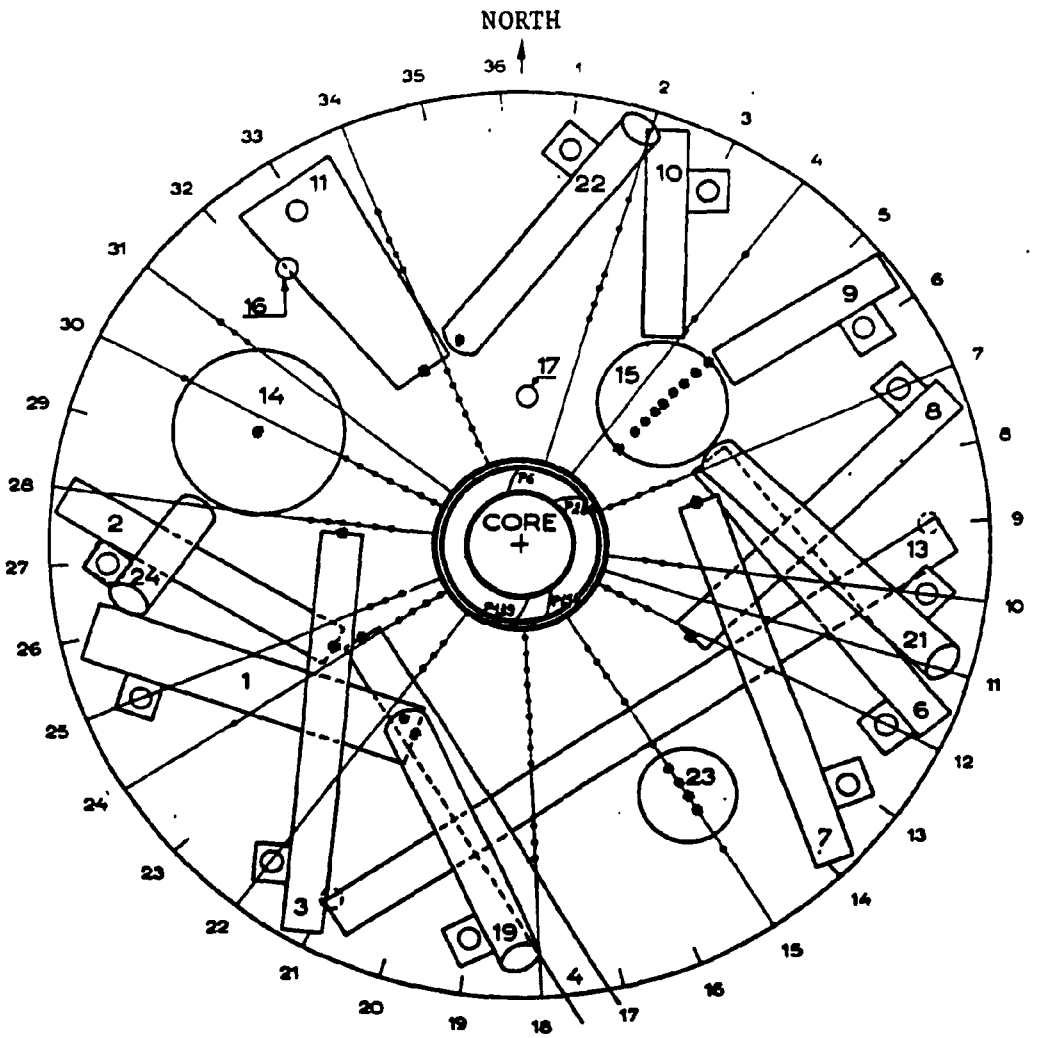

Fig. 5.3.6 Radial and azimuthal distribution of the flux measuring points in the reflector and on the channel noses

For measurement of the "homogeneous" flux distribution, a large number of probes was irradiated; they made it possible to determine the azimuthal flux distribution for different radii and heights and to take the mean graphically.

In Figure 5.3.11 some typical azimuthal flux distributions are plotted. Beginning with the mean values, it is possible to determine the mean radial flux distribution. It is plotted in Figure 5.3.12 for H = 111 cm (reactor midplane). For comparison purposes the flux distribution of the diffusion calculation is also given.

Table 5.3.3 Thermal neutron flux on the beam hole noses at a reactor power of 1 watt. The fluxes are given for the center of the circular disk that forms the channel nose, for a point that lies on the nose 4 cm above the center, and for a point that lies 4 cm below that (R and h have the same meaning as in Table 5.3.1). Schemes I and II refer to the configuration of the beam holes in the reflector, see 5.3.3.5.

	Channel			Flux on the Channel Nose (n/cm^2s) · 10^{-7}			Flux Depression $\frac{\Phi_{channel\ nose}}{\Phi_{unperturbed}}$
		R (cm)	h (cm)	+ 4 cm	center	- 4 cm	
Scheme I	1	55,6	-25	1,010	0,984	0,962	0,781
	2	52	-25	1,093	1,047	1,029	0,753
	3	45	+25	1,637	1,672	1,724	0,874
	4	45	0	1,819	1,798	1,791	0,842
	7	45,3	+15	1,488	1,490	1,497	0,715
	8	47,3	-25	1,196	1,128	1,093	0,721
	11	49,8	-20	1,189	1,128	1,099	0,709
	19	54	+25	1,214	1,192	1,230	0,785
	22	54,1	+25	1,161	1,151	1,166	0,758
Scheme II	1	49,1	-25	1,215	1,173	1,137	0,785
	2	49,0	-25	1,175	1,112	1,090	0,748
	3	43,2	+25	1,579	1,612	1,659	0,740
	4	41,3	0	2,112	2,089	2,083	0,896
	7	45,3	+15	1,549	1,559	1,572	0,748
	8	40,8	-25	1,402	1,324	1,282	0,745

[Commas in the above table should be read as decimal points -- Translator's Note.]

Table 5.3.4. Thermal neutron flux distribution in the hot and cold sources and on Channel No. 17 at a reactor power of 1 watt.
[Commas in the tables below should be read as decimal points]

Hot Source: Flux on the vertical axis of the source (12 = 49.6 cm)

Z (cm)	109,5	115,5	121,5	129,5	135,5
$\phi \cdot 10^{-7}$ (n/cm^{2}s)	1,261	1,268	1,248	1,188	1,103

Radial flux distribution in the midplane of the graphite block

R (cm)	39,6	42,1	45,1	48,1	51,1	54,1	57,1	59,6
$\phi \cdot 10^{-7}$ (n/cm^{2}s)	1,599	1,533	1,418	1,300	1,189	1,081	0,981	0,929

Cold Source: Flux distribution on the axis of the source (R = 70 cm)

Z (cm)	127,8	132,8	137,8	142,8	147,8	152,8	157,8	162,8	167,8	172,8	177,8	182,8
$\phi \cdot 10^{-}$ (n/cm^{2}s)	0,703	0,697	0,672	0,639	0,596	0,551	0,495	0,446	0,408	0,368	0,327	0,288

Channel 17: Flux on the channel side facing away from the core (R = 40.0 cm)

Z (cm)	132,6	142,6	152,6	162,6	172,6	182,6	192,6	202,6	212,6
$\phi \cdot 10^{-7}$ (n/cm^{2}s)	1,927	1,700	1,432	1,160	0,900	0,667	0,467	0,296	0,152

Flux on the channel side facing the core (R = 35 cm)

Z (cm)	132,2	142,2	152,2	162,2	172,2	182,2	192,2	202,2	212,2
$\phi \cdot 10^{-7}$ (n/cm^{2}s)	1,974	1,731	1,453	1,189	0,930	0,687	0,480	0,306	0,157

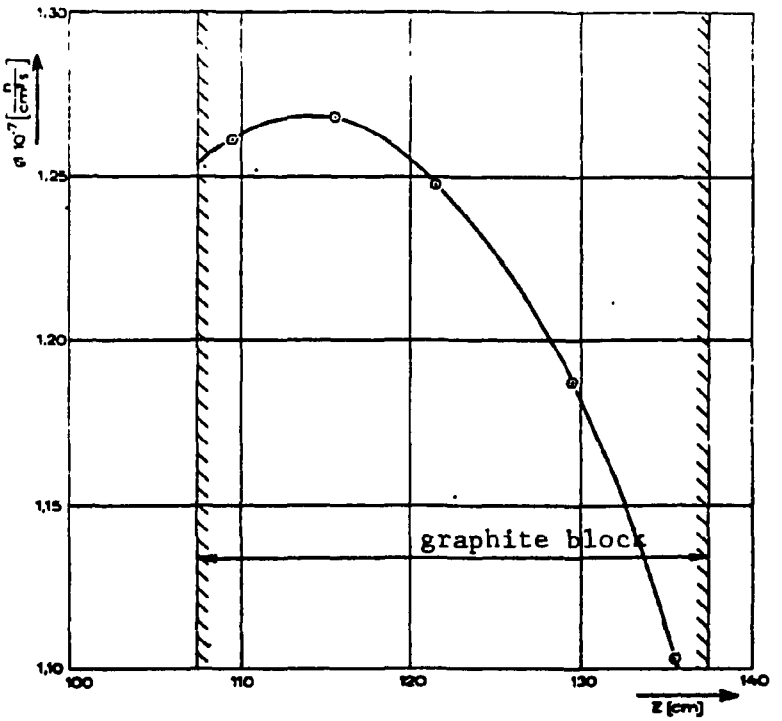

Fig. 5.3.7 Vertical distribution of the neutron flux on the axis of the graphite block of the hot source. Reactor power = 1 watt.

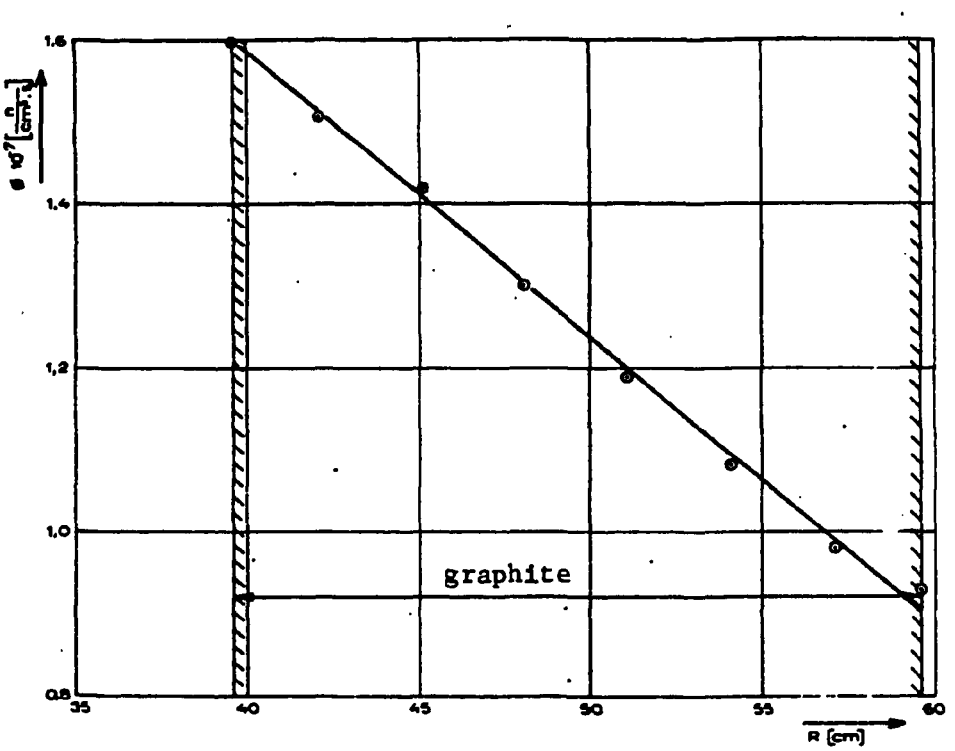

Fig. 5.3.8 Radial neutron flux distribution in the midplane of the graphite block of the hot source. Reactor power = 1 watt.

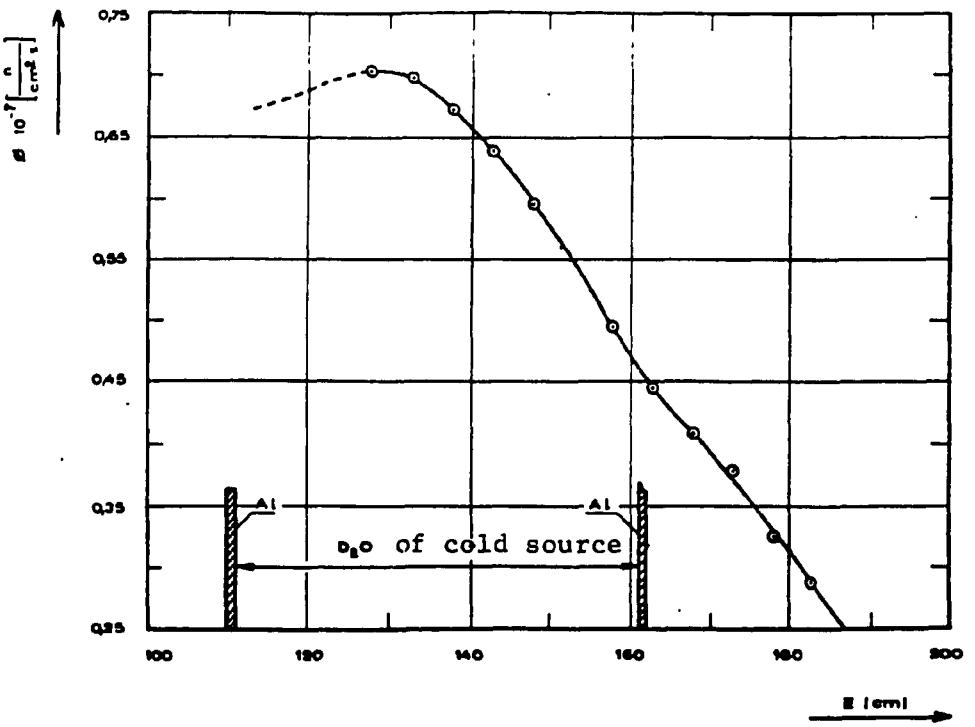

Fig. 5.3.9 Vertical distribution of the neutron flux on the axis of the cold source. Reactor power = 1 watt.

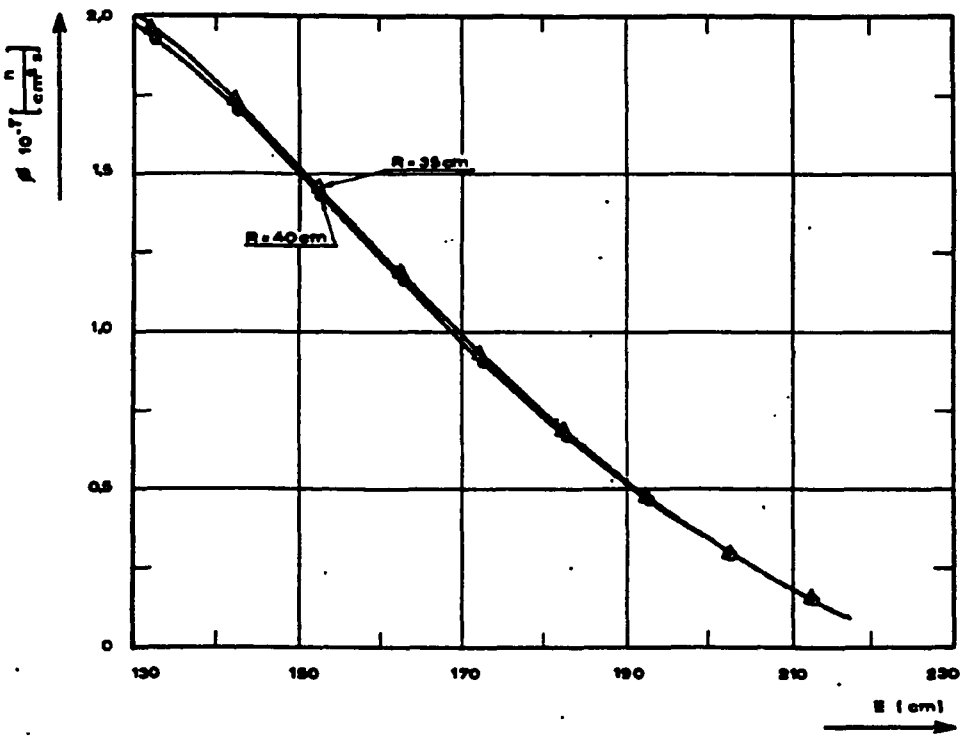

Fig. 5.3.10 Vertical distribution of the neutron flux on the surface of Channel No. 17. R = 35 cm on the side facing the core, R = 40 cm on the side facing away from the core. Reactor power = 1 watt.

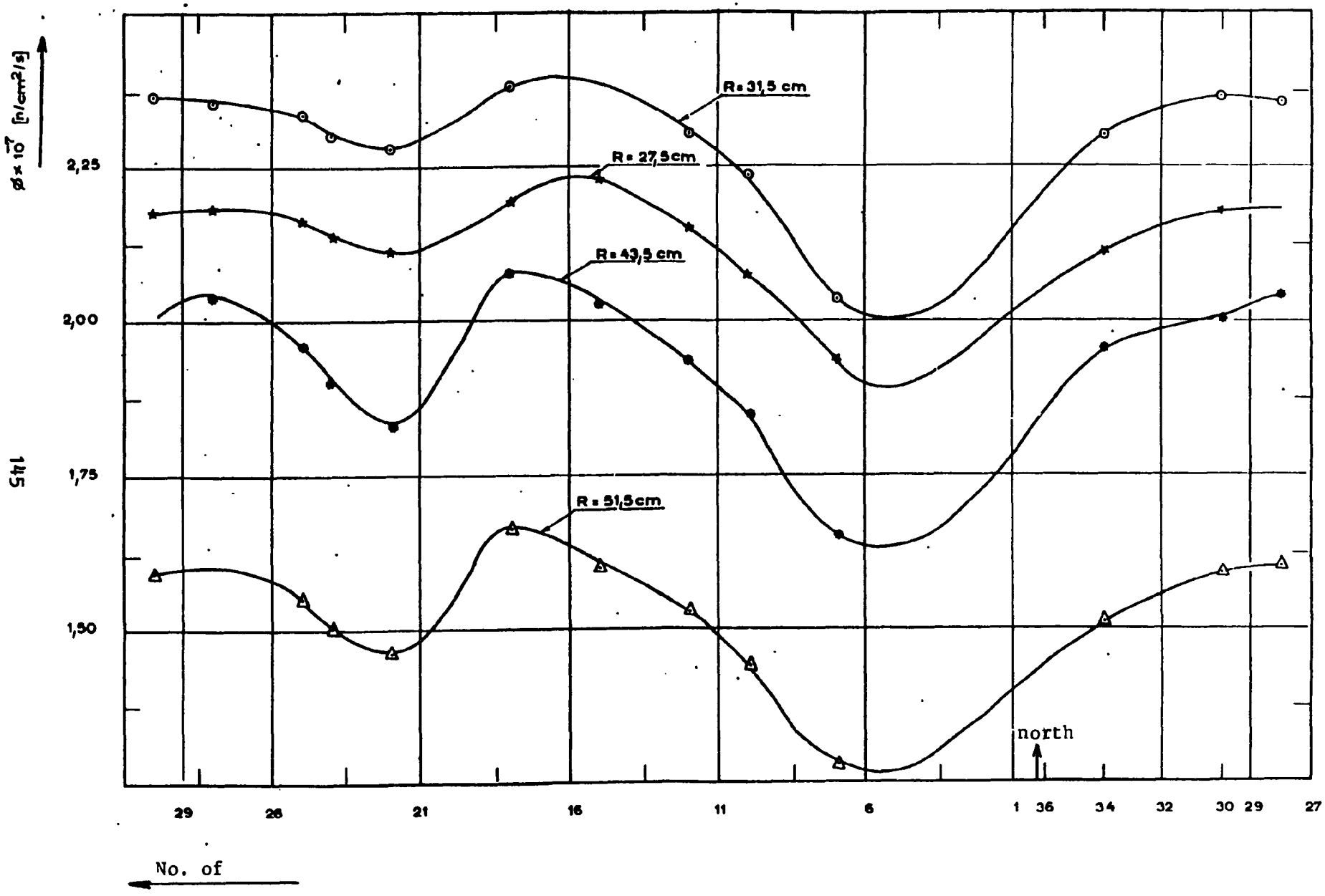

Fig. 5.3.11 Azimuthal distribution of the thermal neutron flux at 1 watt reactor power in the reflector with beam hole dummies

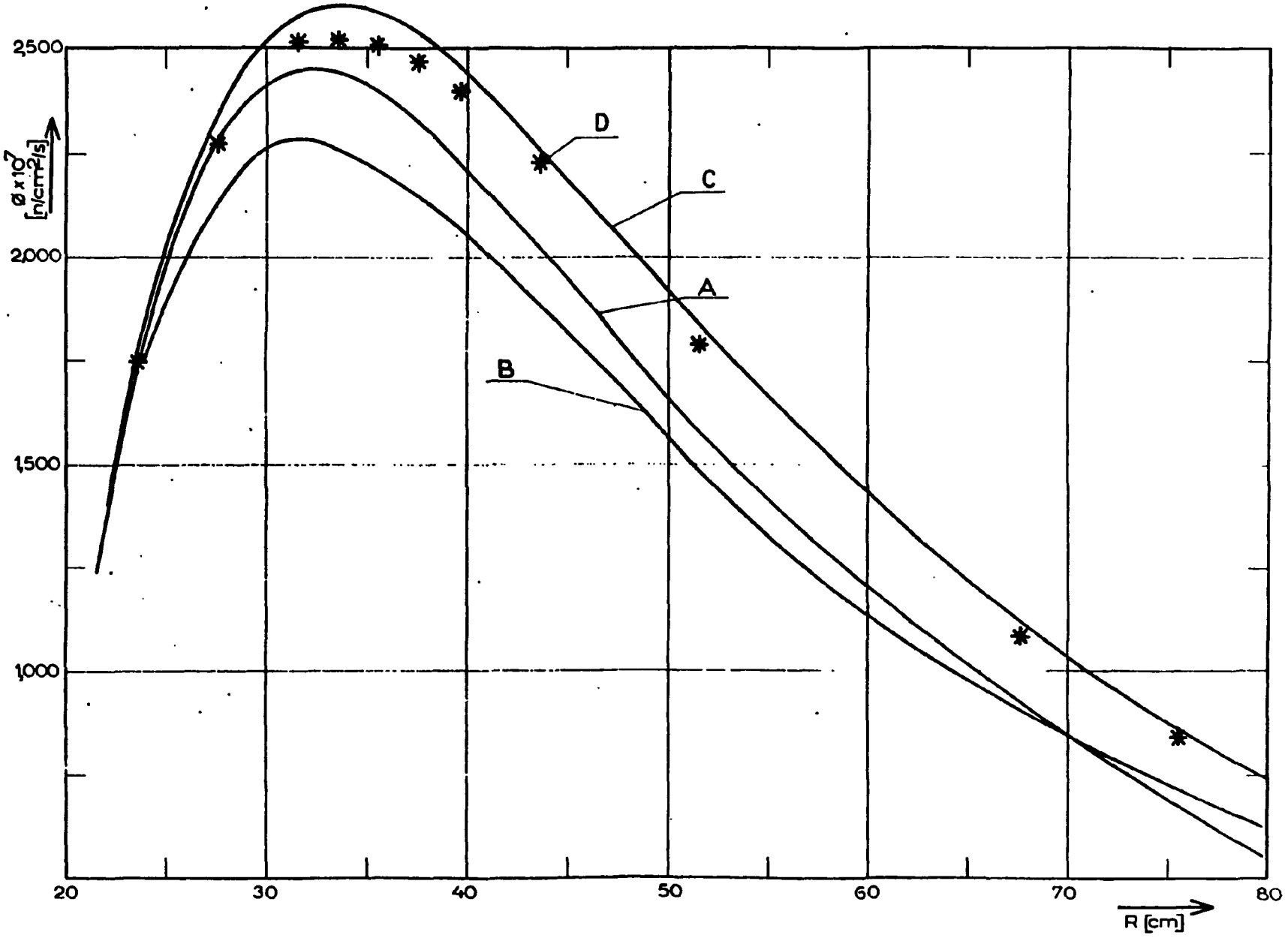

Fig. 5.3.12. "Homogeneous" radial distribution of the thermal neutron flux in the midplane of the reflector. A = calculation, B = measurement. For comparison purposes the flux distribution without beam holes is also given (C = calculation, D = measurement).

5.3.5 The Power Distribution in the Core with Solid Boron and Dummy Beam Holes

The technique used for measuring the power distribution was the same as the one used for States 1 and 2. Because of the flux perturbation of the dummies for the beam holes and sources, measurement involves difficulties that are similar to those encountered with flux measurement. To determine the location and form of the azimuthal power perturbation, Mn probes were irradiated on the surface of the core barrel at different heights. These curves are plotted in Figure 5.3.13. The effect of the hot source (15) is shown very clearly, as is the effect of the five beam hole noses between support structures 20 and 27.

On the basis of these values it was possible to plot an azimuthal flux distribution on the surface of the core barrel averaged over the core height (Figure 5.3.14). It was also assumed that the mean azimuthal power distribution has the same form as the flux distribution on the barrel surface, but with less strongly pronounced deflections, i.e., that the points of maximum, mean and minimum power are known. The power distribution in the core was measured at these points and also at a point where the flux distribution in the reflector has its maximum at R 30.5 and Z = 117. Since the power distribution has practically the same form as for State 2 (see 5.2.5) and due to the time-consuming and complex nature of the measurement and the activity of the irradiated core, we worked with fewer points than for State 2, except for position 154, where we guessed the power maximum would be. The relative mean activity of the four measuring plates is plotted in Figure 5.3.14. The broken line gives the probable axially and radially averaged azimuthal power distribution in the core. The measured values of the power distribution for the four positions mentioned are given in Tables 5.3.6, 5.3.7, 5.3.8 and 5.2.9.

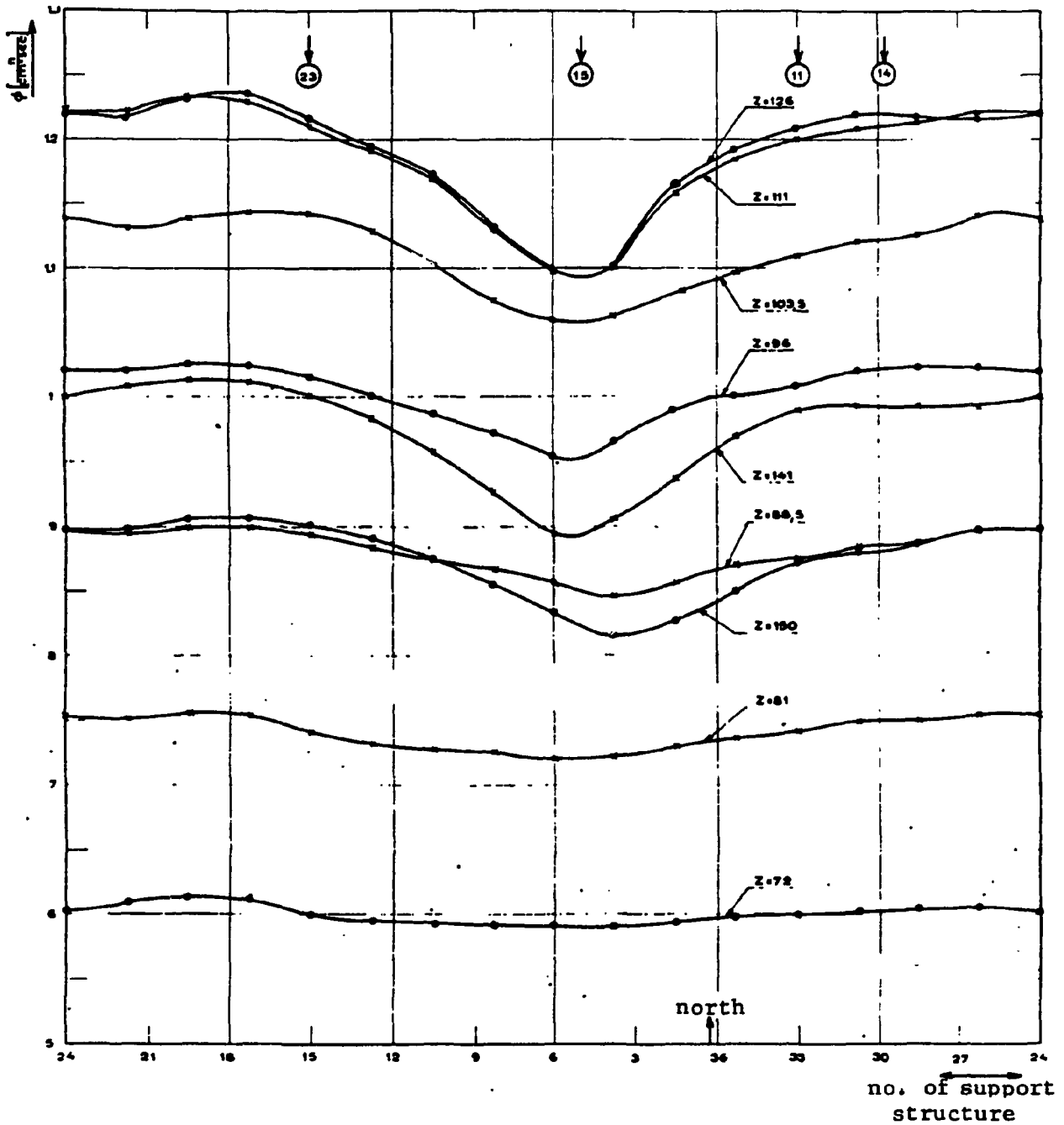

Fig. 5.3.13 Azimuthal distribution of the thermal flux on the surface of the core barrel. The arrows on the upper edge give the position of several dummies in the reflector (see Figure 5.3.1).

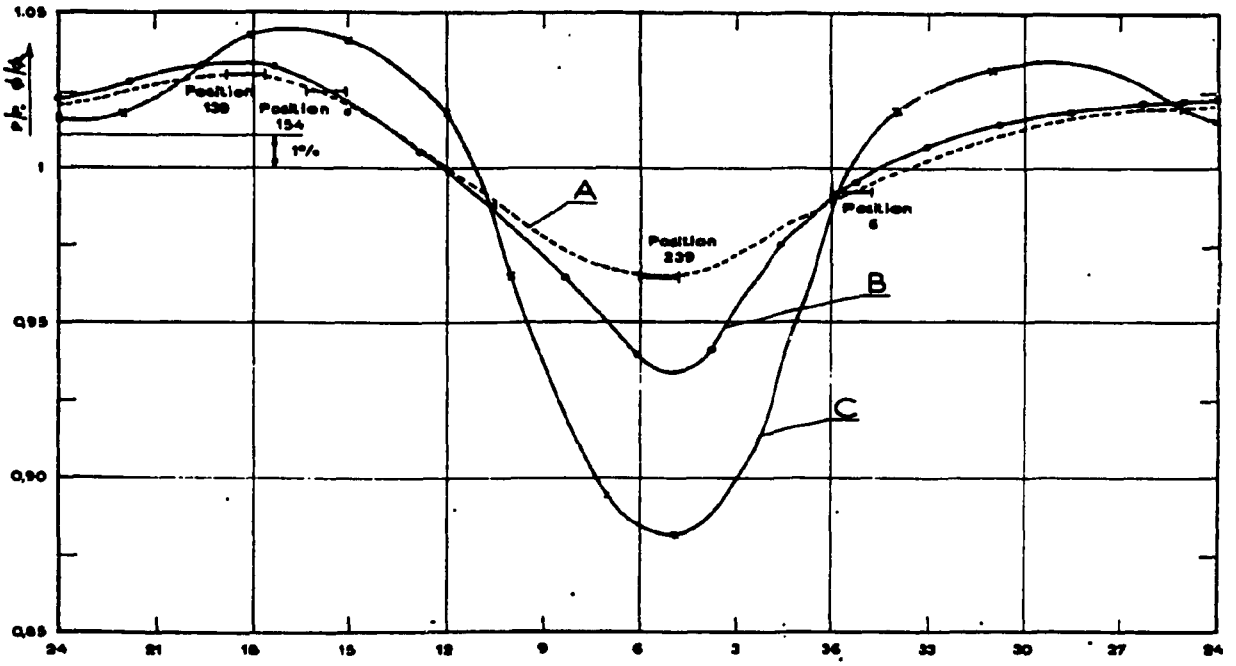

Fig. 5.3.14 Azimuthal flux and power distribution. A = axially and radially averaged power distribution in the core, B = axially averaged distribution of the thermal neutron flux on the surface of the core barrel, C = azimuthal flux distribution in the reflector at R = 30.5 and Z = 117 cm.

Table 5.3.6 Power distribution in fuel plate no. 6, normalized to a core power of 1 [Commas in this and following tables are to be read as decimal points]

Radius R(cm) / Plate Ht. H(cm)	14,35	14,65	14,95	15,25	15,9	16,75	17,6	18,25	18,55	18,85	19,39
79,75			1,0572						1,2353		
79,50											
79,06	1,1528										1,7021
78,55											
78,06											
77,15	1,1000					0,6721					1,6685
75,0			0,8775			0,6873			1,0851		
72,5											
70,0											
62,5			1,0878			0,8808			1,3538		
55,0						0,9431					
47,5						0,9491					
40,0			0,9144			0,8715			1,4189		
32,5						0,8059					
25,0						0,7257					
17,5			0,6508			0,6301			1,0744		
10,0											
7,5											
5,0			0,4540			0,4518			0,7796		
2,85	0,4920					0,4270					1,1787
1,94											
1,45											
0,94	0,6978										1,1654
0,50											
0,25			0,4529						0,8162		

Table 5.3.7 Power distribution in fuel plate no. 139, normalized to a core power of 1

Radius R(cm) / Plate Ht. H(cm)	14,35	14,65	14,95	15,25	15,9	16,75	17,6	18,25	18,55	18,85	19,39
79,75						0,8087					
79,50											
79,06											
78,55											
78,06						0,7320					
77,15											
75,0						0,7338					
72,5											
70,0						0,8077					
62,5		1,2448			0,9393	0,9267	1,0358				
55,0						0,9914					
47,5						0,9967					
40,0	1,0723	1,0076		0,8976	0,8619	0,9080	1,0558	1,2877			2,2595
32,5	0,9741					0,8400					
25,0	0,8721					0,7610					1,9139
17,5	0,7422	0,6923		0,6282		0,6540		0,9698			1,6900
10,0						0,5400					
7,5	0,5524										
5,0		0,4730			0,4239	0,4641	0,5563				
2,85											
1,94						0,4396					
1,45	0,4659										
0,94											
0,50											1,1625
0,25	0,5024	0,4698		0,4483	0,4514	0,5025	0,5966	0,7480			

Table 5.3.8 Power distribution in fuel plate no. 154, normalized to a core power of 1

Radius R(cm) / Plate Ht. H(cm)	14,35	14,65	14,95	15,25	15,9	16,75	17,6	18,25	18,55	18,85	19,39
79,75	1,2958	1,1868		1,0238	0,9489	0,9162	0,9962	1,1537		1,4096	1,8193
79,50											1,8102
79,06											
78,55	1,1691					0,7377					1,7754
78,06	1,1352					0,7250					1,7727
77,15											
75,0	1,1366	1,0165		0,8289	0,7437	0,7300	0,8259	1,0039		1,2778	1,8008
72,5	1,2006					0,7688					1,8309
70,0	1,2275					0,8033					1,9222
62,5	1,3922	1,2400		1,0273	0,9341	0,9191	1,0267	1,2300		1,5757	2,1547
55,0	1,4596					0,9796					2,3081
47,5	1,4230					0,9876					2,3404
40,0	1,0893	1,0012		0,8991	0,8616	0,9031	1,0532	1,2918		1,6688	2,2791
32,5	0,9908					0,8351					2,1373
25,0	0,8886					0,7506					1,9394
17,5	0,7630	0,6978		0,6373	0,6094	0,6473	0,7744	0,9386		1,2503	1,7000
10,0	0,6163					0,5241					1,4217
7,5	0,5512					0,4965					1,3456
5,0	0,5232	0,4673		0,4359	0,4264	0,4553	0,5579	0,6827		0,9152	1,2630
2,85											
1,94	0,4880					0,4251					1,1978
1,45	0,4658					0,4437					1,1969
0,94											
0,50											1,2100
0,25	0,5193	0,4743		0,4501	0,4458	0,4829	0,6064	0,7245		0,9438	1,214

Table 5.3.9 Power distribution in fuel plate no. 234, normalized to a core power of 1

Radius R(cm) / Plate Ht. H(cm)	14,35	14,65	14,95	15,25	15,9	16,75	17,6	18,25	18,55	18,85	19,39
79,75		1,1200			0,8853		0,9302			1,3021	
79,50											1,6263
79,06											
78,55	1,0996					0,6998					1,6215
78,06											1,5885
77,15											
75,0	1,1148	0,9569			0,7092	0,6887	0,7726			1,1871	1,6292
72,5	1,1451					0,7196					1,6891
70,0											1,7431
62,5	1,3400	1,1729			0,8900	0,8745	0,9693			1,4536	1,9552
55,0						0,9342					2,0730
47,5	1,3081					0,9402					2,1224
40,0	1,0048	0,9275			0,8183	0,8574	0,9982			1,5538	2,0975
32,5	0,9230					0,7952					1,9899
25,0	0,8221					0,7257					1,8363
17,5	0,7107	0,6594			0,5910	0,6327	0,7555			1,2041	1,6392
10,0						0,5207					1,3877
7,5	0,5287										1,3041
5,0	0,4890	0,4562			0,4138	0,4527	0,5437			0,8805	1,2160
2,85											
1,94						0,4239					1,1415
1,45	0,4570										1,1345
0,94											
0,50											1,1492
0,25	0,4881	0,4662			0,4414	0,4869	0,5843			0,9033	

The axially averaged radial power distribution for the plate at the power maximum (No. 139) is shown in Figure 5.3.15 in comparison with the power distribution that was measured for State 2. One can see that the deviations on the inner plate edge are the greatest, so that the azimuthal flux perturbation has little effect on the relative power in the "hot thread of stream." It is obtained as

$$F_{rad} = 1.820$$

and thus is about 2% above the power in the "hot thread of stream" without beam holes (State 2). The boron concentration in the core was 0.177 g B-10/liter during the measurement, and the control rod was positioned at H = 47.1 cm.

5.3.6 The "Rendement" of the Reactor with Solid Boron and Dummy Beam Holes

The "rendement" was measured using the methods described above. Seven (7) measuring points on support structure No. 2 on the radii 71.5 and 83.5 cm. For the azimuthally averaged flux distribution (Figure 5.3.12) the "rendement" is obtained as

$$r_{measured} = 2.3 \times 10^7 \text{ n / cm}^2\text{sW} .$$

The error that this value involves amounts to $\pm$ 3%, which is composed of 1.5% for determination of the mean core power, 1% for the azimuthal flux integration and 0.5% for determination of the ratio $A_{U,R}/A_{Mn,R}$ from Equation (4.11). The "rendement" calculated with homogenized beam holes is

$$r_{calculated} = 2.45 \times 10^7 \text{ n / cm}^2\text{sW} ,$$

and is therefore 6.5% higher than the measured value. This error can easily be explained by underestimation of the streaming effect (see above.)

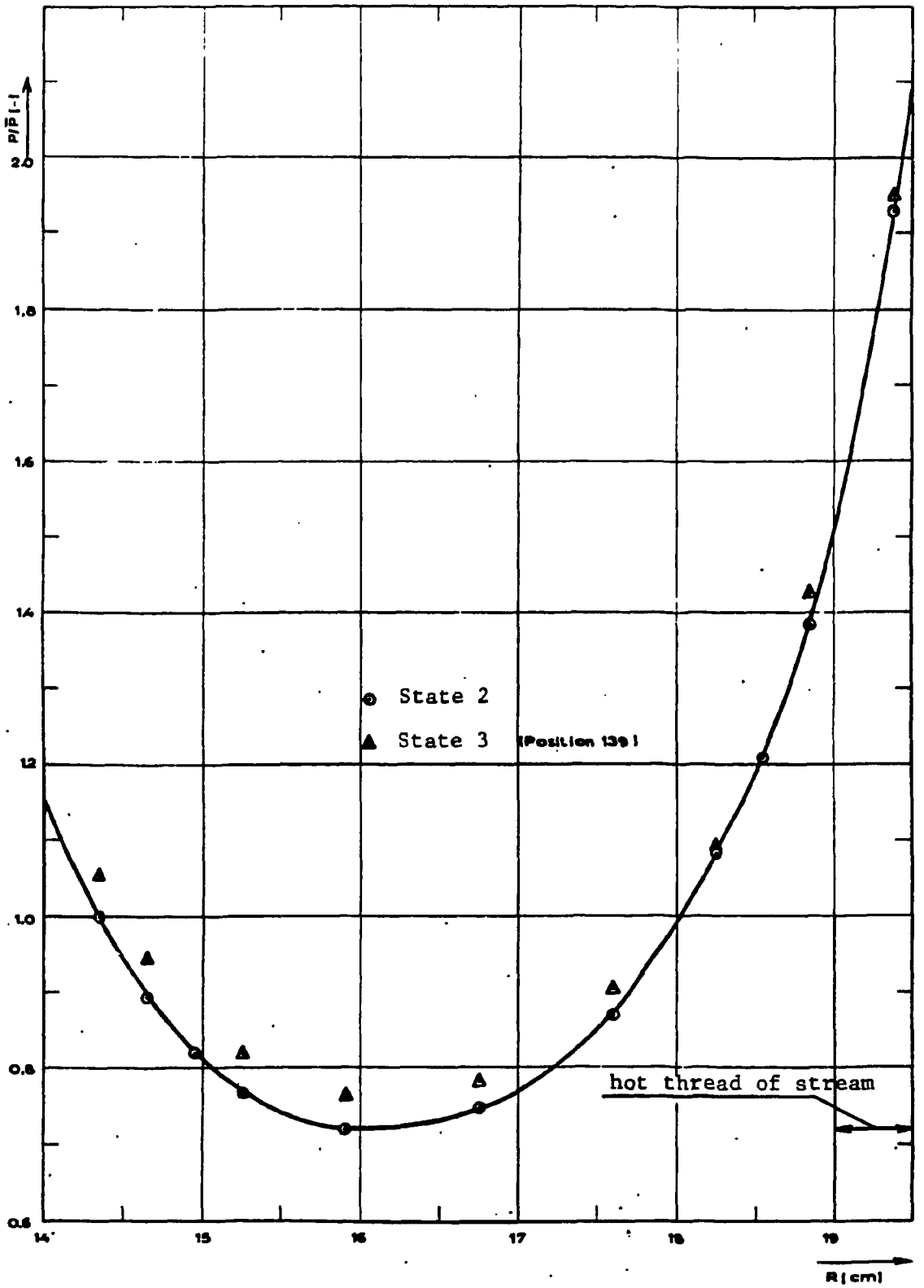

Fig. 5.3.15 Axially determined radial power distribution for plate position 139 in the reactor with solid boron and dummy beam holes and in the reactor with solid boron and without dummy beam holes

5.4 Measurements of Individual Beam Holes

In this measurement series the reactivities of channels of different shapes are measured, in each case a map of the thermal flux in the environment of the channel nose and the thermal, epithermal and fast flux on the axis of the (withdrawing) channel. The reactivities are determined by comparing the stable period and the control rod position with and without a channel; the thermal flux maps are measured using dysprosium probes having a diameter of 0.2 cm and a thickness of 0.005 cm; and the epithermal and fast fluxes are measured using gold probes (under cadmium) and phosphorus probes. As for all flux measurements, the probes are affixed to Mylar tape; The latter is held by suitable frames of Al wire (0.6 cm in diameter) connected to the channel. The position of these frames with respect to the channel nose is accurately known to within approximately $\pm$ 0.2 cm.

Boron poisoning in these tests was 0.249 g B-10/liter, the control rod position approximately H = 47 cm, and the solid boron at the core ends was built in.

5.4.1 Comparison of Cylindrical, Tapered and Square Beam Holes

The dimensions of these channels are given in Fig. 5.4.1. Their wall thickness is 0.2 cm. Like most other beam hole dummies, they are fasted to a holding rod by means of a flange (cf. Fig. 2.8). The location of the channel nose in the direction of the channel axis is precisely known to within $\pm$ 0.1 cm, and the location of the channel axis itself to within approximately $\pm$ 2^{o}.

The location of the channel is characterized as follows:

> The channel axis is in the core midplane at Z = 110 cm,
> the distance between the channel nose and the core axis is 46.1 cm,
> and the channel axis lies tangentially to a circle having a radius
> R = 45 cm around the core axis.

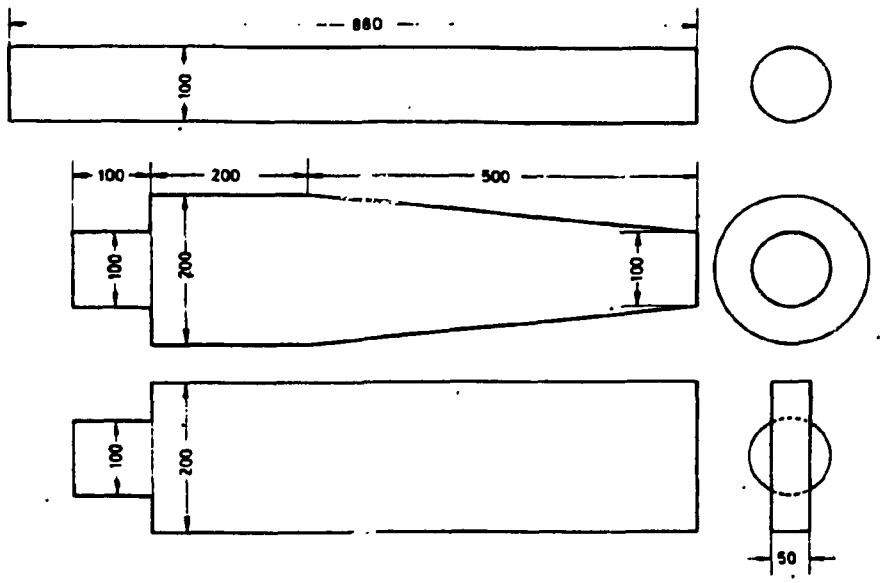

Fig. 5.4.1 Dimensions of rectangular, tapered and cylindrical beam holes

5.4.1.1 Reactivity of the Beam Holes

The reference state with which the reactivity with channel is compared, contains in each case a flange and holding rod. The cylindrical channel was flooded with D_2O; its reactivity was measured both for the empty and for the flooded state.

The measured reactivities are given in Table 5.4.1. The indicated errors relate only to the reactivity measurement; the error that results from imprecise knowledge about positioning is also estimated to be about $\pm$ 5 pcm.

For the cylindrical beam hole therefore the ratio V of aluminum to void reactivity is

$$V = \frac{36 \pm 10}{97 \pm 10} = 0.38 \begin{matrix} + 0.15 \\ - 0.09 \end{matrix} .$$

Table 5.4.1 Reactivity of channels of different shapes

Channel	Reactivity (pcm)
cylindrical, empty	- 133 ± 5
cylindrical, full	- 36 ± 4
tapered	- 290 ± 5
rectangular	- 197 ± 5

5.4.1.2 Thermal Flux in the Environment of Beam Hole Noses

The Dy probes sit on three axes (x, y, z) that are perpendicular to one another and that intersect on the channel nose, i.e., in the center of the circular surface that closes off the channel. The three axes are oriented so that the x axis represents the extension of the beam hole axis, the z axis is in the direction of the core axis, and the y axis is in the core midplane. The measured values on the three axes are plotted in Figures 5.4.2, 5.4.3 and 5.4.4. The comparison with the unperturbed thermal flux, which is also plotted, shows that the local perturbation caused by the beam hole disappears at a distance of about 15 cm from the center of the channel nose. We also find that the perturbation on the side of the beam hole facing away from the core is smaller than on the side facing the core, see Figure 5.4.2. This phenomenon can be explained by the beam hole effect that acts transversely to the beam hole axis and even leads to an increase in flux in the vicinity of the side of the channel facing away from the core. Besides local perturbation, the beam hole generates a global change in the neutron flux distribution, a change in the basic mode. This is especially visible in Figures 5.4.3 and 5.4.4. It is perhaps evident from this phenomenon that the power normalization of the various measurements with different channels was difficult, which was carried out with a flux measurement on a position in the reflector lying at an angle of 120° with respect to the channel nose at R = 85 cm. The thermal flux at this reference position was about 3% higher than in the unperturbed case. However, this was only concluded after further measurements with the exiting beam hole, where the flux measurements described here were carried out for different positions (see below).

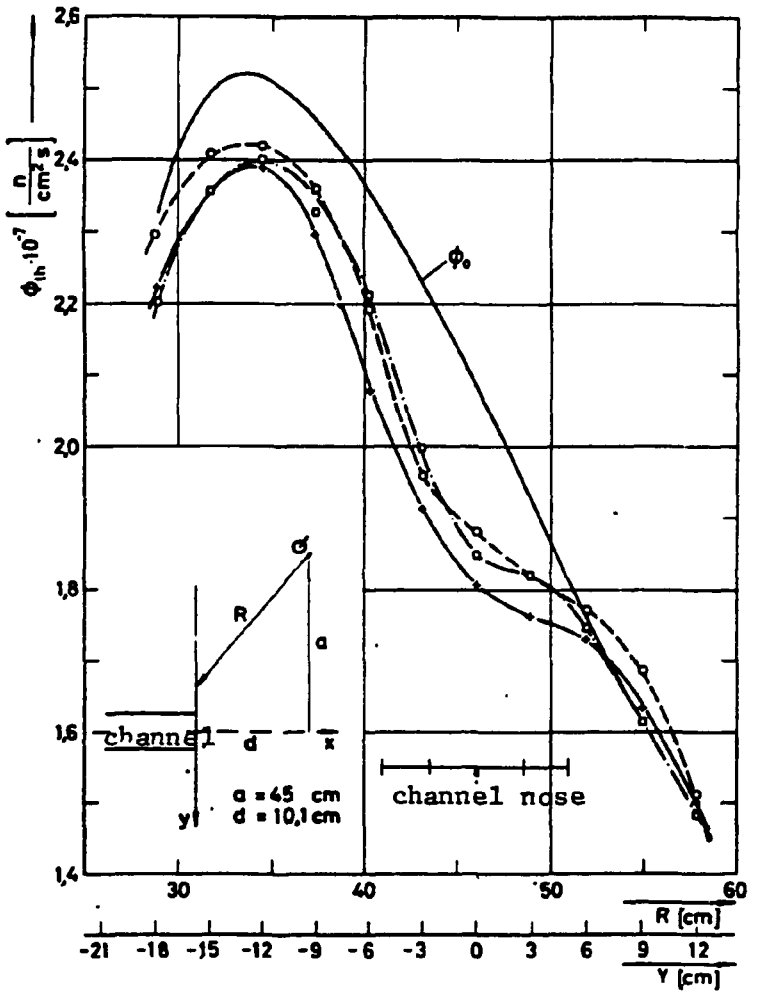

Fig. 5.4.2 Thermal flux in the vicinity of the beam hole nose of cylindrical -o-, tapered -+- and square -□- channels. The y axis is perpendicular to the channel axis in the core midplane, the channel axis on the radius R_o = 46.12 cm. ♂ designates the core midpoint. The reactor power is 1 watt.

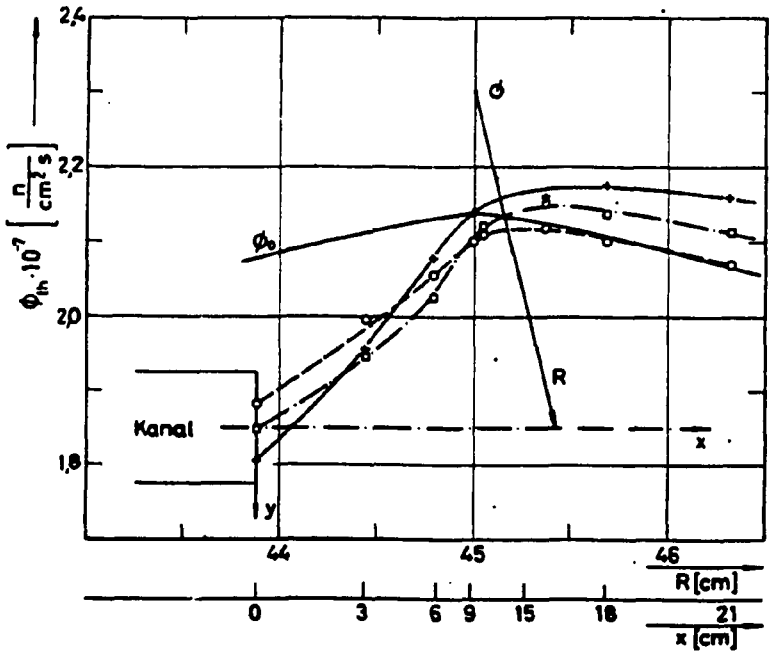

Fig. 5.4.3 Thermal flux in the vicinity of the beam hole nose of cylindrical -o-, tapered -+- and square -□- channels. The x axis is in the core midplane and is tangent to a circle around the core midpoint σ having the radius R = 45 cm. The channel nose lies on the radius R_o = 46.12 cm. The reactor power is 1 watt.

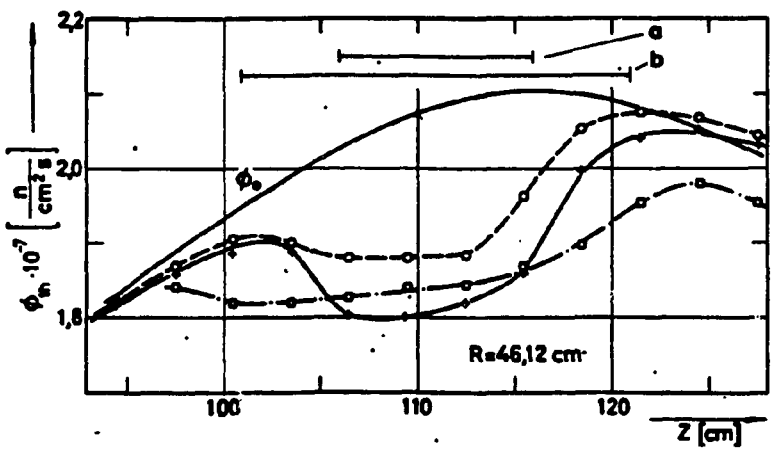

Fig. 5.4.4 Thermal flux in the vicinity of the beam hole nose of cylindrical -o-, tapered -+- and square -□- channels. The z axis runs in the direction of the core axis and intersects the channel nose at R_o = 46.12 cm. The reactor power is 1 watt.

The difference in the local flux depression of the three beam holes used is not considerable and is virtually within the error limits given by the power normalization and positioning. In the following diagram the measured flux depressions are given in percent in a top view of the beam hole nose; the error in each case is probably ± 3%. The reactor axis is at the left.

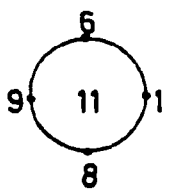

cylindrical

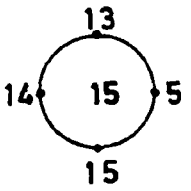

tapered

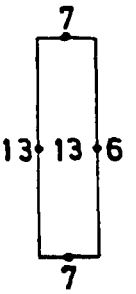

square

A comparison of the three beam hole types on the basis of these measurements is difficult, even disregarding measurement errors. On the local flux depression is superimposed the global perturbation which for its part seems to be different for each beam hole. In the presence of additional beam holes the global perturbation would doubtlessly be different from the one measured here.

5.4.2 Thermal, Epithermal and Fast Flux on the Axis of the Exiting Beam Hole

The axis of the beam hole that corresponds to the x axis defined above is located in this case as well tangentially to a circle having the radius R = 45 cm around the core axis in the reactor midplane at Z = 110. Measurements of the thermal and fast fluxes were carried out for four positions of the channel. If the zero point of the x axis is at R = 45 cm, where the x axis and the radius include a right angle, then channel noses lie at

Position a	x	=	0 cm
Position b	x	=	- 10.1 cm
Position c	x	=	- 18.5 cm
Position d	x	=	- 30 cm.

The measured values are plotted in Figures 5.4.5, 5.4.6 and 5.4.7. The thermal flux (Figure 5.4.5) was measured not only on the x axis but also on the y and z axes defined above. This makes it possible to specify the flux depression on the channel nose on the edges facing and facing away from the core and on the upper and lower edges, as follows (the core axis is on the left):

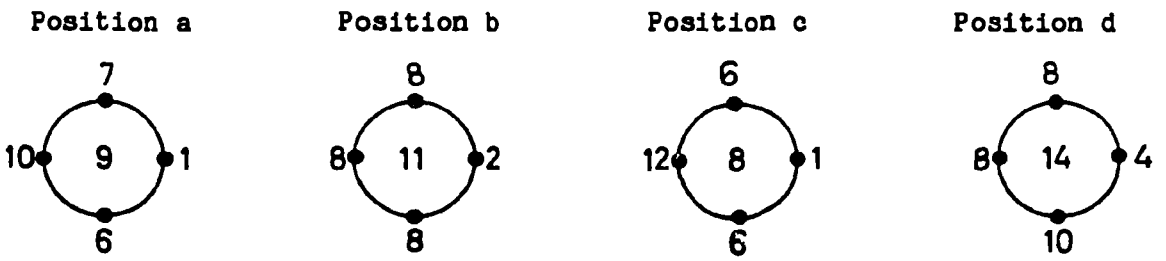

The data apply in percent and involve an error of approximately ± 2 (somewhat more accurate than in the case of the measurements described in 5.4.1, since the holders for the probes outside the channel are fastened not to the channel itself but to the beams above the reflector and thus were more accurately positioned). At Position c the errors are probably somewhat greater.

In measurement of the epithermal and especially the fast flux (Figures 5.4.6 and 5.4.7), the positioning errors have a much greater effect. We estimate that in that case the errors can range as high as 30% at individual points. Because of time reasons it was unfortunately not possible to repeat the measurements, so that it is difficult to give the error more accurately. This is especially true considering the fact that greater inconsistencies appeared than in the case of normalization of individual measurements to one another. The measurements were then normalized, as shown in Figure 5.4.7, such that the measuring point located at the greatest distance outside the beam hole was referred to the unperturbed flux.

A beam of collimated fast neutrons was measured at the outlet of the beam hole using a liquid scintillator. The ring-shaped wooden collimators were arranged so that the scintillator viewed a 50 cm^2 area. Detection of gamma radiation was suppressed by pulse shape discrimination. This measurement

was not suitable for the absolute determination of the emitted stream of neutrons. However, it was shown that the stream at the outlet of the channel has the same value within the error limits for Position a and Position b (see Figure 5.4.7). This result is in agreement with measurements of the fast flux $\emptyset_s$ at the channel nose, if the stream is determined according to the equation

$$J = \frac{\emptyset_s}{4} - \frac{D}{2} \text{ grad } \emptyset_s$$

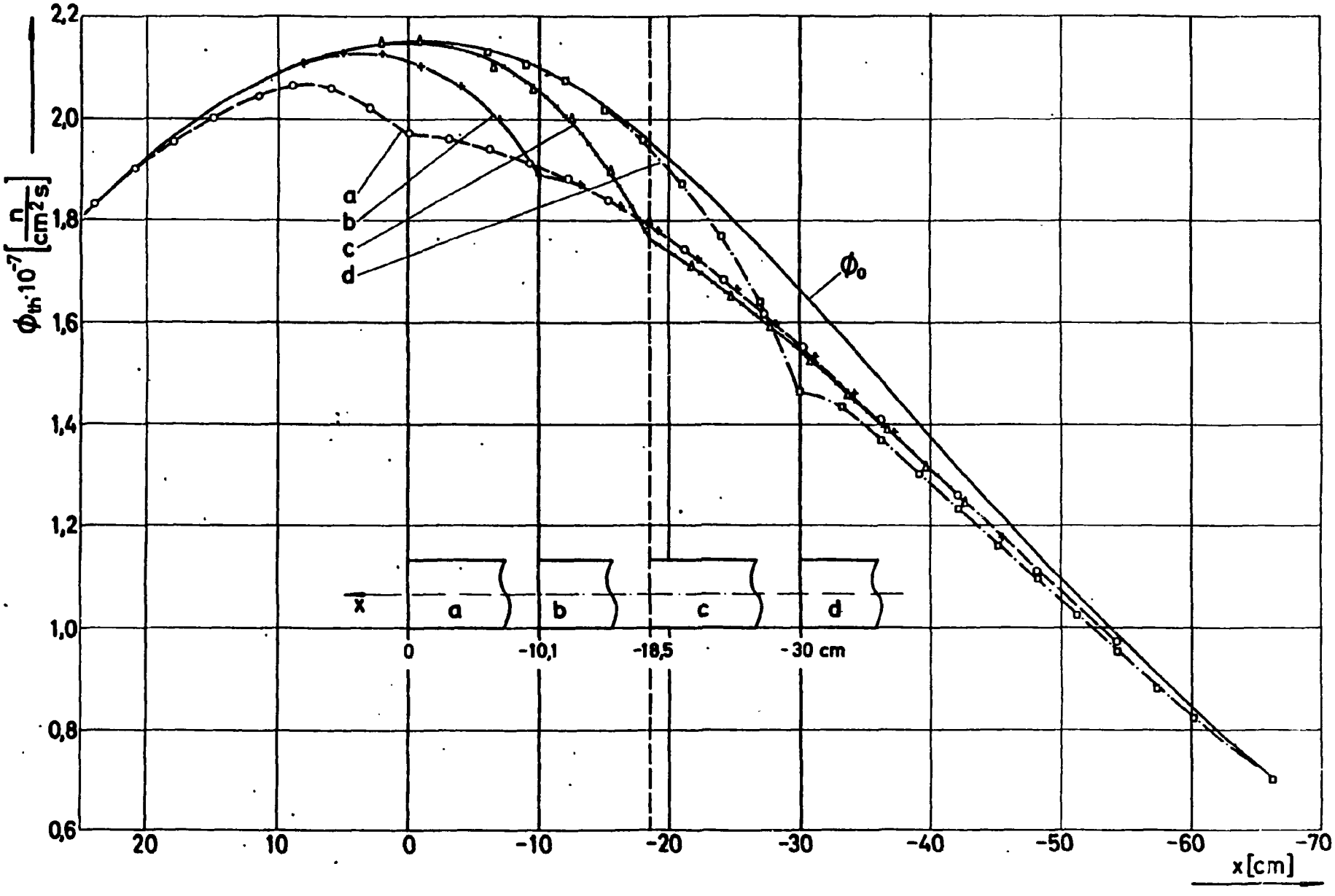

Fig. 5.4.5. Thermal flux on the axis of the exiting beam hole (x axis). The x axis is in the core midplane and is a tangent to a circle having the radius R_o = 45 cm around the core midpoint. The reactor power is 1 watt.

ORNL/TR-91/23

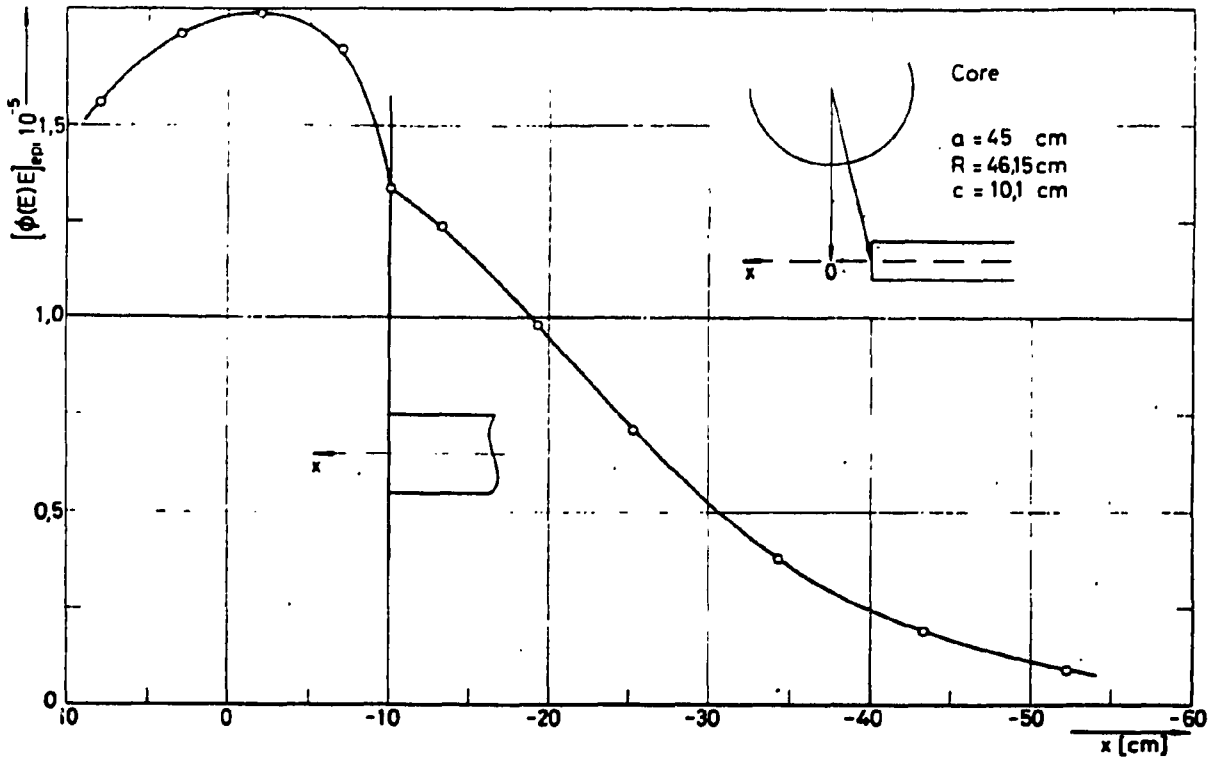

Fig. 5.4.6 Epithermal flux on the axis of the exiting beam hole (x axis). The x axis is in the core midplane and is tangent to a circle having a radius R_o = 45 cm around the core midpoint ⊙. The location of the beam hole corresponds to Position b in Figure 5.4.4. The flux values are related to the lethargy unit and are valid for the reactor power of 1 watt. See Figure 5.1.13 for the unperturbed flux.

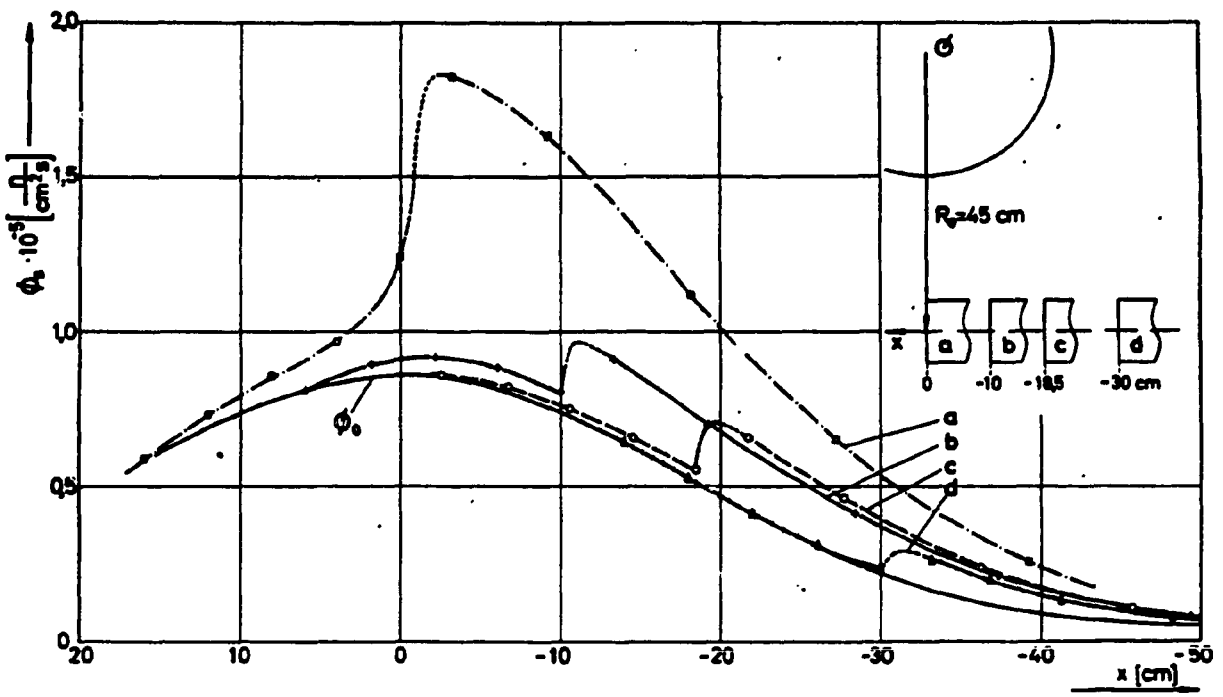

Fig. 5.4.7 Fast flux on the axis of the exiting beam hole (x axis). The x axis lies in the core midplane & is tangent to a circle with a radius R_o = 45 cm around the core midpoint ⊙. The threshold energy is 3 MeV (phosphorus); the reactor power is 1 W.

5.5 Safety Rods

5.5.1 Statement of the Problem

In FOEHN it was possible to install up to 6 absorbing rods that were designed to simulate the safety rods of the High Flux Reactor (see Chapter 2). At a date when the FOEHN design had already largely been determined, the HFR shutdown elements were extensively modified (see 6.1.5), and it was no longer possible take this into account in the FOEHN design. Therefore it was necessary to use 6 vertical rods 9 cm in diameter to determine the characteristics of 5 rods 10 cm in diameter which are slightly angled with respect to the vertical.

The following detailed information is required:

shutdown effect of 3 adjacent rods (worst case involving a scram in which 2 rods do not drop);

reactivity as a function of the insertion depth of the rods at the beginning of their drop travel;

total shutdown reactivity of the rods;

reactivity of a single rod;

reactivity of the rods in withdrawn position;

neutron flux on the rod surface in withdrawn position.

It was shown that the computational method of the equivalent absorber described in Section 3.5 makes it possible to calculate a reactor with safety rods with practically the same level of accuracy as a reactor without rods. Figure 5.5.1 shows the position of the dummy safety rods in the reflector.

5.5.2 Performance of the Measurements

5.5.2.1 Measurement Method

The measurement method is basically the same as used for all other reactivity measurements carried out in FOEHN.

The system is determined by three parameters:

a) by the concentration of the boron dissolved in the core (C),

b) by the position of the control rod (H),

c) by the safety rods, which vary in number, material (Cd or Inox), radius on which the stand (R) and insertion depth (Z).

Only <u>one</u> parameter is varied in each case.

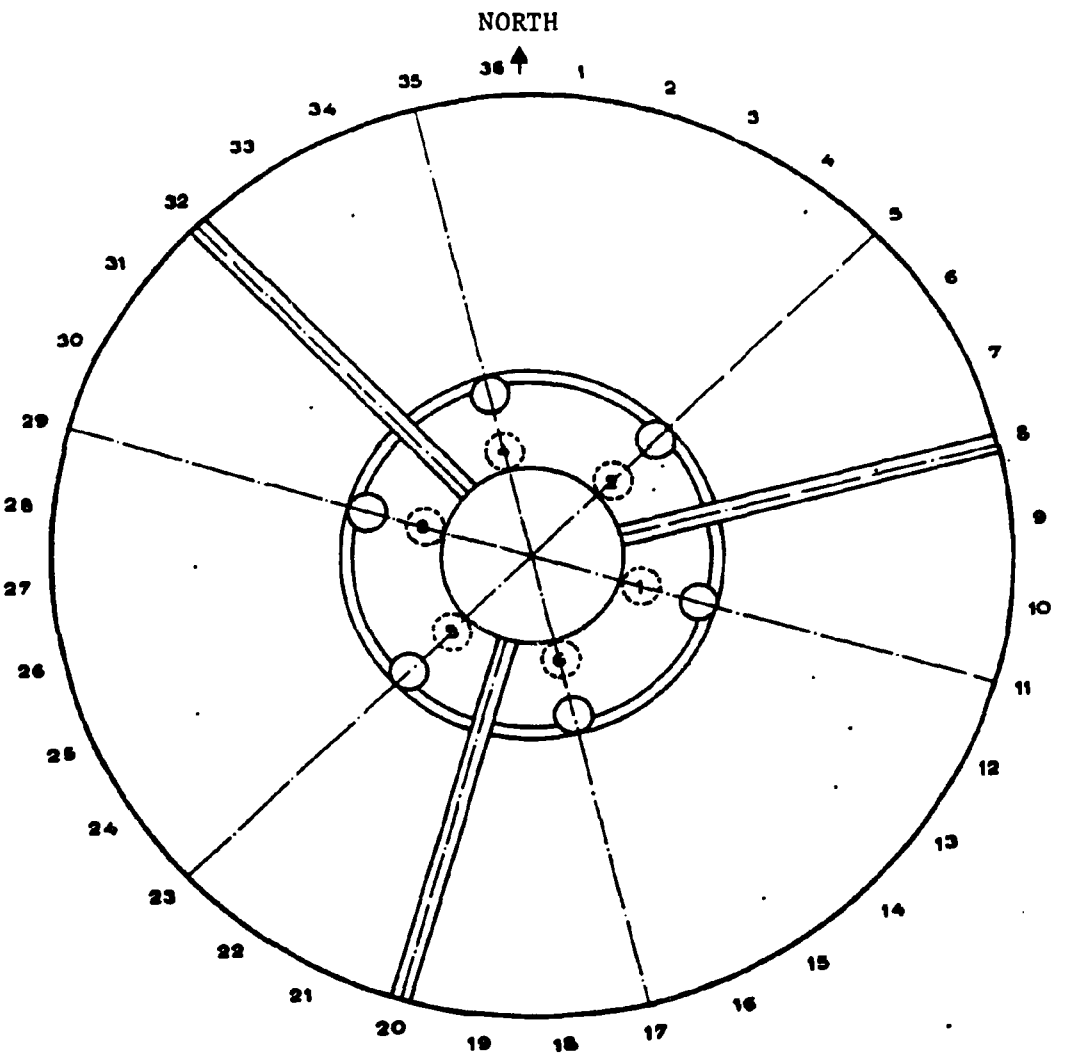

Fig. 5.5.1 Position of the safety rod dummies in the reflector

One begins with a critical state with C_1, H_1, Z_1 and R_1. For this state the differential control rod reactivity is measured ($d\rho/dH$). Then the

position of the rods is varied such that a negative reactivity contribution results, for example $R_2 = R_1 - \Delta R$. Thus we obtain a critical control rod position $H_2 = H_1 + \Delta H$ where $C_2 = C_1$, $Z_2 = Z_1$. Then a continuous run is made, whereby the control rod is totally inserted and yields the reactivity of the control rod between H_1 and H_2, which itself corresponds to the reactivity of R. Thus the reactivity curve $\rho = \rho(R)$ or $\rho = \rho(H)$ can be put together from single pieces. This operation is repeated for various boron concentrations so that it is possible to determine ρ for different control rod positions. In addition, one automatically obtains the differential boron reactivity $d\rho/dC$, which is a function of the presence of the rods to only a slight degree, as it turns out.

Small reactivities, as appeared in measurement of the axial rod characteristics, were determined by period measurement.

No measurements in the subcritical were carried out using the method of the pulsed neutron source, since the interpretation is very doubtful due to the strong dependence of the prompt life on geometry and subcriticality.

5.5.2.2 The Differential Boron Reactivity

The values listed in Table 5.5.1 were determined as the differential boron reactivity using the continuous run method for the individual reactor configurations.

Table 5.5.1 Boron reactivity with safety rods

Reactor State					Boron Reactivity
Solid Boron	Rod Number	R(cm)	Z(cm)	C(g/B-10/ltr)	(pcm/g B-10 x ltr)
yes	6 Cd	33	220-131	0.11-0.33	37,800 ± 2000
no	1 Cd	28.5	71	0.27-0.31	37,600 ± 1300
no	6 Cd	33	171-161	0.44-0.46	34,500 ± 1700
no	3 Cd	33-41.5	71	0.01-0.12	37,400 ± 2000

From the individual measurements we obtain as a weighted mean:

$$\frac{d\rho}{dC} = 37\,000 \pm 2000 \text{ pcm/g } B^{10}/\text{ltr} .$$

5.5.2.3 Measured and Calculated Critical States

The measured critical states for reactors without solid boron and without beam holes are listed in Table 5.5.3, whereby a circle of six cadmium safety rods in the reflector on the radius R = 33 cm had been inserted more or less deeply.

The measured critical states with solid boron and without beam holes are listed in Table 5.5.4. As in Figure 5.5.3, a circle of 6 cadmium rods on R = 33 cm had been inserted more or less deeply into the reflector.

Table 5.5.3 Measured critical reactor states with partially inserted safety rods without solid boron and without beam hole dummies

No.	Boron Concentration C(g B-10/ltr)	Control Rod Position H (cm)	Mean Control Rod Position $\bar{H}$ (cm)	Diff. Rod Reactivity $d\rho/dH$ (pcm/cm)	Position of Safety Rods Z (cm)
1	0.446	61.6	63.0	143 ± 1	221
2	0.446	63.5	65	138 ± 1	191
3	0.446	70.5	72	123 ± 1	171
4	0.446	78.9	81	94 ± 1	161
5	0.469	77.6	79.7	93 ± 1	171
6	0.469	88.5	91.2	78 ± 1	161

Table 5.5.4 Measured critical reactor states with partially inserted safety rods with solid boron and without beam hole dummies

No.	Boron Concentration C(g B-10/ltr)	Control Rod Position H (cm)	Mean Control Rod Position $\bar{H}$ (cm)	Diff. Rod Reactivity $d\rho/dH$ (pcm/cm)	Position of Safety Rods Z (cm)
7	0.214	40.7	41.5	224 ± 3	221
8	0.336	64.1	65.1	167 ± 3	221
9	0.336	64.4	65.4	163 ± 1	201
10	0.336	66.2	67.3	159 ± 4	181
11	0.336	72.8	74.3	133 ± 2	161
12	0.336	82.4	84.5	83 ± 1	151
13	0.306	71.7	72.9	144 ± 3	151
14	0.306	89.8	95.2	35 ± 0.5	141
15	0.231	66.8	67.6	185 ± 1	141
16	0.231	87.1	89.8	62 ± 2	131
17	0.108	59.0	59.7	245 ± 6	131
18	0.108	77.7	78.7	166 ± 2	121
19	0.108	101.8	103.3	30 ± 2	116
20	0.108	98.5	102.4	31 ± 1	116

The critical states for completely inserted safety rods (Z = 71 cm) are listed in Table 5.5.5.

Some of the measured critical states were calculated using the equivalent absorber method. The results are compiled in Table 5.5.6.

Table 5.5.5 Critical reactor states for reactors without solid boron and without beam hole dummies with completely inserted safety rods. (a = 1 Inox rod at Position 2, b = 1 Cd rod at Position 2, c = 6 Cd rods, d = 3 Cd rods at Positions 2, 3 and 6, e = 3 Cd rods at positions 3, 5, and 6 in a reactor with solid boron and beam hole dummies. This reactor was slightly subcritical, k_{eff} = 0.9995.)

No.	Boron Concentration C(g B-10/l)	Control Rod Position H (cm)	Mean Control Rod Pos. $\overline{H}$ (cm)	Diff. Rod Reactivity dρ/dH(pcm/cm)	Pos. of Safety Rods Z (cm)	Safety Rod Reactivity ± 250 pcm (pcm)	Reactor State
21	0.312	55.1		178 ± 5	28.5	4,360	a
22	0.312	63.6		150 ± 12	28.5	5,560	b
23	0.276	55.2		181 ± 2	28.5	5,500	b
24	0.010	60.5	61.5	211 ± 1	41.5	16,800	c
25	0.010	60.5	61.7	202 ± 4	41.5	16,800	c
26	0.010	25.3	26.8	194 ± 3	41.5	10,200	d
27	0.119	44.9	45.8	227 ± 3	41.5	10,020	d
28	0.010	40.2	41.5	242 ± 3	37.0	13,280	d
29	0.119	59.8	60.9	187 ± 2	37.0	12,610	d
30	0.010	55.4	56.8	217 ± 4	33.0	16,020	d
31	0.119	88.2	85.7	91 ± 0.1	33.0	15,870	d
32	0.010	80.8	83.7	104 ± 2	28.5	19,200	d
33	0.010	90.8	93.4	82 ± 1	27.5	20,050	d
34	0.00	103.5	--	--	28.5	14,200	e

Table 5.5.6 Summary of the calculated critical reactors. The numbers correspond to the reactors of Tables 5.5.2, 5.5.3 and 5.5.4.

[Commas should be read as decimal points -- Transl. Note]

No.	4	21	22	25	26	30	32	33	34
Number of rods	6	1	1	6	3	3	3	3	3
Rod position Z (cm)	161	71	71	71	71	71	71	71	71
Rod position R (cm)	33	28,5	28,5	41,5	41,46	33	28,5	27,5	28,5
Boron concentration g B-10/liter in core	0,446	0,312	0,312	0,010	0,010	0,010	0,010	0,010	0,00
Control rod position H (cm)	78,9	55,1	63,6	60,5	25,3	55,4	80,8	90,8	103,5 (k_{eff}=0,9995)
Equiv. Σ_a with control rod (cm^{-1})	-	0,00131	0,0016	0,013505	0,004255	0,006075	0,007915	0,008525	0,005905
Equiv. Σ_a w/o control rod (cm^{-1})	0,01876	0,00131	0,0016	0,014475	0,004255	0,006075	0,009715	0,008525	0,005905
Rod material	Cd	Inox	Cd	Cd	Cd	Cd	Cd	Cd	Cd
Calculated rod reactivity (pcm)	2340	4655	5385	16700	10010	15440	19370	20040	14340
Measured rod reactivity (pcm), accur. $\pm$ 250 pcm)	2060	4360	5560	16800	10200	16020	19200	20050	14200
Calculated k_{eff}	1,0022	-	1,0016	1,0053	1,0076	1,0103	1,0031	1,0042	1,0082

The conversion of the boron concentration difference between the reactor without rods and the reactor with rods to the rod reactivity was based, both for measurement and calculation purposes, on the value determined above of

$$\frac{dg}{dC} = 37\,000 \pm 2000 \text{ pcm/g } B^{10}/\text{ltr}$$

The reactivity of the reactor with beam holes is overestimated by the calculation, since "streaming" is not correctly considered (see 5.3.2). This effect was corrected by 920 pcm. The values in Table 5.5.6 show that reactors with safety rods can be calculated using the equivalent absorber method with the same precision as reactors without rods (see 5.1.1) and thus the calculated reactivity of the safety rods is in good agreement with the measured activity, assuming that the reactivity is defined in the same way, as in the present case, for example, as the difference in boron concentration between two critical reactors with the same control rod position.

5.5.2.4 The Shutdown Reactivity of the Safety Rods

The reactivity that is compensated for by the safety rods in all reactor states shown in Tables 5.5.2, 5.5.3 and 5.5.4 can be determined in two ways:

a) If one compares two reactors, one with and one without safety rods but having the same control rod position ($H_1 = H_2$), then they differ by a difference in boron concentration, the reactivity of which must be exactly equal to the reactivity of the safety rods, since, as mentioned in 5.5.1.1, the boron reactivity is not significantly affected by the presence of the rods.

b) The continuous run method is used to determine the reactivity of the control rod piece H, which differentiates two reactors of the same boron concentration, one with and one without safety rods. Unfortu-

nately the control rod characteristics are strongly affected by the safety rods so that--due to the low number of measuring points--this method can only be used with care. The measurements were carried out for large reactivities, so that an additional uncertainty is added by the imprecise knowledge of the delayed photoneutrons. In order to reduce this error, the group constants determined in 5.11.2 for the delayed neutrons were used in the evaluation. In order to illustrate the dependence of the control rod reactivity on the safety rods, we have plotted in Figure 5.5.2 the differential control rod reactivity as a function of the rod position for different positions of the safety rods. For comparison purposes the curve without safety rods is also given.

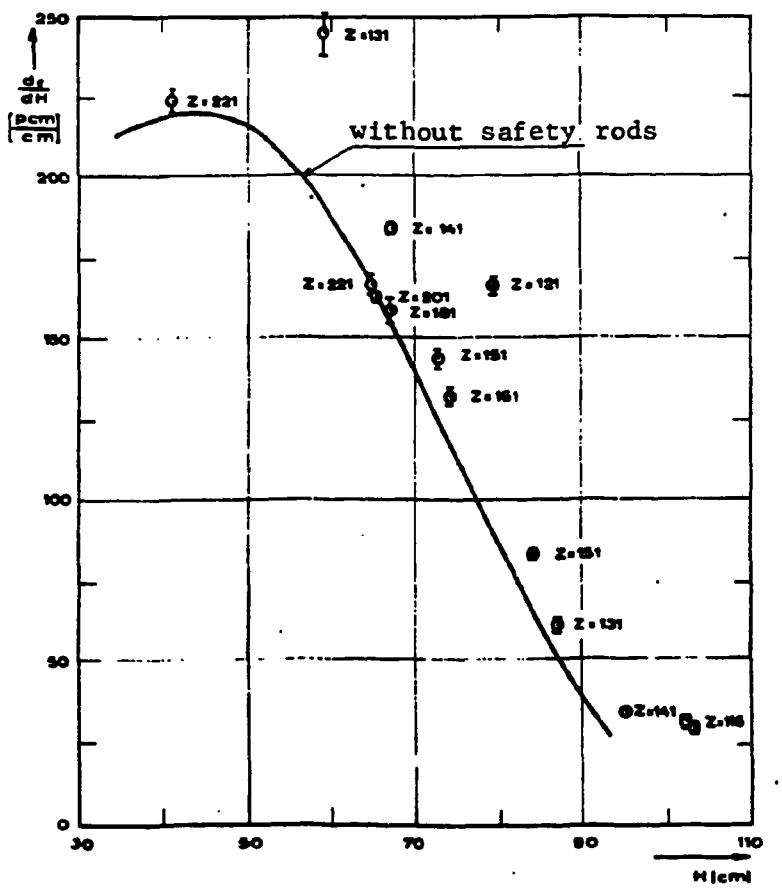

Fig. 5.5.2 Differential control rod reactivity as a function of the control rod position for reactors without solid boron with safety rods on the radius R = 33 cm. The rod insertion depth is in each case Z. The solid like applies to reactors without safety rods.

The reactivity is plotted in Figure 5.5.3 as a function of the axial position for 6 safety rods on the radius R = 33 cm between Z = 220 and 150 cm. The control rod position varies in the measurement involving solid boron between H = 64.1 and 82.4 cm, and in the measurement without solid boron between H = 61.6 and 78.9 cm, whereas the effect of rod position on the result is within the framework of the error limits of ± 3%.

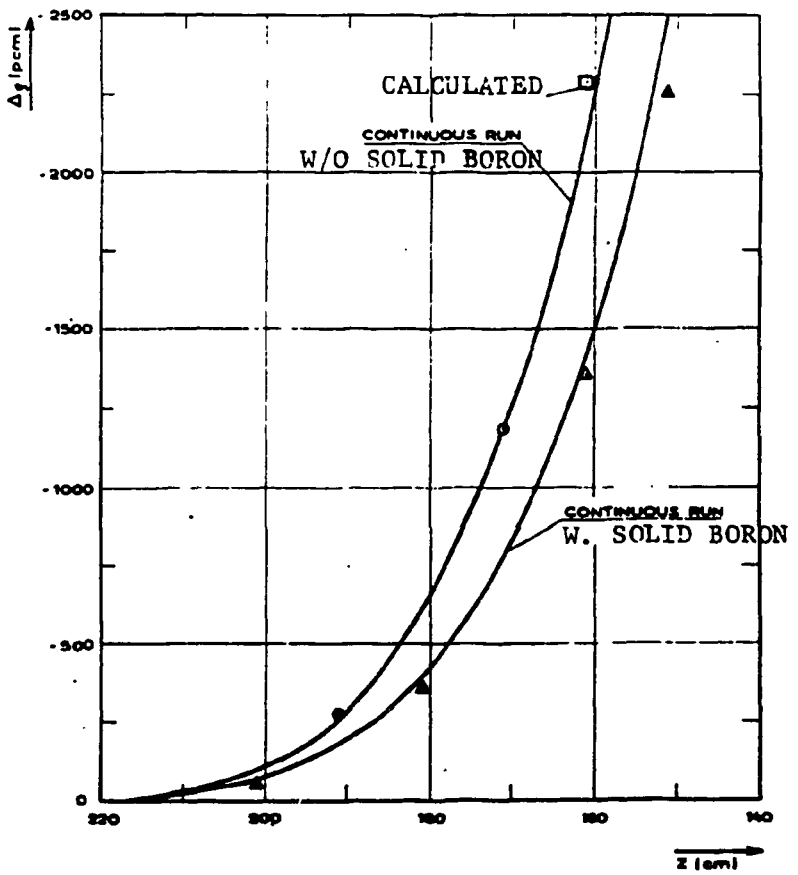

Fig. 5.5.3 Axial reactivity curve for 6 safety rods on the radius R = 33 cm for reactors with and without solid boron. The solid curves indicate the result of continuous run measurement; the points (circles or triangles) are obtained from the difference in the boron concentration of two critical states.

Figure 5.5.4 shows the reactivity of 6 safety rods on R = 33 cm in a reactor with solid boron as a function of their insertion depth. The reactivity was determined using the method described above under a) and also by the continuous run method. From the point where Z > 150 cm it is evident how the position of the control rod affects the reactivity of the

safety rods: the farther the control rod is inserted, the greater the importance of the external reflector becomes and consequently the reactivity of the safety rods also increases.

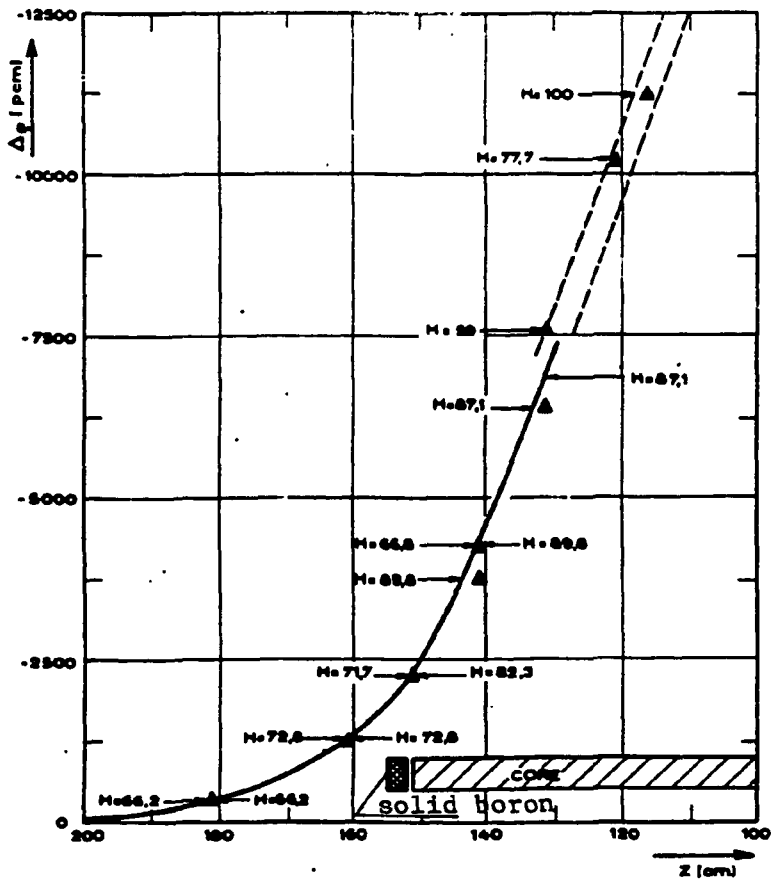

Fig. 5.5.4 Axial reactivity curve for 6 safety rods on R = 33 cm for reactors with solid boron. The solid curve was measured using the continuous run technique. The arrows on the right side of the curve give the control rod position at the beginning of the respective continuous run measurement; the arrow on the left of the curve designate the control rod position at which the different in boron concentration was determined (triangles).

The determination of the reactivity of completely inserted safety rods as a function of the difference in boron concentration using the curves taken from Figure 5.1.2 was done in the same way as described above. The results are listed in Table 5.5.4. For determination of the reactivity of the safety rods using the continuous run method, the characteristics of the

control rod for different rod position radii were measured. They are plotted in Figure 5.5.5. With reference to these characteristics it is possible to determine the reactivity of three safety rods as a function of the radius for different constant control rod positions. These curves are plotted in Figure 5.5.6, along with the values determined by way of boron concentration.

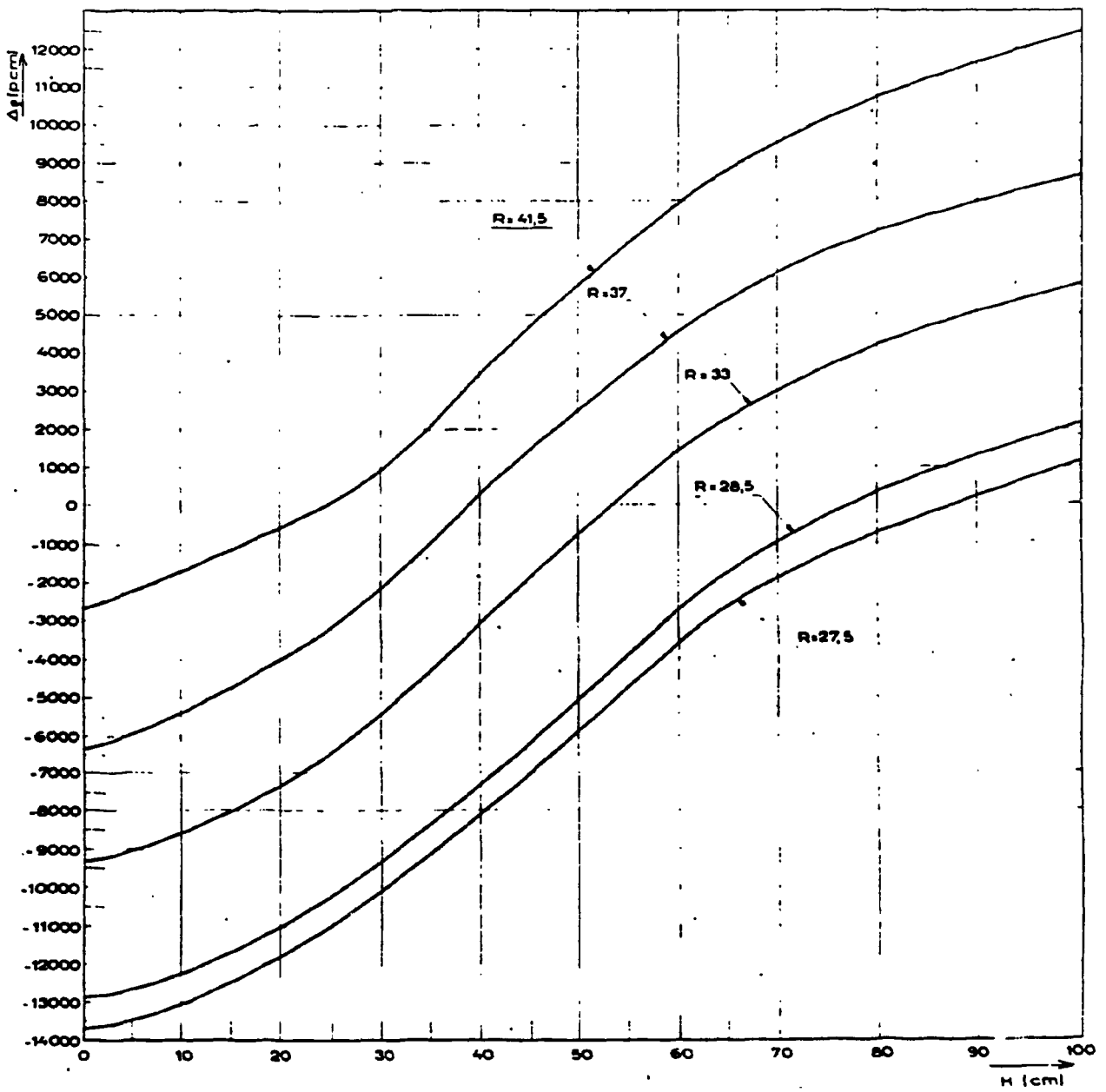

Fig. 5.5.5 Reactivity characteristics of the control rod for the reactor without solid boron with 3 safety rods at Z = 71 for different position radii R

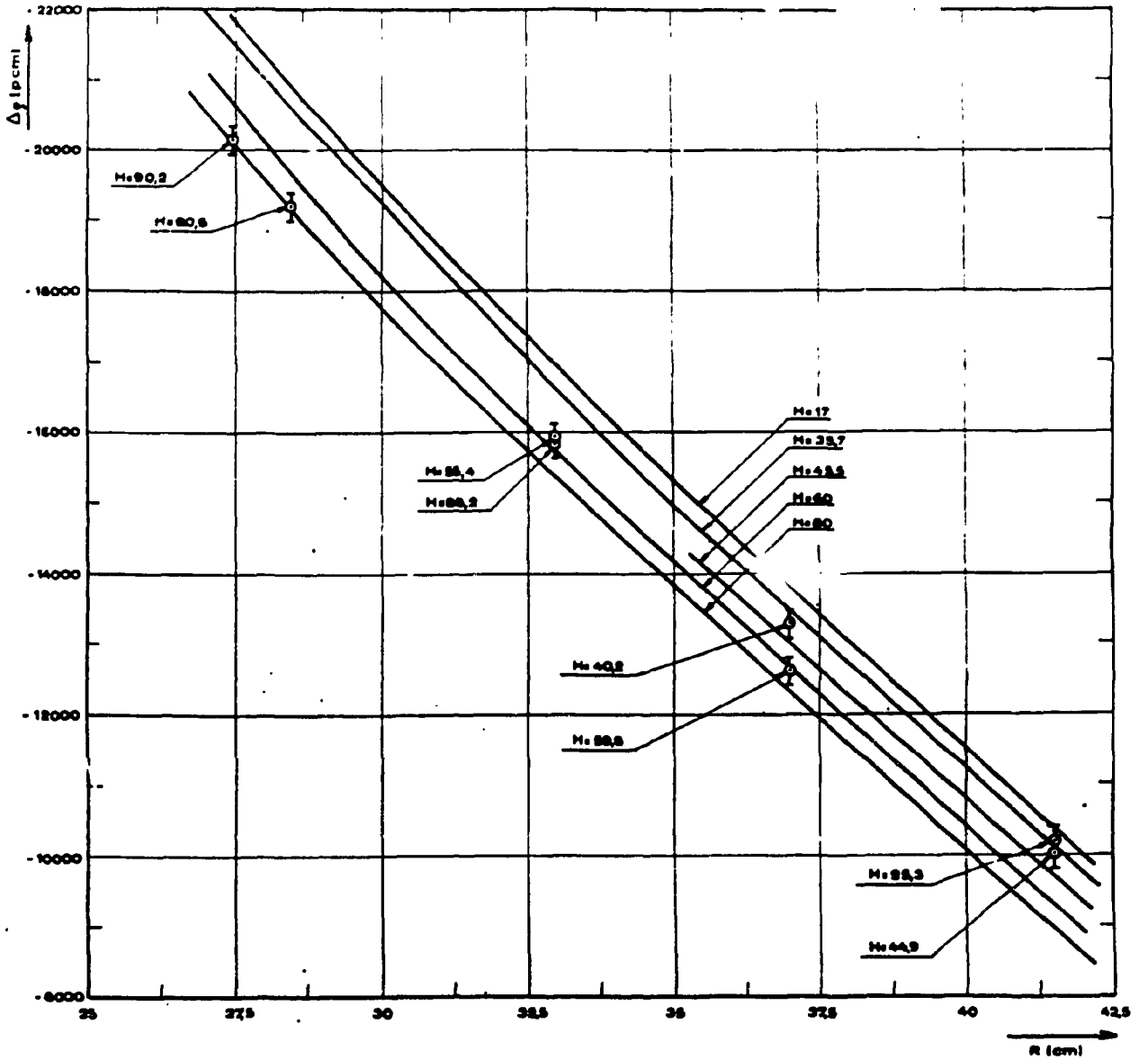

Fig. 5.5.6 Radial characteristics of three completely inserted safety rods in a reactor without solid boron for different control rod positions H. The solid curves were determine by the continuous run technique, and the points are taken from Table 5.5.5.

5.5.3 Comparison of the Reactivity of a Ag-In-Cd Plate and a Cd Plate

In order to investigate the effect of a change in the absorber material of the safety rods, the reactivity of a cadmium plate was compared with a plate made of 80% Ag, 15% In and 5% Cd. The plate had the following dimensions:

Ag-In-Cd	59.6 x 6.2 x 0.31 cm
Cd	59.7 x 6.29 x 0.16 cm.

The Cd plate was clad with 0.05 cm Inox sheet. The plates were suspended vertically in the reflector and symmetrically with the core midplane so that the wide side was both a tangent to the position circle and parallel to the radius. The position radius relates to the vertical plate axis. The measurement results based on the stable period method are listed in Table 5.5.7.

Table 5.5.7 Reactivity of the Ag-In-Cd and Cd plates for different positions

Position	Radius (cm)	Reaktivity	
		Ag-In-Cd (pcm)	Cd (pcm)
tangential	24	- 3190 ± 80	- 2900 ± 30
tangential	28.46	- 2715 ± 14	- 2660 ± 75
tangential	70	- 213 ± 4	- 190 ± 5
radial	31.56	- 2500	- 2360 ± 14

The reactivity of the Ag-In-Cd plate is therefore somewhat greater (5-10%) than the reactivity of the Cd plate.

5.5.4 The Thermal Neutron Flux on the Surface of the Safety Rods

In order to be able to determine the burnup behavior of the safety rods, it is necessary to know the neutron flux on the rod surface when the rods are in their top rest position. The flux was measured on the rod side facing the core and the rod side facing away from the core. The six safety rods were positioned at R = 33 and Z = 181 or 161 cm, the boron poisoning was 0.34 g B-10/liter, the control rod was positioned at H = 63.3 cm for Z = 181 cm and at H = 68.5 cm for Z = 161 cm.

The measured values normalized to 1 watt reactor power are plotted in Figure 5.5.7.

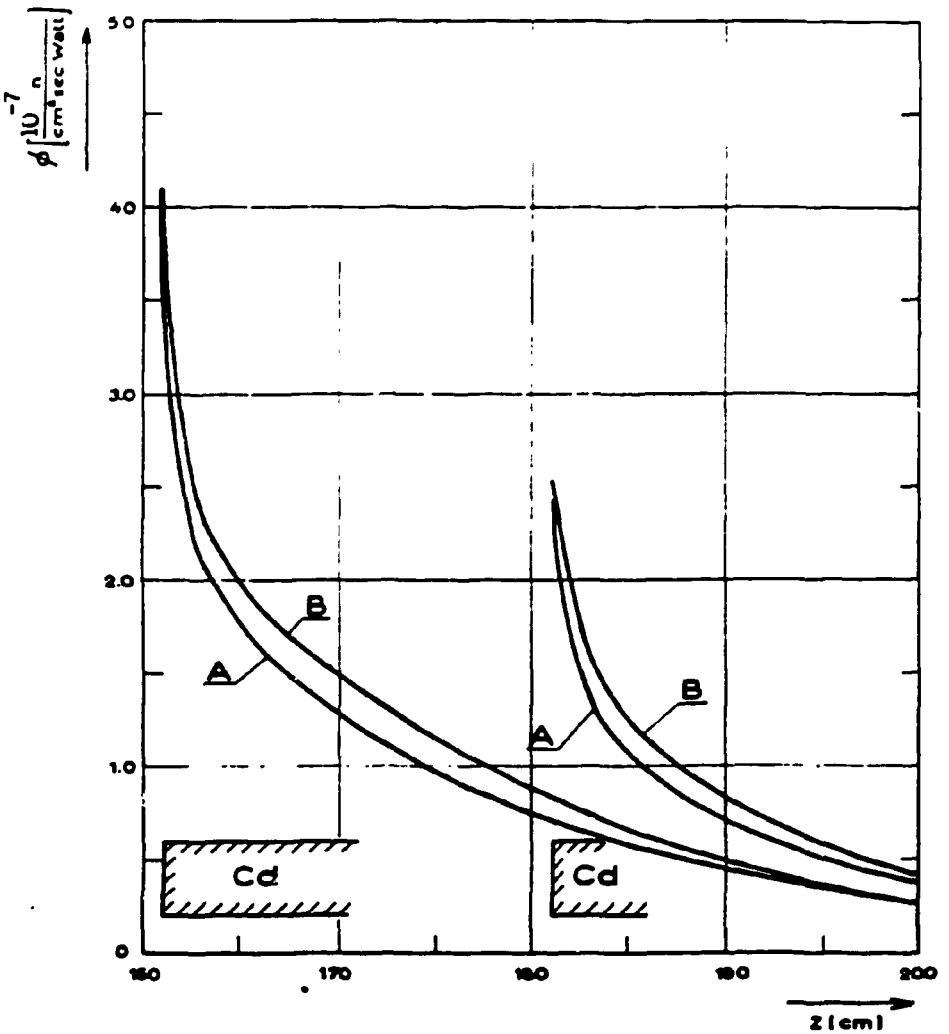

Fig. 5.5.7 Axial distribution of the thermal flux on the surface of the safety rods for the position R = 33, Z = 161 and Z = 181. A on the side facing the core, B on the side facing away from the core, reactor power 1 watt.

5.6 Temperature Coefficient

5.6.1 State of the Reactor

The dependence of reactivity on the temperature of the moderator and reflector was investigated in State 2, i.e., with boron zones and without channels. The boron poisoning was 0.252 g B-10/liter, and the control rod was inserted about halfway.

See 2.1.3 with regard to the heating and cooling loops.

5.6.2 Measurement of Temperature and Reactivity

The temperature was measured in the reflector using four resistance thermometers and one thermocouple, which were mounted in the core midplane so that they were azimuthally distributed to the radii 33.5, 47.5 and 99.5 cm. In the core the temperature was measured using two thermocouples, one each in the upper and lower halves, and also two thermocouples in the stack, which were located in the flux trap at the height of the upper core half.

Measurement of the voltage supplied by the thermometers was done by way of a measuring bridge, which permitted an accuracy of temperature measurement at the thermometer location of $\pm$ 0.1°C. The temperatures used for evaluation are in each case the mean value of the values measured at the various locations within the reflector, core and stack. The deviation of a single value from the mean was never more than $\pm$ 0.2°C during the entire measurement, from which we can deduce a very flat temperature distribution, at least in the reflector.

The reactivity difference $\Delta\rho$ corresponding to a temperature difference ΔT was determined from the respective position of the control rod or the fine control rod, which were operated so that the existing steady state was maintained.

Since the automatic system had failed at the beginning of the measurement, the reactor had to be kept critical manually by observing the flux recorded, whereby the critical state was accurately determined to a maximum of $\pm$ 5 pcm. For control purposes the reactivity difference from the reference state at 20°C was precisely determined from time to time by means of a period measurement.

The test was carried out in three segments. In the first period the reflector was heated from 20 to 60°C. Since the heating rate was low, about 2.7 °C/h, and since there was not thermal insulation between the reflector and the core, a uniform temperature distribution was guaranteed. From this test it was possible therefore to determine a "global" temperature coefficient.

In a second test period the reflector was cooled down from 60 to 40°C. The temperature change over time was about -6°C/h, and the difference between core, stack and reflector temperatures was greater than during the first period, but not so great that a separation of core and reflector temperature coefficients would have been possible.

Finally in the third test period the attempt was made to achieve greater temperature differences between the core and reflector by heating the reflector and cooling the stack, in order to be able to determine the temperature coefficients of these components individually. The phase of this test that is best suited for this project is shown in Figure 5.6.1. Here, too, the temperature difference at the sensors located within a component at different points was no greater than 0.2°C, so that it can be assumed that the temperature gradient on the interface between the stack and reflector, for example, was steep and that the mean temperature for a component was measured accurately to within $\pm$ 0.2°C.

5.6.3 Evaluation and Results

5.6.3.1 Consideration of Boron Poisoning

The D_2O in the core that expands during heating rose into a ventilation pipe that led upward from the core barrel through the stack. In the process the concentration of the dissolved boron also decreased to the same extent as the density of the D_2O. At the same time the expansion of the structural material in the core brought about displacement of boron solution. Both effects lead to a change in the amount of boron dissolved in the core and to a positive contribution to the temperature coefficient. Likewise, the increase in the D_2O level in the reflector, which is established when the reflector is heated, must also be taken into account in the evaluation.

If γ denotes the temperature coefficient $d\rho/dT$, and the subscripts C, K, R represent the core, stack and reflector, C the boron concentration, α and β the spatial expansion coefficient of D_2O and Al, respectively, and if ε stands for the effect of the D_2O level in the reflector, then

$$\gamma = \gamma_C + \gamma_K + \gamma_R - \frac{\partial \rho}{\partial C} (\alpha + {}^2/_3 \beta \cdot f) \cdot C - \varepsilon$$

or

$$\partial\rho \left(1 + \frac{\alpha + {}^2/_3 \beta \cdot f}{\partial C} \cdot C \cdot \partial T_C + \varepsilon \cdot \frac{\partial T_R}{\partial \rho}\right) = \gamma_C \partial T_C + \gamma_K \partial T_K + \gamma_R \partial T_R \quad . \qquad (5.6.1)$$

where f stands for the metal/water ratio in the core:

$$f = 0.706.$$

ε, which represents the variation in reactivity brought about by the variation in the D_2O level H_R in the reflector, was measured. The result obtained was

$$\varepsilon = \frac{\partial \rho}{\partial H_R} \cdot \frac{\partial H_R}{\partial T_R} = 0{,}67 \cdot \frac{\partial H_R}{\partial T_R} \text{ pcm/}^{\circ}\text{C} \quad . \qquad (5.6.2)$$

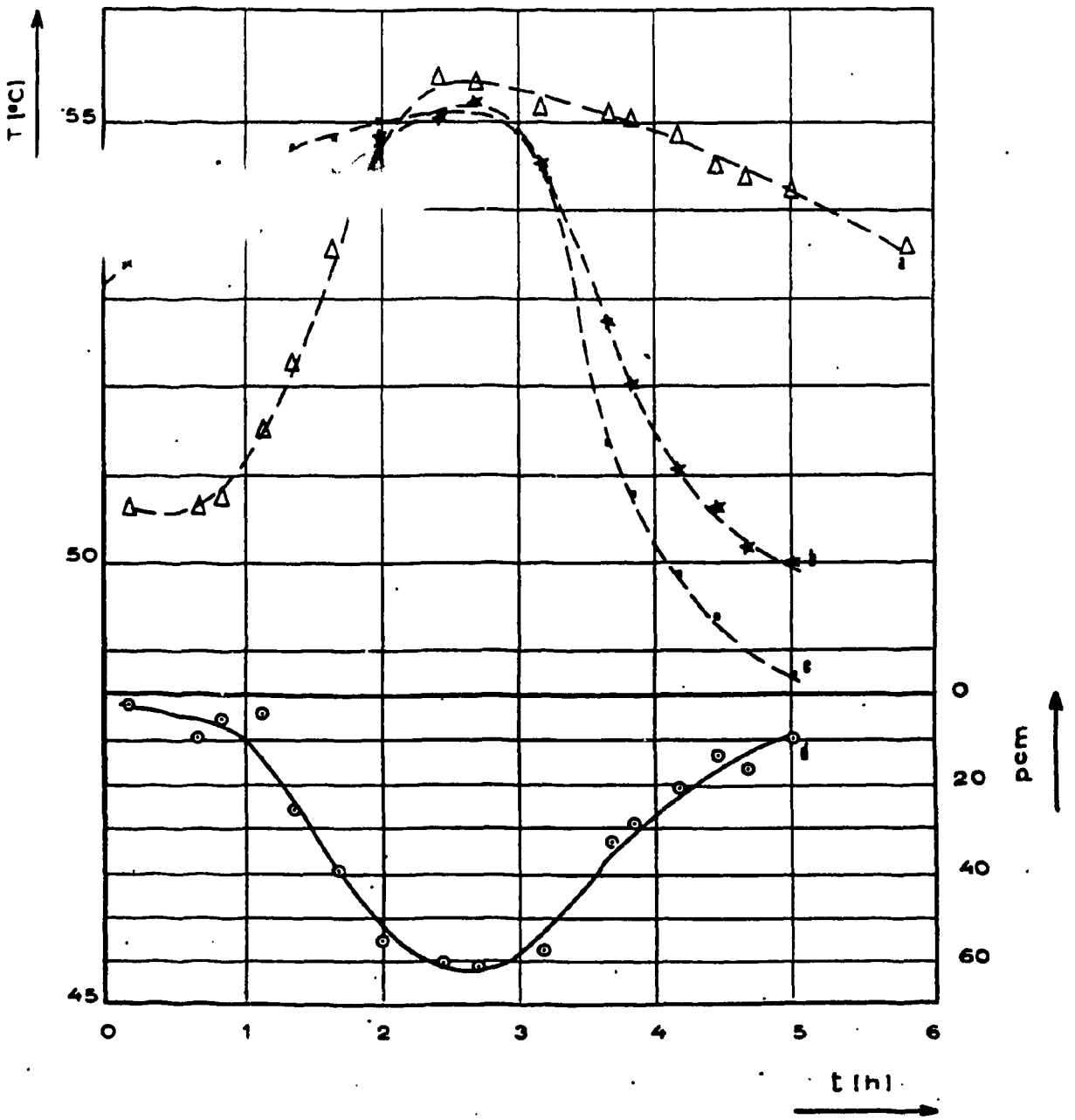

Fig. 5.6.1 Temperature and reactivity curve of the reactor during measurement of the temperature coefficient: a = reflector temperature, b = core temperature, c = reflector temperature, d = reactivity curve.

The function $\partial H_R/\partial T_R$ was obtained as

$$\frac{\partial H_R}{\partial T_R} \approx 2 \cdot 10^3 \cdot \alpha(T_R) \ . \qquad (5.6.3)$$

For calculating $\alpha(T)$, the following formula was used:

$$\alpha(T) = -1.2248 \cdot 10^{-4} + 1.4756 \cdot 10^{-5} T - 7.1391 \cdot 10^{-8} T^2 + 1.71 \cdot 10^{-10} T^3 \qquad (5.6.4)$$

where T is in $^{\circ}C$.

In addition,

$$\beta = 7.1 \cdot 10^{-5} \ ,$$

$$\frac{\partial \rho}{\partial C} = 39.2 \text{ pcm/mg/ltr } D_2O \ .$$

5.6.3.2 Global Temperature Coefficient

The reactivity of the reactor critical at $20^{\circ}C$, corrected according to (5.6.1), is plotted in Figure 5.6.2 against the temperature for the first test period; the temperature is identical in the core, stack and reflector (Curve a). For comparison purposes the reciprocal of density D of the D_2O (Curve e), normalized at $20^{\circ}C$, is also given. It is found that in the temperature range indicated the following is true in good approximation:

$$\rho(T) - \rho(20) \approx -4 \cdot 10^4 \left(\frac{D(20)}{D(T)} - 1 \right) \text{ pcm} \ . \qquad (5.6.5)$$

The slope of Curve a, i.e., the global temperature coefficient, is plotted in Figure 5.6.3 (Curve a') against temperature. In accordance with (5.6.5), the following also applies here in good approximation

$$\gamma = \frac{d\rho}{dT} \approx -4 \cdot 10^4 \, \alpha \cdot \frac{D(20)}{D^2(T)} \qquad (5.6.6)$$

$$\approx -4.4 \cdot 10^4 \cdot \frac{\alpha(T)}{D^2(T)} \text{ pcm}/^{\circ}C \ .$$

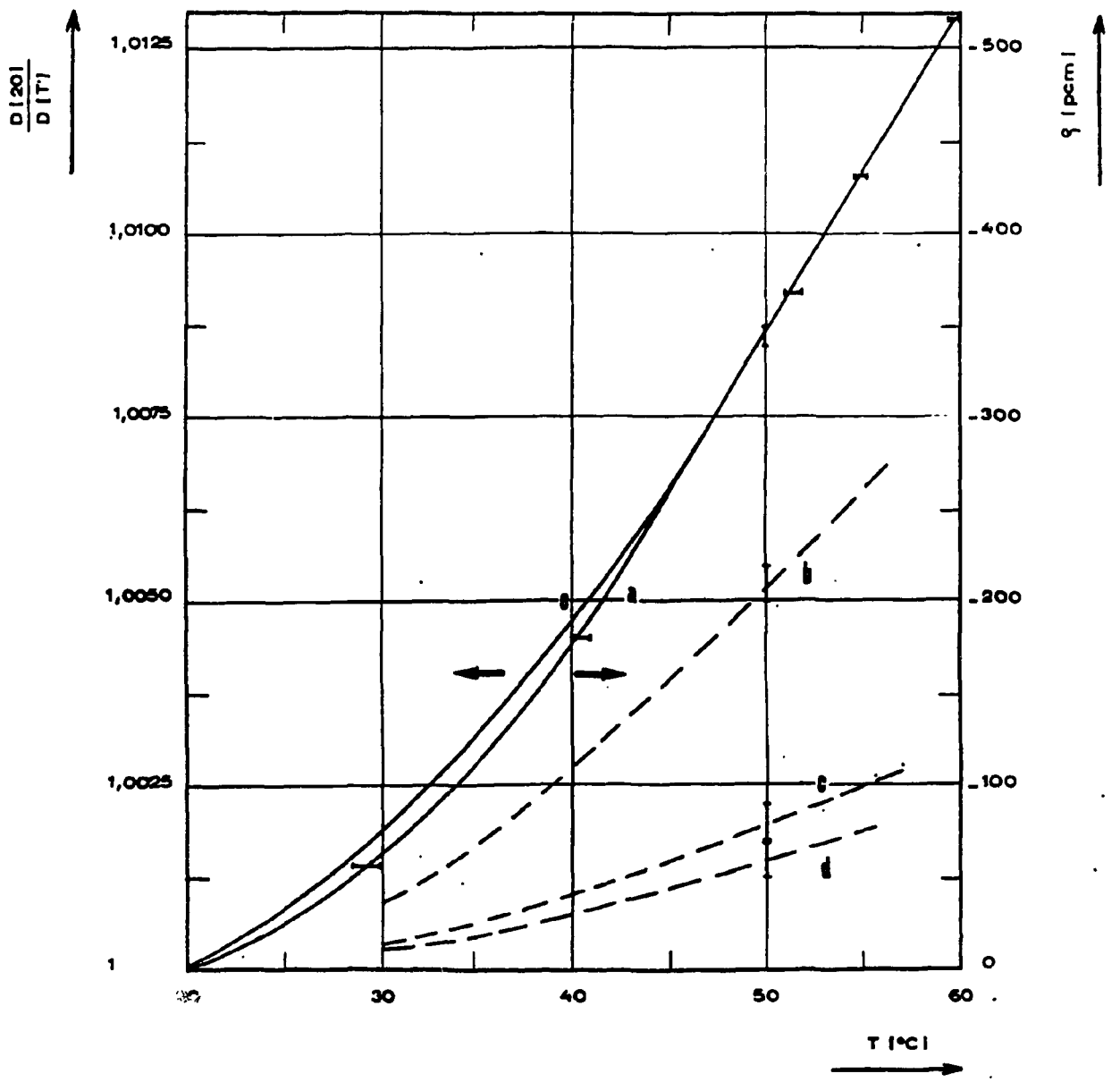

Fig. 5.6.2 a = reactivity of the reactor during heating, normalized to ρ = 0 at 20°C; b = reactivity due to heating of the reflector; c = reactivity due to heating of the core; d = reactivity due to heating of the stack; e = reciprocal of D_2O density as a function of temperature.

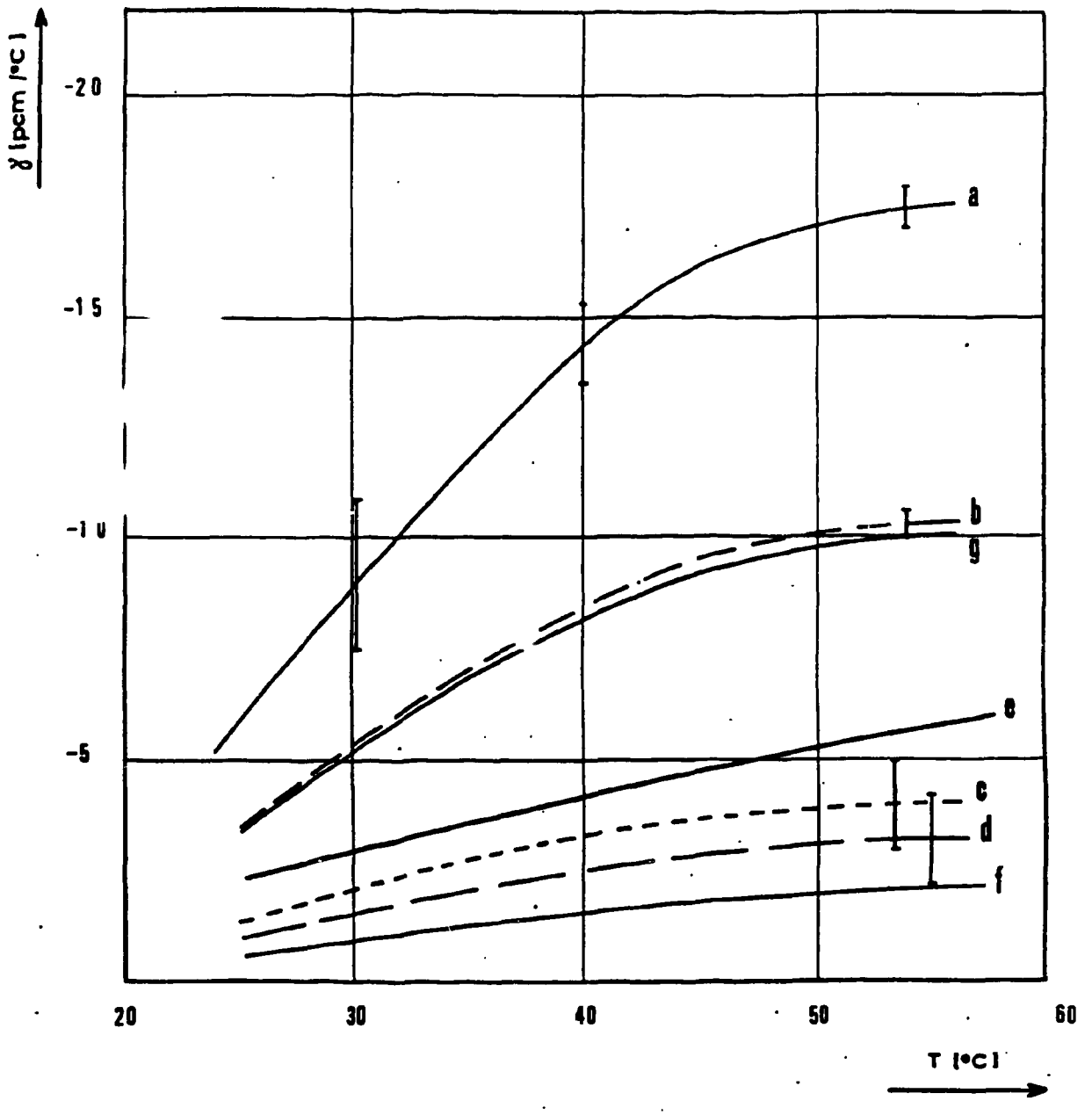

Fig. 5.6.3 Curve of the temperature coefficient $\gamma = \partial\rho/\partial T$ as a function of temperature; a = global measured temperature coefficient; b = measured temperature coefficient of the reflector; c = measured temperature coefficient of the core; d = measured temperature coefficient of the stack; e = calculated temperature coefficient of the core; f = calculated temperature coefficient of the stack; g = calculated temperature coefficient of the reflector.

A global temperature coefficient measured at the beginning of the FOEHN experiment between 20 and 25°C (poisoning = 44.5 mg/liter) had yielded: $\gamma(22) \simeq -1.5 \pm 1$ pcm/°C. This value agrees within the limits of error with the value given by an extrapolation of Curve a in Figure 5.6.3.

The measurement results from the second period will not be given here in detail. There, too, only determination of the global temperature coefficient was possible, which agrees with that obtained in the first period within the limits of error.

5.6.3.3 Temperature Coefficients for Core, Stack and Reflector

The third test period lasted 12 hours; however, only the measuring points shown in Figure 5.6.1 are suitable for evaluation. Due to the lack of thermal insulation between core, stack and reflector, the temperatures of the individual components were more or less parallel, so that the temperature differences ΔT between two measuring points separated by time do not differ significantly from the differences in another component. Thus the coefficients γ_C, γ_K, and γ_R in Equation (5.6.1) can only be determined very imprecisely.

Evaluation of the test phase shown in Figure 5.6.1 yielded the following values for the temperature coefficients in the core, stack and reflector:

$$\begin{aligned} \gamma_C &= -4 \pm 1 && \text{pcm/°C} \\ \gamma_K &= -3.2 \pm 1 && \text{pcm/°C} \quad \text{for} \quad 50 \leq T \leq 55\,^{\circ}\text{C} . \\ \gamma_R &= -10.3 \pm 0.3 && \text{pcm/°C} \end{aligned} \tag{5.6.7}$$

The reactivity calculated with these temperature coefficients is also plotted in Figure 5.6.1 as a solid line, Curve d. It reproduces well the measured reactivity curve.

Under the assumption that the breakdown of the global temperature coefficient in a ratio of 4 : 3.2 : 10.3 for the core, stack and reflector can be carried out independently of temperature, the individual temperature

coefficients are also given in Figure 5.6.3 as a function of temperature (Curves b, c, d), and Figure 5.6.2 shows the reactivity that must be applied in each case with respect to the cold state at 20°C.

The effect of dilution of D_2O in the core of 10%, which was calculated by a diffusion calculation, yields a temperature coefficient in the core that lies somewhat outside the limits of error of the measured temperature coefficient: see Figure 5.6.3, Curve e. This discrepancy may be explained by the fact that the reactivity is not exactly inversely proportional to the density of the D_2O, so that the extrapolation of a 10% dilution to a dilution of about 1%, as exists in reality, leads to inaccurate values.

5.6.4 Calculation of the Temperature Coefficients

For calculating the temperature coefficient in the core it was assumed that it is caused only be a dilution of the D_2O and that changes in the core dimensions or changes in the neutron spectrum have no effect. This assumption is also justified when the density variations are slight and when the fissile material and parasitic absorber have approximately the same effective cross section curve, i.e., when resonance effects of one or the other play a subordinate role. The temperature coefficient in the core was determined using a diffusion calculation in which the D_2O in the core was diluted by 10%. This void effect was obtained as $\partial\rho/\partial V = 0.427$ pcm/cm^3 void. Thus we obtain the temperature coefficient for the core:

$$\gamma_C = \left(\frac{\partial\rho}{\partial T}\right)_C = \left(\frac{\partial V}{\partial T}\right)_C \cdot \frac{\partial\rho}{\partial V}$$

$$= (\alpha + {}^2/_3\,\beta \cdot F)\, V_{D_2O} \cdot \frac{\partial\rho}{\partial V} \qquad (5.6.7)$$

where α is according to (5.6.4) and

$$V_{D2O} = 27{,}000 \text{ cm}^3,$$

and thus we obtain in the range between 50 and 55°C

$$\gamma_C(\text{calculation}) = -5.5 \text{ pcm/}^\circ\text{C}.$$

The curve of the calculated value γ_C is shown in Figure 5.6.3 as Curve e. For the temperature coefficient in the stack and reflector it was assumed that

$$\frac{\partial \rho}{\partial T} = \left(\frac{\partial \rho}{\partial T}\right)_{\text{density}} + \left(\frac{\partial \rho}{\partial T}\right)_{\Sigma_a} + \left(\frac{\partial \rho}{\partial T}\right)_{\Sigma_s} , \qquad (5.6.8)$$

whereby the variation in the absorption cross section and the scattering cross section, respectively, were assumed as follows:

$$\Sigma_a = \Sigma_{a,o} \cdot \sqrt{\frac{T_o}{T}}$$

$$\Sigma_s = \Sigma_{s,o} \cdot \left(\frac{T_o}{T}\right)^{0.1}$$

These two effects were determined by diffusion calculations in which first the absorption cross section and then the diffusion coefficient of the D_2O were varied. The result was

$$\left(\frac{\partial \rho}{\partial T}\right)_{\Sigma_a} = +2.05 \text{ pcm/}^\circ\text{C}$$

$$\left(\frac{\partial \rho}{\partial T}\right)_{D} = -1.81 \text{ pcm/}^\circ\text{C} .$$

The effects are therefore opposite and of practically the same magnitude. The density coefficient $(\partial\rho/\partial T)_{\text{density}}$ was calculated with approximately a 1% D_2O dilution in the reflector and stack. Thus we obtain in the range T = 50-55°C:

$$\gamma_R = -10.0 \text{ pcm/}^\circ\text{C}$$

$$\gamma_K = -2.1 \text{ pcm/}^\circ\text{C}.$$

The development of γ_C, γ_K and γ_R is also plotted in Figure 5.6.3 as Curves e, f and g.

The global temperature coefficient between 50 and 55°C is thus obtained from the sum of the three single coefficients:

$$\gamma = \gamma_C + \gamma_R + \gamma_K = -17.6 \text{ pcm/}^{\circ}\text{C} .$$

This value agrees well with the measured values, and also the temperature coefficient for the reflector, whereas for core and stack there were differences. However, those differences are opposite and therefore cancel one another out.

5.7 The Void Coefficient in the Core

For reasons of safety theory it is useful to know what reactivity amount is consumed if all the D_2O in the core evaporates. Since this case cannot be treated by means of the computational methods used in this research, a measurement was carried out. Two critical states of a reactor without beam hole dummies and with solid boron zones were compared.

Boron Concentration C (g B-10/liter)	Control Rod H (cm)
0.211	50.3
empty core	53.2

The rod position H = 53.2 cm would correspond to a boron concentration of 0.227 g B-10/liter (where $d\rho/dC$ = 37,550 pcm/g), i.e., the void is equivalent to 0.227 g B-10/liter. Unfortunately, the boron value between 0 and 0.25 g B-10/liter could not be measured.

It was therefore assumed that the calculated value in this region involves the same error as between 0.25 and 0.55 g B-10/liter, i.e., that it is 3% higher than the value that was measured by the stable period method. Using the results from Table 5.2.2 we obtain the boron value of

$$\frac{d\rho}{dC} = 40\,500 \text{ pcm/g } B^{10}\text{.ltr} .$$

Thus the reactivity that is consumed when the D_2O in the core is removed is

$$\Delta\rho_{Void} = -9200 \text{ pcm.}$$

5.8 The Reactivity Effect of Aluminum in the D_2O Reflector and the Tank Effect

The reactivity effect of aluminum in the reflector was measured by means of a plate between the radii R = 65.0 and 80 cm and by means of a cylinder between the radii R = 23 and 65 cm. Plate and cylinder were suspended during the measurement so that they were vertical and symmetric to the core midplane. The had the following dimensions:

Plate:	height	50	cm
	width	20	cm
	thickness	1	cm
	volume	1000	cm^3
Cylinder:	height	50	cm
	diameter	2.5	cm
	volume	245	cm^3.

The test was carried out on a core with solid boron and without beam hole dummies. The boron concentration in the core was 0.252 g B-10/liter, and the control rod was positioned at H = 45.8 cm. The reactivity of the aluminum was determined by the stable period measurement technique.

The measurement results are listed in Table 5.8.1.

Table 5.8.1 Aluminum reactivity in the reflector

Position of Al Specimen (cm)	Specimen Reactivity (pcm)	Aluminum Effect (pcm/cm^3)
cylinder R = 23	- 93	0.38 ± 0.012
cylinder R = 35	- 93	0.38 ± 0.012
cylinder R = 50	- 41	0.17 ± 0.012
cylinder R = 65	- 14	0.057 ± 0.012
plate R = 65	- 72	0.072 ± 0.003
plate R = 80	- 24	0.024 ± 0.003

When the Al effect was calculated, the Al cylinder or plate was replaced by an annular zone having a height of 50 cm and symmetrical to the core midplane in which Al and D_2O were homogenized in equal volume fractions. The width of the zone was selected so that it brought about the same local flux perturbation as the Al cylinder or plate. Figure 5.8.1 shows the Al effect in the reflector midplane as a function of the radius. The measurement error is assumed to be $\pm$ 3 pcm.

A thickening of the aluminum tank around the core was simulated by a 0.1 cm thick Al sheet, which was placed around the core barrel symmetrical to the midplane. The height of the sheet was 104.4 cm and its total volume was 1300 cm^3. The reactivity effect was measured as

$$\Delta\rho = - 216 \text{ pcm.}$$

5.9 Gamma Heating

The energy transferred to the structural material by gamma radiation was measured for three reactor states. The use of glass dosimeters (see 4.1.4.1) permitted a large number of measuring points. A number of monitor glass monitors were also irradiated at reference positions close to the core in order to check the reproducibility of the measurements. Power calibration was done in each case using Mn probes at evenly distributed standard positions.

The given measurement errors are essentially caused by the errors in power calibration and by the lack of knowledge about sensitivity to thermal neutrons.

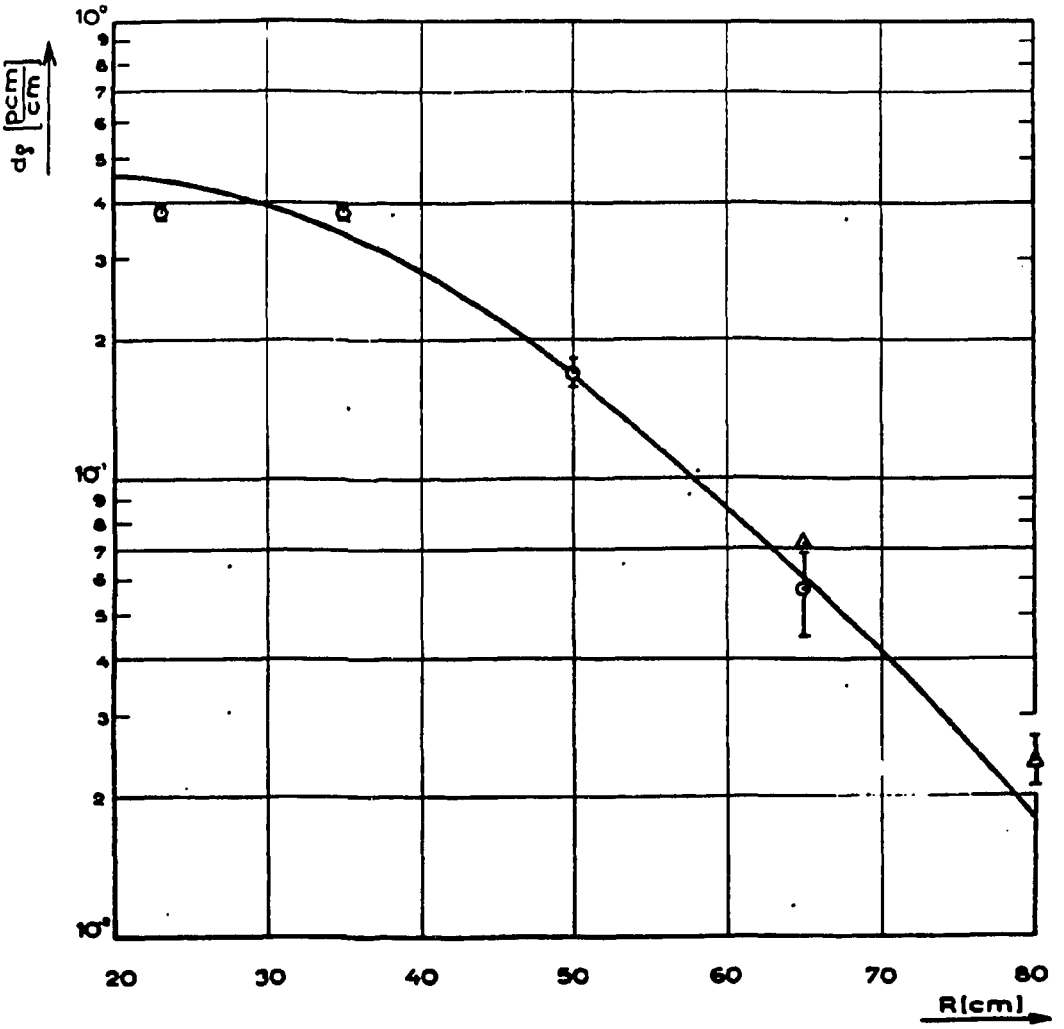

Fig. 5.8.1 Aluminum reactivity in the reflector midplane as a function of the radius. The circles are the values measured with the Al cylinder, and the triangles are values measured with the plate; the solid curve was calculated.

5.9.1 Reactor without Solid Boron and Without Reflector Internals

In this test the gamma flux adjacent to the core was measured in the external reflector and on the core midplane extending to the outer tank wall. At the same time several points in this configuration were measured with an ionization chamber, which yields values that are in satisfactory agreement with those obtained by the glass dosimeters. The results are plotted in Figures 5.9.1 and 5.9.2. As in the following the values are referenced to a reactor power of 1 watt. The reactor power during one-hour irradiation

was 30.7 ± 1.1 watt. Figure 5.9.2 shows not only the heating power due to gamma radiation but also the dose converted to W/g that is generated by thermal neutrons in the glass dosimeters.

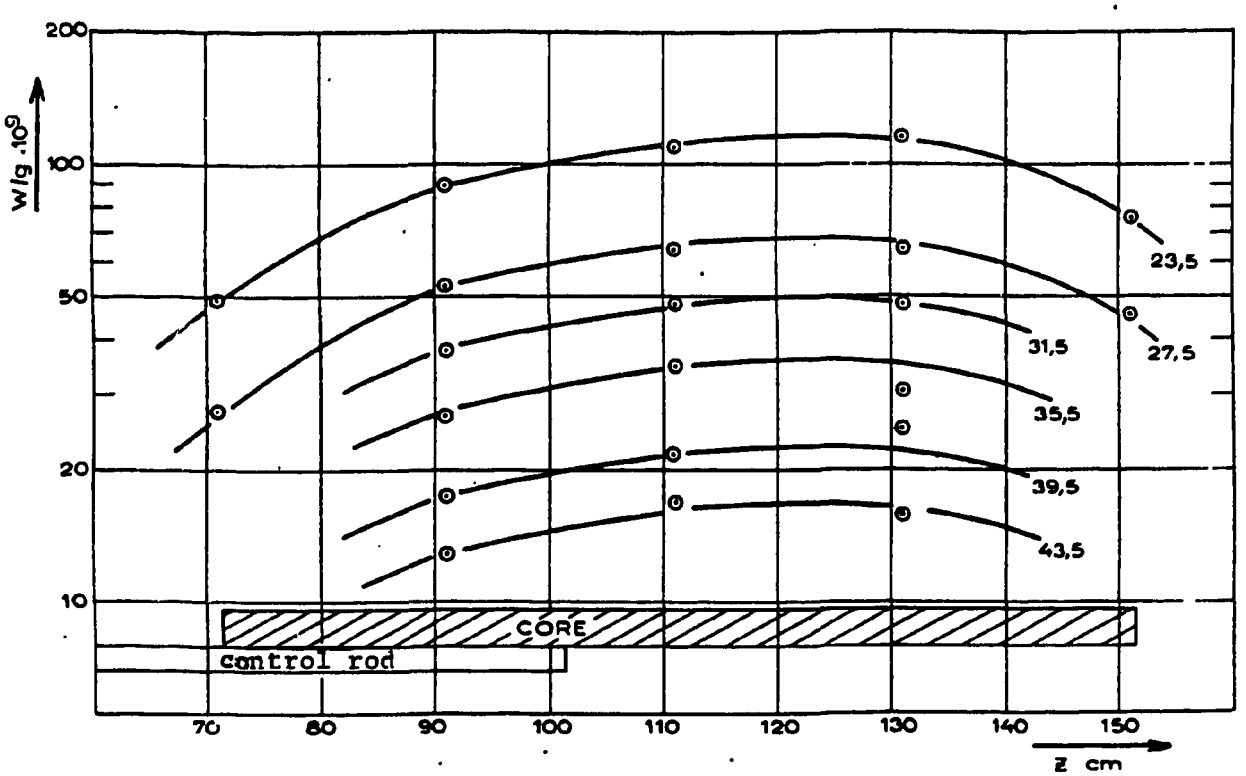

Fig. 5.9.1 Gamma heating in the reflector, measured with glass dosimeters. The parameter is the distance from the core axis z. Configuration without beam holes, without solid boron. Reactor power = 1 watt.

5.9.2 Reactor with Solid Boron and with One Channel (No. 4)

In this test the gamma dose on the axis of the exiting beam hole in the position given in Figure 5.9.3 was investigated. Figure 5.9.3 shows the measured values (Curve a). The comparison with the curve for the unperturbed gamma flux, which is also plotted (Curve b, taken from Figure 5.9.2), shows that if a channel is present the gamma dose increases considerably in the vicinity of the channel and especially in the beam hole itself. This is due both to a basic beam hole effect (displacement of

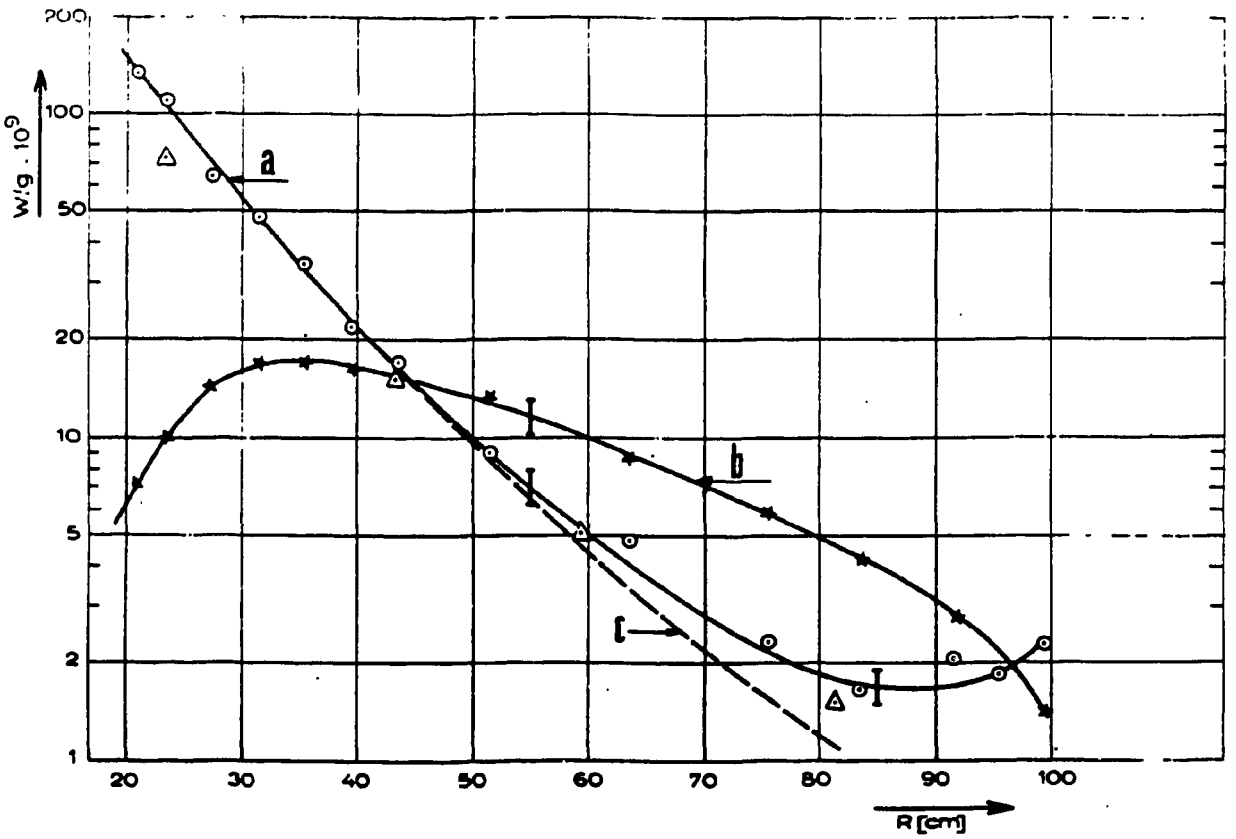

Fig. 5.9.2 Gamma heating in the reflector, measured with glass dosimeters and an ionization chamber in the midplane of the core at z = 110 cm. Curve a designates the detected dose from gamma radiation, Curve b the dose generated by activation from thermal neutrons. The triangles represent the measuring points for the ionization chamber, and the broken line, Curve c, the theoretical values. Configuration without beam holes, without solid boron; for control rod position see Figure 5.9.1. Reactor power = 1 watt.

absorber between source and detector) and to the gamma radiation of the activated structural material of the channel. It appears that the second effect predominates. Unfortunately the measurement is not accurate enough to be able to separate the two effects.

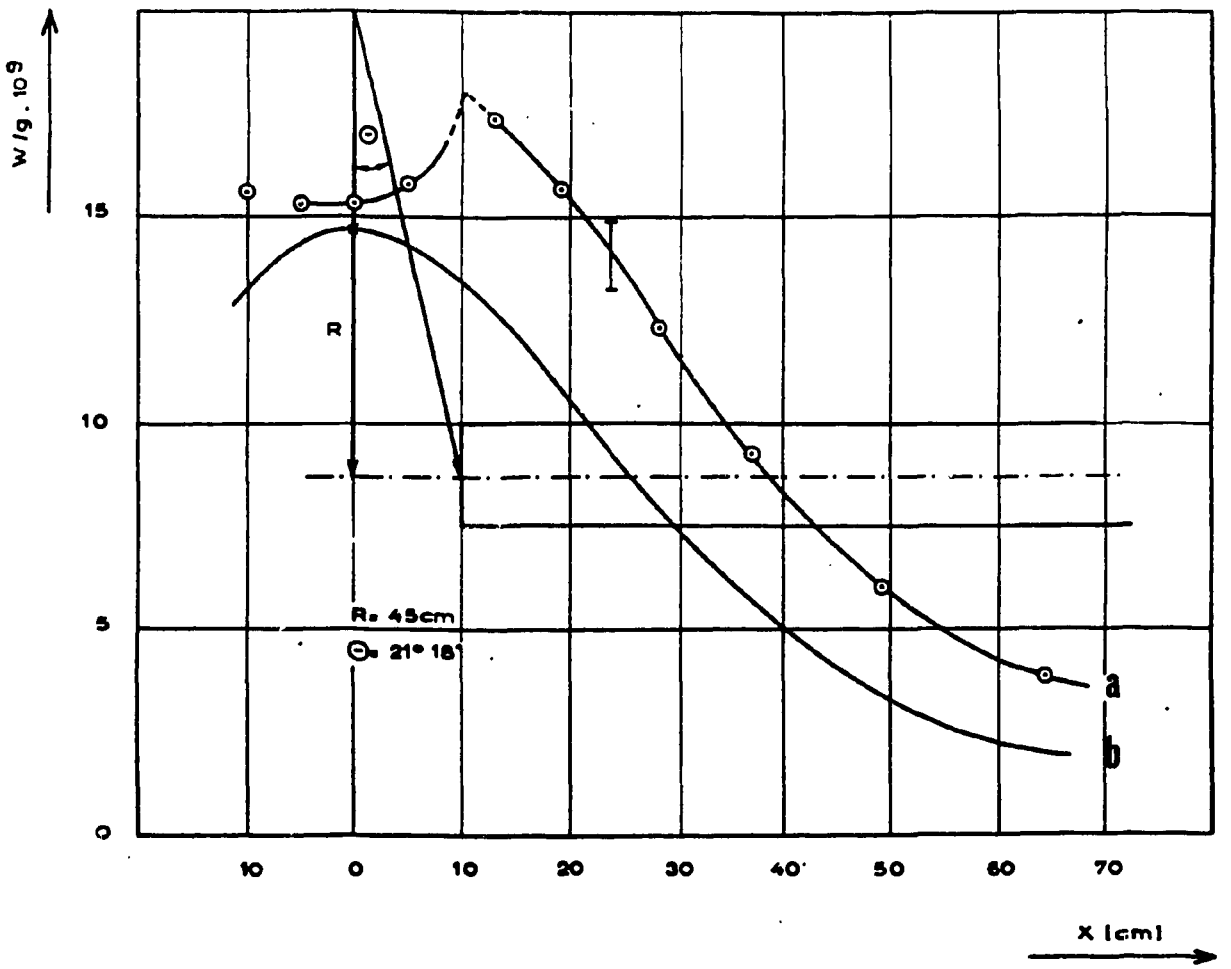

Fig. 5.9.3 Curve a: gamma heating on the axis of the exiting beam hole, measured with glass dosimeters. Curve b: gamma heating on the same axis without beam hole. The location of the channel corresponds to Position b in Figure 5.4.7. Configuration: one beam hole and solid boron on the core ends. Reactor power = 1 watt.

5.9.3 Reactor with All Internals; Gamma Dose in the Cold and Hot Sources

The gamma dose in the cold source was measured on its longitudinal axis at a distance R = 70 cm from the core axis. The measured values are plotted in Figure 5.9.4. For technical reasons it was not possible to insert glass dosimeters into the cold source any further than Z = 136 cm, so that the measured values are all in the upper half of the source. The extrapolation indicated in Figure 5.9.4 up to the bottom of the source at approximately Z

= 110 cm was carried out with the values measured in the reflector without internals (Figures 5.9.1 and 5.9.2), taking into account the slightly altered control rod position. The comparison with the measured values of the reflector without channels also shows that about half the dose at the location of the axis of the source stems from the structural material of the environment and half from the core.

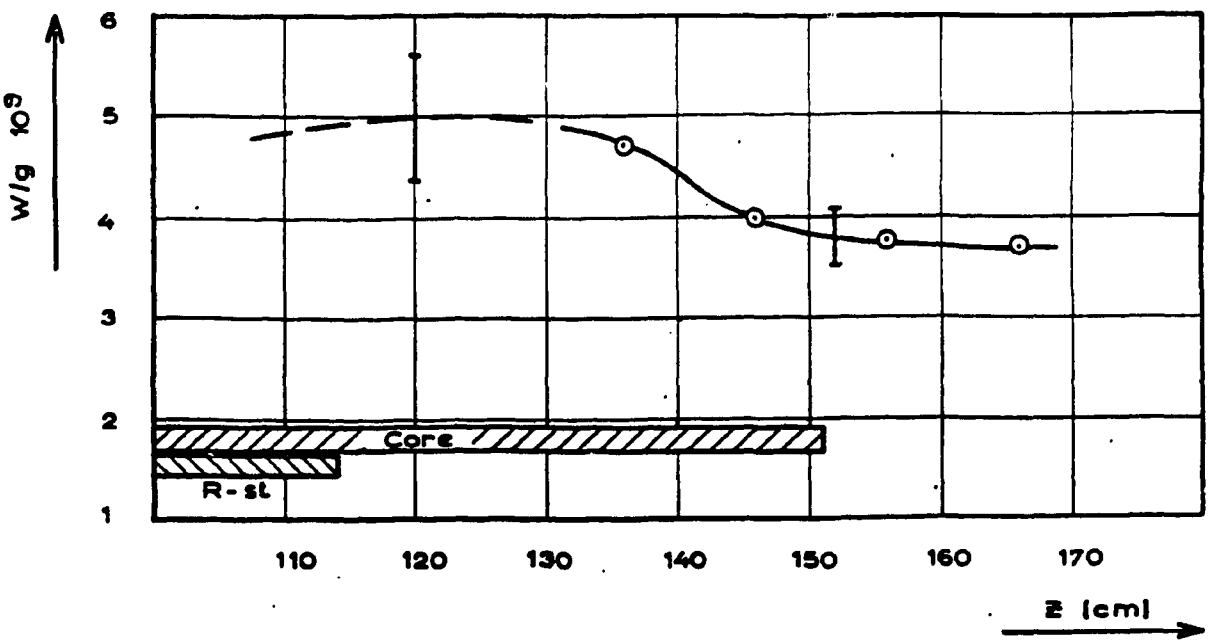

Fig. 5.9.4 Gamma heating on the longitudinal axis of the cold source on the radius R = 70 cm, measured with glass dosimeters. The bottom of the source is at Z = 110 cm. Configuration: with all beam holes (Scheme I), with solid boron. Reactor power = 1 watt.

The gamma dose in the hot source was investigated both on its longitudinal axis and on a diameter lying in the midplane of the source in the direction of the radius vector to the core axis. The axis of the source was on the radius R = 49.6 cm. During irradiation the glass dosimeters were located in channels having a diameter of 1.7 cm (see Figure 2.12). The interspaces between the glass dosimeters were filled with appropriate graphite plugs. The results of this test are shown in Figure 5.9.5: in Curve a as a function of the radius R, in Curve b as a function of the height Z. The broken line, Curve C, represents the distribution of the "unperturbed" gamma flux

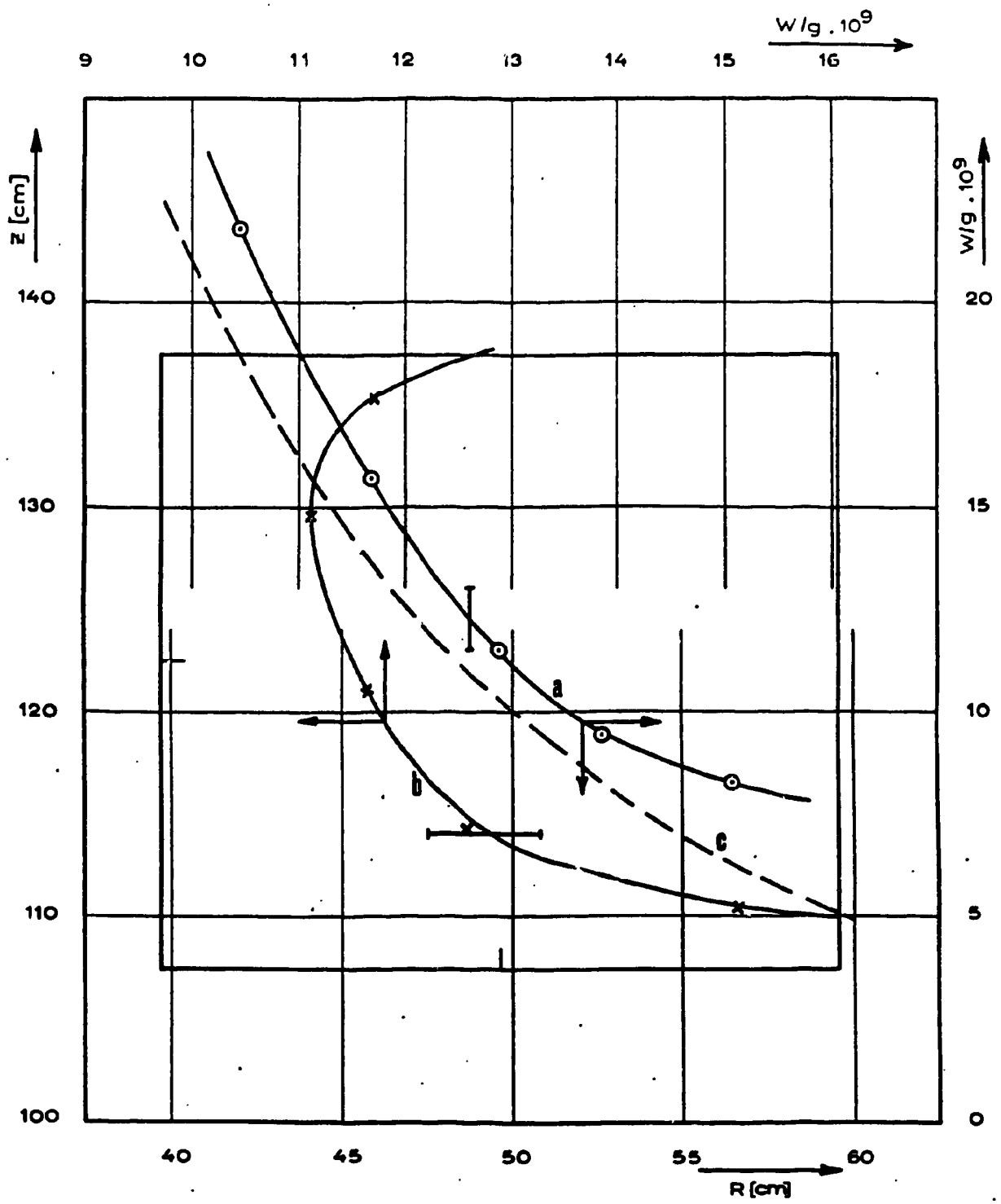

Fig. 5.9.5 Gamma heating on the longitudinal axis (Curve a) and on the transverse axis lying in the direction of the reactor radius R (Curve b) of the hot source, measured with glass dosimeters. z denotes the reactor axis. The broken line, Curve c, represents gamma heating without reflector internals. Configuration: with all beam holes (Scheme I), with solid boron. Reactor power = 1 watt.

in a radial direction. The comparison with Curve a shows that in this case the contribution of gammas from the structural material of the source and its environment relative to the core gammas is smaller than the contribution from the cold source, which is further from the core. The difference between this and the unperturbed gamma flux clearly becomes greater in the direction of the edges of the source, especially on the side facing away from the core. This phenomenon is even more pronounced for the longitudinal distribution, since there is relatively more structural material on the bottom and cover of the source (see Figure 2.12) than on the sides.

5.10 The Effect of the Placement of Source and Detector on the Counting Rate During Startup of the Subcritical Reactor

In the High Flux Reactor the startup source and the neutron detector, via which the flux development during reactor startup is observed, will each be installed on the periphery of the D_2O tank. To demonstrate that this will not lead to unrealistic 1/N curves (N = counting rate), an experiment was carried out in which the detector (BF^3 counting tube, Type 8E31) was fastened to support structure no. 5 at R = 99.5 cm and Z = 111 cm, and the neutron source (Am-Be, 300 mC) was mounted in one case on support structure No. 31 at R = 99.5 cm and Z = 111 cm (Position A) and in another case on support structure No. 23 at R = 99.5 cm and Z = 111 cm (Position B).

As usual the reactor was run critical, i.e., with safety rods withdrawn, control rod at H = 0, core and central stack filled with D_2O, the external reflector was gradually filled with D_2O until the level 220 was reached, and then the control rod was gradually withdrawn until the critical rod position was reached. The counting rates that were recorded in each of these steps are listed in Table 5.10.1; the inverse counting rate (1/N) is plotted as a function of the D_2O height and the control rod position in Figure 5.10.1.

The geometry of the reactor corresponded to State 3, i.e., with solid boron and beam hole dummies in the reflector (Scheme 1).

Table 5.10.1 List of the counting rates in the subcritical reactor

D_2O Level (cm)	Control Rod Position H (cm)	Counting Rates for 60 sec. Position A	Position B
116	0	1 800	
120	0	1 991	1 288
130	0	2 514	1 630
140	0	3 516	2 334
150	0	5 460	3 825
160	0	8 093	6 001
170	0	10 296	7 855
180	0	11 953	9 364
190	0	12 957	10 320
200	0	13 708	10 814
210	0	14 032	11 061
220	0	14 410	11 345
220	5	14 557	11 436
220	10	14 732	11 671
220	15	15 286	12 283
220	20	16 390	13 219
220	25	17 922	14 890
220	30	20 900	17 886
220	35	26 078	23 320
220	40	38 149	35 526
220	44	66 088	64 532
220	46	110 658	108 982

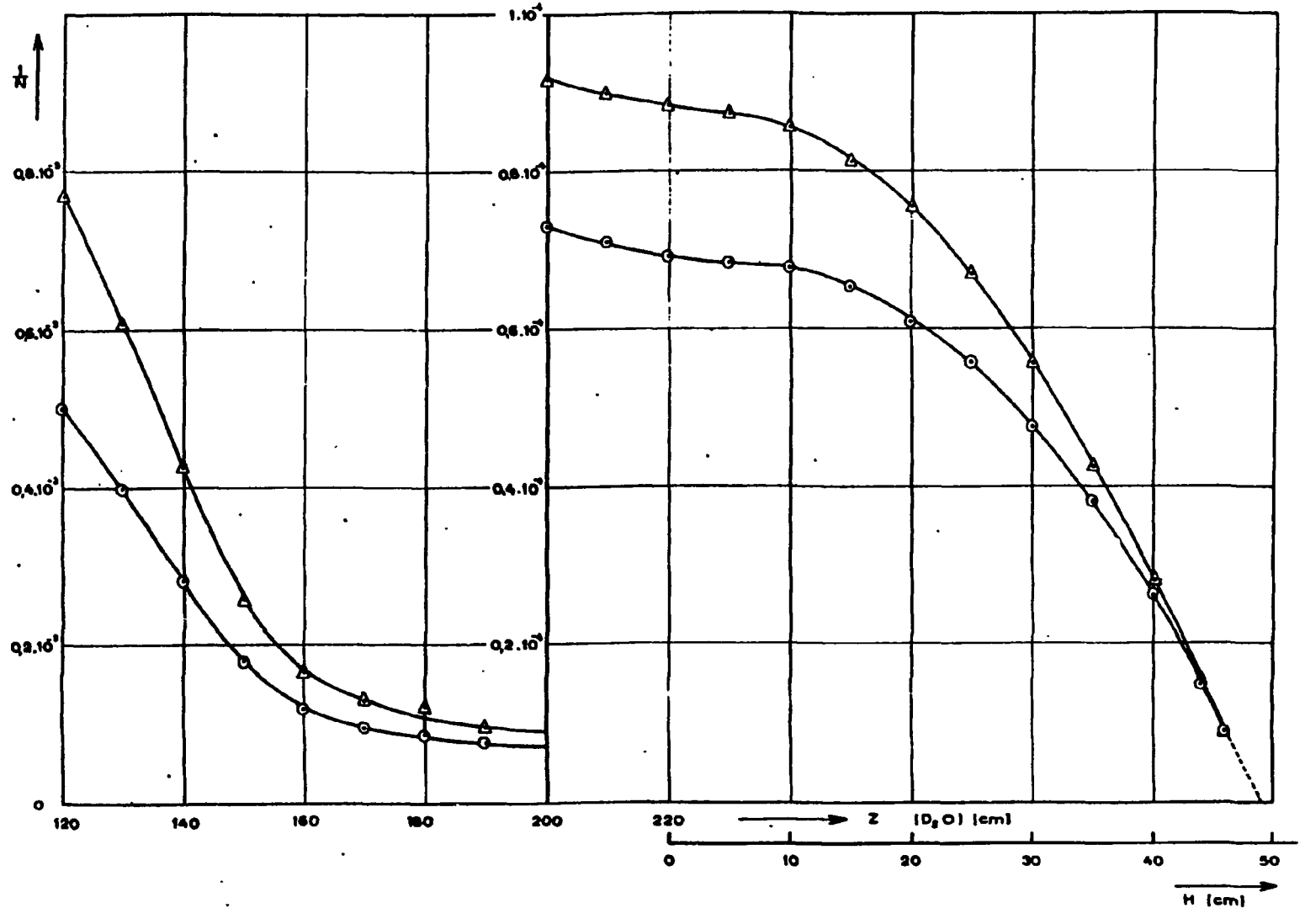

Fig. 5.10.1 Curve of the inverse counting rate during reactor startup. Triangles: source in Position A, circles: source in position B.

5.11 The Kinetic Parameters

5.11.1 The Life of the Prompt Neutrons

The life l_o of the prompt neutrons was determined using the pulsed neutron source method, as described in Section 4.4.3. This method makes it possible to measure the decay constant of the prompt neutron field, whereby for the critical reactor the following is true:

$$\alpha_c = \frac{\beta_{eff}}{l_o} ,$$

β_{eff} = effective fraction of delayed neutrons.

α_c is very much a function of the state of the reactor, i.e., of the control rod position and the internals in the reflector.

A calculation shows in the event of a great perturbation in the reflector, caused by 6 safety rods, α_{eff} increases by only 3.55% compared with the state without safety rods. Thus β_{eff} can be viewed as constant, and thus the dependence of α_c on the reactor state is caused by a variation in l_o.

Table 5.11.1 lists the α_c and l_o values for different reactor states.

The life was determined from α_c under the assumption that the calculated β_{eff} is correct:

$$\beta_{eff} = 0.00712.$$

Figure 5.11.1 shows the dependence of the decay constants in the critical reactor (α_c) as a function of the control rod position in different reactor states.

Table 5.11.1 Life and α for different reactor states

Reactor State	Control Rod Position H (cm)	α_c measured (sec^{-1})	l_o measured (sec)·10^{-3}	α_c calculated (sec^{-1})	l_o calculated (sec)·10^{-3}
without solid boron, without beam holes	0			7,52	0,947
	18,3	7,6 ± 0,1	0,94		
	36,4	7,7 ± 0,1	0,92		
	46,2	7,96 ± 0,1	0,89		
	50			8,20	0,868
STATE 1	60,6	8,1 ± 0,1	0,88		
	61,1	8,2 ± 0,1	0,87		
	82			8,54	0,834
	87,4	8,6 ± 0,1	0,83		
	100,1	8,9 ± 0,1	0,80		
with solid boron, without beam holes	36,6	8,5 ± 0,1	0,84		
	47,2	8,7 ± 0,1	0,82		
	47,7			8,74	0,815
	62,8	9,0 ± 0,1	0,79		
STATE 2	68,7	9,3 ± 0,1	0,77		
	85,7	9,5 ± 0,1	0,75		
with solid boron and beam holes	24,1	10,4 ± 0,1	0,68		
	47,2	10,6 ± 0,1	0,67		
	50			10,64	0,669
	57,8	11,2 ± 0,1	0,64		
STATE 3	68,2	11,0 ± 0,1	0,65		
	81,1	11,6 ± 0,1	0,61		

[Commas should be read as decimal points -- Transl. Note]

5.11.2 Delayed Neutrons

As was explained in Section 4.4.2, the result of a continuous run measurement is affected more by the knowledge of the groups of delayed neutrons, the longer the test lasts. The fact that the continuous run method yields false results in such long tests--longer than 100 sec--was easily shown by the fact that the calculated reactivity did not remain constant, even if the reactor remained in the subcritical state after a rod movement. The attempt was then made to adjust the constants of the delayed photoneutrons so that this phenomenon disappears. This was achieved in a preliminary test using an analog computer, whereby the group constants given in Table 5.11.2 were obtained. A more precise description is given in [30] and [17].

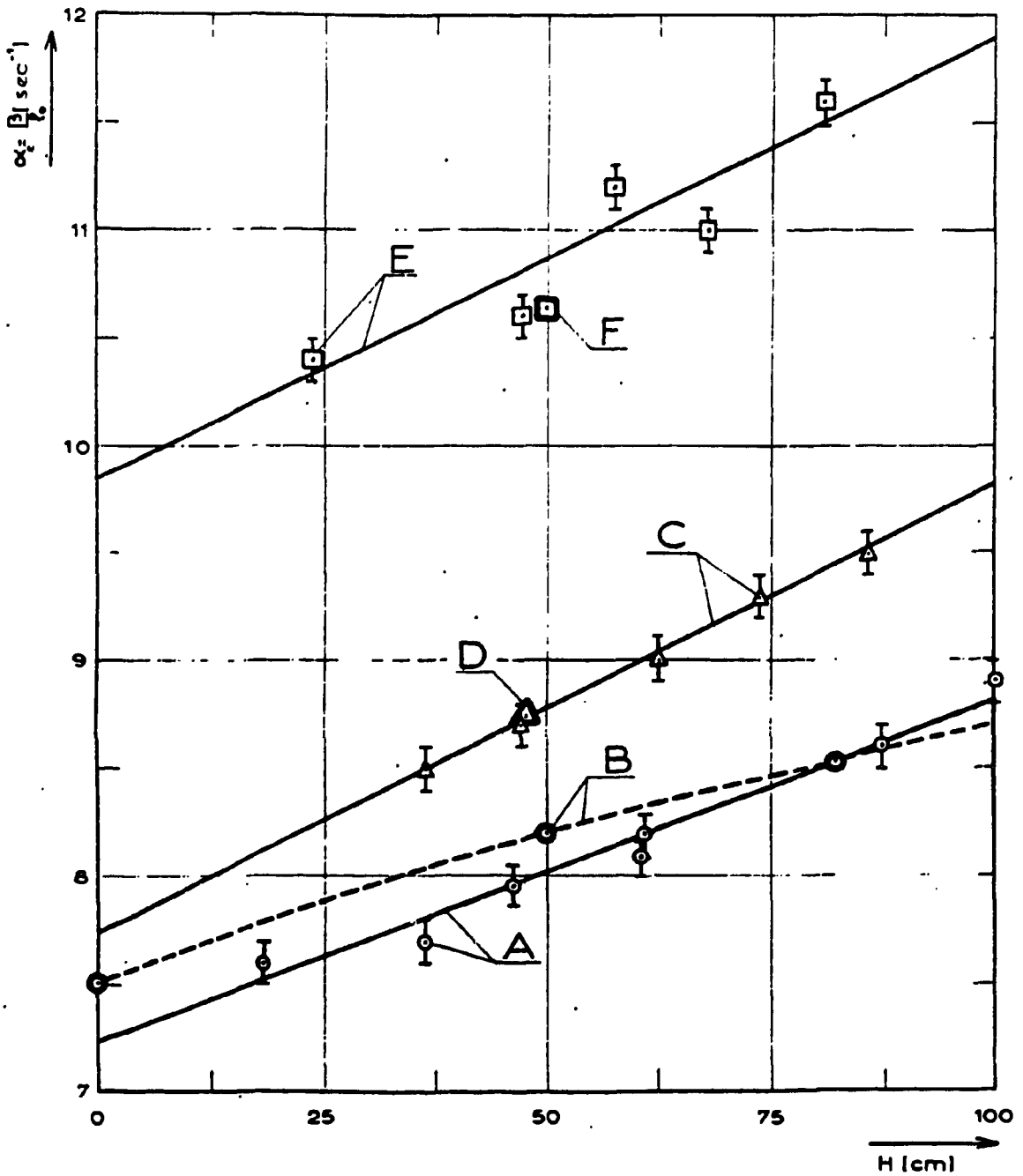

Fig. 5.11.1 α_c as a function of control rod position. A = measured value for the reactor without solid boron and without beam holes, B = calculated values for the reactor without solid boron and without beam holes, C = measured values for the reactor with solid boron and without beam holes, D = calculated values for the reactor with solid boron and without beam holes, E = measured values for the reactor with solid boron and with beam holes, F = calculated values for the reactor with solid boron and with beam holes.

Table 5.11.2 Data for delayed neutrons after adjustment using an analog computer to reactivity curves measured using the continuous run technique.

Group		a_i	$\beta_{i,eff}$	λ_i (sec^{-1})
Uranium 235	1	0,0315	0,000224	0,0124
	2	0,2093	0,001488	0,0305
	3	0,1875	0,001333	0,111
	4	0,3772	0,002682	0,301
	5	0,110	0,000782	1,13
	6	0,0399	0,000284	3,00
Photoneutrons	7	0,0302	0,000214	0,2772
	8	0,00281	0,00002	0,0169
	9	0,0115	0,000082	0,004813
	10	0,0007	0,000005	0,000428
	11	0,0007	0,000005	0,000117

[Commas should be read as decimal points -- Transl. Note.

5.12 Measurement of the (n,α) Reaction on the Stack

For the core tank the production of helium by the (n,α) reaction in the aluminum represents a metallurgical problem, since the material becomes embrittled by the helium. The level of the (n,α) reaction was measured with aluminum probes under cadmium:

$$\text{Al-27 } (n,\alpha) \text{ Na-24} \qquad T_{1/2} = 15 \text{ h.}$$

The effective reaction cross section is

$$\bar{\sigma}_F = 0.61 \text{ mb} \pm 5\%.$$

The probes were calibrated in the fission spectrum of uranium by comparison with nickel probes (Ni-58(n,p)Co-58, $\bar{\sigma}_F$ = 100 mb).

For the test the Al probes were mounted on the outer wall of the stack in the core midplane and irradiated for 3 hours at approximately 30 watts. A helium production of

$$1.5 \times 10^2 \quad \alpha/W/cm^3/sec$$

is obtained. According to the diffusion calculation the rise in the fast flux between the measuring point on the outside of the stack (R = 20.96 cm) and the inside of the core tank (R = 19.56 cm) is 35%, so that the maximum helium production rate on the radius R = 19.56 is determined as

$$2.0 \times 10^2 \quad \alpha/W/cm^3/sec.$$

The measurement error is 10%, of which 5% results from calibration of the probes and 5% from the imprecise knowledge of the reactor power during irradiation.

6. APPLICATION OF TEST RESULTS TO THE DESIGN OF THE HIGH FLUX REACTOR

Figures 6.1 and 6.2 show a vertical and a horizontal section through the D_2O tank of the High Flux Reactor. From the comparison with Figures 2.1 and 5.3.1 and on the basis of the differences between the High Flux Reactor and FOEHN listed in Section 2.4, it follows that not all values measured in FOEHN can necessarily be applied to the HFR. It is basically true that the comparisons made in this report between calculation and measurement also apply to the HFR, i.e., that a calculation performed for the HFR geometry will involve the same error as the corresponding calculation for FOEHN.

6.1 Reactivity

6.1.1 The Reactivity of the Reactor without Beam Holes and without Solid Boron

As shown in Section 5.1, the calculation overestimates the reactivity of the reactor without solid boron and without beam holes by about 600 pcm. The excess reactivity, that was calculated for the High Flux Reactor, will accordingly involve the same error.

6.1.2 The Reactivity of the Control Rod

Compared with the measurement by the stable period method, the calculation overestimates the effect of the control rod by 4.5%. The control rod of the High Flux Reactor must therefore be designed so that the calculation will yield a 4.5% higher reactivity than is necessary in reality.

6.1.3 The Reactivity of the Solid Boron Zones

The boron 10 loading of the solid boron zones used in FOEHN was 1.5167×10^{-4} A/cm^3, if the boron is homogenized in the entire zone, or 8.34 g B-10 overall. The loading of the 0.1 cm thick borated Al plates, of which the

boron zones were constructed, was 0.94×10^{-3} g/cm^2. The reactivity of the boron zones is overestimated by the calculation by about 8%. In order to keep the absolute amount of this error small in the HFR, the boron concentration should be selected to be as low as possible. Under the assumption that the calculated error is proportional to the boron concentration, we obtain for 1.0×10^{-4} B-10 A/cm^3 an error of 5.3% and a reactivity of - 4000 pcm for the control rod position H = 50 cm. The lack of reactivity would have to be canceled out by increasing the reactivity of the control rod.

6.1.4 The Reactivity of the Experimental Equipment

In comparison with the beam hole dummies used in FOEHN, the beam holes and experimental equipment of the High Flux Reactor (see Figure 6.2) differ in the following points (all values apply to the control rod position H = 50 cm):

The HFR channels are slightly tapered, have a wall thickness of 0.4 cm and are sealed off at the end by a semi-spherical shell having a wall thickness of 0.2 cm. The measured reactivity of the channel dummies without hot and cold sources is obtained according to 5.3.2 and 5.3.3 as -2000 pcm, of which 950 pcm is caused by the aluminum. If the channel wall thickness is doubled, it follows that $\Delta\rho$ (channels) = -2950 pcm.

The hot source will not have any cladding tube in the HFR, but the cavity required for insulation will be increased from 14 to 21 liters, so that its reactivity will amount to -790 pcm (see 5.3.3).

The cold source planned for the HFR will contain about 33×10^3 cm^3 more void and 7×10^3 cm^3 more aluminum than the dummy. This results in a reactivity of -500 pcm.

The hemispherical channel noses having a wall strength of 0.2 cm yield a positive contribution of +50 pcm over flat disks having a thickness of 0.4 cm.

The modifications of channels H5, H9, V4 and V6 as compared with the dummies used in FOEHN yield -400 pcm.

The total reactivity of the experimental equipment in the High Flux Reactor, as shown in Figure 6.2, is accordingly

$\Delta\rho$ = -4550 pcm,

if the control rod is in the core midplane.

6.1.5 The Safety Rods

The shutdown elements of the High Flux Reactor are formed by 5 rods that are slightly slanted with respect to the vertical and that are inserted into the reflector from above. The absorber section consists of a 80 Ag - 15 In - 5 Cd alloy in the form of a tube having an outside diameter of 10 cm and a wall thickness of 0.4 cm. In the inserted state the rods are located on the middle radius R = 28.8 cm, and the absorber section extends to the lower core edge.

In order to be able to apply the reactivity values measured in FOEHN to this safety system, we make the following assumptions:

Absorption is a surface effect and thus proportional to the total rod surface;

the Ag-In-Cd alloy has the same absorption effect as the Cd sheet used in FOEHN.

Thus we obtain the following values for the High Flux Reactor:

Five completely inserted rods with the control rod at H = 80 cm

$\Delta\rho$ = - 31,800 pcm,

five completely inserted rods with the control rod at H = 17 cm

$\Delta\rho$ = - 34,800 pcm,

three completely inserted rods grouped on one core side (worst position) with the control rod at H = 100 cm

$\Delta\rho$ = - 13,000 pcm,

a single, completely inserted rod with the control rod at H = 55 cm

$\Delta\rho$ = - 6,100 pcm,

reactivity of five rods in withdrawn position 40 cm above the upper

core edge at the end of the cycle, i.e., the solid boron zones are largely burned up, with the control rod at H = 70 cm

$$\Delta\rho = -230 \text{ pcm.}$$

The curve "without solid boron" in Figure 5.5.3 can be used directly as the reactivity characteristic of the safety rods of the High Flux Reactor at the beginning of the cycle at the start of their travel in the event of a scram.

The reactivities given apply naturally only in the sense of the definition given in Section 5.5, i.e., as equivalence values for boron dissolved in the core. No calculations of the safety system of the High Flux Reactor were carried out in conjunction with this research, but it was shown that the equivalent absorber method also achieves good results in the present case for complicated rod positions.

6.2 The Flux Distribution

The distribution of the thermal, epithermal and fast neutron flux can be calculated easily for the unperturbed reflector using the methods given. For the thermal fluxes on the beam hole noses, the values given in Table 5.3.3 can be directly applied to the High Flux Reactor. The flux-power calibration of the reactor instrumentation at low power can be based particularly on the flux value measured on beam hole No. 17 (V4 in the High Flux Reactor).

6.3 The Power Distribution

The calculated power in the "hot thread of stream" agrees with the measurements to within $\pm$ 1%. Due to the presence of experimental equipment in the reflector, particularly the hot source, the power distribution bulges in the azimuthal direction so that the power in the "hot thread of stream" is 2% above the expected value (see Figures 5.3.14 and 5.3.15).

6.4 The "Rendement"

The measured "rendement" (yield) for the reactor without beam holes is 3% below the calculated value. For the reactor with "homogenized" beam holes, the calculation overestimates the "rendement" by 6.5%. The "rendement," when referred to the individual beam hole noses, corresponds to the flux values in Table 5.3.3.

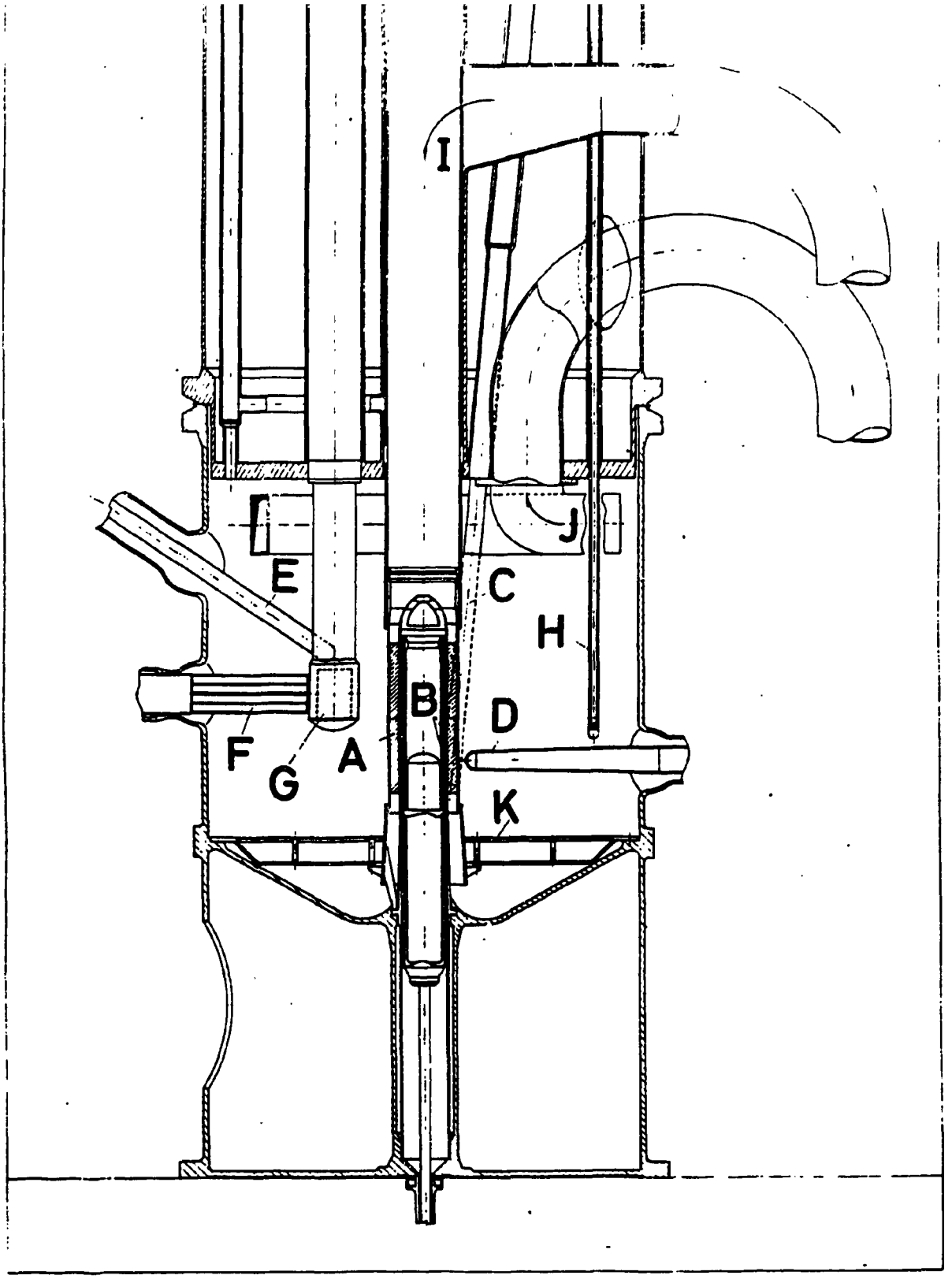

Fig. 6.1 Longitudinal section through the reactor unit of the Franco-German High Flux Reactor for comparison with Fig. 2.1. A = core, B = control rod, C = one of the five safety rods, D = horizontal standard beam hole, E = slanted beam hole, F = rectangular beam hole pointing toward the hot source (= G), H = vertical pneumatic tube, I = D_2O inlet, J = D_2O outlet, K = lattice for flow stabilization.

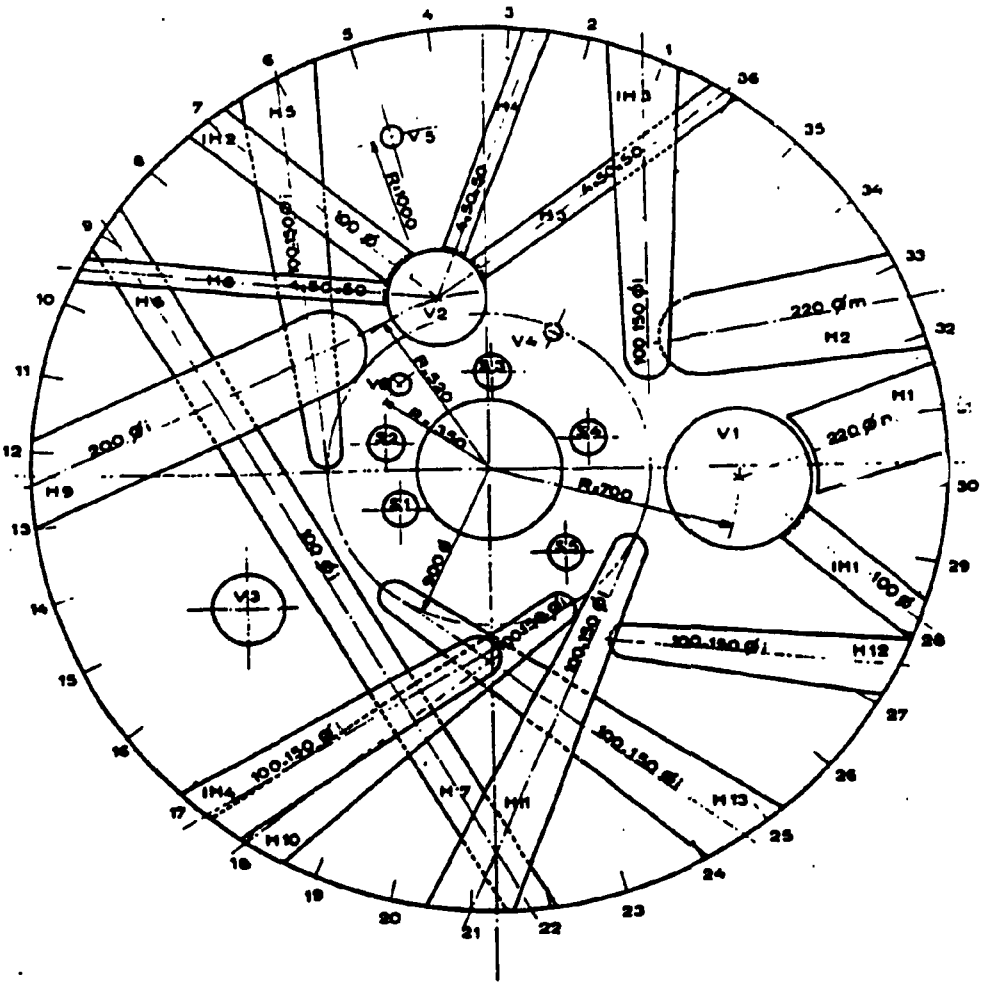

Fig. 6.2 Cross section through the reflector of the High Flux Reactor (cf. Figure 5.3.1 and Table 5.3.1). H1 - H13 = horizontal beam holes, IH1 - IH4 = slanted beam holes, V1 = cold source, V2 = hot source, V3 = beam holes for conversion electrons, V4 - V6 = vertical irradiation devices, S1 - S5 = safety rods (cut in the core midplane.

SUMMARY

The critical experiment FOEHN for the Franco-German High Flux Reactor was carried out from March 4, 1968, to January 31, 1969, in the reactor EOLE in the Cadarache Research Center in France.

FOEHN represented an exact model of the High Flux Reactor with respect to neutron physics. The excess reactivity was compensated for using a central absorber rod (nickel) and boron 10, which was dissolved in the heavy water of the fuel zone.

The experiments can be divided into five groups.

A. Measurements on the Reactor without Solid Boron Zones, Beam Hole Dummies and Safety Rods

This phase was used essentially for a comparison between calculation and experiment. The calculated k_{eff} values are a maximum of 600 pcm above the measured values, and the reactivity of the control rod is overestimated by the calculation by 4.3% (or 590 pcm). The calculated neutron flux distributions agree well with the measured values (2-3% for the thermal flux, 15% for the epithermal flux for R = 50 cm and 20% for the fast flux for R = 60 cm), as does the power distribution in the fuel zone. The ratio of power in the hot thread of stream to the mean core power is overestimated by the calculation by 0.4%. The "rendement" ($\Phi_{max,th}$/power) is overestimated by the calculation by 2.2%. The gamma flux distribution in the reflector was measured by ionization chambers and glass dosimeters and compared with the calculation.

B. Measurements on the Reactor with Solid Boron Zones, without Safety Rods and Beam Hole Dummies

In this phase the reactivity of the solid boron zones (zones that contain the burnup poison of the High Flux Reactor) and its effect on the reactor

were investigated. The reactivity of the solid boron zones is overestimated by the calculation by about 8% (or on the average 360 pcm). The effect on the reactivity of the control rod and on the flux and power distribution is reproduced well by the calculation (error as in A). The measured neutron density distribution in the solid boron zones agreed with the calculation with a deviation of $\pm$ 4%.

C. Measurements on the Reactor with Solid Boron Zones and Beam Hole Dummies, But Without Safety Rods

The beam holes and experimental equipment that were installed in the reflector of the High Flux Reactor were simulated in FOEHN by dummies such that the test results can be applied to the real geometry of the High Flux Reactor.

The reactivity of the totality of beam hole dummies was obtained as -3300 $\pm$ 160 pcm for a control rod position of H = 50 cm. The calculation, based on a simple homogenization model and disregarding the "streaming effect," yields -2380 pcm.

In addition, the reactivity of a few typical dummies was measured (hot and cold source, thermal neutron conductor) and also the effect of changes in the configuration of the dummies (switching of individual beam holes, moving beam holes closer to the core). The thermal neutron flux was measured on all beam hole noses and in the cold and hot source as well as on many points in the reflector, so that an azimuthally averaged flux distribution could be determined. The "rendement" was determined for this mean distribution. At r = 2.3 x 10^7 n/(cm^2sec W) it is 6% lower than the calculated value.

D. The Safety Rods

The safety rods of the High Flux Reactor were simulated by 6 tubes made of Cd sheet. Their reactivity was determined for numerous radial and axial

positions. A calculation method was developed that makes it possible to calculate a reactor of the present time with safety rods with practically the same accuracy as a reactor without rods.

E. Special Effects

In this test phase the following effects were investigated:

reactivity and flux perturbation of beam holes of different geometries,
the temperature coefficient of the reactor,
the void coefficient in the core,
the aluminum coefficient in the reflector,
the effect of the position of source and detector on the counting rate during startup of the subcritical reactor,
the prompt life and the β_{eff} value.

In a final chapter the application of the results of FOEHN to the design of the High Flux Reactor was examined.

REFERENCES

/1/ BECKURTS, K.H., R. DAUTRAY: Project Studies for the Franco-German High Flux Reactor. CONF-660925 Santa Fe, New Mexico, Sept.19-23, 1966.

/2/ CHATOUX, J., W. EISERMANN: Der deutsch-französische Hochflußreaktor in Grenoble. Atomwirtschaft, Jan. 1969. [The Franco-German High Flux Reactor in Grenoble]

/3/ GOLINELLI, C., H. TELLIER: Etude Neutronique d'un Coeur à Eau Legère Reflechi par de l'Eau Lourde. CEA-R-3318, 1967. [Neutron Study of Light Water Core Reflected by Heavy Water]

/4/ SCHARMER, K.: ALIZE III - First Critical Experiment for the Franco-German High Flux Reactor Calculations. CEA-R-3393(E), 1968.

/5/ EOLE-Rapport Général de Sûreté. CEA-SEN-188. [General Safety Report]

/6/ EOLE-Deuxième Rapport Particulier de Sûreté. CEA-SPM-990. [Second Detailed Safety Report]

/7/ BAYARD, J. et al.: Specification d'un Code de Diffusion Multigroupe à Deux Dimensions: ALCI CEA-R-2747, 1965. [Specification for a Two-Dimensional Multigroup Diffusion Code]

/8/ BOHL, H., Jr. et al.: MUFT-IV, Fast Neutron Spectrum Code for the IBM-704. WAPD-TM 72, July 1957.

/9/ HONECK, H.C.: Nucl. Sci. Eng. 8, 193-202 (1960).

/10/ THEYS, M.H.: Integral Transport Theory of Thermal Utilization Factor in Slab Geometry. Nucl. Sci. Eng. 7, 1, 58-63 (Jan. 1960).

/11/ BECKURTS, K.H., K. WIRTZ: Neutron Physics, Springer-Verlag, 1964.

/12/ KEAR, G.H., M.H. RUDERMANN: GEAP-3937, May 1962.

/13/ SPINKS, N.: AAEC/E 134, April 1965.

/14/ SPINKS, N.: Nucl. Sci. Eng. 22, 87-93 (1965).

/15/ KEEPIN, G.R. et al.: Phys. Rev. 107, 4, 1044 (1957).

/16/ Reactor Physics Constants, Sec. 5.3, ANL-5800, 2.Ed., 1963.

/17/ ECKERT, H.G., K. SCHARMER: to be published

/18/ BERNSTEIN, S. et al.: Phys. Rev. 71, 9, 573 (1947).

/19/ BROSE, M.: Nukl. 6, 134 (1964).

/20/ JIRLOW, JOHANSSON: J. Nucl. Energy 11 (1960).

/21/ BRISBOIS, J., M. LOTT, G. MANET: CEA-R-2491 (1964).

/22/ Fast Flux Measurements in Zero-Energy Reactors. AERE-R-4205.

/23/ ECKERT, H.G., R. JAQUEMART: to be published.

/24/ BRANDICOURT, G., J. CULAMBOURG: Programme NIOBE. CEA-583.

/25/ DEVILLERS, C.: Programme MERCURE III, CEA-R-3264.

/26/ BEAUCOURT, Ph. de, et al.: CEA-N-627.

/27/ BARTHE, J.P.: CEA-N-571.

/28/ BEHRENS, D.J.: The Effect of Holes in a Reacting Material on the Passage of Neutrons. The Proc. of the Phys. Soc., Sec.A, Vol.62, 7 (July 1949).

/29/ CARTER, C., R.J. JARVIS: J. Nucl. Energy, Parts A/B, Vol.15, 113-119 (1961).

/30/ LE BOT, M., Ch. DI FALCO, R. JAQUEMART: to be published.